Probing the Inner Regions Near Accreting Black Holes and Neutron Stars with Chandra

by

Nicolas Trueba

A dissertation submitted in partial fulfillment
of the requirements for the degree of
Doctor of Philosophy
(Astronomy and Astrophysics)
in The University of Michigan
2022

Doctoral Committee:

Professor Jon M. Miller, Chair
Professor Nuria Calvet
Professor August Evrard
Associate Professor Elena Gallo
Professor Jelle Kaastra - SRON Netherlands Institute for Space Research

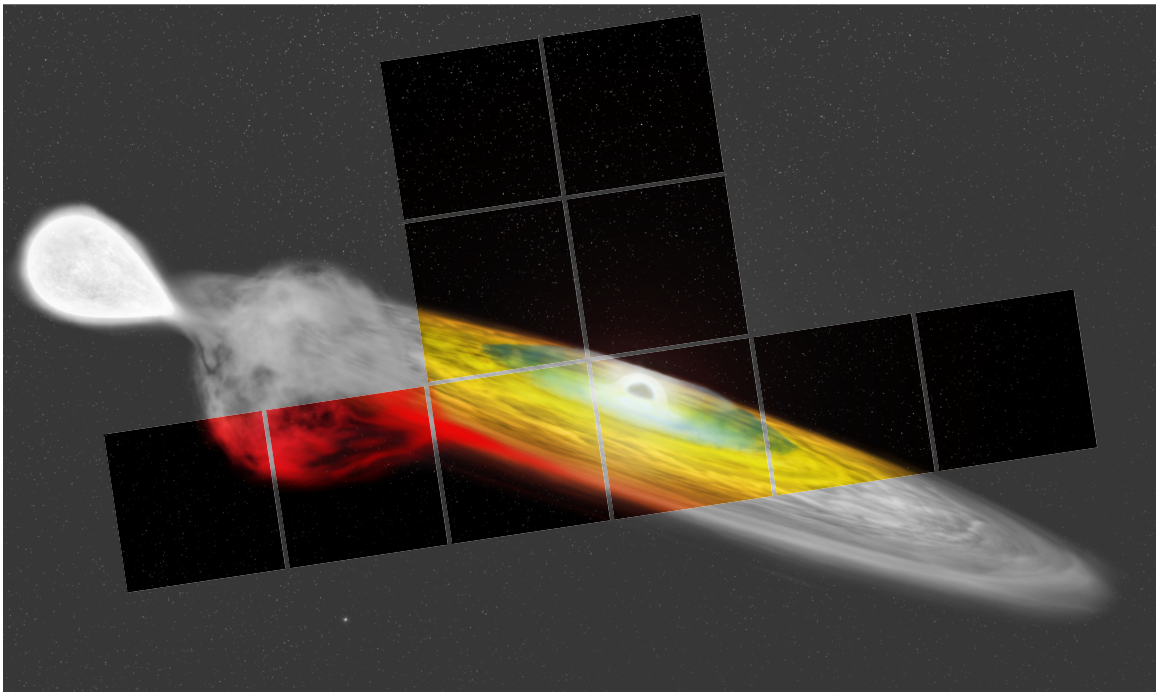

Credit: NASA/CXC/M. Weiss, modified by N. Trueba

Nicolas Trueba

ntrueba@umich.edu

ORCID iD: 0000-0002-3564-4506

ACKNOWLEDGEMENTS

"It is the struggle itself that is most important. We must strive to be more than we are. It does not matter that we will never reach our ultimate goal. The effort yields its own rewards."

—Lt. Cmdr. Data

I would like to thank my advisor, Jon M. Miller. It has been privilege to get a PhD in such a beautiful branch of astrophysics research under your guidance. Thank you for sharing your science with me, for your mentorship, and for always putting me in a position to succeed. I would also like to thank the members of thesis committee, professors Nuria Calvet, August Evrard, Elena Gallo, and Jella Kaastra. Thank you for your support, encouragement, and patience. Thank you Eric and Nuria for being there for the highs and lows of my time here. Massimo, thank you for guidance from the very start of my scientific career. Special thanks to John Raymond and Daniel Proga for their support and kindness.

It is impossible to adequately put into words how important the support of my friends and family has to been, and this statement of my appreciation will inevitably fall short. Thank you to my amazing wife, Ana. You supported me every step of the way. You always believed in me, even in moments when it was impossible for me to believe in myself. I would not be here without you. Thank you for being you, thank you for being in my life, and I cannot wait to continue our journey together.

To my parents, your unconditional support and belief in me is a debt I can never repay. To my mom, Elena, thank you for nurturing my love of science and my curiosity for the natural world from a young age. You introduced the world to me through books on

dinosaurs, sharks, and history, and shaped the way I look at the world. I could not ask for a better childhood. To my dad, Gabriel, you never pressured me into this career path, but your passion for science and understanding the world has always been more contagious than any pathogen in your lab. You will always be my hero and I hope one day I will be half the scientist you are. Thank you for supporting my choice to pursue music career wholeheartedly, and thank you for believing I was capable of getting to this point when I decided to pursue Astronomy.

To my sisters, Ana Francisca and Gabriela, I am in awe of what both of you have achieved and your strength in pursuing your goals. You are both trailblazers and you give me the courage to pursue my goals even when the road may seem terrifying. Thank you for being there in my most difficult moments. To my nephews, Gabriel and Nicolas, thank you for bringing pure happiness to all of us. Thank you to all the members of the Trueba and Yepez families for your support.

To Daniel, you will always be my best friend. I regret not being there for so much of the last 15 years but I take comfort in that our friendship is stronger than any physical distance. You are an amazing human being. To Sebastian, you are the greatest anomaly in my life. You are one of the few people that can truly understand what this journey has been like and I am in awe to have such a gifted musician, talented doctor, and amazing friend in my life.

To Kevin and Larissa, you are my grad school family. I did not realize until now that the hardest thing about graduate school will be leaving the two of you behind. It is a privilege to count myself as one of your friends. To Aleksandra, Adi, Erin, Kamber, and Renee, you are the scientists I could only hope to become, and then some. Thank you for being great mentors and, most importantly, amazing friends. I also need to thank my friends for introducing me to wonderful people like Kori and Jim. I am grateful to have both you in my life. To Matt, you are one of the best conversation partners I have ever encountered. Thank you for being my friend all those weekends and late nights we spent at the office.

Finally, thank you to all the graduate students I have had the pleasure of knowing these last five years, and thank you for tolerating the endless arguments between Matt and I.

TABLE OF CONTENTS

LIST OF FIGURES

Figure

LIST OF TABLES

Table

LIST OF APPENDICES

Appendix

ABSTRACT

Accretion disks are among the most important and well-studied objects in astrophysics. Disks play a critical role in both star formation and later stellar evolution, and are the site of planet formation. Compact objects accreting from a stellar companion may result in luminous and rapidly evolving UV or X-ray disks for white dwarf (WD) or stellar-mass black hole and neutron star (BH or NS) accretors, respectively. At the largest scales, accretion onto supermassive black holes is known to power active galactic nuclei (or, AGN). These are among the most powerful phenomena in the observable universe and their activity can have a profound effect on star formation and evolution of the host galaxy. Despite the astrophysical importance of the accretion process, as well as considerable observational and theoretical efforts, critical questions regarding specific physical mechanisms remain unanswered. There is broad theoretical consensus that angular momentum and mass transfer within the disk are likely mediated via magnetic processes; however, observational signatures of specific physical mechanisms are few and largely indirect, complicating efforts to characterize underlying processes. Likewise, magnetic processes may be central to the physics of the X-ray corona, potentially a cloud of hot in AGN and accreting NSs/stellar-mass BHs that imparts additional energy to disk photons via inverse Compton scattering. Our understanding of the geometry, energetics, and underlying physics of the X-ray Corona is limited and requires knowledge of its compactness - a difficult property to constrain observationally.

In this dissertation, I demonstrate how high-resolution X-ray spectroscopic studies of accreting black holes and neutron stars can address some of these issues. Specifically, I characterize absorption phenomena occurring above the disk's surface, such as disk winds and atmospheres, using astrophysical plasma models in order to probe the physical processes

that underlie the accretion disk. We find that the highly ionized disk winds (outflowing at $0.1\% - 1\%$ c) in BH candidate 4U 1630−472, for instance, are likely magnetic; the radial structure of these outflows may be indicative of magnetically driven accretion (Chapter II). Moreover, I present the discovery of gravitationally redshifted disk atmospheres in a sample of short-period neutron star systems. Like disk winds in BH systems, the location of these absorbers means that the atmosphere may require strong magnetic pressure support (Chapter III). Finally, I developed a new methodology for constraining the size of the central emitting regions of these systems, providing new angles on the physical nature of these emitters (Chapter IV).

CHAPTER I

Introduction

1.1 Accretion Disks: Overview

Accretion disks are central to the formation and evolution of a large fraction of the luminous structures in the universe. They are a necessary stage that allows large clouds of cold gas to collapse and form stars; the specifics of how this process occurs thereby dictates stellar evolution, as well as the formation, composition, and locations of planets born in the disk. Beyond star formation, accreting systems themselves are among the brightest astrophysical objects in the universe: accretion disks feeding supermassive black holes (or, SMBHs) power the luminous cores of galaxies that harbor active galactic nuclei (or, AGN). In addition to extreme luminosities, AGN expel powerful jets at galactic scales and massive winds which, in turn, can dramatically affect the evolution of the host galaxy by regulating star formation (see *Fabian*, 2012). Finally, accreting binary systems, especially those that include a compact object, power bright X-ray sources and are among the most rapidly and violently evolving systems in the galaxy.

Despite its importance, critical aspects of the accretion process are either poorly understood from a theoretical perspective or lack a robust observational basis. In this dissertation, I demonstrate how high-resolution X-ray spectroscopy of accreting stellar compact objects can help test theoretical models in two key areas: The role of magnetic fields in regulating angular momentum and mass transfer within the disk, and the nature of the X-ray corona

in accreting black holes and neutron stars. In this Chapter, I will first introduce the relevant theoretical background (Section 1.2). I will then discuss how X-ray binaries are excellent laboratories in which to test theoretical models (Section 1.3). Finally, I will discuss the importance of disk winds and other absorption phenomena for answering these questions (Section 1.4).

1.2 The Magnetic Nature of Accretion Disks

Accretion disks are complicated dynamic systems subject to multiple fluid and radiative processes. From relatively cold protoplanetary disks to the extreme X-ray emitting disks around black holes, the prevailing view is that magnetic processes play a central role in regulating the accretion process as a whole, and are responsible for much of the extreme phenomena observed in these systems (*Shakura and Sunyaev*, 1973; *Blandford and Payne*, 1982; *Balbus and Hawley*, 1991; *Hawley et al.*, 1995; *Calvet et al.*, 1993; *Hartmann and Kenyon*, 1996; *Armitage*, 2011; *Miller*, 2017; *Fukumura et al.*, 2017).

1.2.1 Mass and Angular Momentum Transport

Be it the collapse of a cold molecular cloud or the envelope of a star exceeding its Roche lobe within a binary system, conservation of angular momentum will eventually restrict the gas to a disk geometry around the accreting object. To first order, accretion disks are rotationally supported: like any orbiting body, gas orbiting around the accretor will maintain its motion unless it is subjected to some force. As gas travels inward, gravitational potential energy is first converted to kinetic energy that is then dissipated via viscous interactions as heat that is then radiated as light. Accretion disks are, therefore, powered by the gravitational energy of the accreted matter. Crucially, this process must not only dissipate energy, but also conserve angular momentum, l, given by

$$l = \mathbf{r} \times m\mathbf{v}, \tag{1.1}$$

where m is the mass and v is the velocity of the orbiting mass.

In a Keplerian disk, the orbital velocity is given by $v = \sqrt{GM/r}$, and therefore angular momentum can be written in terms of the orbital radius, r, as

$$l \propto r^{1/2}. \tag{1.2}$$

This means that some angular momentum is lost as gas travels inward within the disk. Angular momentum must be conserved, and therefore some material must carry this excess angular momentum outward.

The transport of angular momentum and dissipation of kinetic energy require some form of viscosity within the gas, analogous to friction acting on portions of a fluid moving relative to each other. In its simplest form, molecular and atomic collisions within the fluid would provide sufficient viscous interactions for accretion to occur. In the context of accretion disks, the magnitude of this type of molecular viscosity is negligible compared to the large viscosities required for a disk to accrete efficiently (*Shakura and Sunyaev*, 1973). The overwhelming consensus is that viscous transport arises from turbulent motions within the disk, where random bulk motion in the gas results in an effective viscosity between gas components with different relative velocities. *Shakura and Sunyaev* (1973) developed the now famous α-disk prescription to model viscous transport in turbulent accretion disk. The α-disk model successfully predicted much of the observed behavior of accreting systems prior to observation (e.g. the spectrum of X-ray binary disks before the launch of X-ray observatories; *Mitsuda et al.*, 1984; *Li et al.*, 2005; *Remillard and McClintock*, 2006); it is the standard for modeling the observed behavior of thin disks and the basis of most theoretical and numerical models of accretion disks. A relativistic treatment of the α-disk model was published by *Novikov and Thorne* (1973).

The α-disk prescription assumes some ad-hoc turbulent viscosity, the specific nature of

which is inconsequential to the model, parameterized using the α parameter as

$$\nu = \alpha c_s H, \tag{1.3}$$

where c_s is the local soundspeed, H is the scale height, and $\alpha < 1$. Limiting the value of α below unity is a consequence of how the model is designed: In a turbulent gas, any individual eddy must be subsonic and, naturally, smaller than the vertical extent of the disk. Equation 1.3 guarantees that neither limit is exceeded. The expected value of α from numerical models is $<< 1$, as observed in protoplanetary disks (e.g. *Hartmann et al.*, 1998; *Hueso and Guillot*, 2005), though in X-ray binaries it is found that $\alpha \sim 0.1 - 0.4$ (*King et al.*, 2007), or may even approach unity (see *Tetarenko et al.*, 2018).

Despite the success of the model, the ad-hoc nature of the α-viscosity does not provide many insights into the physics that drives turbulence in disks. It is unlikely that turbulence in disks can be attributed to a single process in its entirety, especially when considering different classes of accretors. The consensus is that turbulence in disks is likely driven, in large part, by a magnetohydrodynamic (MHD) instability known as the magnetorotational instability (MRI; *Balbus and Hawley*, 1991). The MRI is thought to be the dominant source of turbulent viscous transport in the hot, ionized disks in X-ray binaries as well as AGN. In cool and relatively neutral protoplanetary disks other processes are important and likely dependent on specific conditions, however, the MRI is still thought to play an important role (*Hawley et al.*, 1995; *Gammie*, 1996).

A useful, albeit simplified description of the MRI considers a thin accretion disk with vertical magnetic field lines within the disk itself. Due to complex MHD interactions, the discrete volume of gas surrounding a specific magnetic field line provides some degree of tension, meaning that relative motion between portions of this gas volume will produce a torque. Simplifying further, a commonly used toy model (see Figure 1.1 from *Hung et al.*, 2019) then treats this gas volume as two masses connected by a spring, lying vertically

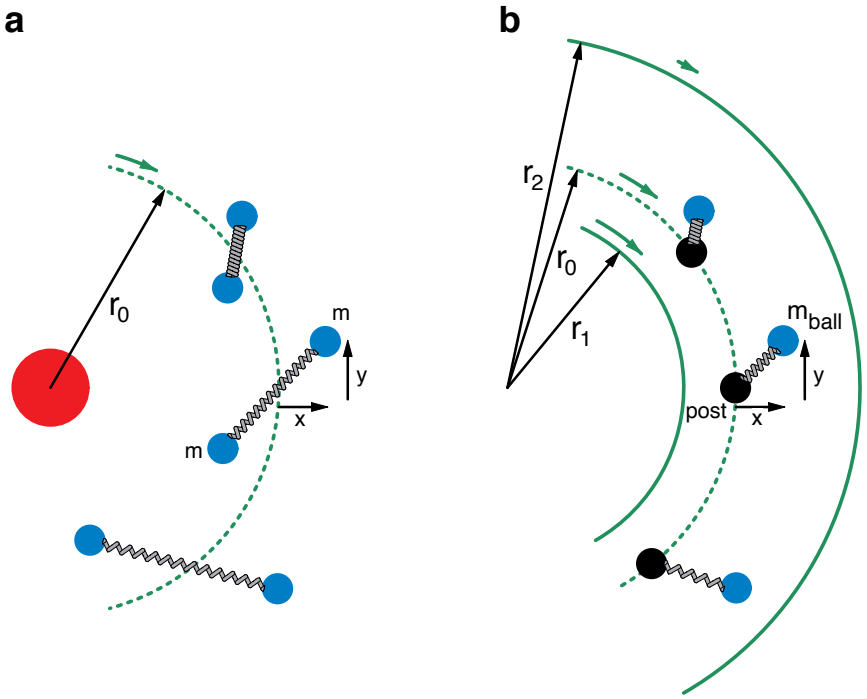

Figure 1.1: *Hung et al.* (2019) schematic of the MRI masses connected by springs analogy

in the disk. If one of these masses is subject to a perturbation that adds some angular momentum, then it will drift radially towards larger radii. Although angular momentum increases with radius, Keplerian velocity decreases. The resulting difference in velocity between the perturbed mass and the more rapidly rotating unperturbed mass produces a torque that removes some angular momentum from the inner mass and transfers it to the outer mass. This allows one mass to move radially inward while the other carries excess angular momentum outward.

Extensive studies since *Balbus and Hawley* (1991) have resulted in a robust theory of MRI disks, where substantial theoretical support has led to a strong consensus that the instability drives turbulence in disks (*Hawley et al.*, 1995, 1996; *Armitage*, 2011). Despite solid theoretical foundations, direct observational signatures of the MRI are virtually non-existent: the observational case for the instability, instead, relies mostly on indirect evidence which has not yet led to a detailed characterization of its behavior. Promising results based on an ALMA detection of Zeeman splitting in protoplanetary disk AS 209 (see *Harrison*

et al., 2021) may allow direct constraints on the local magnetic field strength. A similar study in TW Hya resulted in a non-detection, however, suggesting signatures of Zeeman splitting in protoplanetary disk are often too weak even in the most sensitive ALMA data (*Vlemmings et al.*, 2019). Ultimately, the lack of observational support for magnetically mediated angular momentum transfer not only limits our understanding of a central component of accretion physics, but limits our understanding of other disk phenomena that are likely magnetic in nature.

1.2.2 X-ray Corona

In addition to thermal continuum emission from the accretion disk, the observed spectra of accreting black holes (including both supermassive and stellar-mass black holes) and neutron stars often display a distinct X-ray emission component characterized by a non-thermal spectral energy distribution (or, SED). This bright X-ray component is particularly notable in AGN, as the accretion powered disk is expected (and observed) to peak in the UV. The shape of this non-thermal component is characteristic of inverse Compton scattering: Comparatively lower energy photons emitted from the dense accretion disk interact with a diffuse cloud of much hotter electrons (*Shapiro et al.*, 1976; *Sunyaev and Titarchuk*, 1980; *Zdziarski et al.*, 1998). Energy from the hot electrons is transferred to scattered photons, producing a harder spectrum and cooling the electron cloud. The character of the reprocessed spectrum depends on the temperature and optical depth of the electron cloud, and the shape of the incoming spectrum (*Titarchuk*, 1994).

Unlike disk emission, the properties and geometry of the X-ray corona both in AGN and X-ray binaries are harder to study observationally. Extensive timing and spectral studies of these systems strongly suggest the X-ray corona is compact and, to first order, co-spatial with the central black hole (*Fabian et al.*, 2015; *Wilkins and Fabian*, 2011; *Reis and Miller*, 2013). Studies of coronal X-rays reflected off the surface of the disk, in particular, suggest the X-ray corona is compact and located *above* the central black hole along the rotation

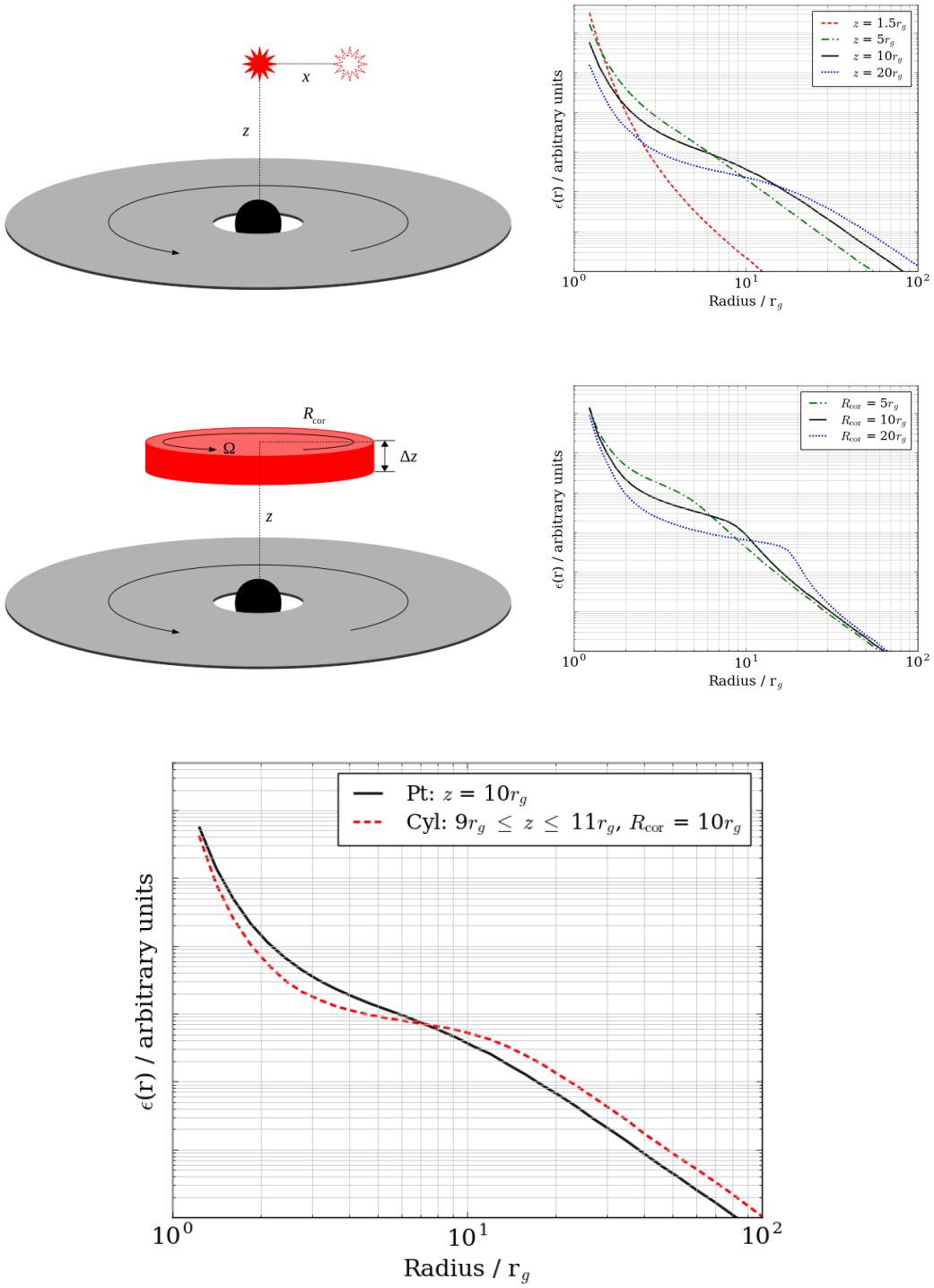

Figure 1.2: *Gonzalez et al.* (2017) toy models of point-like (top) and radially extended (middle) X-ray coronae, as well as the resulting disk emissivity profiles of reflected coronal emission. Radially extended coronal geometries in AGN are inferred from departures from point-like emissivity profiles (bottom, see *Wilkins and Fabian*, 2012; *Wilkins and Gallo*, 2015). See Figure 1.3 for more.

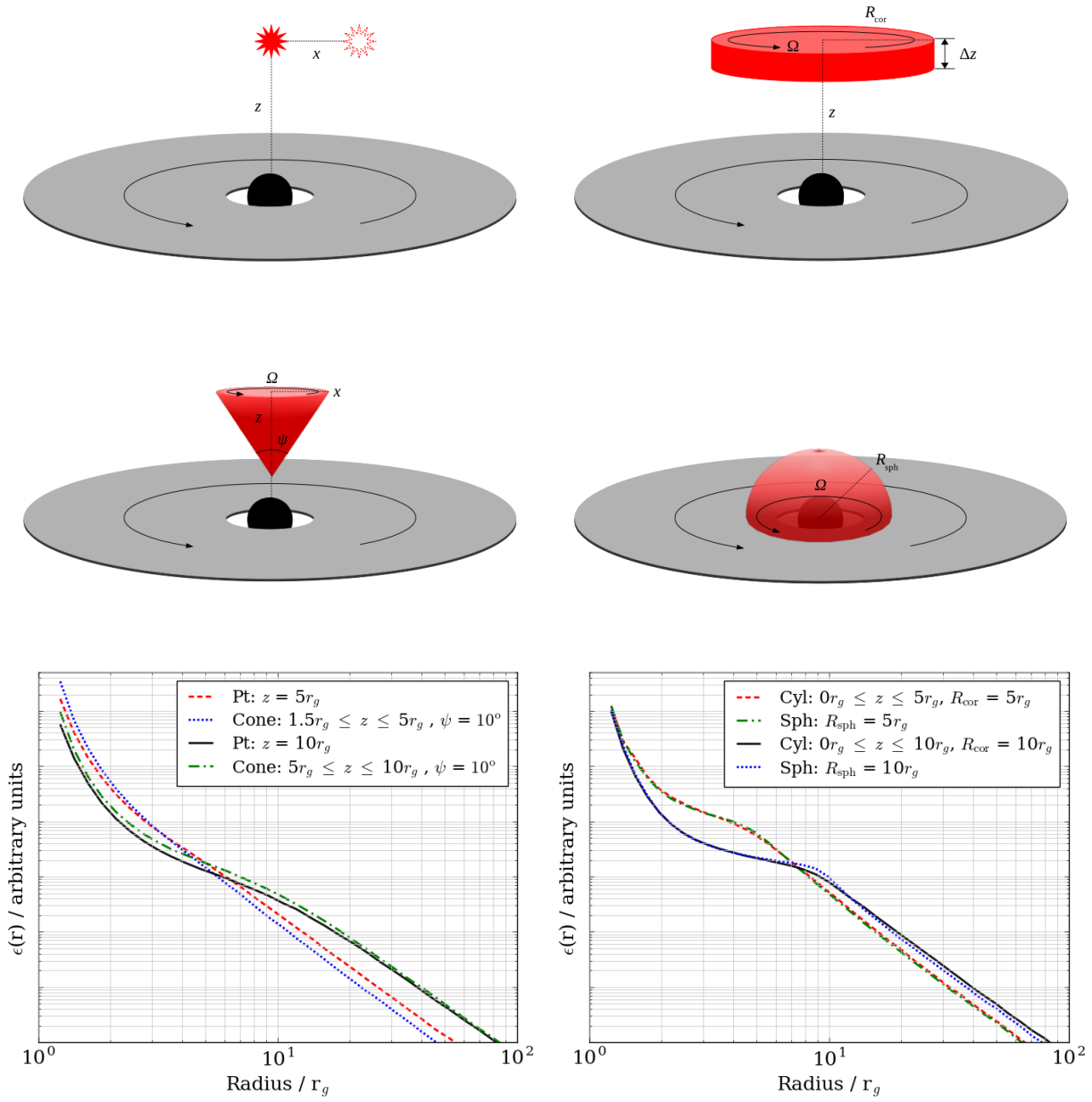

Figure 1.3: *Gonzalez et al.* (2017) emissivity profiles for additional toy model geometries of AGN corona. Left panels show point-like (top) and a conical (middle) geometries, the latter motivated by a plausible (albeit simple) geometry for the base of a jet. Right panels show extended cylindrical (top) and spherical (middle) geometries, where the latter represents a more physically motivated geometry for radially extended coronae. Profiles suggesting a compact corona are consistent with emission originating base of a jet (for beaming effects, see *Gonzalez et al.*, 2017), while extended geometries may indicate a broadly spheroidal geometry.

axis (see *Dauser et al.*, 2013, top panels of Figure 1.2). Observations of X-ray coronae, however, are not unambiguous and this simplified picture is likely to fall short. Conflicting observations of radially extended "coronae" (middle panels of Figure 1.2 *Gonzalez et al.*, 2017) are perhaps more indicative of a hot accretion disk atmosphere (middle-right panels of Figure 1.3) concentrated near the inner disk (e.g *Wilkins and Fabian*, 2012; *Wilkins and Gallo*, 2015).

The geometry and energetics of X-ray coronae pose important questions regarding the physics in these systems. There is broad agreement that these represent a magnetic phenomenon (see *Fabian et al.*, 2015), perhaps the base of a relativistic jet (*King et al.*, 2017, left panels in Figure 1.3). Evidence of variable coronae in AGN evolving between compact and extended geometries suggest these phenomena are likely related, where a magnetically confined extended corona evolves into a collimated jet (compact) that is later dissipated (e.g. Mrk 335, *Wilkins and Gallo*, 2015). Magnetic processes are likely central to the energetics of the corona, as *Merloni and Fabian* (2001) show that the thermal energy of electrons heated by an external source (possibly the disk) would require a large corona (with $r > 10^3\ GM/c^2$) to be in thermal equilibrium. A volume so large is incompatible with both observation and the known physics of accretion disk and, instead, the authors argue that the corona itself is a "reservoir" of magnetic energy. The specifics, however, remain unclear. It is also unclear whether the energy budget of disk emission is enough to power the luminous X-ray corona (*King et al.*, 2013; *Fabian et al.*, 2015), especially in X-ray binaries (or, XRBs) during radiatively inefficient states in which coronae are more commonly observed. Instead, seed photons may originate in the base of the jet itself in the form of optically-thin synchrotron emission (*Falcke et al.*, 2004). The main criterion for testing these scenarios is, again, the compactness of the source, a difficult property to constrain.

The X-ray corona may be a window into the nature of AGN and XRB jets, allowing for important connections with the dominant magnetic processes occurring within the disk: The *Blandford and Payne* (1982) mechanism, for instance, may be responsible for both

powering jets in radiatively inefficient states, as well as transporting angular momentum outwards in the form of winds in radiatively efficient states.

1.3 X-ray Binaries

The ubiquity of binary stellar systems provides yet another avenue for the formation of accretion disks, especially those with small orbital separations. The Roche lobe defines the surrounding volume where material is gravitationally bound to a star in a binary system. If material from one star extends beyond its Roche lobe, such as strong stellar winds from a massive star or the outer envelope of an expanding star evolving past the main sequence, then mass transfer will occur. Though this process can occur in binary systems consisting of many stellar types, the brightest disks are those in which the accretor is a compact stellar remnant (white dwarf, neutron star, or stellar-mass black hole).

Far from mere curiosities, accreting compact objects are excellent laboratories for testing models of accretion, in part because their emitted spectrum is often simple and closely follows predictions from the α-disk model (see Figure 1.4; *Davis et al.*, 2006; *McClintock et al.*, 2014; *Shakura and Sunyaev*, 1973). The thermal emission from accreting white dwarfs peaks in the ultraviolet, while more compact stellar-mass black holes and neutron stars result in a disk that peaks in X-rays (hence the term X-ray binaries). In contrast, the observed spectrum from both protoplanetary disks (PPDs) and AGN often diverge significantly from the thin-disk prediction, indicative of the complex radiative interactions (such as strong irradiation from the central star in PPDs) that further complicate efforts to identify specific signatures of accretion physics.

1.3.1 Low Mass X-ray Binaries

Low Mass X-ray Binaries (LMXBs) consist of a compact object accreting via Roche-lobe overflow from an evolved low-mass ($< 1 M_{\odot}$) stellar companion. BH LXMBs are often transient systems, switching between low-luminosity quiescent states to actively accreting

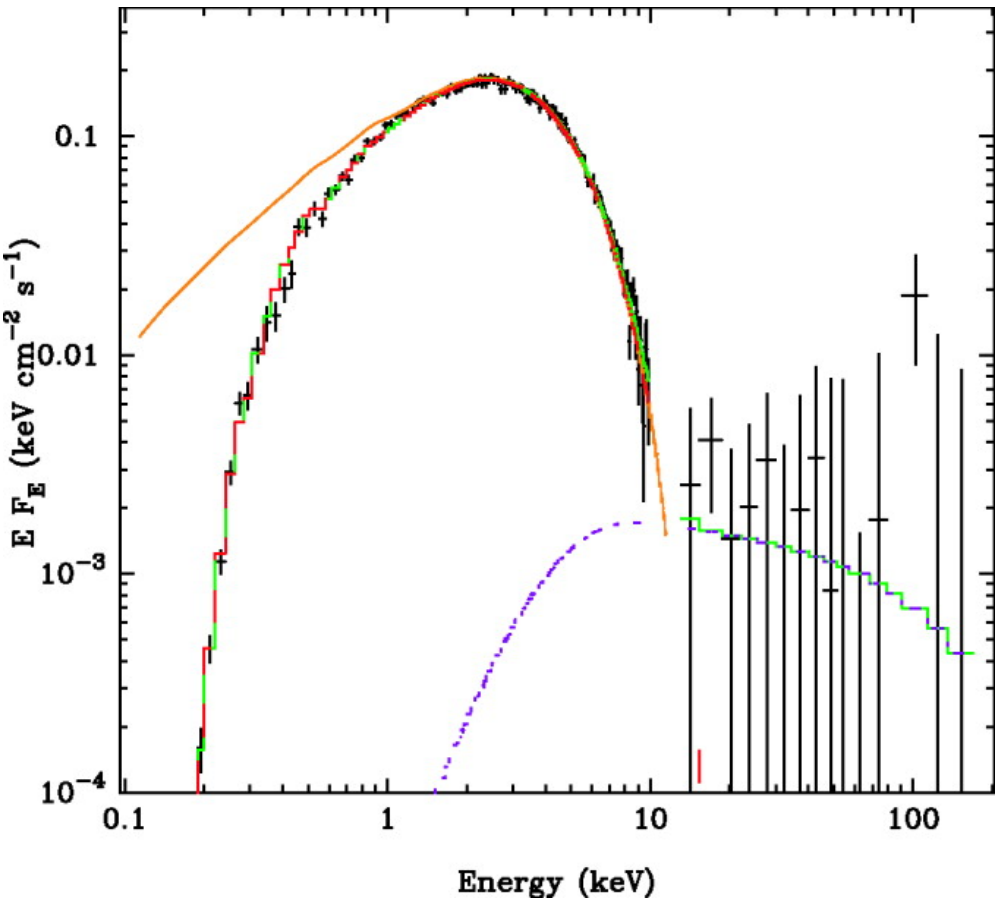

Figure 1.4: *Davis et al.* (2006) model of LMC X-3 in the soft state. The data are well-described using a disk blackbody model, modified by interstellar absorption (orange line shows the unabsorbed model continuum). Any non-thermal/power law component (violet line) is negligible. Image credit: *Davis et al.* (2006)

luminous outburst states. Timescales for outbursts vary significantly between sources: BH candidate 4U 1630−472 displays recurring outbursts spaced by about $\sim 600 - 700$ days and lasting ~ 200 days (*Capitanio et al.*, 2015), while others systems have outburst that span several decades (e.g. GRS 1915+105; *Miller et al.*, 2020). Temporal changes in the observational appearance of BH LMXBs are categorized into separate states based on flux and spectral character spanning multiple wavelength bands (radio to X-rays *Gallo et al.*, 2003; *Remillard and McClintock*, 2006), indicative of transitions between different physical phases of accretion. Historically, these are broadly categorized and labelled within the framework of separate X-ray flux/spectral states, though they are more accurately described as multi-wavelength states.

Three canonical X-ray states have been identified that are characteristic of BH LMXBs: The high-soft thermal state, dominated by a thermal emission from the disk (disk black-body); the low-hard state, dominated by a non-thermal emission that can be described with an X-ray power law with photon index $1.4 < \Gamma < 2.1$; and a very-high (or steep power law) state, characterized by emission from both the disk and a soft ($\Gamma > 2.4$) power law, high ($L > 0.2L_{edd}$) Eddington fraction (see *Remillard and McClintock*, 2006). The power law component is typically attributed to Comptonization from a central hot X-ray corona. Hard X-rays from the corona are often reprocessed by the disk as relativistically broadened X-ray fluorescent lines (*Fabian et al.*, 1989), reflection features that are mostly found in hard spectral states.

Though broad connections between BH and NS LMXBs states can be identified, the spectral variability in often persistent NS LMXBs is more complex, in large part, due to the presence of emission from the NS surface. These are broadly categorized as either "atoll" or Z-sources based on the shape produced on a color-color diagram (here, color refers to the flux ratio between two X-ray bands) as the source evolves through different spectral states (*Hasinger and van der Klis*, 1989). Of the three NS LMXBs considered in this dissertation, both 4U 1916−053 (*Galloway et al.*, 2001) and AX J1745.6−2901 (*Maeda et al.*, 1996)

are classified as atoll sources. While the poorly studied XTE J1710−281 is not classified as either atoll or Z-source, its low Eddington fraction of $\sim 0.04 L_{Edd}$ at peak brightness (*Galloway et al.*, 2008) is largely incompatible with the high luminosities ($L > 0.5 L_{Edd}$) typical of Z-sources (*Hasinger and van der Klis*, 1989). We therefore limit this discussion to atoll sources.

Atoll sources display similar spectral variability as BH LMXBs, covering a similar luminosity range (10^{-3} to L_{Edd}), as well as distinct hard and soft spectral states analogous to those in BH systems (*Muñoz-Darias et al.*, 2014; *Done et al.*, 2007, and references therein). Emission from the NS surface contributes to the overall spectrum and provides another source of seed photons for additional Comptonization components, complicating efforts to characterize these states. However, it is clear that thermal emission from the disk is prominent during the soft state, as in BH LMXBs (e.g. *Armas Padilla et al.*, 2017).

This dissertation focuses primarily on high-soft states during which the disk can be broadly described within the framework of the α-disk prescription, as opposed to states that diverge from this prescription at near-Eddington luminosities or during radiatively inefficient hard states. Crucially, absorption from disk winds is almost exclusively found during the thermal state of accreting stellar-mass BHs (*Miller et al.*, 2006a). Similar correlations between the presence of ionized absorption and spectral state have been observed in some atoll NS sources, as well (e.g. *Ponti et al.*, 2018b).

1.4 Disk Winds and other Absorbers

Disk winds are a nearly ubiquitous phenomenon in accreting systems, and often are among the most prominent observational features both in absorption and emission. Evidence of Magneto-centrifugal winds (*Blandford and Payne*, 1982) in PPDs (e.g. *Calvet et al.*, 1993) suggest these winds are integral to the outward transport of angular momentum and thus a critical component of the accretion flow. Massive winds in AGN may originate from the disk or the torus, confuse observations of AGN SED, and affect galactic evolution. Though

radiation pressure likely plays a role in driving some AGN winds (*Kallman and Dorodnitsyn*, 2019), the presence of higher ionization warm absorbers (e.g. MCG−6−30−15; *Young et al.*, 2005) and so-called ultra-fast outflows (or, UFOs; *Tombesi et al.*, 2014) are likely indicative of magnetic driving.

Since the launch of NASA's Chandra X-ray Observatory, observations using the High-Energy Transmission Grating Spectrometer (HETGS) have revealed rich absorption features owing to massive disk winds in XRBs. Specifically in BH systems, estimates of wind mass outflow rates are often found to match and sometimes even exceed the mass accretion rate onto the BH, and therefore are an important component of the broader accretion flow (*King et al.*, 2013). Moreover, their high ionizations and outflow velocities are generally incompatible with winds driven via radiation pressure. This is a common stellar wind driving mechanism in high-mass stars, as well as in disk winds found in accreting white dwarfs (e.g. *Drew and Proga*, 2000). Magnetic driving has therefore been identified as a likely candidate for driving the extreme winds in systems such GRO J1655−40, GRS 1915+105, and 4U 1630−472, based on wind launching radii, densities, and outflow velocities (see *Miller et al.*, 2015a). This interpretation, however, is not universally accepted, with some arguing these are simply thermally driven outflows (e.g *Done et al.*, 2018).

Despite some disagreement in the field, disk winds BH XRBs have emerged as excellent indicators of magnetic activity within the disk, with considerable efforts dedicated towards establishing driving mechanisms. This section presents a brief overview of the last 20 years of Chandra/HETG science on XRB disk winds (primarily BH LMXBs).

1.4.1 Winds in X-ray Binaries

Strong evidence of narrow X-ray absorption features in XRBs was first reported by *Miller et al.* (2002) in the Chandra/HETG spectrum of the BH candidate XTE J1650−500. This was followed-up with the detection of blueshifted absorption lines detected in the HETG spectrum of GX 339−4, of a possible disk wind analogous to AGN warm absorbers (*Miller*

et al., 2004a,b).

A pivotal breakthrough resulted from a 2005 Chandra/HETG observation of the BH LMXB GRO J1655−40 during outburst, which revealed a rich spectrum containing multiple blueshifted absorption lines. The analysis by *Miller et al.* (2006a, 2008) revealed absorption line originating from multiple charge states (i.e H-like and He-like) and transitions of ionized elements such as Ne, Si, Ar, Ca, and Fe, among others. Blueshifts for individual lines were found to range from 100s to 1000s km s^{-1}, indicating a wind complex composed of multiple velocity and ionization components which would be confirmed by subsequent analyses (*Miller et al.*, 2015a; *Fukumura et al.*, 2017). Crucially, the quality of the spectrum allowed for the gas density of the wind to be estimated via line ratios of different Fe XXII line transitions. An independent constraint of the gas density, n, is key when estimating the distance of an absorber from a photoionizing source

$$r^2 = \frac{L}{n\xi}, \tag{1.4}$$

where L is the luminosity of the source and ξ is the X-ray photoionization parameter used by various X-ray codes. This distance is a good proxy for the launching radius, the location in the disk from which a wind is launched, and it is a key criterion for ruling-out thermal driving as an alternative launching mechanism. Models of thermally driven winds postulate that X-rays from the central engine irradiating the cooler outer regions of the disk can provide enough heating (via compton scattering) to drive a wind from the disk surface. The gas cannot be heated beyond the temperature of irradiating photon field, meaning that a wind can only be launched if thermal motions exceed the local escape velocity. This limits effective thermal driving to radii larger than $0.1R_c$ (*Woods et al.*, 1996) where R_c is the Compton radius, defined as the radius at which the gravitational potential energy of the gas matches its thermal energy due to Compton heating (*Begelman et al.*, 1983).

Modelling the photoionized absorption in GRO J1655−40 revealed a wind launched from

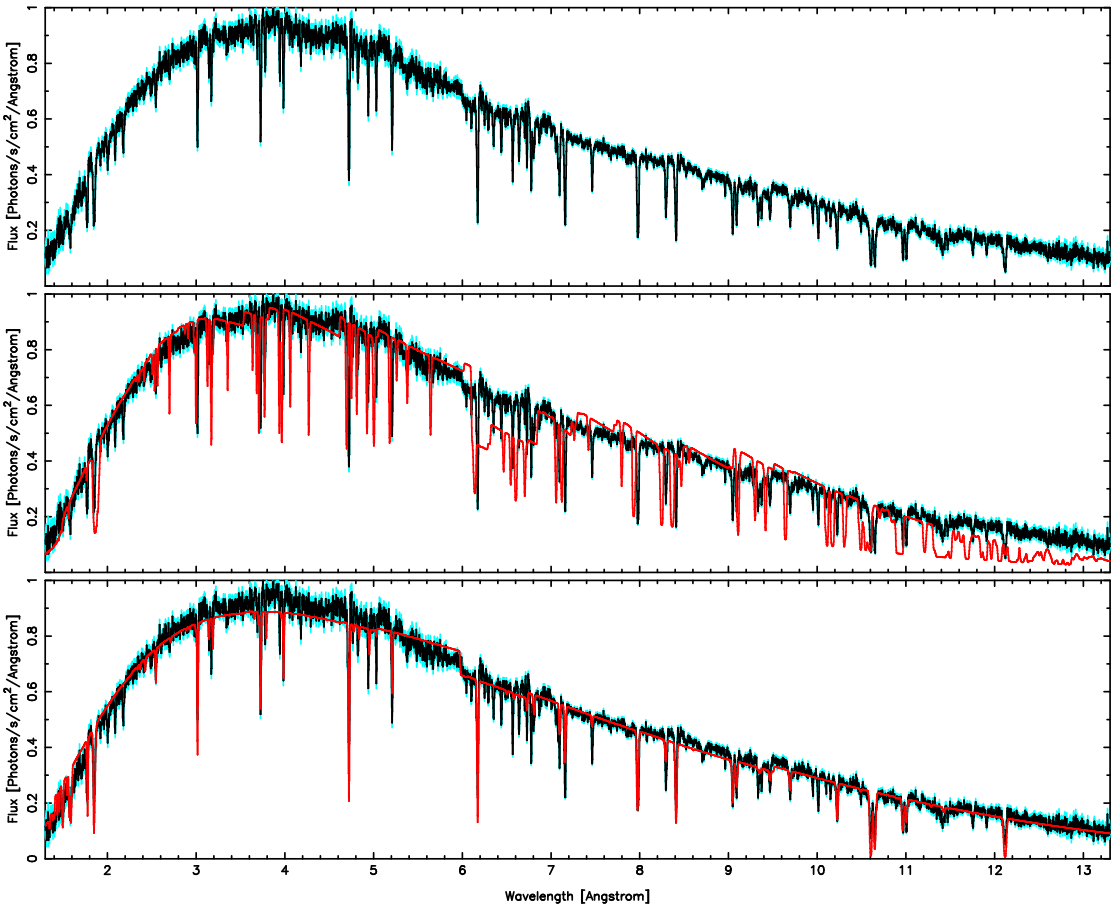

Figure 1.5: *Miller et al.* (2008) spectrum of GRO J1655−40 (top panel), comparing thermal (middle panel) and magnetic wind (bottom panel) photoionized absorption models.

small orbital radii inconsistent with thermal driving, and mass outflow rates drastically exceeding those predicted by thermal wind models (*Miller et al.*, 2006a, 2008). Figure 1.5 shows fits to the Chandra/HETG spectrum of GRO J1655−40 from *Miller et al.* (2008), where a magnetic wind models provides a much better description of the data compared to the thermal wind model. These results were key in establishing a likely magnetic origin for the most extreme disk winds in BH X-ray binaries.

Subsequent observations of other BH LMXBs (e.g. *Kallman et al.*, 2009; *King et al.*, 2012, 2013; *Neilsen and Homan*, 2012; *Miller et al.*, 2015a, 2016) have revealed common characteristics among these outflows: Large absorbing columns ($N_H \sim 10^{21}$ to 10^{24} cm^{-2}), outflow velocities (v_{out} ∼100s to 1000s km s^{-1}), and ionizations (log $\xi > 3.0$). The high degree of ionization in these winds is incompatible with radiation pressure driving, as UV transitions required for line-driving (as in the stellar winds in some high-mass stars) are largely unavailable in ions that are largely stripped of their electrons (*Proga*, 2003). Winds are generally found in sources viewed at high-inclinations, suggesting the outflows are largely equatorial, driven at small angles relative to the surface of the disk (*Miller et al.*, 2006b,a). Small launching radii are common, though many wind components have been found to originate at large radii where thermal driving cannot be ruled-out, though many of these constraints rely on some assumed gas density. Robust upper-limits using the column density, however, as well as constraints of the local Keplerian velocity via P-Cygni profiles (wind re-emission), suggest small radii relative to R_C (see *Miller et al.*, 2015a, 2016).

Estimates of wind mass outflow rates ($\dot{M}_{out}$) based on spectral models are often found to expel a large fraction of the mass accretion rate onto the black hole and, sometimes, even exceeding it (e.g. *King et al.*, 2013; *Miller et al.*, 2015a). This points towards the importance of winds to the overall accretion flow of the system, removing a large fraction of material from the disk before it can be accreted onto the black hole. Moreover, large $\dot{M}_{out}$ values may perhaps be indicative of the importance of winds as outward carriers of angular momentum if driven by magnetocentrifugal forces, as is the case in FU Ori systems

(*Blandford and Payne*, 1982; *Calvet et al.*, 1993). Alternatively, massive outflows driven by MHD pressure could be a direct consequence of magnetic process in MRI disks (*Hartmann and Kenyon*, 1996; *Miller et al.*, 2016; *Fukumura et al.*, 2017).

A final key feature of BH LMXBs disk winds is their strong dependence on the accretion/spectral state of the source, and the strong anti-correlation with the presence of a relativistic jet (*Miller et al.*, 2006b, 2008; *Neilsen and Lee*, 2009; *King et al.*, 2012). The strongest disk wind absorption is nearly exclusively found during soft, disk dominated spectral states. While tenuous wind absorption can be seen within intermediate states, winds appear to be entirely absent in hard spectral states strongly linked to the presence of relativistic jets. It is possible that the hard X-ray tail of the non-thermal emission component could further ionize the absorbing gas and entirely strip most ions from their electrons, resulting in a wind that produces no detectable absorption lines yet is still present. While hard X-rays should almost certainly contribute to increased ionization in hard states, analyses of the photoionizing flux in these states strongly indicate that winds are indeed absent (*Miller et al.*, 2012). Moreover, analyses of radio observations show little to no jet activity in state in which winds are strongest (e.g. *Fender et al.*, 2004).

The anti-correlation between winds and jets may indicate a shared physical origin: Different configurations of the disk's magnetic field geometry may be more conducive to one type of outflow (*Miller et al.*, 2012). This is supported by the fact that the relation between the kinetic power of winds and jets appears to span the entire BH mass scale (*King et al.*, 2013). Higher velocity wind components ($> 0.01c$), UFOs, may even represent a a transition between winds and jets given that their energetics more closely resemble those of jets (*King et al.*, 2013).

In addition to disk winds, we have seen other absorption phenomena in the disk with analogous behavior to disk winds. Some systems display absorption with no detectable velocity shift, suggesting a portion of the disk atmosphere has a large enough scale-height to intercept the line-of-sight (e.g. *Ponti et al.*, 2018b). Observationally, their similarity to

disk winds suggests that their lack of apparent acceleration is a minor distinction and that perhaps these phenomena are closely related and dependent upon the Eddington fraction, as will be discussed in Chapters III and IV. The increased sophistication of analysis techniques, the growing archive of Chandra/HETG observations, and the anticipation of next-generation X-ray spectroscopy missions (XRISM, ATHENA, and ARCUS) show promise of answering open questions about the physics of disk winds.

1.5 Dissertation Overview

Chapter II presents a study of the disk winds in black hole candidate 4U 1630−472, consisting of six archival Chandra/HETG observations. I used PION, a self-consistent photoionized absorption/emission spectral model within SPEX (*Kaastra et al.*, 1996, 2018), to model both the photoionized absorption and dynamically broadened re-emission of the disk wind complex. The spectrum for most observations required 2 distinct "photoionization zones" (absorption + emission) with different ionizations, columns, and outflow velocities to capture the absorption features. We found wind launching radii, densities, and outflow velocities that are inconsistent with thermal driving and, therefore, indicative of magnetic driving. In addition, the average wind density and velocity structure (derived from 4 separate observations) is consistent with predictions of winds driven by MHD pressure.

In Chapter III I performed an analysis of the NS ultra-compact X-ray binary (or, UCXB) 4U 1916−053 on a 250ks Chandra/HETG campaign. We found redshifted absorption owing to a disk atmosphere. The orbital radius of the absorption based on the photoionization, as well as various estimates of the system's relative radial velocity, suggest the shift is likely gravitational in origin. In addition, we identified redshifted absorption lines in archival Chandra/HETG spectra of two additional short-period NS XRBs: XTE J1710−281 and AX J1745.6−2901.

Chapter IV presents a study of how the velocity-width of absorption lines is affected by the size of the central engine when the absorber is located at small orbital radii. I develop

the theory and methodology for constraining the central engine size in accreting compact objects by measuring this width. I then apply the method on Chandra/HETG spectra of the 3 ultra-compact/short-period X-ray Binaries from Chapter III. In addition, this Chapter follows-up on the results from Chapter III by making the case for gravitational redshift on these three sources.

Finally, Chapter V presents concluding remarks and some recommendations for immediate follow-up to the work presented in this dissertation.

CHAPTER II

A Comprehensive Chandra Study of the Disk Wind in the Black Hole Candidate 4U 1630−472

2.1 Preface

This chapter appears in the Astrophysical Journal, Volume 886(2), pp 104 (Trueba et al., 2019). The paper is co-authored by Jon M. Miller, Jelle Kaastra, Abderahmen Zoghbi, Andrew C. Fabian, Timothy R. Kallman, Daniel Proga, and John Raymond, and is reproduced here with minor stylistic revisions.

2.2 Abstract

The mechanisms that drive disk winds are a window into the physical processes that underlie the disk. Stellar-mass black holes are an ideal setting in which to explore these mechanisms, in part because their outbursts span a broad range in mass accretion rate. We performed a spectral analysis of the disk wind found in six Chandra/HETG observations of the black hole candidate 4U 1630−472, covering a range of luminosities over two distinct spectral states. We modeled both wind absorption and extended wind re-emission components using PION, a self-consistent photoionized absorption model. In all but one case, two photoionization zones were required in order to obtain acceptable fits. Two independent constraints on launching radii, obtained via the ionization parameter formalism

and the dynamical broadening of the re-emission, helped characterize the geometry of the wind. The innermost wind components ($r \simeq 10^{2-3}\ GM/c^2$) tend towards small volume filling factors, high ionization, densities up to $n \simeq 10^{15-16}\mathrm{cm}^{-3}$, and outflow velocities of $\sim 0.003c$. These small launching radii and large densities require magnetic driving, as they are inconsistent with numerical and analytical treatments of thermally driven winds. Outer wind components ($r \simeq 10^5\ GM/c^2$) are significantly less ionized and have filling factors near unity. Their larger launching radii, lower densities ($n \simeq 10^{12}\mathrm{cm}^{-3}$), and outflow velocities ($\sim 0.0007c$) are nominally consistent with thermally driven winds. The overall wind structure suggests that these components may also be part of a broader MHD outflow and perhaps better described as magneto-thermal hybrid winds.

2.3 Introduction

A detailed analysis of the disk winds from low-mass X-ray binaries (LMXBs) is critical to understanding the accretion flow in these systems and, more generally, in forming a complete picture of accretion onto compact objects. Indeed, winds are a sizable component in terms of mass transfer in the disk– estimates of wind mass-loss rates range from a fraction of the accretion rate to, in some cases, drastically exceeding the mass inflow rate. A highly non-conservative accretion flow of this kind would impact several aspects of cusrrent LMXB evolution models. Moreover, the scale of these outflows suggests that disk winds may play a fundamental role in accreting systems.

Insights gained from studying stellar-mass black hole winds may further our understanding of outflows spanning the black hole mass scale. Analyses of AGN winds through Chandra/HETG deep exposures (e.g., *Young et al.*, 2005) have revealed highly ionized X-ray wind components associated with the broad line region (BLR), similar to the wind found in some stellar-mass black holes (e.g., *Miller et al.*, 2006b). These similarities in column density, ionization, and outflow velocity (and consequently kinetic power and launching radii) suggest that LMXB winds may probe similar physics as these inner disk AGN winds. Unlike

supermassive black holes, however, analyses of stellar-mass black hole winds are unimpeded by complex SEDs (including wind absorption components not associated with the inner disk) and can be performed at higher sensitivities.

Most notably, understanding the mechanisms driving disk winds may bring insights into the physical processes mediating angular momentum and mass transport within the disk. Evidence of magnetically driven winds has been uncovered in several black hole LMBXs, including GRO J1655-40 (*Miller et al.*, 2006b, 2008, 2015a; *Fukumura et al.*, 2017; *Neilsen and Homan*, 2012; *Kallman et al.*, 2009), GRS 1915+105 (*Miller et al.*, 2015a, 2016), IGR J17091-3624 (*King et al.*, 2012), V404 Cyg (*King et al.*, 2015), and H1743-322 (*Miller et al.*, 2015a). These tentative results suggest that magnetic processes may not only drive disk winds, but mediate mass transfer within the disk itself. Simulations of magnetically viscous disks, wherein turbulence arises due to the magnetorotational instability (MRI; *Balbus and Hawley*, 1991), predict the presence of disk winds driven via the resulting magnetohydrodynamic (MHD) pressure. Alternatively, magnetocentrifugal acceleration (*Blandford and Payne*, 1982) can drive winds that transport angular momentum as they are accelerated outwards along magnetic field lines. These outflows would be compact analogs to those seen in some FU Ori and T Tauri systems (*Calvet et al.*, 1993). With the prevailing view of accretion as a fundamentally magnetic process, disk winds are a key observational counterpart to theoretical work.

There are other mechanisms apart from magnetic forces that can drive a disk wind, namely radiative and thermal driving. The dominant absorption components in black hole binaries are often too ionized to be driven via radiation pressure: Ions in the absorbing gas have been stripped of most electrons involved in the UV transitions where cross-section spikes occur. Alternatively, Compton heating of the disk can effectively drive a thermal wind from outside the Compton radius (or, R_C), though this limit may extend down to $0.1R_C$ (see *Begelman et al.*, 1983; *Woods et al.*, 1996). However, Compton heating cannot account for winds launched nearest to the black hole. Robust estimates of wind launching

radii are therefore the primary means in identifying and differentiating magnetic winds.

Assuming the bulk of the absorbing gas column density is located at or near its launch point, wind launching radii, kinetic power, and outflow rates can be estimated through photoionized absorption (or, PIA) modeling. The ionization parameter, $\xi = L/nr^2$, links the degree of ionization of the gas to its density, source luminosity, and distance to the photoionizing source. Although this is possible in a few sources (e.g. GRO J1655-40 and MAXI J1305-704, where Fe XXII line ratios suggest a density of n $\simeq 10^{14}$cm^{-3}, see *Miller et al.*, 2008, 2014), gas densities cannot be directly measured in most cases. Instead, only an upper limit can be set using the column density via $r \leq L/N\xi$, the limit at which the wind has a filling factor of unity.

Previous efforts have also included re-emission from the same absorbing gas and obtained independent launching radii estimates based on dynamical broadening, assuming winds rotate at the local Keplerian velocity. Wind re-emission is visually apparent in a handful of LMXB spectra, such as strong P-Cygni profiles corresponding to He-like Fe XXV found in some observations of GRS 1915+105 (*Miller et al.*, 2015a, 2016). Evidence of Fe K band P-Cygni profiles has been uncovered in the NuSTAR and XMM Newton spectra of some AGN, including PDS 456 (*Reeves et al.*, 2018), PG1211+143 (*Pounds and Reeves*, 2009), and Cygnus A (*Reynolds et al.*, 2015). Photoionization modeling of these features is complicated by overlapping Fe K reflection, while high outflow velocities (ranging from 0.08-0.25c) means that a large portion of the broadening is not Keplerian. The Chandra HETGS spectrum of NGC 7469 shows clear P-Cygni profiles (e.g. Ne X Lyα), yet again the emission line broadening is dominated by the wind outflow velocity rather than the orbital motion of the gas (*Mehdipour et al.*, 2018). Obtaining geometric information from these sources will require more sensitive spectra and at higher resolution. In LMXBs, the lack of obvious emission features would point towards highly broadened emission and/or a small wind covering factor, depending on the assumed geometry. Alternatively, models that neglect re-emission lack full self-consistency and often yield worse statistical fits, as

line ratios can be significantly affected by emission lines (see Section 2.5.3.1).

Modeling of X-ray winds through single and multiple absorption zones has improved in recent years; the physical self-consistency of this approach outweighs the simplicity of line-by-line fitting through Gaussian functions, given statistically acceptable fits. Despite the success of leading ionization codes such as `Cloudy` (*Ferland et al.*, 2017) and `XSTAR` (*Kallman and Bautista*, 2001), photoionization grid models still lack self-consistency: the initial estimate of the illuminating unabsorbed continuum used to calculate the grid rarely coincides with the resulting continuum after fitting, and iterating this process until convergence is inefficient in more complex problems. This issue is compounded when using multiple absorption zones, as electron scattering from inner absorbing zones can significantly change the ionizing continuum incident on each successive zone. If the absorbing wind column is large, then using the same grid model for each zone would be less physical than calculating separate grids for each zone. However, trying to converge individual continua for each grid is inefficient.

In this work, we performed photoionization analysis on all Chandra/HETG observations of 4U 1630−472 for which a wind can be confidently detected. We utilized the spectral analysis package `SPEX` (*Kaastra et al.*, 1996) and modeled the wind absorption with `PION`, a self-consistent photoionized absorption model. Instead of assuming an input SED, `PION` calculates a new ionization balance as the source spectrum changes, allowing for simultaneous fitting of the absorber and the intrinsic source continuum. When using multiple `PION` components, each successive layer is illuminated by a different, successively more obscured ionizing continuum. This is an improvement over the pre-calculated photoionization grid models discussed earlier, as accounting for the reprocessing of the continuum incident on each layer yields more robust constraints on wind geometry. This level of self-consistency is required when testing alternative forms of wind driving: If winds launched below the Compton radius are not magnetic, but instead are the pressure confined outer layer of a highly ionized thermal wind, these two components should be nearly co-spatial yet illuminated by

very different continua. We modeled the wind with two absorption zones and included wind re-emission from the same absorbing gas layer. Throughout this work we refer to these wind absorption plus emission zones as "photoionization zones".

The black hole candidate 4U 1630-472 lies close to the Galactic center, at an estimated distance of 10 kpc (*Augusteijn et al.*, 2001). This line of sight carries a very high ISM column density ($N_{H,ISM} \simeq 10^{23}$ cm^{-2}; e.g. *King et al.*, 2014). Previous efforts have been unable constrain its mass given the difficulties in identifying an optical or IR counterpart. In this work, we assumed a mass of 10 $M_{\odot}$ based on work by *Seifina et al.* (2014). 4U 1630-472 is likely viewed at a high inclination ($\theta \sim 70°$; e.g. *Tomsick et al.*, 1998; *Seifina et al.*, 2014), in line with disk winds being largely equatorial (*Miller et al.*, 2006a; *King et al.*, 2012; *Ponti et al.*, 2012).

The recurring disk wind in 4U 1630-472 has been detected in absorption numerous times. Photoionization analyses have been performed on NuSTAR and XMM-Newton spectra (see *King et al.*, 2014; *Díaz Trigo et al.*, 2014; *Wang and Méndez*, 2016), yet a robust analysis of these winds require the superior energy resolution and absolute calibration of Chandra/HETGS. Of the six Chandra/HETG observations of 4U 1630−472 with strong evidence of wind absorption, ObsID 13715 was been the subject of detailed photoionization analysis. *Miller et al.* (2015a) identified two distinct wind components in this spectrum with different outflow velocities, ionization, and column density; this was modeled with `XSTAR` photoionization grids and included wind re-emission. Concurrent with this work, *Gatuzz et al.* (2019) analyzed these six observations using the photoionized absorption model "warmabs", an analytic implementation of the `XSTAR` code. Their work only used one absorption zone for each observation and did not include wind re-emission.

Table 2.1: Observation Details

ObsID	Obs Label	Duration (10^3 s)	Count Rate (Avg.)	Start Date (YYYY/MM/DD)	Data Mode	Wind Absorption
4568	I1	49.99	77.64	2004/08/04	CC	Yes[a]
13714	S1	28.92	66.84	2012/01/17	TE	Yes[b]
13715	S2	29.28	65.82	2012/01/20	TE	Yes[b]
13716	S3	29.28	62.71	2012/01/26	TE	Yes[b]
13717	S4	29.44	69.56	2012/01/30	TE	Yes[b]
19904	I2	30.93	68.95	2016/10/21	CC	Yes[b]
14441	...	19.00	...	2012/06/03	CC	No[c]
15511	...	49.39	...	2013/04/25	TE	No
15524	...	48.91	...	2013/05/27	TE	No[d]

Basic parameters for all nine Chandra/HETG observations of 4U 1630-472 are listed above. The columns list Chandra ObsID, exposure time, start date, ACIS data mode, and whether there is significant evidence of wind absorption. See text for details. Comments: [a]Absorption line at 7 keV; [b] Strong Fe XXV and Fe XXVI; [c] Dips in HETG effective area, no real lines; [d] Source in quiescence.

2.4 Observations and Data Reduction

4U 1630-472 has been observed in outburst[1] by *Chandra* with the High Energy Transmission Grating (or, HETG) on eight occasions, five of which show clear evidence of wind absorption (ObsID 13714, 13715, 13716, 13717, and 19904). A single feature near 7 keV, perhaps a weak Fe XXVI absorption line, is present in each remaining observations (ObsID 4568, 14441, and 15511), possibly indicating weak wind absorption. We found that the features in ObsID 14441 and 15511 are likely instrumental, and therefore we did not include these observations in our analysis (see Section 2.5).

The data for all eight archival HETG observations of 4U 1630−472 considered in this work (including the two observations without evidence of line absorption) were reduced using CIAO version 4.9 and CALDB version 4.7.6. While the bulk of data analysis was performed on first-order HEG spectra, we also extracted third-order HEG spectra due to its higher spectral resolution, at the cost of significantly lower sensitivity. Due to the lower resolution and collecting area in the Fe K band of the MEG, this work makes use of the

[1]An additional observation (ObsID 15524) took place while 4U 1630-472 was in quiescence.

HEG exclusively.

Spectral files for HEG first and third orders were extracted from level-2 event files using the routines `tg_finzo`, `tg_create_mask`, `tg_resolve_events`, and `tgextract`. In order to reduce the contamination of dispersed MEG photons overlapping with the HEG Fe K band, the `tg_create_mask` parameter `width_factor_hetg` was set to a value of 10 (significantly lower that the default of 35), resulting in a narrower extraction region for the HEG and thus allowing for better sensitivity at higher energies. The corresponding RMF and ARF response files for each separate order were created using the CIAO routines `mkgrmf` and `fullgarf`.

In order to increase the sensitivity of the HEG first and third-order spectra, the `combine_grating_spectra` routine is used to combine the plus and minus components for each order, therefore combining the HEG first-order spectra into a single spectrum, and the HEG third-order spectra into an independent single spectrum. Combined RMF and ARF response files were also created using the `combine_grating_spectra` routine.

Of the eight observations considered in this work, three were made with the ACIS-S array in "continuous clocking" (or, CC) mode (ObsID 4568, 14441, and 19904), while the remaining five were made using "timed exposure" (or, TE) mode (ObsID 13714, 13715, 13716, 13717, and 15511). With the exception of ObsID 15511, a "grey" filter was applied to the zeroth-order of all observations, creating a window (100 by 100 in TE-mode, 1024 by 100 in CC-mode) around the zeroth-order order where only one in 10 or one in 20 events is recorded. This prevents frames in the ACIS S3 chip from being dropped in the telemetry stream if the zeroth order is too bright. The photon flux for this observation, however, is on par with the other observations we are considering, and thus the zeroth-order suffers from significant pile-up and frames were likely dropped from the telemetry stream. This results in a lower effective exposure for ObsID 15511.

Table 2.2: Continuum Parameters

ObsID	Obs. Label	$T_{\rm i,\ Dbb}$ (keV)	$T_{\rm max,\ Dbb}$ (keV)	$T_{\rm e,\ Comt}$ (keV)	$\tau_{\rm plasma}$	$L_{\rm Comt}/L_{\rm Dbb}$ (13.6 eV - 13.6 keV)
13714	S1	3.03 ± 0.02	1.52 ± 0.01	...	...	...
13715	S2	2.96 ± 0.02	1.48 ± 0.01	...	...	...
13716	S3	2.92 ± 0.02	1.46 ± 0.01	...	...	...
13717	S4	3.13 ± 0.02	1.57 ± 0.01	...	...	...
4568	I1	2.26 ± 0.06	1.13 ± 0.03	50.0 (fixed)	0.3 (fixed)	0.25
19904	I2	2.35 ± 0.06	1.17 ± 0.03	50.0 (fixed)	0.3 (fixed)	0.09

NOTE – Parameters of the best-fit continuum model for each observation of 4U 1630−472. All errors are 1σ. Observations are modeled either as a thermal disk only ("Dbb" in SPEX), and as a disk blackbody plus Comptonization ("Comt" in SPEX), as required. Interstellar absorption was modeled with "Absm", with N_H fixed at $9.17 \times 10^{22} cm^{-2}$. We report both the nominal disk temperature (T_i, free parameter in "Dbb" model) as well as the maximum temperature of the disk, T_{max}, which is more representative of the average disk photon energy. Due to difficulties in constraining the parameters of the thermal Comptonization component, I1 and I2 were modeled with a fixed plasma optical depth and electron temperature at assumed values of $\tau = 0.3$ and $T_{\rm e,\ Comt} = 50$ keV, while the temperature of the seed spectrum, $T_{\rm seed,\ Comt}$, was coupled to the disk temperature, T_{max}. Please see the text for additional details.

2.5 Analysis & Results

Spectral analysis for all observations was performed using SPEX version 3.03.00 and SPEXACT (SPEX Atomic Code and Tables) version 3.03.00. Fitting of wind parameters was primarily done through MCMC analysis, using `emcee` (*Foreman-Mackey et al.*, 2013), a python Markov chain Monte Carlo (MCMC) package. Fits of the underlying source continuum were obtained using the internal fitting routines in SPEX (see Section 2.5.4). This includes fitting the continuum normalization at each step of a chain during the MCMC phase, where the normalization is treated as a nuisance parameter (see Section 2.5.4). We used the χ^2 fit statistic exclusively throughout our analysis, with the standard (data) weighting. The data did not require any additional binning. All errors reported are at the 1σ level.

Unlike XSPEC, the plasma routines in SPEX require the use of physical dimensions, rather than ratios, when defining parameters such as normalization, meaning that a distance must be specified before spectral fitting. A distance of 10 kpc was assumed for all spectra based on work by *Augusteijn et al.* (2001), and also for the purpose of convenient scaling

Our initial efforts at modeling the wind absorption via the built-in fitting routines in SPEX revealed major issues with this approach. First was the complexity of the eight-

dimensional parameter space: Broadband fits (3-10 keV range) were generally unsatisfactory (particularly in the Fe K band) and yielded poorly constrained parameters. In contrast, fits over the 5-10 keV range generally resulted in over-predicting of the dominant Fe XXV and XXVI lines while failing to capture lines at other energies (Fe XXV and XXVI β lines at higher energies, and Ar XVIII and Ca XX lines at lower energies). These issues were compounded by long computation times, as implementing the full plasma physics and re-emission in SPEX comes at a considerable computational cost.

Markov chain Monte Carlo either addressed or eliminated most of these issues. In addition to sampling the parameter space more efficiently and allowing for dynamic parameter ranges, implementing MCMC allowed us to treat the continuum normalization as a nuisance parameter: at each step of a chain, a best-fit normalization value was obtained (via the built-in fitting routines) before implementing the full SPEX plasma physics needed to fit the line absorption separately. This treatment vastly reduced the computation time of analysis by reducing the number of free parameters. It also allowed for the use of separate specialized fitting ranges for the broadband continuum and wind absorption. For more detail see Section 2.5.1. A fitting range of 3-10 keV minus small portions corresponding to the strongest absorption lines was used when fitting the continuum. When fitting the wind absorption, a segmented range consisting of 6.5 to 7.2 keV (Fe XXV and XXVI), 7.7 to 8.7 keV (Ni and Fe β), plus 4.08 to 4.13 keV (Ca XX), was used instead. This choice of fitting range ensures that the χ^2 used when fitting wind parameters is mostly determined by how well it models the line profiles relative to the continuum, rather than the quality of the continuum fit. Again, this is only possible because, at each point of parameter space, a best fit continuum is obtained before calculating a χ^2 for the absorption lines.

The superior effective area of the MEG near 1 keV could allow us to fit additional absorption lines (such as Fe XXIV) at energies where the HEG spectrum becomes too noisy. We found that, between high galactic absorbing column combined with the loss of sensitivity of the ACIS detector at lower energies, the MEG contains no useful flux near 1

keV. We limited our analysis the HEG first-order.

Of the eight Chandra/HETG spectra of 4U 1630-472 in outburst, only six displayed blueshifted absorption lines at a confidence above the 3σ level. In the case of both ObsID 14441 and 15511, possible absorption features coincide with large and narrow drops in the HETG/ACIS effective area, and were ruled out as non-detections. The feature in ObsID 4568 can be detected above the 3σ level while avoiding any narrow dips in effective area by $0.1-0.2$ keV.

Unsurprisingly, the detection of a wind in an observation matches its location in the MAXI hardness-intensity diagram (Figure 2.1): observations with the strongest wind absorption (e.g. ObsID 13716 and 13717, blue and cyan) are in a high-soft state. Despite the comparatively weaker absorption lines and the presence of an additional non-disk component in the continuum of ObsID 19904 (magenta), the system appears to be in a comparable accretion state as the high-soft state (when the strongest winds are detected). The lack of winds in ObsID 15511 (yellow) and 14441 (red) is consistent with the disappearance of winds during spectrally hard states, the former occurring as the system transitioned to low-hard state (as in ObsID 15524 $\sim$ 32 days later, in green), while the latter as the system transitioned from a luminous hard state to a low-hard state. For a more detailed discussion, see *Neilsen et al.* (2014).

The six spectra considered in this work is divided into two distinct groups. The first comprised of the four consecutive observations that occurred during a relatively flat phase of the same outburst (ObsID. 13714, 13715, 13716, and 13716). These spectra display disk-dominated continua and the strongest absorption lines. The spectra in second group (ObsID. 4568 and 19904) display significantly weaker absorption lines and their continua cannot be described by a disk blackbody alone. For simplicity, we refer to these groups as either soft-state or intermediate-state observations, while using S1-S4 (ObsID. 13714, 13715, 13716, and 13716) and I1-I2 (ObsID. 4568 and 19904) when referring to individual observations (see Table 2.1).

2.5.1 Continuum Fits

In addition to strong absorption lines, photoionized gases produce continuum absorption through various processes. At lower ionizations, the opacity is dominated by bound-free transitions and the attenuation of the continuum is stronger at lower photon energies. Fitting the shape of the underlying continuum in a source obscured by a gas of lower ionization would depend strongly on the ionization and absorbing column of the gas. At higher ionizations (above $\log \xi \sim 3.0$), electron scattering becomes the primary source of opacity and the attenuation is largely independent of photon energy. We did not find any of the strong lines that would suggest significant absorption of a gas below $\log \xi \sim 3.0$ in our spectra of 4U 1630-472, meaning that the majority of the observed absorption lines originate in wind layers with $\log \xi > 3.0$. During the fitting process, we assumed that any attenuation of the continuum by the absorbing wind is be due to electron scattering (and therefore mostly act as a grey absorber). This allowed us to fit the underlying continuum shape before introducing wind absorption. Once wind absorption is implemented, the additive continuum components would then only require a shift in normalization to compensate for the attenuation, reducing the number of free parameters.

All HEG first-order spectra were modeled in SPEX with a phenomenological multi-temperature disk blackbody model ("Dbb") plus, in the case of I1 and I2, an optically thin thermal Comptonization model ("Comt"), modified by interstellar absorption ("Absm"). We found that replacing "Comt" with an unbroken power-law model resulted in complete ionization of the absorbing gas due to additional heating via free-free absorption of low energy photons. Although SPEX defines the ionization parameter using a 1-1000 Rydberg flux range, the entire SED is utilized when calculating the ionization balance (including heating processes). On the other hand, the ionization balance is largely insensitive to X-ray photons above 13.6 keV. Given the relatively low luminosity of the powerlaw component, there was no noticeable change in χ^2 regardless of whether a high energy cutoff is present. This insensitivity to hard X-ray photons is also true when using "Comt": there with no

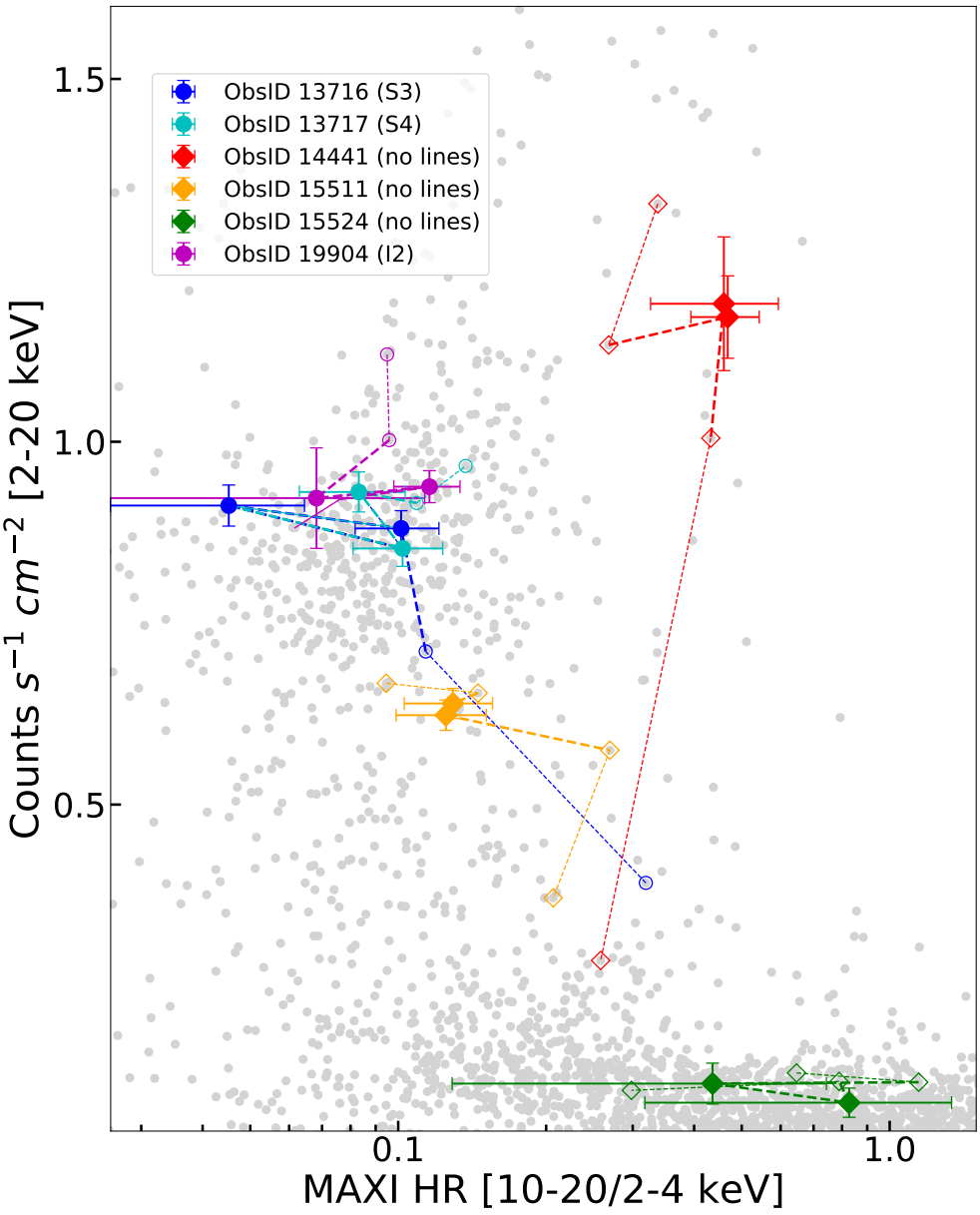

Figure 2.1: MAXI hardness-intensity diagram for 4U 1630−472. Filled markers represent the two MAXI data points closest to the time at which each Chandra observation occurred, each color coded by ObsID. Empty markers connected by dashed lines plot additional MAXI points contemporaneous with each Chandra observation, and are meant to roughly contextualize the spectral state at the time of observation.

significant change in χ^2 regardless of the specific model parameters provided that the continuum in the Chandra energy band is fit properly. This is not to say that hard X-rays are irrelevant in this scenario, as they are known to affect both the thermal stability and Compton temperature of the gas (*Chakravorty et al.*, 2013; *Higginbottom and Proga*, 2015; *Bianchi et al.*, 2017). However, the lack of simultaneous observations with facilities such as NuSTAR makes it difficult to properly explore these effects.

In principle, the flux responsible for setting the photoionization balance is almost entirely encapsulated between 13.6 eV and 13.6 keV (as per the definition of the ionization parameter in SPEX). Although the contribution by photons below 13.6 eV may ultimately be important, an unbroken powerlaw is likely a poor description of the flux at these energies. Given that I2 occupies the same space in the hardness-intensity diagram as the soft-state observations (Figure 2.1), we chose to model this component with a physically motivated Comptonization model, with some parameters fixed at canonical values (see *Tomsick et al.*, 2005), as it is likely a more realistic description of the flux below the energy range available to us.

Table 2.2 lists the best-fit continuum parameters. Given the agreement in column density of the neutral absorber when each spectrum was fit separately, the fits listed in Table 2.2 were obtained with N_H fixed at the weighted average of 9.17×10^{22} cm^{-2}. The continua in S1 to S4 (occurring within 13 days of the same outburst) are well described solely with disk blackbody model with well constrained parameters. SPEX's "Dbb" includes the torque-free condition at the inner boundary of the disk, where T_i is the fitting parameter ($T_{max} \simeq 0.49 T_i$ roughly corresponds to the temperature in "diskbb").

Continuum parameters in I1 and I2, primarily those in "Comt", were much harder to constrain in the limited energy range of Chandra and (at low energies) given the high ISM column. After coupling the seed photon energy (T_0) to T_i in "Dbb" by a factor of 0.49, electron temperature (T_1) and optical depth (τ), in particular, remained highly degenerate. We adopted fixed values of $T_1 = 50$ keV and $\tau = 0.3$ (resulting in a photon index of $\Gamma \sim 2.5$,

see *Titarchuk*, 1994) and fit the continua with "Dbb" and "Comt" normalizations, as well as coupled disk and plasma seed temperatures, as free parameters. In section 2.5.2, "Comt" normalization is coupled to disk normalization by the same relative factor in the best-fit model.

"Absm" models the transmission of the neutral gas in the ISM with fixed *Morrison and McCammon* (1983) abundances. This model has drawbacks– most importantly, fixed abundances and imperfect location of absorption edges. The SPEX user manual recommends using the collisional ionization equilibrium slab model "Hot" (fixed at a low temperature) if more higher precision is required when modeling these features. This resulted in a noticeable shift in the location of some absorption edges, but with negligible change in χ^2 and similar best-fit $N_{H,ISM}$. We opted for "Absm" given the small impact of absorption edges in our analysis.

2.5.2 Photoionization analysis

Compared to line-by-line fitting, photoionized absorption grid models (including XSTAR and Cloudy) are a vastly superior tool for characterizing the physical properties of an absorbing gas, but do not achieve full self-consistency. In these models, the ionization balance of the absorbing gas is pre-calculated by assuming the shape and luminosity of photoionizing continuum (i.e. the naked source continuum) before spectral fitting of the combined absorption and continuum models. After importing and fitting this pre-calculated absorber, the resulting best-fit continuum may diverge significantly from the assumed continuum (initially used to create the grid model) if the optical depth is high enough. This mismatch can become problematic when using multiple absorbers, where the ionizing flux from the central engine is reprocessed repeatedly as it passes through each successive absorption layer. The ionization balance in a particular photoionization zone is therefore dictated by this new incident flux, reprocessed by the absorbers located between the central engine and the zone in question, and not the naked source continuum. As the optical depth increases,

using the same pre-calculated grid to model multiple absorption layers would lack some self-consistency. In order to address these concerns, we modeled the photoionized wind absorption in our spectra with PION, a self-consistent PIA model within SPEX.

SPEX requires the user to define a geometry, where a source continuum is first chosen from standard additive components and, most importantly, where the order in which multiplicative components reprocess the flux of the additive components is specified. When PION is included as an absorber, this same reprocessed flux is what SPEX utilizes to calculate the ionization balance of the absorber. For a given geometry, SPEX can fit the continuum and PIA simultaneously using its internal plasma routines. PION also calculates re-emission from the same plasma, where an emission covering factor (as well as the fraction of backwards/forwards emission) can be specified. This acts as an additional additive component.

For each PION component in our analysis, we set fixed values of hydrogen number density at $n_H = 10^{14}$ cm^{-3} and turbulent velocity of $v_{turb} = 400$ km/s (*Miller et al.*, 2015a). It is important to note that, given the parameter regime, energy range, and resolution of the data, changing n_H by several orders of magnitudes in either direction has no observable effect on the model and produces no change in χ^2. The n_H values derived in Section 2.5.4 were not obtained through fitting. The emission covering factor ($\Omega/4\pi$) determines the normalization of the re-emission component, which is calculated internally. Given our limited understanding of wind geometry, we assumed a fixed value of $\Omega/4\pi = 0.5$ (*Miller et al.*, 2015a). We performed an additional test fit of S3 with a significantly lower $\Omega/4\pi = 0.2$ to test the validity of this assumption. The mix parameter in PION allows you to specify the geometry of the emitter. A value of mix = 1 would result in only forwards emission (a lamp-post geometry where your X-ray source would be behind a slab), while mix = 0 would result in all backwards emission (where the slab is behind the X-ray source). We assumed that we observe roughly equal amounts of re-emission from forwards and backwards portions of an axially symmetric wind, and set a fixed value of mix = 0.5.

In the analysis by *Miller et al.* (2015a), the complexity and asymmetry of Fe XXV and Fe

Table 2.3: Parameters for Best Fit Wind Model

Obs.	Zone	N_H (10^{22}cm^{-2})	log (ξ)	v_{abs} (km/s)	σ_{emis} (km/s)	L_{illum} (10^{38} erg/s)	χ^2/ν
S1	1	$54^{+15\dagger}_{-17}$	$5.25^{+0.12}_{-0.16}$	-1000^{+190}_{-180}	15000^{*}_{-3500}	$2.93^{+0.30}_{-0.22}$	159/155 = 1.03
	2	$14.4^{+3.8}_{-3.0}$	4.02 ± 0.10	-160 ± 80	1000 ± 200	$1.89^{+0.05}_{-0.06}$	
S2	1	43.5^{+14}_{-17}	$5.40^{+0.11}_{-0.19}$	-1010^{+280}_{-320}	15000^{*}_{-4200}	$2.68^{+0.29}_{-0.21}$	139/155 = 0.90
	2	$17.6^{+3.6}_{-3.4}$	$3.90^{+0.07}_{-0.07}$	-210^{+80}_{-80}	900^{+200}_{-100}	$1.91^{+0.06}_{-0.06}$	
S3	1	38.4^{+11}_{-10}	4.95 ± 0.10	-600^{+120}_{-90}	15000^{*}_{-3100}	$2.35^{+0.19}_{-0.16}$	156.07/155 = 1.01
	2	$12.4^{+1.7}_{-1.4}$	$3.39^{+0.09}_{-0.07}$	$-120^{+50\dagger}_{-70}$	1000^{+300}_{-200}	$1.77^{+0.02}_{-0.02}$	
S4	1	$56^{+16\dagger}_{-17}$	$5.21^{+0.14}_{-0.12}$	-890^{+180}_{-140}	15000^{*}_{-3100}	$3.19^{+0.39}_{-0.16}$	165.4/155 = 1.07
	2	21.3 ± 3.7	3.86 ± 0.06	-240 ± 70	900 ± 100	$1.92^{+0.05}_{-0.07}$	
I1	1	$23.7^{+15.4}_{-6.0}$	$5.41^{+0.18}_{-0.27}$	-420^{+210}_{-280}	$13200^{+1800\dagger}_{-3400}$	$3.11^{+0.25}_{-0.11}$	129.27/130 = 0.99
I2	1	$3.5^{+2.4}_{-1.8}$	$4.51^{+0.17}_{-0.07}$	-1260^{+450}_{-430}	15000^{*}_{-4300}	$2.92^{+0.05}_{-0.02}$	167.4/155 = 1.08
	2	$7.7^{+2.2}_{-2.4}$	4.38(6)	-240^{+130}_{-20}	7100 ± 3500	$2.87^{+0.03}_{-0.05}$	

NOTE – The table above lists the best-fit wind model for each observation, grouped by spectral state. Quoted errors are at the 1σ level and were obtained empirically from MCMC analysis. Parameter values are listed for both inner and outer photoionization zones, listed as Zone 1 and 2, respectively. Errors marked with * indicate that a parameter is unconstrained within 1σ in that direction (as is the case for the upper limit of $\sigma_{\rm emis}$ in Zone 1). Errors annotated with † indicate a parameter with unconstrained behavior at more than 1σ away, as in the case of N_H in Zone 1 of S1 and S4 (see Figures 2.7 & 2.8).

XXVI lines in first-order HETG spectra of S2 strongly suggested separate wind components with different outflow velocities and ionization, in agreement with individual lines found when examining higher resolution third-order HETG spectra. Using Gaussians, we find a similar trend in outflow velocity and relative ionization between photoionization zones in S1-S4 and I2 as Miller et al. (2015) did in S2, requiring the use of at least two distinct photoionization zones. However, we still performed single-zone fits to select observations for comparison to our two-zone models (see Section 2.5.3.1).

For each observation, our model was constructed in the following manner: The additive components of the naked continuum are first reprocessed by two successive photoionization zones, such that the flux incident on the outer photoionization zone (Zone 2) is the absorbed source continuum after reprocessing by the inner zone (Zone 1). Wind re-emission (an additive component in PION) for both zones were each modified with "Vgau", a Gaussian

velocity-broadening model, to model the dynamical broadening due to Keplerian motion of the orbiting gas. Finally the entire model was then modified by "Absm", with N_H fixed at $9.17 \times 10^{22}\mathrm{cm}^{-2}$. With only one absorption feature in Observation 1, the model was constructed with a single photoionization zone. This velocity broadening is applied only to the re-emission component: the pencil-beam geometry of the absorber relative to the emitting region of the inner disk means that the orbital motion of the absorber is almost entirely perpendicular to our line-of-sight. Instead, the broadening of the absorber could arise due to turbulent motion in the gas, or perhaps as a result of velocity shearing due to large changes in orbital velocity within a single gas layer. We account for these effects using the v_{turb} parameter.

For each wind zone, we fit four free parameters: The equivalent neutral hydrogen column density (N_H), the ionization parameter (ξ), the radial velocity ($v_{\rm abs}$), and the velocity broadening ($\sigma_{\rm emis}$). The first three parameters dictate the gas properties of both absorption and re-emission for that zone. The continuum normalizations (either just K_{disk} or the coupled $K_{\rm disk} + K_{\rm Comt}$) are free, but are treated as nuisance parameters in our analysis (see Appendix A).

In principle, the systematic radial velocity of re-emission in an axially symmetric wind should be zero. Currently, PION does not allow for separate absorption and emission velocities, requiring two components in order to model each wind zone. After several experiments, we found that fits with separate velocities (e.g. $\chi^2/\nu = 161/155$) yielded nearly identical results to fits with a single velocity (e.g. $\chi^2/\nu = 159/155$). It is important to note that the data still require re-emission, as the observed ratio of Fe Kα and Kβ lines cannot be achieved with absorption lines alone. While the model is still sensitive to the degree of broadening of re-emission, in this particular case it is largely insensitive to the systematic velocity of the emitter given the absence of strong P-Cygni profiles. In soft-state observations, the systematic velocity of the absorber was either too small compared to the absorption line width ($v_{\rm abs} \sim 150$ km/s and $v_{turb} \sim 400$ km/s, Zone 2) or too small compared to the broad-

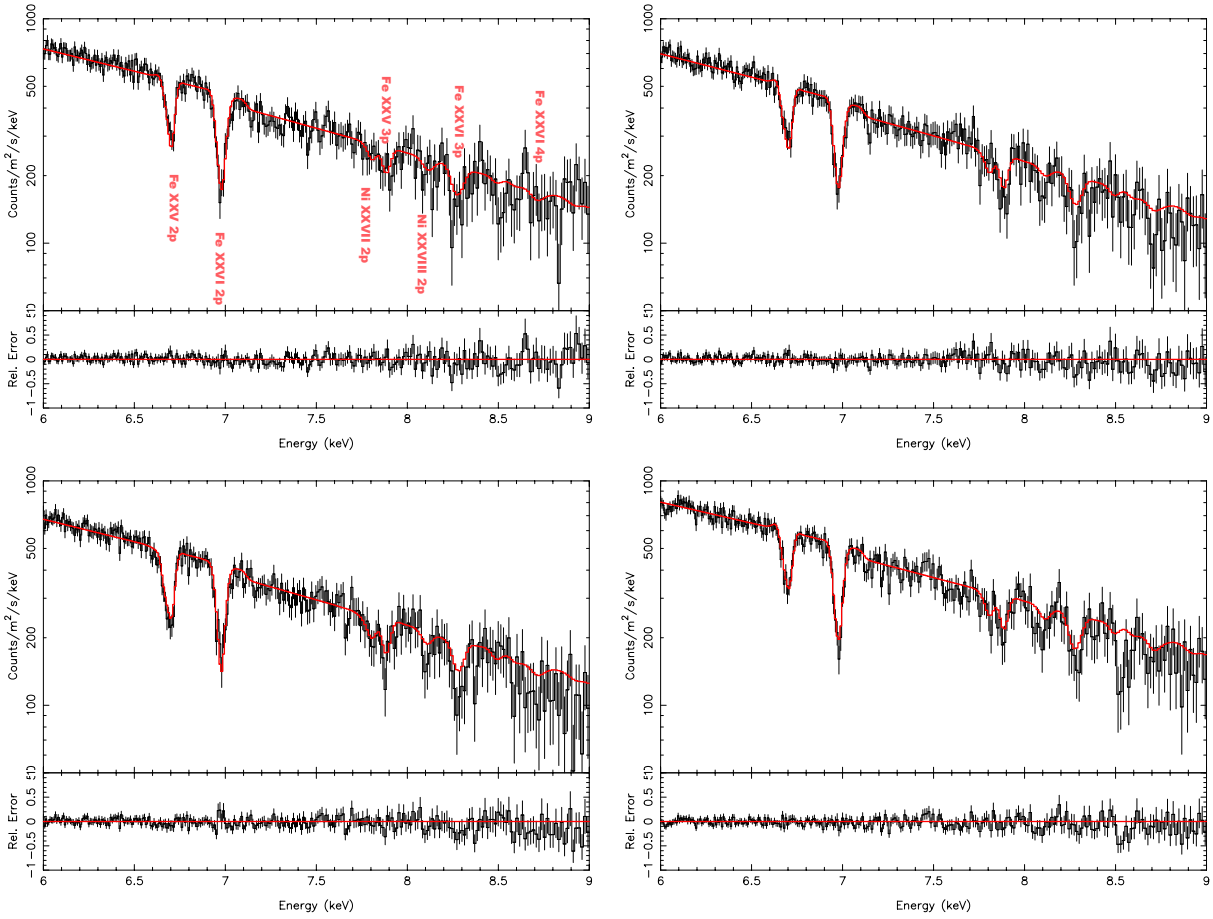

Figure 2.2: The first-order HEG spectrum of observations S1 (ObsID. 13714, top-left), S2 (ObsID. 13715, top-right), S3 (ObsID. 13716, bottom-left), and S4 (ObsID. 13717, bottom-right) of 4U 1630−472, fit with the two photoionization zone models listed in Table 2.3. The data require a dynamically broadened emission component for each corresponding photoionization zone in order to achieve the α/β line ratio for Fe XXV and Fe XXVI. Please see the text and Table 2.3 for additional details. There is feature in the spectrum of S4 (bottom-right) at ~ 8.5 keV that coincides with a discrete drop in the HEG effective area. This feature has a significance of less than 2σ (via Gaussian fitting) and therefore may be instrumental.

ening of the re-emission ($v_{\rm abs} \sim 1000$ km/s and $\sigma_{\rm emis} \sim 15000$ km/s, Zone 1). For Zone 2 in particular, the outflow velocity is small enough that the combined emission-plus-absorption line profile is largely unaffected regardless of whether the emission line is centered at $v = 0$ (6.700 keV) or at $v = v_{\rm abs} \sim -150 km/s$ (6.704 keV), but is sensitive to how much flux from the broad emission line lies within the core of the absorption line, which is primarily controlled by the dynamical broadening of the re-emission.

We initially constrained the wind equivalent hydrogen column density to $10^{22} \leq N_H \leq 10^{24}$ in cm^{-2}, the upper bound corresponding to Compton-thick winds. The ionization

parameter was restricted to $3.0 \leq \log \xi \leq 6.0$, although these bounds were tightened as minima where found. Winds require a net outflow velocity, so we constrained $v_{\rm abs} \leq 0$ km/s. Finally, the velocity broadening was constrained between $500 \leq \sigma_{\rm emis} \leq 15000$ in km/s, therefore constraining orbital radii to $R_{\rm orbital} \geq 400\ GM/c^2$.

2.5.3 Fits

Results of our MCMC analysis of the photoionized absorption in both soft- and intermediate-state observations, including best-fit parameter values with 1σ errors and χ^2 values, are detailed in Table 2.3. The luminosities listed correspond to the illuminating luminosity incident on a specific wind layer, which in the case of Zone 1 corresponds to the projection of the intrinsic luminosity of the disk at our viewing angle (more detail in Section 2.5.4). The best-fit models for each observation are shown in Figures 2.2 and 2.6, while corner plots of parameter posterior distributions are show in Figures 2.7−2.8. Figure 2.4 shows the contribution of the dynamically broadened re-emission to the line depths of Fe XXV and XXVI.

2.5.3.1 Soft State Observations

Modeling of S1-S4 resulted very good statistical fits: χ^2/ν values range from $139/155 = 0.90$ to $165.4/155 = 1.07$. The models also do a good job fitting the lines in the 7.5 to 9 keV region, as can be seen in Figure 2.2. Figure 2.3 shows that our best-fit models also do a good job describing the lines in the 3 to 5 keV range, despite including only a few bins of this range during fitting. This demonstrates the strength of our specialized fitting range: Although satisfactory χ^2/ν values can be obtained by fitting over the 6-10 keV range, χ^2 is dominated by the prominent Fe XXV and XXVI α lines. The resulting fits failed to capture the 7.5-9 keV (Fe Kβ and Ni XVIII) and the 3-5 keV energy bands. Our approach of anchoring the fit to a small portion of the low energy spectrum achieved the right balance between the Fe K and the 3-5 keV energy bands. By not allowing either region to dominate,

we obtain good fits to the Fe K band while still capturing the 7.5-9 keV and the 3-5 keV energy bands.

In our models, most of the observed Fe XXV absorption originates in a gas with lower ionization relative to those found by *Miller et al.* (2015a): Fe XXV intercombination lines become more prominent at these ionizations and, at HETG resolution, blend with the primary resonance line into a single, highly asymmetric line profile. This is consistent with Fe XXV line shape seen in all soft-state observations, as well as the abundance of lower energy lines. This lower ionization gas makes up only a portion of the Fe XXVI line; the rest originates in a highly ionized gas with large absorbing columns. Outflow velocities for this component are about half those found by *Miller et al.* (2015a).

For comparison, the analysis by *Gatuzz et al.* (2019) was the result of fitting a single absorption zone and therefore represents a rough weighted average of the wind properties of the system. For the soft-state observations, they obtain outflow velocities of about -600 km/s (as opposed to two separate zones at -200 km/s and -1000 km/s) and ionizations closer, but systematically higher to our outer wind zones ($\Delta \log \xi \sim 0.1$). These ionizations are needed in order to achieve the Fe XXV/Fe XXVI line ratios, while the larger outflow velocity is required to fit Fe XXVI at line center. However, the large outflow velocities are inconsistent with lower energy lines such as Ca XX, which is why their model does a comparatively poor job at fitting most prominent lines below the Fe K band. In our single-zone fit to S3, we obtained a considerably worse $\chi^2/\nu = 198/159 = 1.25$ compared to the two-zone model ($\chi^2/\nu = 156/155 = 1.01$). In this case, the best-fit ionization (driven by the Fe XXV/Fe XXVI line ratio) results in almost no Ca XX absorption, while the best-fit velocity (-200 km/s) fails to capture a significant blue wing in Fe XXVI. Even in S1, the soft-state observation with the weakest Ca XX absorption, the single-zone model yielded worse fits ($\chi^2/\nu = 1.18$) compared to the two-zone model ($\chi^2/\nu = 1.03$).

Gatuzz et al. (2019) did not implement wind re-emission (which is necessary in order to achieve the Fe Kα/β ratio, see Figure 2.4) and instead obtained approximate fits to the Fe

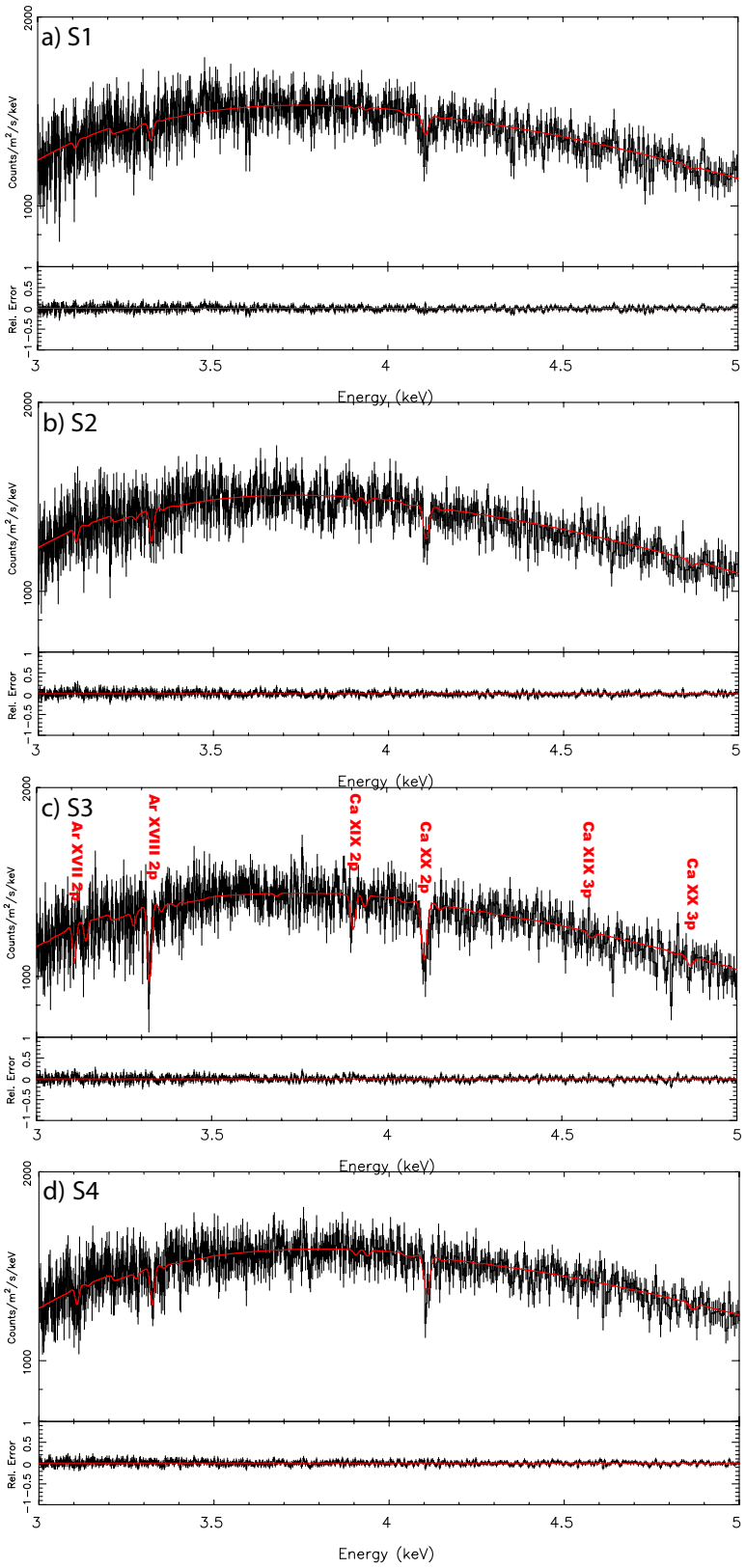

Figure 2.3: The 3−5 keV HEG spectrum of all soft-state observations of 4U 1630−472, fit with the two photoionization zone models listed in Table 2.3. Our fits adequately reproduce most of the absorption lines at lower energies despite the fact that only a few bins from this part of the spectrum (4.08 to 4.13 keV) were included during spectral fitting. Please see the text and Table 2.3 for additional details.

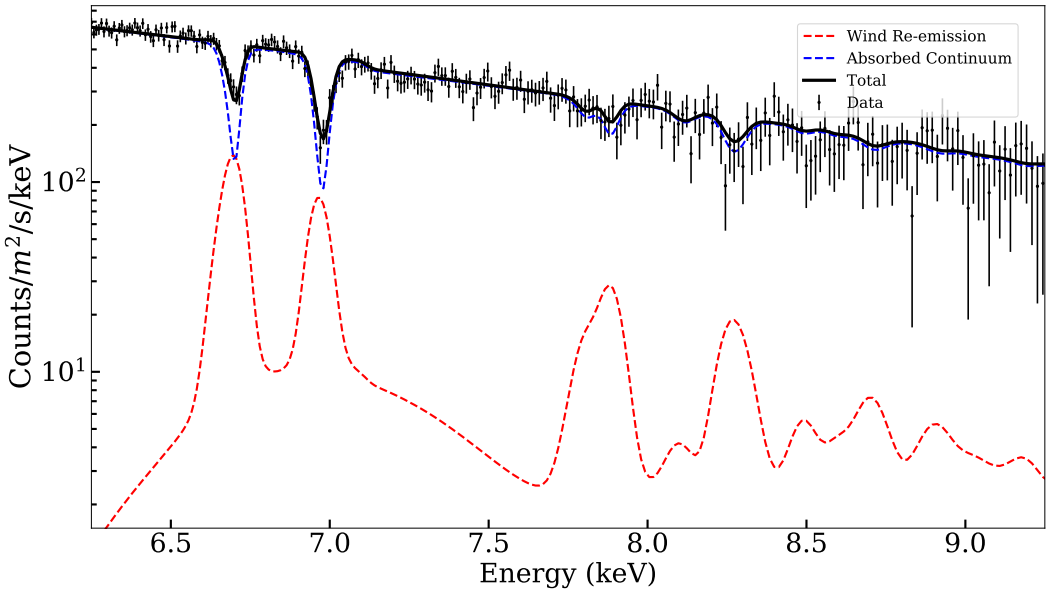

Figure 2.4: Dynamically broadened re-emission (red, both zones) contributes significantly to the line depths of Fe XXV and XXVI near 6.7 and 6.97 keV. Compared to the absorption only model (blue, both zones), re-emission has a much weaker effect on the corresponding Fe Kβ lines. This is vital for achieving the observed Fe Kα/β line ratios.

Kβ line complex by relaxing v_{turb} when fitting the "warmabs" model. At log $\xi \sim 4.0$, the Fe XXVI α line transitions to the flat portion of curve of growth at $N_H \sim 10^{23}$ cm^{-2}, where its equivalent width (EW) becomes sensitive to the turbulent velocity broadening. Due to their lower oscillator strengths, Fe XXVI β lines are still in the linear regime and their EWs depend only on N_H. Their best-fit α/β ratios require turbulent velocities of $\sim 150 - 200$ km/s, which are substantially lower than those typical of LMXB winds (300-500 km/s, *Miller et al.*, 2008, 2015a; *Lee et al.*, 2002). If the observed velocity broadening is dominated velocity shearing between wind layers, then $\sigma_v \sim \Delta r \times (dv/dr) = 0.5(\Delta r/r) \times v_{\rm orbital}$ (*Fukumura et al.*, 2010, 2017). Their launching radius estimates at a filling factor of unity would correspond to a velocity broadening of 420 km/s.

As an additional test, we fit Voigt profiles to select lines that almost entirely originate in Zone 2 and therefore do not appear broadened due to blending with Zone 1 lines. Two Voigt profiles were used to model the doublets for each H-like line profile with their normalizations coupled using their laboratory measured ratios. With their Lorentzian γ frozen at

laboratory values, we coupled the velocity shift of all the lines in question within a single observation and then coupled their velocity broadening across all four soft-state observations. By simultaneously fitting the velocity broadening in these four observations, we obtained a 1σ confidence interval on the turbulent velocity of Zone 2 (after accounting for thermal motions) ranging from 340 to 560 km/s, consistent with our assumed $v_{turb} = 400$ km/s. Although relaxing the turbulent velocity parameter may help achieve the observed line ratios when modeling a large set of lines with a single absorber, this closer examination of line profiles suggests that the turbulent velocities in Zone 2 are considerably higher than those obtained in *Gatuzz et al.* (2019), and therefore the data likely require some re-emission.

Our implementation of wind re-emission, however, is dependent on the geometry of the wind. Notably, we assumed a wind emission covering factor of $\Omega/4\pi = 0.5$, when (in a simplified geometry) this value could be lower. Roughly, the lower-limit on Ω would be the inclination angle at which the system is observed relative to the disk surface (as it is the minimum vertical extent of the wind), integrated over the entire azimuthal angle. As a simple test of our assumed geometry, we performed the same fitting procedure to S3 using a two-zone model with Ω=0.2, corresponding to the minimum vertical extent of this wind given an inclination between 20 and 30 degrees relative to the disk surface. The resulting best-fit parameter values do not change significantly from those obtained with $\Omega = 0.5$, yet the fit is noticeably worse ($\chi^2/\nu = 186/155 = 1.2$ compared to $156/155 = 1.01$). Ultimately, our incomplete understanding of the wind geometry is a weakness of this type of analysis. However, our choice of Ω did not qualitatively affect our results, while Ω=0.5 yielded better statistical fits.

Although we found that the turbulent velocities in Zone 2 are likely higher than those required to model the data without re-emission (as in *Gatuzz et al.*, 2019), we performed two alternative fits to S3 assuming $v_{turb} = 200$ km/s and either $\Omega = 0.25$ or $\Omega = 0.5$ in order to explore the degeneracy between these parameters. For Zone 2, we found in the first case ($\Omega = 0.25$) that lowering the emission covering factor results in essentially the same fit as the

results listed in Table 2.3 ($\Omega = 0.5$ and $v_{turb} = 400$ km/s), with $N_H = 11 \pm 1 \times 10^{22} cm^{-2}$ (vs. $N_H \sim 12.4 \pm 1.5$), $\log \xi = 3.35 \pm 0.05$ (vs. $\log \xi = 3.39 \pm 0.08$), and $\sigma_{\rm emis} = 1200^{+1000}_{-400}$ km/s (vs. $\sigma_{\rm emis} = 1000^{+300}_{-200}$ km/s). This suggests a positive correlation between v_{turb} and Ω that does not appear to add significant scatter to the best-fit parameters when comparing extreme values for either. In the second alternative scenario, however, a lower turbulent velocity combined with a high emission covering factor resulted in a higher discrepancy among best fit parameters, with $N_H = 9 \pm 1 \times 10^{22} cm^{-2}$, $\log \xi = 3.20 \pm 0.08$, and $\sigma_{\rm emis} = 2100^{+1000}_{-700}$ km/s. This fit, however, likely lies in an unphysical region in parameter space: With $\Omega = 0.5$ and $\log \xi \sim 3.20$, the re-emission is prominent and therefore the model is sensitive to $\sigma_{\rm emis}$. Physically, the increased dynamical broadening of the re-emission, lower ionization, and lower absorbing column would result filling factors of $f = 0.024^{+0.029}$. This high degree of clumpiness would likely result in variability that is not observed in the lightcurves of any of our observations, as in the case of the highly clumpy stellar winds in high-mass X-ray binaries such as Cygnus X-1 (*Hanke et al.*, 2009; *Grinberg et al.*, 2015; *Miškovičová et al.*, 2016) and Vela X-1 (*Grinberg et al.*, 2017). Although we cannot ultimately rule out the possibility of very clumpy yet homogeneous structure, as could be the case in the cold and partially neutral gas in the BLR and/or tori of AGN, it is unlikely for such a small filling factor to occur in either a hot thermal wind (T > 1 keV) or highly ionized magnetic wind without some additional instability to drive this highly specific type of clumpiness.

Given that (a) fitting Voigt profiles suggest larger v_{turb} values consistent with our assumed 400 km/s, (b) small covering factors yield poor fits given $v_{turb} = 400$ km/s, (c) a small v_{turb} (200 km/s) with a small covering factor yields nearly identical fits to our original fits, and (d) a small v_{turb} (200 km/s) with a large covering factor yields questionably small filling factors, it is likely that the best fit models listed in Table 2.3 (with $v_{turb} = 400$ km/s and $\Omega = 0.5$) provide a better description of the winds in this system. The remainder of this work focuses exclusively on the results listed in Table 2.3.

Our results also demonstrate the benefits of PION's self-consistency. The L_{Illum} col-

umn in Table 2.3 lists the effective luminosity each PION layer "sees" when calculating its ionization balance. In soft-state observations, after the naked source continuum has been reprocessed by Zone 1, the effective luminosities incident on Zone 2 are between 25-40% lower than those incident on Zone 1. The ionization parameter is defined as $\xi = L/r^2 n$, which means that any densities (or, upper limits on the launching radii, $r < L/N_H \xi$) derived without this correction may be overestimated by as much as 40%. In addition, this has a significant effect on the re-emission component: using the exact same model parameters, the re-emission in Zone 2 is 60% more luminous if it is instead illuminated by the naked source continuum. By switching the order in which each layer absorbs the continuum, our fits worsened from $\chi^2/\nu = 1.03$ to 1.56.

In this particular case, the attenuation of the continuum is mostly due to electron scattering and has little overall effect on the shape of the continuum, meaning that the ionization balance in Zone 2 is not affected by a change in the shape in the ionizing flux. Winds with lower ionizations have been observed in other accreting black holes (e.g. GRO J1655-40), in which case a change in the shape of the ionizing flux may also have a noticeable effect.

The spectra for the four soft-state observations display well-behaved disk-dominated continua, absorption lines of similar depth, and very little change in measured flux between them. This stability is reflected in the flatness of the MAXI light curve during this 13 day period, meaning that best-fit wind models for these observations must be broadly consistent with each other. This was very helpful at discarding local minima: We do not expect, for example, in the four days separating S3 and S4, the system to evolve from being highly obscured and luminous to a low luminosity state obscured by low N_H winds, particularly when the measured flux, line depths, and model temperatures trend in the opposite direction.

Our best-fit wind models for the soft state observations achieve this consistency. The general picture is that of two distinct photoionization zones: An inner and outer absorption layer (Zone 1 and Zone 2) with high/low values for wind ionization, column density, outflow velocities, and dynamical broadening, respectively. Zone 2 values for N_H, $v_{\rm abs}$, log ξ, and

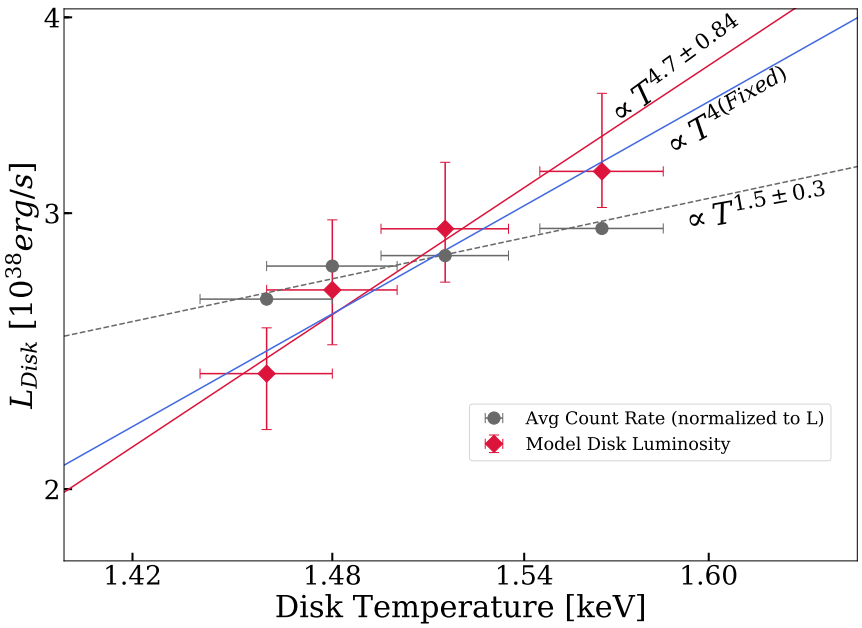

Figure 2.5: Intrinsic disk luminosity in soft-state observations, versus disk color temperature. We also plot the luminosities implied by the average detector count-rate in grey which, for visual comparison, were normalized to the average model luminosity. Our model luminosities reflect the with the T^4 scaling expected in disk-dominated states and are a strong indication that $L < L_{Edd}$. This seems to support the high N_H values we found in Zone 1 (and large changes in N_H between observations), over models with small N_H values.

$\sigma_{\rm emis}$ are well-constrained and generally display modest variation between observations. The dip in ionization seen in S3 is consistent with its spectra containing the highest number of low-ionization lines and, according to the best-fit model, the lowest Zone 2 incident flux.

As in Zone 2, we observe consistent trends across observations in Zone 1. Outflow velocities ($v_{\rm abs}$) are well constrained and roughly five times greater than those in Zone 2. Values of $\sigma_{\rm emis}$ trend towards the upper bound of 15000 km/s (or 0.05 c) for all observations. For N_H (which displays some degeneracy with ξ), the trend is towards high values (38×10^{22} cm$^{-2} \leq N_H$) and, as with $\sigma_{\rm emis}$, values approach the upper boundary for some observations. The behavior of $\sigma_{\rm emis}$ in Zone 1 is not due to the priors described in Section 2.5.2: Despite high $N_{H,1}$ and ξ_1 values, $GM/\sigma^2_{\rm emis}$ is still three to ten times smaller than $L/N_H\xi$.

The presence of unconstrained parameters requires further examination. Implementing wind re-emission is not only crucial in order to achieve the observed Fe α/β line ratios, but as evidenced by our fits of Zone 2, it is possible to constrain the velocity broadening even

in the absence of strong P-Cygni profiles. At very high velocities, emission lines become so broad that the model becomes insensitive to $\sigma_{\rm emis}$. We chose a limit of $\sigma_{\rm emis} \leq 0.05c$, or $r \geq 400\ GM/c^2$, allowing us to extract velocity information from gas orbiting at small radii without imposing an arbitrarily large cutoff radius, affecting the quality of the fit, or giving meaninglessly small radius values.

The partially unconstrained behavior of N_H in Zone 1 of some observations is due to only one prominent line (a portion of Fe XXVI α) originating from this zone. At the spectral resolution of the HEG first-order, this means that N_H and ξ can become degenerate and explode towards higher values. Once a wind reaches $N_H \sim 10^{24}{\rm cm}^{-2}$, it becomes Compton-thick. These winds are clumpy and result in highly variable light curves (*King et al.*, 2015), neither of which we observe in our spectra. Assuming N_H would converge well below this point, we allowed an initial fitting range up to $\sim 10^{24}{\rm cm}^{-2}$. If instead N_H became unconstrained and started approaching Compton limit, we tightened this limit down to $6 \times 10^{23}{\rm cm}^{-2}$ and reported where it becomes unconstrained. The value of the lower error bar would then be set to the lower bound on the top 68% of posterior distribution. For all observations, we found that N_H for Zone 1 is constrained within 1σ from the peak of the posterior distribution, and only becomes unconstrained beyond 2σ above the peak in observations S1 and S4 (see Figures 2.7 & 2.8).

The model unabsorbed source luminosities for these observations are not flat, as suggested by the average detector count rate, but instead are rank-correlated with disk temperature. As can be seen in Figure 2.5, our model luminosities are consistent with the T^4 scaling expected in disk-dominated states and are a strong indication that $L < L_{Edd}$ (*Kubota et al.*, 2001; *Kubota and Makishima*, 2004; *Gierliński and Done*, 2004; *Abe et al.*, 2005; *McClintock et al.*, 2009, 2014). This trend seems to favor our models which have large N_H values in Zone 1 (and large changes in N_H between observations), over models with small N_H values (which have a much flatter $T^{1.5}$ scaling).

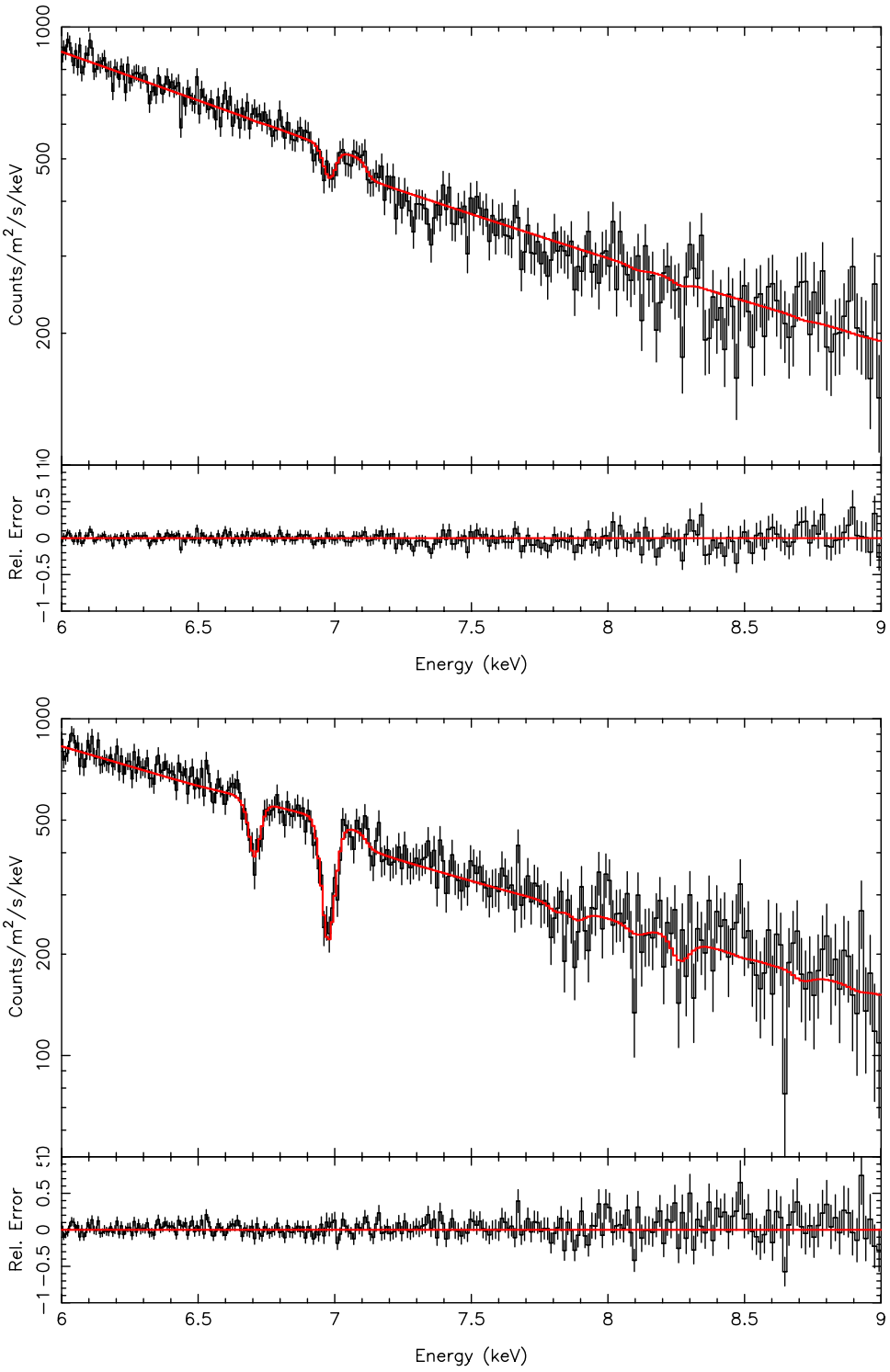

Figure 2.6: Top: the first-order HEG spectrum of observation I1 (ObsID. 4568) of 4U 1630−472, fit with the single photoionization zone model listed in Table 2.3. In addition, the data requires a dynamically broadened emission component for each corresponding photoionization zone. Bottom: the first-order HEG spectrum of observation I2 (ObsID. 19904) of 4U 1630−472, fit with the two photoionization zone model listed in Table 2.3. The data requires a dynamically broadened emission component for each corresponding photoionization zone in order to achieve the α/β line ratio for Fe XXV and Fe XXVI. Please see the text and Table 2.3 for additional details.

2.5.3.2 Intermediate State Observations

Fits to I1 and I2 still resulted in good statistical fits, with χ^2/ν values of $129/130 = 0.99$ and $167/155 = 1.08$, respectively. The relative lack of strong absorption features in these spectra, however, made it considerably harder to constrain wind parameters.

Our best-fit model for I2 consists of two photoionization zones of "moderate" ionization ($\log \xi = 4.4$ to 4.6) with low absorbing columns ($N_H \sim 4 \times 10^{22} \mathrm{cm}^{-2}$ in Zone 1, a near order of magnitude decrease when compared with S1-S4). As with the soft-state spectra, the same trend of inner winds having higher ionizations, outflow velocities, and velocity broadening is observed. Velocity broadening in Zone 2 is well constrained but at higher velocities, corresponding to an increase in ionization at smaller radii, while it trends towards the upper bound of 15000 km/s for Zone 1.

The bounds on ξ for Zone 1 were also tightened in order to only probe the minima in which Zone 1 contributed Fe XXV line absorption. We found that models in which Zone 1 becomes ionized to the point where it only contributes to Fe XXVI absorption resulted in worse statistical fits. The combined Fe XXV profile is too broad for a single Zone at "moderate" ionizations, while the total lack of low energy lines and symmetry of the lines rules out a "low" ionization gas.

At first glance, strong Fe XXV and XXVI α absorption lines in I2 seem to indicate winds similar to those in S1-S4. The stark differences between the best-fit model for I2 and the high N_H winds in soft-state spectra are consistent with discrepancies outside these two lines. First, although individual low-count bins coincide with the location of Ni and Fe lines above 7.5 keV, the spectrum is far too noisy for any of these lines to be significant. Moreover, the complete lack of low energy lines indicates that differences between I2 and soft-state spectra are greater than the Fe XXV and XXVI line profiles would suggest. Physically, our best-fit model is consistent with winds being correlated with disk activity: the connection between the presence of the additional continuum component and weaker absorption lines is mainly due to a decrease in the measured absorbing column of the wind, not over-ionization from

powerlaw photons. In particular, the presence of Fe XXV absorption lines constrains the fit away from the much higher ionizations that, in turn, would require higher columns. Especially in the case of I2, our fits strongly indicate that the observed absorption lines originate in absorbers with low column densities. This picture is also consistent with I2 appearing in the same location as soft-state observations in Figure 2.1, and further reinforces the notion that most of the flux responsible for dictating ionization balance is within the Chandra energy band. However, this does not rule out the possibility that additional over-ionized and optically-thin absorbers with high columns may be present, as these are inherently difficult to detect. This is further complicated by the lack of simultaneous observations with other facilities that would allow us to constrain the broadband continuum. Although the disappearance of winds in spectrally-hard states may indicate an anti-correlation between disk winds and jets (*Miller et al.*, 2012), the disappearance of winds at different spectral states may instead signal a change in disk geometry (*Ueda et al.*, 2010), or a combination of lower columns and increased ionization (*Díaz Trigo et al.*, 2014).

With a single absorption feature, it is difficult to justify the use of two photoionization zones when modeling I1 given the spectral resolution of the HEG first-order. Our best-fit single-zone model for I1 details a highly ionized ($\log \xi \sim 5.4$) wind with a well constrained outflow velocity (570^{+350}_{-130} km/s), launched from small radii ($\sigma_{\rm emis} = 15000^{*}_{-4000}$ km/s). The largest difficulty in fitting this model was the degeneracy between ξ and N_H. As shown in Figure 2.8, the posterior distribution is not Gaussian, and although there is clearly a preferred minimum in the 2-D histogram between these parameters, it neither corresponds to the median or peak of the 1-D distributions of either parameter. We take the point of highest 2-D probability as the best-fit value for both parameters.

2.5.4 Wind Launching Radii and Outflow Properties

Estimates for wind launching radii derived from our best-fit models, as well as estimates on wind density and filling factor, are listed in Table 2.4. Errors for launching radii and

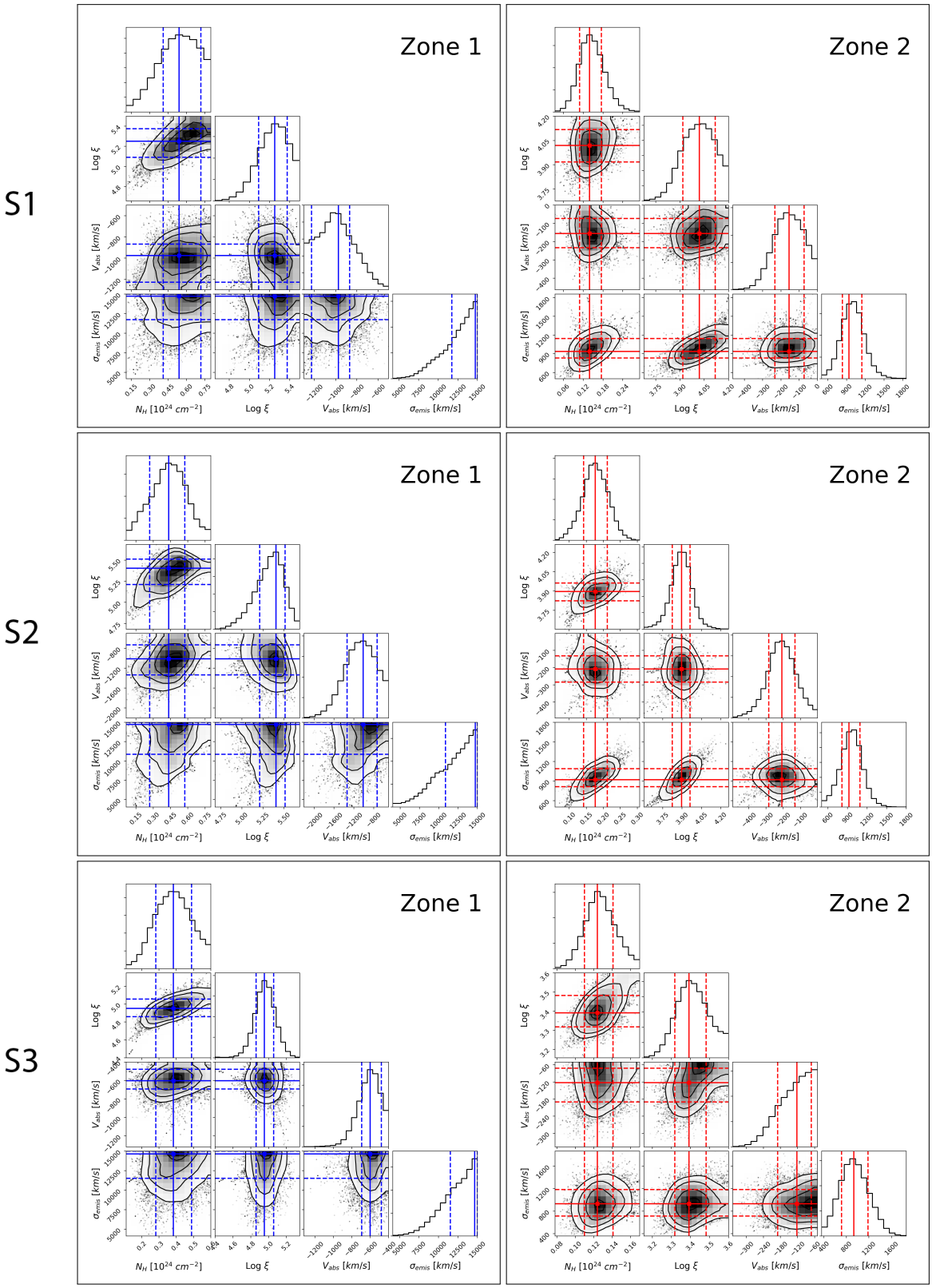

Figure 2.7: Posteriors of wind absorbing column, ionization parameter, outflow velocity, and emission velocity broadening for observations S1 (top), S2 (middle), and S3 (bottom). See text for details.

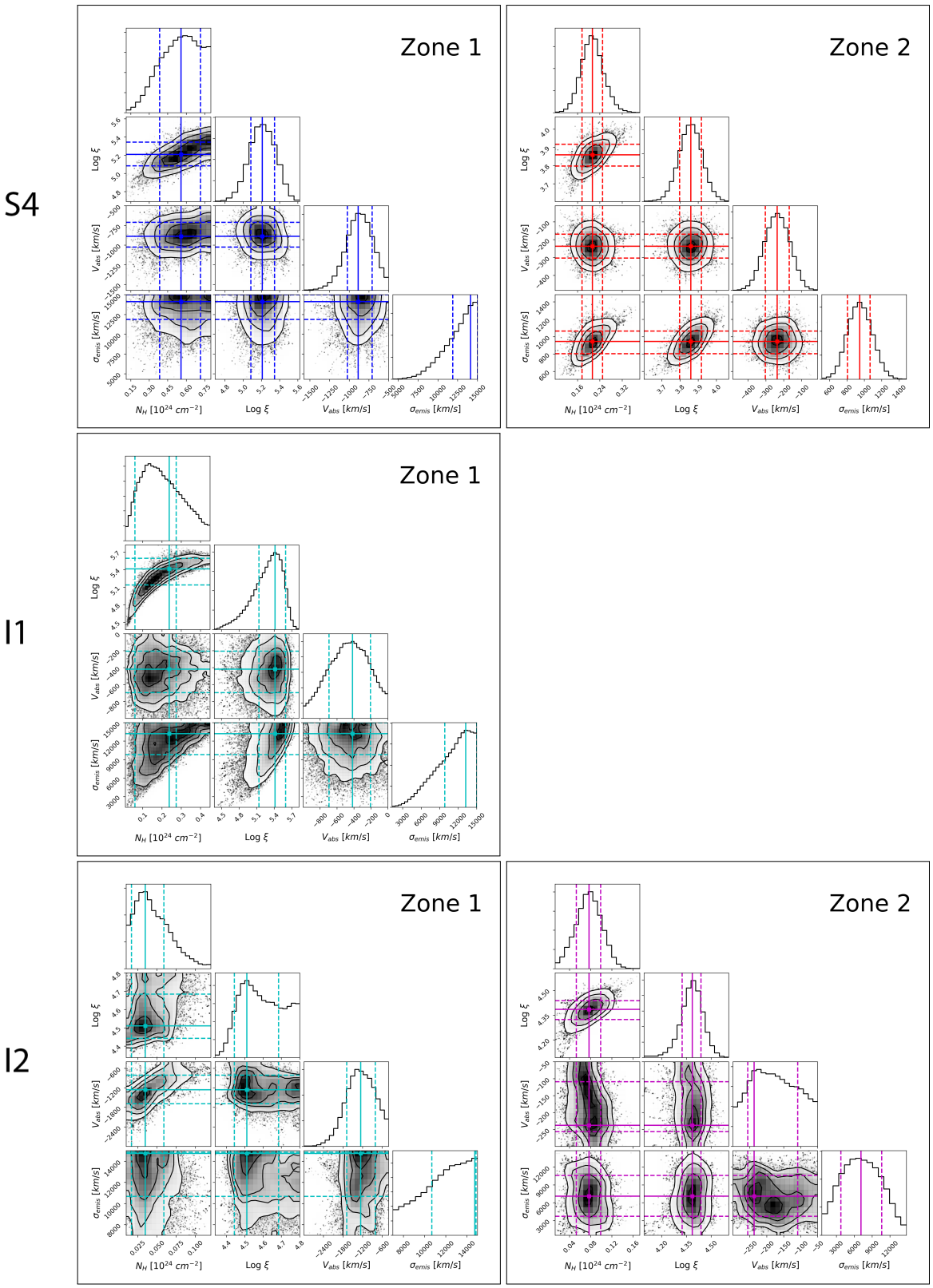

Figure 2.8: Posteriors of wind absorbing column, ionization parameter, outflow velocity, and emission velocity broadening for observations S4 (top), I1 (middle), and I2 (bottom). See text for details.

Table 2.4: Wind Launching Radii

Obs.	Zone	$R_{phot}/10^3$ (GM/c^2)	$R_{\rm upper}/10^3$ (GM/c^2)	$R_{\rm upper}/R_c$	$R_{\rm orbital}/10^3$ (GM/c^2)	$R_{\rm orbital}/R_c$	$\log n$ (cm^{-3})	f
S1	1	$2.8^{+0.3}_{-0.4}$	$2.1^{+0.6}_{-1.1^\dagger}$	0.005	$0.4^{+0.2}_{*}$	0.001	$15.4^{+0.2}_{-0.3}$	$0.3^{+0.1}_{-0.2}$
	2	$9.1^{+1.2}_{-0.9}$	80^{+26}_{-27}	0.2	77^{+39}_{-17}	0.20	$12.0^{+0.2}_{-0.2}$	$1.0^{*}_{-0.215}$
S2	1	$2.3^{+0.3}_{-0.4}$	$1.3^{+1.4}_{-0.2^\dagger}$	0.003	$0.4^{+0.4}_{*}$	0.001	$15.2^{+0.2}_{-0.4^\dagger}$	$0.35^{+0.1}_{-0.2}$
	2	$11.0^{+0.700}_{-0.800}$	93^{+16}_{-34}	0.24	97^{+22}_{-32}	0.25	$12.0^{+0.3}_{-0.2}$	1.0(1)
S3	1	3.4 ± 0.3	4.1 ± 1.7	0.01	$0.4^{+0.3}_{*}$	0.001	$15.6^{+0.2}_{-0.3}$	$0.10^{+0.08}_{-0.04}$
	2	$18^{+1.8}_{-1.5}$	395^{+54}_{-140}	0.99	104^{+36}_{-58}	0.26	$12.5^{+0.3}_{-0.4^\dagger}$	$0.3^{+0.1}_{-0.2^\dagger}$
S4	1	$2.9^{+0.4}_{-0.3}$	$2.4^{+0.7}_{-1.3^\dagger}$	0.006	$0.4^{+0.2}_{*}$	0.001	$15.6^{+0.1}_{-0.3}$	$0.13^{+0.21}_{-0.04}$
	2	11 ± 0.6	78^{+24}_{-18}	0.21	102^{+20}_{-34}	0.28	$12.1^{+0.1}_{-0.2}$	$1.3^{+0.1}_{-0.3}$
I1	1	$2.4^{+0.8}_{-0.4}$	$3.7^{+7.7}_{-0.3^\dagger}$	0.007	$0.5^{+0.5}_{-0.1^\dagger}$	0.001	$15.1^{+0.2}_{-0.4^\dagger}$	$0.16^{+0.18}_{-0.05}$
I2	1	$6.5^{+0.4}_{-1.3}$	120^{+60}_{-75}	0.20	$0.4^{+0.4}_{*}$	0.001	$15.9^{+0.2}_{-0.4^\dagger}$	$0.004^{+0.004}_{-0.003}$
	2	$7.4^{+0.4}_{-0.5}$	89^{+44}_{-30}	0.18	$1.8^{+1.3}_{-1.3^\dagger}$	0.004	$15.2^{+0.5}_{-0.4^\dagger}$	$0.017^{+0.013}_{-0.015^\dagger}$

NOTE – The table above lists estimates of wind launching radii, wind density, and volume filling factors derived from the best-fit models listed in Table 3.1. Quoted errors are at the 1σ level. Errors marked with * indicate that a parameter is unconstrained within 1σ in that direction, while those annotated with † indicate a parameter with unconstrained behavior outside the 1σ confidence interval. For comparison, we included a column for the photoionization radius, R_{phot}, assuming a density of $n = 10^{14}$. Launching radii were derived as $R_{upper} = L/N_H\xi$ and $R_{\rm orbital} = (c^2/\sigma^2_{\rm emis})$ GM/c^2, where $R_{\rm upper}$ is the upper limit on the photoionization radius. We also list the ratio of these radii over the corresponding Compton radius (or, R_c) given the disk color temperature at the time of the observation (see section 3.4). Filling factor and density estimates derived using $f = \Delta r/r = r/R_{\rm upper}$ and $n = L/r^2\xi$, with $r = R_{\rm orbital}$.

other wind properties were determined empirically: For complex dependencies on observed parameters, as is the case for most wind properties, propagating errors analytically can result in either greatly over or underestimating the propagated error. Chains constructed during spectral fitting contain important information about parameter correlations that more accurately represent the uncertainty on a model parameter. This is particularly useful when dealing with unconstrained parameters, where unbounded behavior can be cancelled out by a reciprocal correlation.

In cases where the gas density can be measured directly, the wind absorption radius (or, photoionization radius) is given by $R_{phot} = \sqrt{L/n_H\xi}$. If gas density is not known, an upper limit on this radius can be obtained directly from observables, $r \leq R_{\rm upper} \equiv L/N_H\xi$. Finally, the velocity broadening of the re-emission give us a measure of the local Keplerian velocity in an axially-symmetric disk-wind, and therefore we can obtain an independent launching radius estimate of $R_{\rm orbital} = GM/\sigma^2_{\rm emis}$. We provide estimates for wind launching radii via these three metrics, including R_{phot} assuming a fiducial density of $\log\, n_H = 14$ (based on Fe XXII line ratios of other LMXB winds, *Miller et al.*, 2008), as a point of comparison. Filling factor and density estimates listed in Table 2.4 were derived by assuming $r = R_{\rm orbital}$, where $n = L/r^2\xi$ and $f = \Delta r/r = (N_H/n)/r$ is arithmetically equivalent to $f = (N_H\xi/L) \times r^2/r = r/R_{\rm upper}$.

Measurements and estimates of BH and NS disk wind densities span several orders of magnitude, an uncertainty that is often not reflected in many published radius estimates that rely on assumed densities. For R_{phot}, assuming a density is equivalent to assuming radius. For the remainder of our analysis, we relied exclusively on $R_{\rm upper}$ and $R_{\rm orbital}$, which are mutually independent and derived strictly from observables. Despite their individual limitations, the combined information from $R_{\rm upper}$ and $R_{\rm orbital}$ is far better representation of the wind launching radii, their uncertainty, and their limits, than an assumed R_{phot}. This also allows us to obtain density estimates, as well as density-dependent wind parameters.

Figure 2.9 shows a plot of wind launching radii estimates for all six observations and

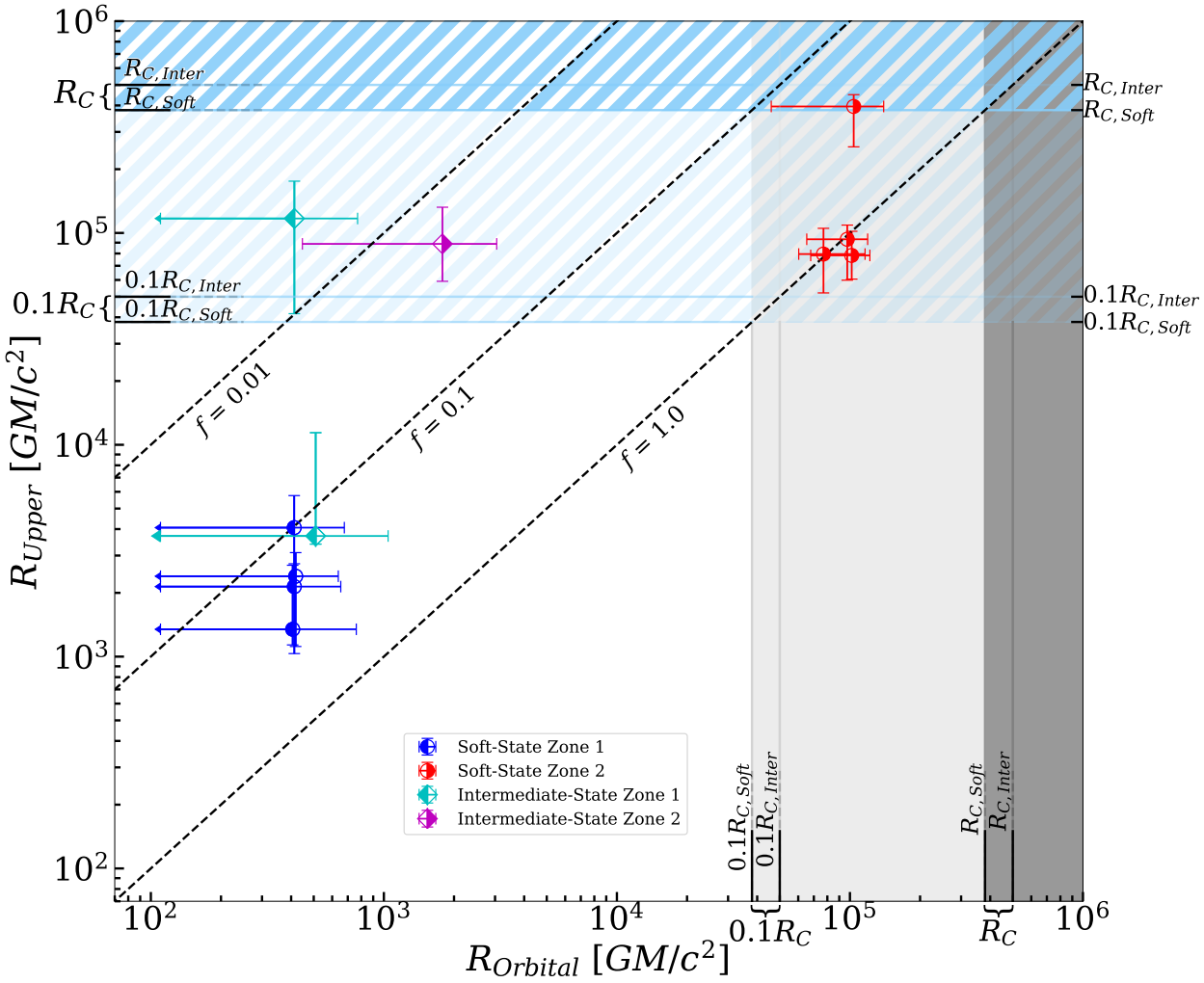

Figure 2.9: Wind launching radii for all observations plotted in radius vs. radius space, with $R_{orbital}$ and R_{upper} corresponding to the x and y coordinates, respectively. Dark-grey shaded and dark-blue hatched regions correspond to radii above $1.0R_C$ (and above $0.1R_C$ in light-grey and light-blue) for $R_{orbital}$ and R_{upper}, respectively. Points in the white region lie below this limit in both coordinates and therefore rule out thermal driving. An arrow at the end of an error bar indicates that a parameter is unconstrained in that direction. Lines of constant volume filling factor are plotted as dashed diagonal lines. By design, no points should have filling factors significantly above unity (see Appendix A).

photoionization zones, in radius vs radius space. The x- and y-coordinate values for each point correspond to their $R_{\rm orbital}$ and $R_{\rm upper}$ values, respectively. Since R_{upper} is simply R_{phot} with a filling factor of unity, y-axis values should be interpreted as an upper limit with errors on its value. Points with arrows indicate that the parameter is unconstrained in that direction: For example, cases in which $\sigma_{\rm emis}$ trends towards values above the upper bound $0.05c$, $R_{\rm orbital}$ would then be unconstrained towards very small radii. Soft-state outer and inner zones are plotted in red and blue, respectively, while intermediate state inner and outer zones are plotted in cyan and magenta, respectively. Because we use $f = R_{\rm orbital}/R_{upper}$, we can plot lines of constant filling factor in this space. Because of the priors set while fitting, no points should lie significantly below the $f = 1.0$ line (see Appendix A).

Radiation pressure can drive winds via line interactions and/or electron scattering. Line-driven winds are gases of relatively low ionization: Although the force multiplier at $\log \xi \sim 3$ is non-zero, the line force becomes negligible above $\log \xi \geq 2$ (*Proga et al.*, 2000; *Proga*, 2000). Electron scattering is significantly weaker than line-driving, requiring near-Eddington luminosities in order to efficiently drive a wind (Proga et al. 2003a). Given that $L \leq 0.25 L_{Edd}$ and $\log \xi \geq 3.4$ in all photoionization zones, we can rule out radiation pressure as a driving mechanism. This leaves thermal and magnetic driving as the remaining possibilities.

Compton heated winds can be driven ballistically from R_C (*Begelman et al.*, 1983), though *Woods et al.* (1996) suggests that this limit may extend down 0.1-0.2R_C. The precise nature and location of this boundary between a gravitationally bound corona and a free thermal wind is likely sensitive to many disk parameters and the subject of much debate. Radiation pressure enhancement at luminosities near Eddington and pressure confinement of outer layers via completely ionized winds have been suggested as plausible scenarios in which these outflows may still be thermal in nature (*Proga and Kallman*, 2002; *Done et al.*, 2018). For a more detailed discussion on how our results compare to these alternative scenarios, see Section 2.6.

In this section, we will discuss our results relative to R_C and $0.1R_C$ as described by

(*Begelman et al.*, 1983), where R_C is a function of the temperature at the surface of disk and the mass of the black hole. The disk surface is assumed to be in thermal equilibrium as it is Compton heated by flux from the inner disk, so we can approximate this temperature as being equal to the disk color temperature. Our Compton radius is then $R_C = 10^{10} \times (M_{BH}/M_\odot)/T_{C8}$ cm or $R_C = (5.82/kT_{\rm keV}) \times 10^5\ GM/c^2$. In the latter definition, both R_C and $R_G = GM/c^2$ are proportional to the mass of the accretor, and therefore the value of R_C is independent of mass when measured in gravitational radii. For soft state observations, these range from $R_{C,Soft} \simeq 5.5$ to 5.9×10^{11} cm, or $R_{C,S} \simeq 3.9 \times 10^5\ GM/c^2$. For intermediate state observations, $R_{C,Inter} \simeq 5.1 \times 10^5\ GM/c^2$. The light and dark shaded regions in Figure 2.9 correspond to values of $R_{\rm orbital}$ that lie above $0.1R_C$ and R_C, respectively. For R_{upper}, these values are plotted as light and dark blue dashed regions

Values of both R_{upper} and $R_{\rm orbital}$ lie comfortably below R_C for both soft-state inner wind components (blue) and on average two orders of magnitude smaller than $0.1R_C$, the lowest estimate on the thermal driving limit. From launching radii alone, these components are likely magnetic in origin. Likewise, intermediate-state (cyan and magenta) values of $R_{\rm orbital}$ are 1-2 orders of magnitude below $0.1R_C$, yet some of their corresponding R_{upper} values lie around $0.2R_C$. Because R_{upper} is simply an upper bound on the photoionization radius and, even when interpreted literally, these values just barely exceed the strictest limit on thermal driving, it is possible that these components are magnetic as well.

For Zone 2 soft-state wind components (red), both R_{upper} and $R_{\rm orbital}$ launching radii estimates lie above $0.1R_C$ (~ 0.25) and, in the case of S3, R_{upper} extends up to $\sim 1R_C$. Again, R_{upper} is only an upper limit and given the agreement in both $R_{\rm orbital}$ and R_{upper} among soft-state observations, it is likely that the launching radius of S3 is closer to its $R_{\rm orbital}$ value. The large volume filling factors of these outer components approach unity and may be more consistent with thermal winds in this sense, especially when compared to the small filling factors of the potentially magnetic components.

The simultaneous detection of both a magnetic inner wind and an outer thermal wind

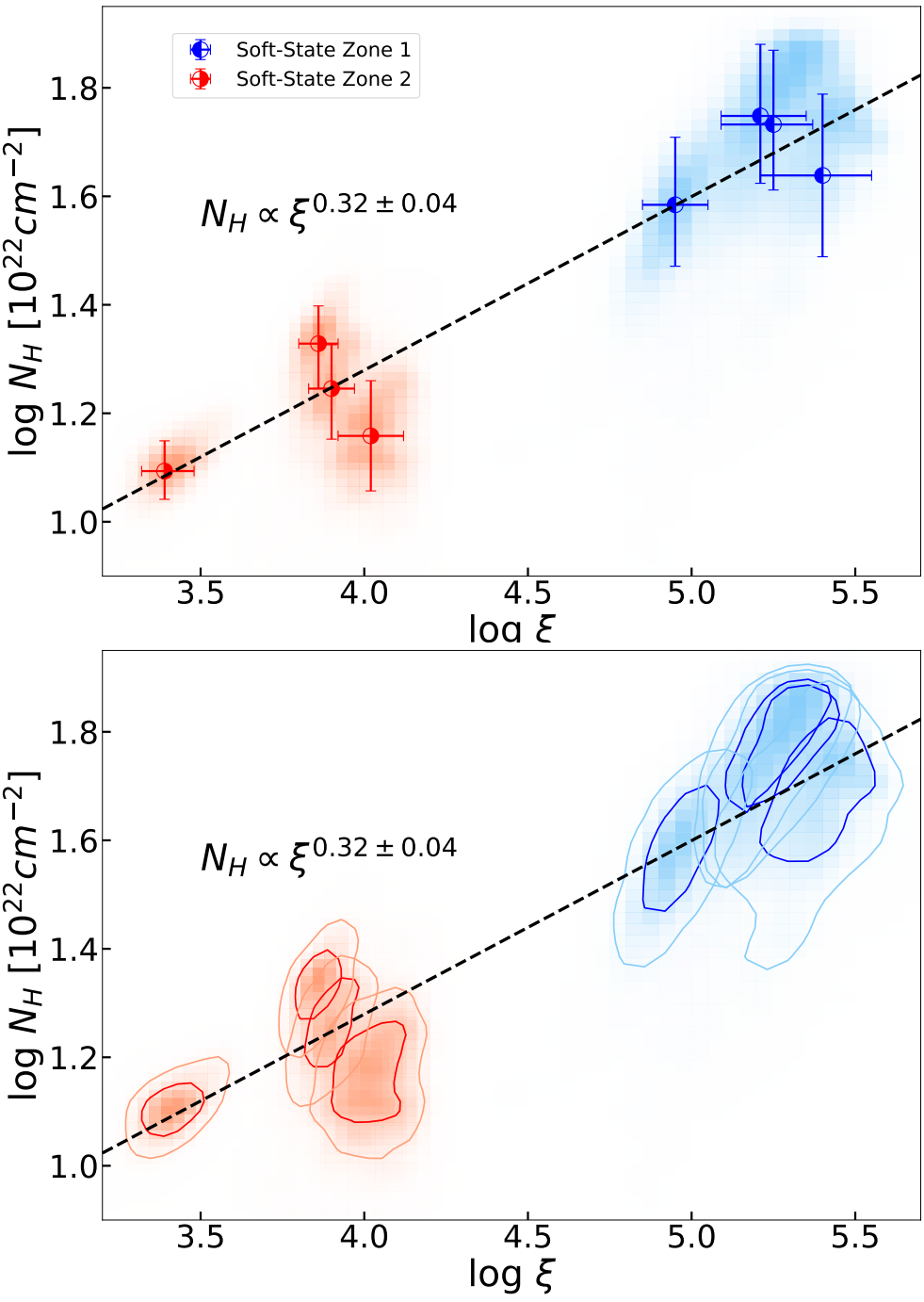

Figure 2.10: Average absorption measure distribution (AMD) for soft-state observations. Top panel: best-fit values and their 1σ errors as listed in Table 2.3. A 2−D histogram of the MCMC chains are plotted as red and blue shaded regions. Bottom panel: same as the top panel except points are replaced by contours corresponding to the 68 and 90% confidence intervals of the 2−D distribution. The resulting correlation appears to be largely unaffected by any degeneracy in some Zone 1 parameters

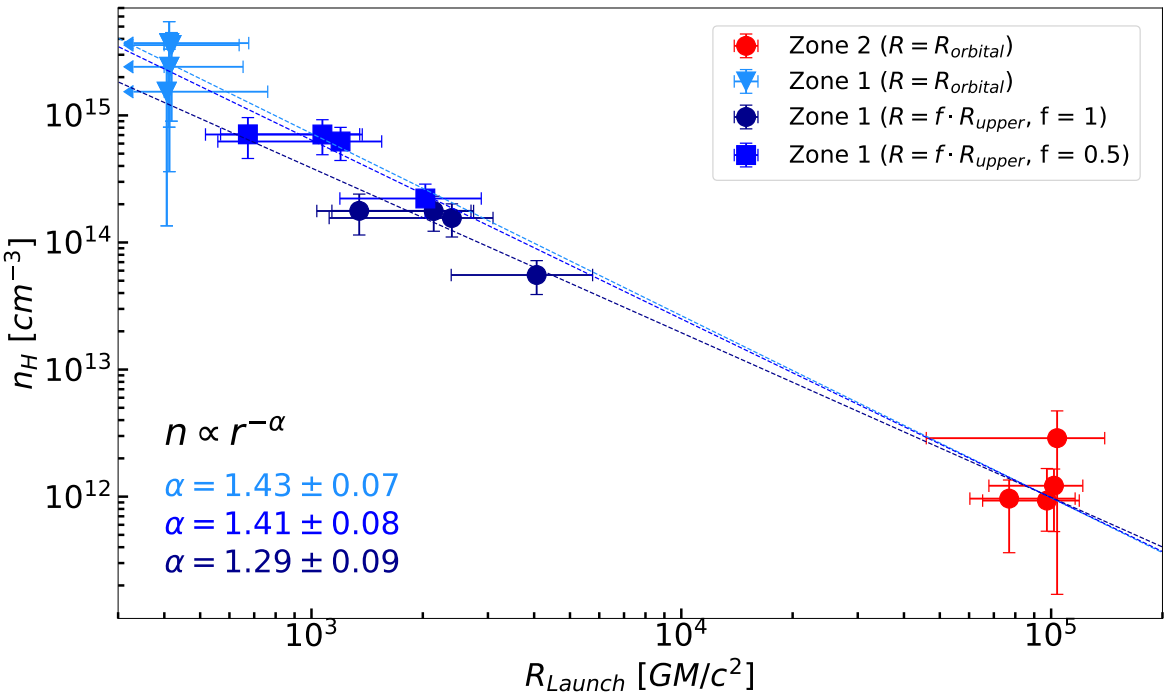

Figure 2.11: Equivalent hydrogen wind density values for soft-state observations plotted as a function of wind launching radius (R_{Launch}). An arrow at the end of an error bar indicates that a parameter is unconstrained in that direction. Zone 2 components were plotted as function of $R_{orbital}$, as their emission velocity broadening values are both well-constrained and yield $R_{orbital}$ values that are broadly consistent with the upper limit on the photoionization radius (or, R_{upper}). In the case of Zone 1 components, emission velocity-broadening values imply small orbital radii but are not well-constrained. Wind density values for Zone 1 components are therefore plotted as a function of 3 different measurements of R_{Launch}: (a) $R_{orbital}$, (b) R_{upper} assuming a filling factor of 1, and (c) R_{upper} assuming a uniform filling factor of 0.5 for all observations. Option (b) contains the combined largest radius and smallest density values for Zone 1 components. Separate radial wind density scalings were found using the combined Zone 2 $R_{orbital}$ values with each of the three R_{Launch} (and corresponding density values) for Zone 1. Dashed lines represent the best-fit linear scalings (in logarithmic space) of $n_H \propto r^{-\alpha}$ corresponding to each separate measurement of R_{Launch} for Zone 1. The resulting radial density structure is consistent regardless which measurement of Zone 1 R_{Launch} is used, as the best-fit values for scaling parameter α lie within 1σ of each other. The best-fit scaling found by Fukumura et al. (2017) for the MHD wind model of GRO J1655-40 ($n_H \propto r^{-1.2}$), is also within 1σ of option (b). Our data are consistent with an MHD outflow, as both the resulting density structure and specific density values are in agreement with numerical work on magnetic winds. Please see the text for details.

would not be entirely unexpected, as Shakura-Sunyaev disks (*Shakura and Sunyaev*, 1973) are predicted to have strong magnetic fields. Magnetic forces could then drive winds at the small radii where thermal driving becomes inefficient. This is perhaps the case during soft-state observations of 4U 1630-472, as the geometry of the wind suggests two distinct components of different origin. A more complete picture, however, requires an examination of the physical properties and radial structure of these outflows.

Although analytical treatments suggest that Compton heating can drive winds at higher densities and outflow velocities than previously thought (*Done et al.*, 2018), simulations have not been able to achieve outflow velocities larger than $v_{\rm out} \sim 200$ km/s for wind densities above $n \sim 10^{12}{\rm cm}^{-3}$ (*Higginbottom and Proga*, 2015; *Higginbottom et al.*, 2017). These values are similar to those we obtained for Zone 2 wind components in the soft-state ($v_{\rm out} \sim 200$ km/s and $n \sim 10^{12-12.5}{\rm cm}^{-3}$). As with their launching radii, thermal driving cannot be ruled-out for these outer components based on their outflow velocities and densities. Conversely, we find that the innermost wind components that we previously identified as magnetic (again, via launching radii estimates) also have considerably higher densities ($n \sim 10^{15-16}{\rm cm}^{-3}$) and outflow velocities ($v_{\rm out} \sim 400 - 1300$ km/s) than the largest values predicted by these simulations. This could be further indication that we may be simultaneously detecting both a magnetic wind component and a (separate) thermal wind component.

2.5.4.1 Wind Structure

Our models were constructed as two separate wind zones, and our best-fit models suggested that the physical properties of these zones diverge significantly. However, at the resolution of the HEG, it is not clear whether these zones are truly separate wind components. Although the data require two separate zones to model the absorbing wind, our models could simply be capturing two different portions of a continuous self-similar outflow, or perhaps something in-between.

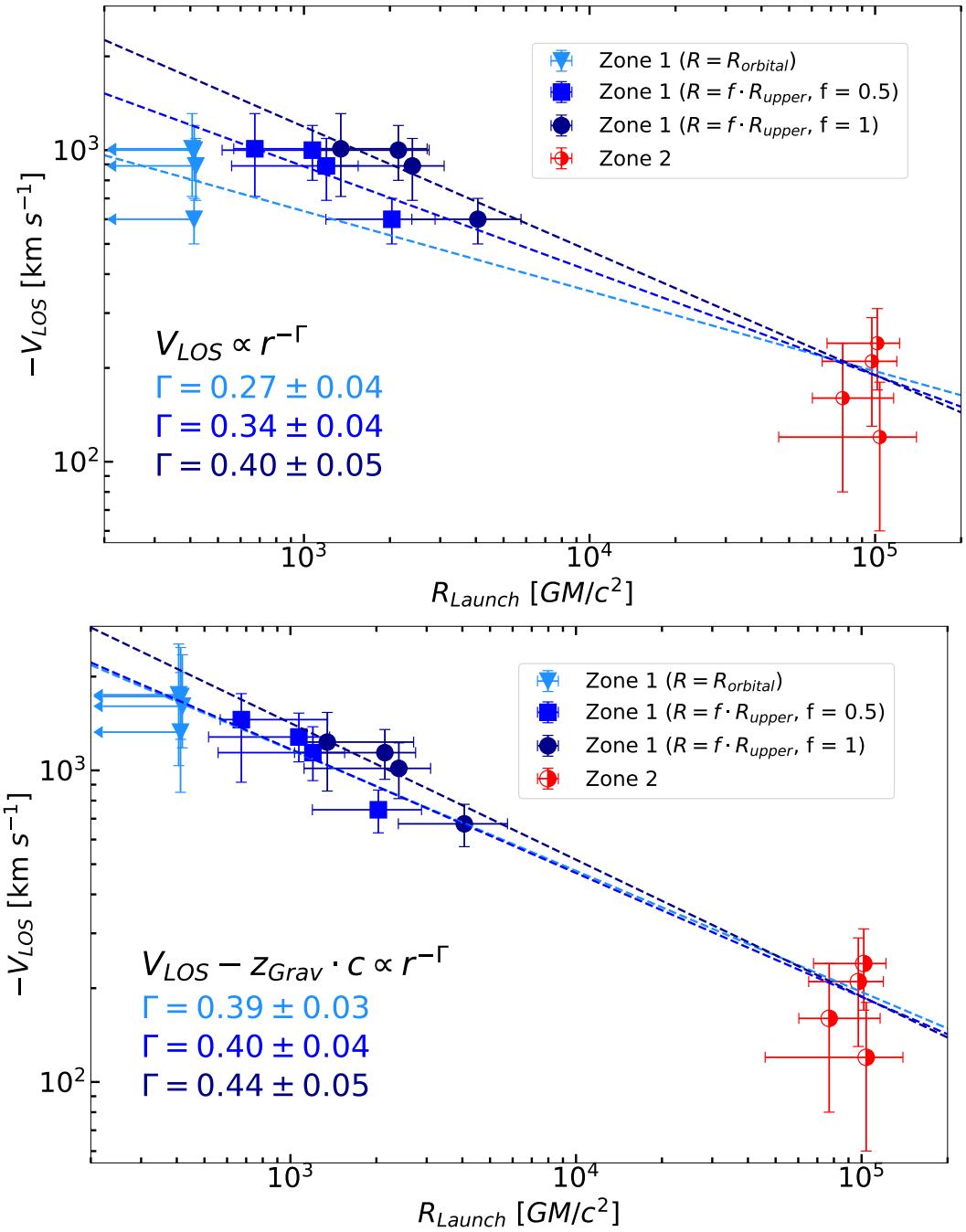

Figure 2.12: Left: wind radial outflow-velocity structure for soft-state observations. As in Figure 2.11, Zone 2 components are plotted as function of $R_{orbital}$, while Zone 1 components are plotted using 3 separate measurements for R_{Launch}: (a) $R_{orbital}$, (b) R_{upper} assuming a filling factor of 1, and (c) R_{upper} assuming a uniform filling factor of 0.5 for all observations. Best-fit scalings ($v_{LOS} \propto r^{-\Gamma}$, dashed lines) vary significantly depending on how R_{Launch} of Zone 1 is measured. In addition, the observed line-of-sight velocity scalings are significantly flatter than the $v \propto r^{-0.5}$ scaling required for self-similarity. Right: same as the left panel, except observed Zone 1 line-of-sight velocities are corrected for gravitational redshift ($z_{Grav.} = \frac{GM}{c^2}/R_{Launch}$). In Zone 1, the increase in v_{LOS} ranges between 70 and 220 km/s if $R_{Launch} = R_{upper}$, increasing up to $\sim$ 700 km/s if $R_{orbital}$ is used instead. This correction is negligible for Zone 2. Once corrected for $z_{Grav.}$, the resulting velocity structure is largely independent of how R_{Launch} is measured in Zone 1, as the best-fit values for Γ lie within 1σ of each other. Compared to the left panel, these corrected scalings converge much closer to a $v \propto r^{-0.5}$ scaling, suggesting that this may be a self-similar wind

Figure 2.10 shows the *average* absorption measure distribution (or, AMD) for the four soft-state observations. The AMD relates two independently measured quantities (ionization and absorbing column), both of which depend on the density and geometry of the absorber. The underlying radial density structure of the absorber can be revealed once constraints on the system can be obtained independently. Figure 2.11 shows wind density values, n_H, plotted against launching radii, $R_{\rm Launch}$ for the four soft-state observations. This plot presents the same information as Figure 2.10, with the added constraint of including the distance of the absorber (and therefore the filling factor, f). For Zone 2, $R_{\rm orbital}$ provides a reliable estimate of $R_{\rm Launch}$ as it is both well-constrained and largely agrees with $R_{\rm upper}$, the latter being easier to measure[2]. This is not the case for Zone 1- although the broadening values of the re-emission suggest $R_{\rm orbital}$ is small, this value is not well constrained. Therefore we provide three separate estimates for $R_{\rm Launch}$ (and corresponding density value) in Zone 1, each of which we compare against $R_{\rm orbital}$-derived values of Zone 2: (a) $R_{orbital}$, (b) R_{upper} assuming a filling factor of 1, and (c) R_{upper} assuming a uniform filling factor of 0.5 in Zone 1 across all observations. For the latter two, R_{upper} is relatively well-constrained and fairly uniform across all observations, with $f = 1$ resulting in the combination of the largest possible radii and lowest possible density values.

Strikingly, the underlying radial density structure of the wind is largely insensitive to which estimate of $R_{\rm Launch}$ is adopted for Zone 1. When fit separately, the resulting $n \propto r^{-\alpha}$ scalings (with α ranging from 1.29 ± 0.09 to 1.43 ± 0.07) are all within 1σ of each other. Given the constancy of the wind during these four observations, we deemed using a uniform value of f as an acceptable assumption. However, the strong agreement between the scalings plotted in Figure 2.11 suggests even if f in Zone 1 varied significantly between observations, the resulting scaling would lie somewhere in this narrow range. The specific values of α cluster around the $\alpha = 1.4$ scaling reported by *Chakravorty et al.* (2016) in their theoretical

[2]The degeneracy between $\sigma_{\rm emis}$, the assumed turbulent velocity of the absorber (v_{turb}), and the emission covering factor (Ω) is discussed in Section 2.5.3.1. We found that lowering v_{turb} and Ω has little effect on the resulting best-fit values and would likely only contribute some additional scatter in these plots. For simplicity, we only discuss the results of our original fits.

work on MHD winds in XRBs. This scaling, however, corresponds to their most extreme warm MHD solution and they were unable to produce outflows at the densities and small radii typical of XRB winds within the scope of their work.

Unlike *Chakravorty et al.* (2016), *Fukumura et al.* (2017) used their theoretical MHD wind framework in order to reproduce the absorption features in the Chandra/HETGS spectrum of GRO J1655-40. They found that an MHD wind model with $\alpha = 1.2$ best describes the wind absorption present in that particular source, with outflow velocities up to $v_{\rm out} \sim 4000$ km/s and very high absorbing columns ($N \sim 10^{24}$ cm^{-2} for some ions). They also find wind density values of $n \sim 0.7 \times 10^{15}$ and $n \sim 0.9 \times 10^{11}$cm^{-3} at $r = 400$ and $r = 10^5 GM/c^2$ (characteristic radii of the inner and outer soft-state components in 4U 1630-472), respectively. These values are close to what we found in 4U 1630-472 despite specifically being fit to the spectrum of GRO J1655-40 and only require increasing the density normalization ($\tilde{n}_{17}$, where $n = \tilde{n}_{17} \times (r/r_g)^{-1.2}$) by a factor of three in order to be *broadly* consistent with our density structure. Most notably, perhaps, the scaling of $\alpha = 1.2$ found by *Fukumura et al.* (2017) is 1σ away from what we obtained using $f = 1$. These similarities could perhaps mean that our outer soft-state components (which we previously identified as thermal) are a part of a broad MHD outflow.

The left panel in Figure 2.12 shows how the line of sight outflow velocity scales with R_{Launch}. As with figure 2.11, we provide separate best-fit scalings of $v_{\rm LOS} \propto r^{-\Gamma}$, for each of the three different estimates of R_{Launch} in Zone 1. The resulting scalings diverge from each other, and the underlying velocity structure appears to be highly dependent on how R_{Launch} is estimated. In addition, self-similarity requires for $v \propto r^{-1/2}$ (*Fukumura et al.*, 2010, 2015, 2017; *Chakravorty et al.*, 2016; *Zanni et al.*, 2007; *Blandford and Payne*, 1982), a scaling which is well outside the range the $\Gamma = 0.27 \pm 0.04$ to $\Gamma = 0.40 \pm 0.05$ we observed in this case.

The effect of gravitational redshift in the measured outflow velocities of black hole winds is rarely discussed. This effect is negligible in many cases (e.g. in Zone 2, this redshift would

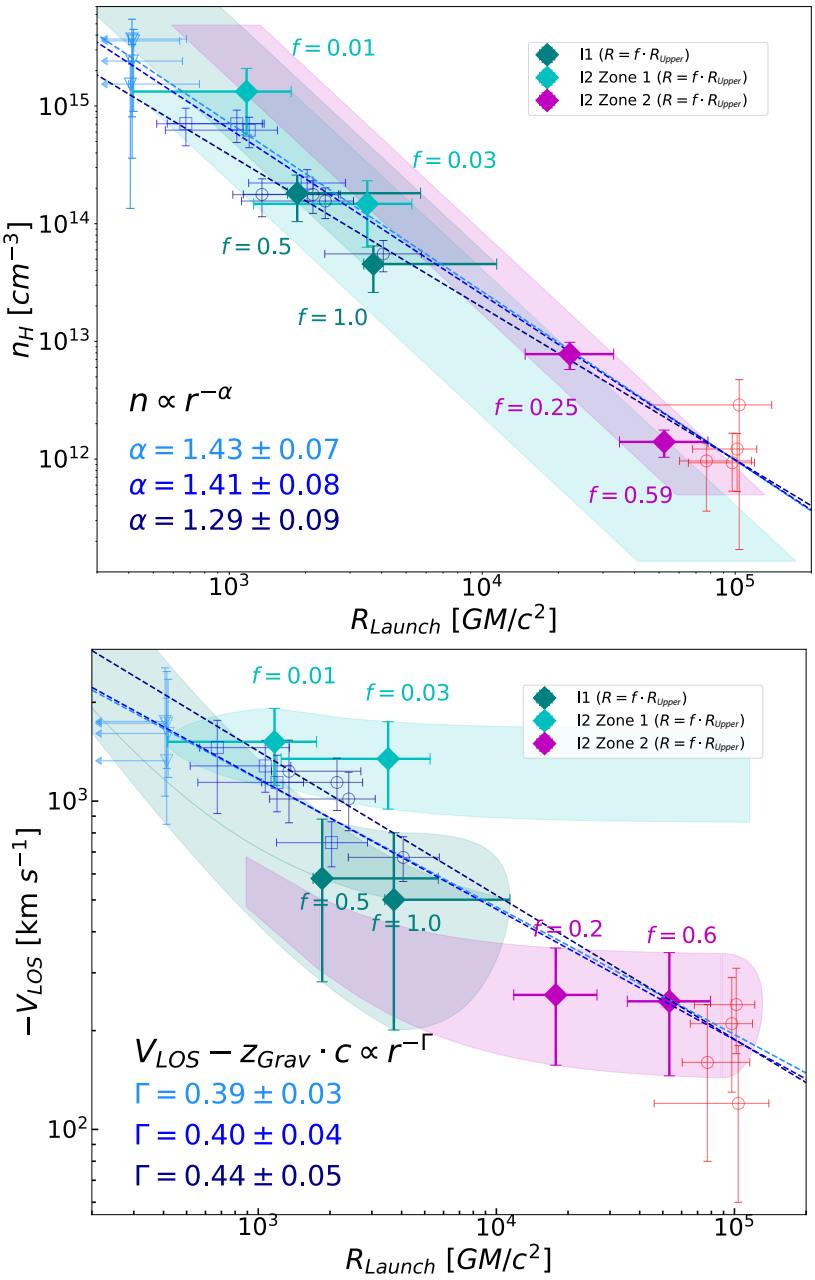

Figure 2.13: Same as Figures 2.11 (left pandel) and 2.12 (right panel), except intermediate-state observations are included in both plots. These plots are meant simply to illustrate both how the observed winds in intermediate-state observations may fit a coherent picture along with soft-state observations, while still highlighting the uncertainties involved when analyzing weakly absorbing and emitting winds. For visual clarity, points from soft-state observations are faded. Due to the difficulties in constraining $R_{orbital}$, each intermediate-state wind component is plotted as function of $R_{Launch} = f \cdot R_{upper}$ as shaded regions. Each region spans a range of filling factor values (from 0.01 to 1) and its extent is determined by the 1σ error at each point. For each wind component, the endpoints at which a region which is simultaneously $\sim 1\sigma$ away from both the density and velocity scalings (obtained using soft-state observations) are plotted explicitly with error bars and labelled with the corresponding filling factor values. These points are meant to very roughly define the plausible range of filling factors and launching radii might be for these components if the wind density and velocity structure between soft and intermediate state observations is similar, and should not be interpreted literally.

likely not exceed 10 km/s based on plausible values of R_{Launch}), yet R_{upper} places a strict lower limit on what this correction should be. The right panel of Figure 2.12 shows the resulting radial outflow velocity structures for the three different estimates of R_{Launch} in Zone 1 after correcting velocity values by the gravitational redshift at that specific radius. Although this correction can be as small as $100 - 200$ km/s given $f = 1$, or as large as 700 km/s when using $R_{orbital}$, the underlying velocity structure appears largely insensitive to the choice of R_{Launch} estimate, with $\Gamma = 0.39 \pm 0.03$, 0.4 ± 0.04, and 0.44 ± 0.05. Besides consistency, these values also cluster much closer to a $v \propto r^{-1/2}$ scaling (just shy of 1σ away when using $f = 1$). Once outflow velocities are corrected for gravitational redshift, the velocity structure of the wind during soft-state observations closely resembles a self-similar wind. This would again be consistent with a single, continuous MHD outflow, rather than separate thermal and magnetic wind components.

The large discrepancy between $R_{orbital}$ and R_{upper} in intermediate-state observations poses a challenge in trying to include them in this picture. Although the discrepancy between these two values is not inherently problematic (small filling factors are common in many astrophysical plasmas), the discrepancy arises because re-emission in this wind is not very prominent, and therefore $R_{orbital}$ is hard to constrain. The left and right panels of Figure 2.13 are the same plots as Figures 2.11 and 2.12, respectively, with intermediate-state observations included as shaded regions. Given the uncertainty with $R_{orbital}$, these regions are plotted entirely function of $R_{Launch} = f \cdot R_{upper}$, trancing its 1σ along a range of filling factor values. Although our fits strayed away from the small re-emission velocity broadening values that would correspond to large filling factors, the shaded regions span a range of $f = 0.01$ up to 1.0.

The left panel of Figure 2.13 shows that, for a range of filling factors, these regions lie within 1σ of the plausible density structure obtained by fitting soft-state observations only. On the right panel, and especially for observation I2, this range is narrower by comparison. We also explicitly plotted the points at which each region was $\sim 1\sigma$ away from the nearest

Table 2.5: Wind Outflow Parameters

Obs	Zone	$\dot{M}_{wind}$ (10^{18} g/s)	$\dot{M}_{wind}/\dot{M}_{edd}$	$\dot{M}_{wind}/\dot{M}_{in}$	L_{rad}/L_{edd}	L_{wind} (10^{32} erg/s)	L_{wind}/L_{rad} (10^{-7})
S1	1	$0.48^{+0.27}_{-0.16}$	$0.034^{+0.020}_{-0.012}$	$0.15^{+0.08}_{-0.05}$	$0.23^{+0.03}_{-0.02}$	17^{+24}_{-7}	58^{+82}_{-24}
	2	$3.5^{+0.7}_{-2.7}$	$0.25^{+0.05}_{-0.20}$	$1.1^{+0.2}_{-0.8}$	..	$3.7^{+3.3}_{-3.7\dagger}$	$20^{+17}_{-20\dagger}$
S2	1	$0.49^{+0.23}_{-0.30}$	$0.035^{+0.017}_{-0.021}$	$0.17^{+0.08}_{-0.10}$	0.21(2)	$30^{+18}_{-27\dagger}$	$110^{+70}_{-100\dagger}$
	2	5.7 ± 2.2	0.41(16)	1.9(8)	..	$12.5^{+7.9}_{-12.5\dagger}$	$65^{+41}_{-65\dagger}$
S3	1	$0.20^{+0.12}_{-0.07}$	$0.014^{+0.009}_{-0.005}$	$0.08^{+0.05}_{-0.03}$	0.18(1)	$2.9^{+3.8}_{-1.3}$	12^{+16}_{-6}
	2	$3.2^{+1.2}_{-2.5\dagger}$	$0.23^{+0.08}_{-0.18\dagger}$	$1.2^{+1.4}_{-1.0\dagger}$	..	$2.4^{+2.6}_{-2.3\dagger}$	$14^{+15}_{-13\dagger}$
S4	1	$0.40^{+0.26}_{-0.15}$	$0.029^{+0.019}_{-0.010}$	$0.11^{+0.07}_{-0.04}$	$0.25^{+0.03}_{-0.01}$	14^{+17}_{-4}	45^{+55}_{-14}
	2	$5.9^{+1.7}_{-2.5}$	$0.42^{+0.13}_{-0.18}$	$1.7^{+0.45}_{-0.7}$	..	16^{+9}_{-15}	86^{+45}_{-79}
I1	1	$0.10^{+0.11}_{-0.06}$	$0.007^{+0.008}_{-0.004}$	$0.03^{+0.03}_{-0.02}$	$0.25^{+0.02}_{-0.01}$	$0.49^{+2.51}_{-0.01\dagger}$	$1.60^{+8.10}_{-0.04\dagger}$
I2	1	$0.04^{+0.04}_{-0.02\dagger}$	$0.003^{+0.003}_{-0.002\dagger}$	$0.013^{+0.012}_{-0.007\dagger}$	$0.232^{+0.004}_{-0.002}$	$2.2^{+4.8}_{-2.0\dagger}$	$7.7^{+16}_{-6.7\dagger}$
	2	$0.05^{+0.03}_{-0.04}$	$0.003^{+0.002}_{-0.003}$	0.01(1)	..	0.08(8)	$0.28^{+0.26}_{-0.28\dagger}$

NOTE – The table above lists estimates for various wind outflow parameters dervied from the best-fit models listed in Table 3.1. Quoted errors are at the 1σ level. Errors annotated with † indicate a parameter with unconstrained behavior outside the 1σ confidence interval. Mass outflow rates were calculated by correcting for volume filling factor via $\dot{M}_{out} = 2\pi\mu m_p \cdot v_{abs} \cdot f \cdot L/\xi$, which is equivalent to $\dot{M}_{out} = 2\pi\mu m_p GM \cdot v_{abs} \cdot N_H/\sigma^2_{emis}$ (where L is the illuminating luminosity incident on a zone and not the intrinsic luminosity of the disk, μ is the mean molecular weight and fixed at 1.23, m_p is the proton mass, and M is the black hole mass). Wind kinetic luminosity values were calculated using these filling factor corrected outflow rates via $\dot{L}_{wind} = 0.5\dot{M}_{out}v^2_{abs}$. The intrinsic luminosity of the disk (L_{rad}; equivalent to L_{illum} for Zone 1) was used to estimate the mass accretion rate, $\dot{M}_{in}$, using an assumed efficiency of $\eta = 0.1$. Errors listed for L_{rad} are based solely on the correlation with N_H of the absorbing wind. See text for additional details.

scaling in *both* panels simultaneously, representing a very rough acceptable range of filling factors if the wind in intermediate-state observations had the same structure as those during soft-state observations. It is important note that these points specifically, and Figure 2.13, are mainly included in this work for illustrative purposes. Even if the scalings found by fitting our results from soft-state observations are real, the winds found in intermediate-state observations do not necessary have to follow them, or even have the same normalizations.

2.5.4.2 Outflow Parameters

Table 2.5 lists wind outflow properties derived from our best-fit models. The intrinsic source luminosity is given by the illuminating luminosity incident on Zone 1 (corrected for viewing angle), and a corresponding accretion rate of $\dot{M}_{in} = L/\eta c^2$, with $\eta = 0.1$. The wind mass outflow rate was calculated using:

$$\dot{M}_{\rm out} \simeq 2 \times (2\pi\mu m_p \cdot v_{\rm abs} \cdot r^2 n \cdot f),$$

where $2\times$ accounts for outflows on both sides of the disk. With $r^2 n = L/\xi$ and $f = R_{\rm orbital}/R_{upper} = (N_H \xi/L) \cdot GM/\sigma^2_{\rm emis}$, this becomes:

$$\dot{M}_{\rm out} = 4\pi\mu m_p GM \cdot v_{\rm abs} \cdot N_H/\sigma^2_{\rm emis}.$$

Wind kinetic luminosities were calculated using $L_{\rm wind} = 0.5\dot{M}_{\rm out} v^2_{\rm abs}$.

Although winds launched from Zone 1 only make up a small fraction of the total outflow rate, they constitute the majority of the total wind kinetic luminosity. Once corrected for f, $\dot{M}_{\rm out}$ is no longer dependent on luminosity, making it possible to track how mass outflow rates evolve with each other without making circular arguments. Unsurprisingly, outflow rates trend roughly towards higher $\dot{M}_{\rm out}$ with luminosity. However, all datasets can be considered flat within errors, and Zone 1 and total $\dot{M}_{\rm out}$ not are not even rank-correlated with luminosity.

2.6 Discussion and Conclusions

We have re-analyzed all archival Chandra/HETG spectra of 4U 1630-472 that show definitive evidence of an absorbing disk wind. The analysis was performed using PION (*Kaastra et al.*, 1996), a SPEX absorption model that calculates the ionization of the absorbing plasma self-consistently with the unabsorbed source continuum. Extended wind re-emission was implemented and dynamically broadened to the order of the local Keplerian velocity. Fitting these self-consistent models using Markov chain Monte Carlo with

physically motivated priors and a specialized fitting procedure resulted in: (1) Better statistical fits in Fe K band while simulateously capturing lines at lower energies (Ca XX and Ar XVIII) and the Fe K α/β line ratios (2), a better understanding of parameter errors and how they propagate when deriving outflow properties.

With the exception of I1 (ObsID 4568), the spectra of 4U 1630-472 required two distinct photoionization zones to model the absorbing winds. For the four soft-state observations, we find that these photoionization zones follow the same pattern: A highly ionized and broadened inner wind component (Zone 1) launched at large outflow velocities, and an outer component (Zone 2), launched at a much lower velocity, ionization, and broadening. This trend in ionization and velocities is consistent with that found by *Miller et al.* (2015a) for S2, and with what is generally expected in these sources. Our results, however, indicate that the lower and higher ionization components are much lower and higher in ionization, respectively, than previously suggested. We also find the absorbing column of the inner component to be much larger than previously reported, with values for S1 and S4 being somewhat unconstrained (due to higher ionization in Zone 1) and approaching the regime of Compton-thick winds, a scenario that can be ruled-out by the lack of variability. There are strong indications that these higher ionization parameter and equivalent hydrogen column density values are real: 1) The absorbing columns in S2 and S3 are similarly large, yet well constrained and well below the Compton-thick regime; 2) The model luminosities for all soft-state observations strongly follow a T^4 trend despite very different absorbing columns, especially when compared to the models without wind absorption; and 3) the presence of lines at lower energies require a gas of lower ionization than what previously reported.

Compared to the results by *Gatuzz et al.* (2019) using a single absorption zone and "warmabs", we were able to achieve better fits for the broad absorption spectrum in the soft-state observations, including the strong Ca XX and Ar XVIII lines which their fits fail to capture, by using two separate absorbers. Gatuzz et al. (2019) obtained adequate Fe α/β line ratios by fitting the turbulent velocity of the absorber down to values of 150-200

km/s, below what is typically observed in these sources. The addition of wind re-emission in our model resulted in better fits to this Fe Kβ region.

We report values for wind launching radii based on the velocity broadening of wind re-emission, and well as the upper limit on the photoionization radius. These estimates do not assume a fiducial density. In both cases, estimates for wind launching radii rule out thermal driving for all Zone 1 components in soft-state observations ($r \sim 10^{2-3}\ GM/c^2$), as well as for all intermediate-state components. Launching radii estimates of the remaining soft-state Zone 2 winds lie between $0.1R_C$ and $1.0R_C$ ($r \sim 10^5\ GM/c^2$), meaning that thermal driving cannot be ruled-out based on this criteria alone. The launching radii reported by *Gatuzz et al.* (2019) are broadly consistent with these Zone 2 winds, though their results assume a density.

It has been suggested that massive thermal winds could be launched from radii below $0.1R_C$ as the source approaches L_{Edd}, once factors such as radiation pressure enhancement are implemented that more in realistic treatments of Compton heated winds (*Done et al.*, 2018), with this limit extending down to $0.01R_C$ at $L \sim 0.67L_{Edd}$ (*Proga and Kallman*, 2002). This is likely not the case in 4U 1630-472, as the highest model luminosity we obtain is $0.25L_{Edd}$ for S4. Again, it is very likely that $L < L_{Edd}$ given that continuum is disk-dominated and their luminosities follow a T^4 scaling. Using our highest model luminosity of $0.25L_{Edd}$, *Done et al.* (2018) and the equations in *Proga and Kallman* (2002) would predict that thermal winds could be launched from radii as small as $R_{in} \sim 10^5 GM/c^2$, or $\sim 0.25R_C$. This limit is still orders of magnitude larger than the launching radii of the innermost wind components, while outermost wind components in the soft-state lie right at this limit.

Done et al. (2018) also propose that an additional, high-N_H, completely ionized thermal wind could perhaps drive these outer components via pressure confinement. In this case, L would be approaching L_{Edd} but appear less luminous due to electron scattering from this completely ionized component that is undetected due to the lack of absorption lines. As mentioned earlier, there is significant evidence pointing to L being significantly lower than

L_{Edd}. In addition, our best-fit models already have relatively high absorbing columns, and therefore an additional, nearly co-spatial, high-N_H component would result in a Compton-thick photoionization zone. These outflows would be clumpy (*King et al.*, 2015) and would result in high variability, something which we do not observe in our light curves.

Depending on the accepted theoretical model, the components lie at or below the lower limit for thermal driving ($\sim 0.25R_C$). However, if the conditions in the disk are such that a thermal wind can be efficiently driven from $0.25R_C$, then the lack of any wind components above $1R_C$ (where most of the mass loss occurs for thermal winds; *Done et al.*, 2018) should raise some suspicions. Our best-fit models suggest that Compton heating is failing to drive disk winds at the very radii where it is expected to be the most efficient. One plausible explanation could be changes in the disk geometry that may obscure the central engine from the disk surface at large radii, but this is highly speculative. If instead these outer components are magnetically driven, then the lack of massive thermal winds at large radii may simply mean that, at the time of these observations, Compton heating is inefficient at all radii compared to magnetic driving.

Some magnetic outflows may be the product of both magnetic and thermal driving, with varying degrees of contribution from each physical process (*Waters and Proga*, 2018; *Bai et al.*, 2016). These outer components may be one of these magneto-thermal hybrid winds (such as those suggested via wind evolution in the 2005 outburst of GRO J1655-40; *Neilsen and Homan*, 2012), with strong contributions from both magnetic and thermal driving. This could explain why these outer winds might be thermal in appearance (low density, low velocity, and high filling factor), yet are both the only thermal components detected in the source and are launched from the smallest radius possible for thermal driving.

A third plausible explanation could be that magnetic processes may, in some scenarios, suppress thermal winds. In their simulations of disk winds in LMXBs, *Waters and Proga* (2018) found that by adding strong poloidal magnetic fields to systems with Compton-heated thermal winds, the existing converging-diverging geometry which is conducive to

wind acceleration can be disrupted at about $\sim R_C$. This change in geometry may suppress thermal winds at their characteristic radii, while still allowing for magnetic outflows and magnetically enhanced thermal winds. This may explain both why we see such high mass loss rates from these "thermal" winds in our model despite being launched from the smallest radius possible for thermal driving, and why we do not see any thermal winds above $1R_C$. However, *Waters and Proga* (2018) only perform their simulations down to $0.5R_C$, so we cannot make comparisons with the rest of our wind components.

Finally, our two wind zones may be different regions of a single continuous outflow, as we cannot tell from the data whether these are truly separate components. Our results are similar to those obtained by *Fukumura et al.* (2017), where they modeled the wind absorption in GRO J1655-40 using their MHD wind models. Although our radial density structure is slightly steeper (at $n \propto r^{-\alpha}$, $\alpha = 1.29 \pm 0.09$ to 1.43 ± 0.07), we obtain similar wind density values at similar radii and our data is broadly consistent with the their best fit $n \propto r^{-1.2}$ scaling (Figure 2.11). Our wind absorption measure distribution ($N_H \propto \xi^{(\alpha-1/\alpha-2)}$) is also similar to their findings ($\alpha = 1.24$ vs 1.2), although this depends on how this scaling is defined (see Section 2.5.4).

One strong discrepancy with *Fukumura et al.* (2017) is their assumed $v^{-1/2}$ scaling, a product of self similarity. Although this scaling might indeed be a real description of the velocity structure of these outflows, this is not necessarily the case for the measured line-of-sight velocity, $v_{\rm LOS}$. We find that our velocities have a significantly flatter scaling of $v_{\rm LOS} \propto r^{-\Gamma}$, $\Gamma = 0.27 \pm 0.04$ to 0.4 ± 0.05) and are highly dependent on how R_{Launch} is measured in Zone 1. Once outflow velocities are corrected for gravitational redshift, the resulting scalings are much closer to self-similarity ($v_{\rm LOS} \propto r^{-\Gamma}$, $\Gamma = 0.39 \pm 0.03$ to 0.44 ± 0.05), and are mostly insensitive the R_{Launch} estimate used. If these outflows are indeed self-similar, then a plausible explanation for the remaining discrepancy could be that the angle between the LOS and the outflow velocity vector decreases with radius. This would mean that the wind velocity vector would become increasingly orthogonal to the disk surface at smaller radii,

a feature that is observed in simulations of MHD disk winds but rarely quantified (*Waters and Proga*, 2018). Another factor is that faster wind components at smaller radii may be observed at lower elevations from the disk surface, and have not been fully accelerated along magnetic field lines (*Luketic et al.*, 2010). Although this correction may perhaps be useful when connecting simulations of MHD winds to observation in the future, this will likely require the higher resolving power and sensitivity of the next generation of X-ray telescopes.

We would like to thank the anonymous referee for comments and suggestions that improved this manuscript. We acknowledge helpful discussions with Juliette Becker and Christopher Miller.

CHAPTER III

A Redshifted Inner Disk Atmosphere and Transient Absorbers in the Ultra-Compact Neutron Star X-ray Binary 4U 1916−053

3.1 Preface

This chapter appears in the Astrophysical Journal Letters, Volume 899, Letter 16 (Trueba et al., 2020). The paper is co-authored by Jon M. Miller, Andrew C. Fabian, Jelle Kaastra, Timothy R. Kallman, Anne Lohfink, Daniel Proga, John Raymond, Christopher Reynolds, Mark Reynolds, and Abderahmen Zoghbi, and is reproduced here with minor stylistic revisions.

3.2 Abstract

The very small accretion disks in ultra-compact X-ray binaries (UCXBs) are special laboratories in which to study disk accretion and outflows. We report on three sets of new (250 ks total) and archival (50 ks) Chandra/HETG observations of the "dipping" neutron-star X-ray binary 4U 1916−053, which has an orbital period of $P \simeq 50$ minutes. We find that the bulk of the absorption in all three spectra originates in a disk atmosphere that is redshifted by $v \simeq 220 - 290$ km s^{-1}, corresponding to the gravitational redshift at radius of

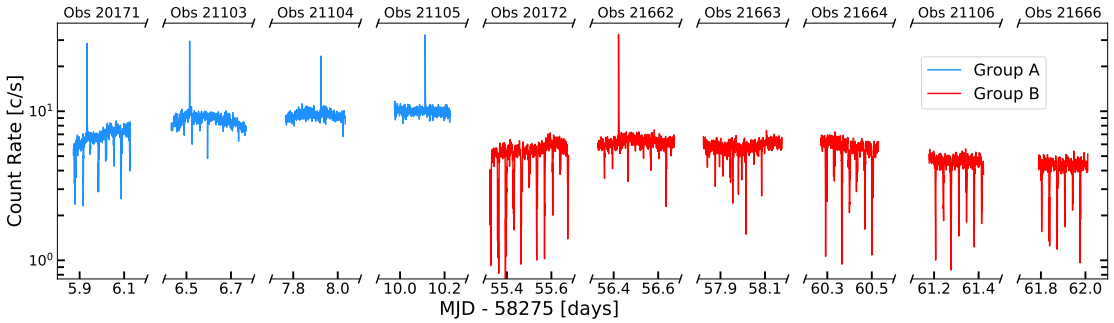

Figure 3.1: Barycenter-corrected Chandra/HETG lightcurve for the 10 observations of 4U 1916−053. The spectra where grouped (Group A and Group B), based on their relative intensity and the 45-day gap between the two groups.

$R \sim 1200\ GM/c^2$. This shift is present in the strongest, most highly ionized lines (Si XIV and Fe XXVI), with a significance of 5σ. Absorption lines observed during dipping events (typically associated with the outermost disk) instead display no velocity shifts and serve as a local standard of rest, suggesting that the redshift is intrinsic to an inner disk atmosphere and not due to radial motion in the galaxy or a kick. In two spectra, there is also evidence of a more strongly redshifted component that would correspond to a disk atmosphere at $R \sim 70\ GM/c^2$; this component is significant at the 3σ level. Finally, in one spectrum, we find evidence of disk wind with a blue shift of $v = -1700^{+1700}_{-1200}$ km s^{-1}. If real, this wind would require magnetic driving.

3.3 Introduction

Compact, short-period X-ray binaries are remarkable systems, but 4U 1916−053 is special even within this class. Whereas many short-period binaries are faint, 4U 1916−053 is relatively bright, typically exhibiting an X-ray flux of $F \geq 0.2$ Crab in soft X-rays (e.g., *Galloway et al.*, 2008). This fact, and the low interstellar column density along its line of sight ($N_H \simeq 2.3 \times 10^{21}$ cm^{-2}; *HI4PI Collaboration et al.*, 2016), facilitate detailed spectroscopy and timing studies of 4U 1916−053 (e.g., *Díaz Trigo et al.*, 2006; *Iaria et al.*, 2015; *Gambino et al.*, 2019).

The detection of Type-1 X-ray bursts (e.g., *Galloway et al.*, 2008), and coherent oscillations within the bursts (Galloway et al. 2001), clearly signal that the binary harbors a neutron star. 4U 1916−053 does not exhibit eclipses, but the presence of strong dips in its X-ray light curve (*Walter et al.*, 1982) – likely associated with structures in the outer disk (e.g., *Díaz Trigo et al.*, 2006) – signals that it is viewed at a high inclination. These dips, and optical properties, point to an orbital period of just $P \simeq 50$ minutes (*White and Swank*, 1982; *Walter et al.*, 1982). Given these system parameters, it is likely that the companion is degenerate ($M = 0.065 \pm 0.01\ M_{\odot}$, assuming a $M = 1.4\ M_{\odot}$ primary; *Heinke et al.*, 2013), and that the accretion flow is dominated by helium rather than hydrogen (e.g., *Joss*, 1978). This composition is confirmed by optical spectroscopy (e.g., *Nelemans et al.*, 2006).

4U 1916−053 has been extensively studied with modern X-ray telescopes. The detection of ionized absorption lines, including He-like Fe XXV and H-like Fe XXVI, was first reported in an analysis of *XMM-Newton* data (*Boirin et al.*, 2004). A later study with the *Chandra*/HETGS found no credible velocity shift, even in these most ionized lines, and associated the lines with the extreme outer disk (*Juett and Chakrabarty*, 2006). A more comprehensive study of ionized absorption in X-ray "dippers" concluded that variations in ionized absorbing regions in the outer disk cause the dipping phenomenon (*Díaz Trigo et al.*, 2006). A recent analysis of archival *Suzaku* data also concluded that the absorption is associated with the outer accretion disk (*Gambino et al.*, 2019).

It is not clear if ionized but static disk atmospheres are related to blue-shifted disk winds, or if they are disconnected. It is possible that such atmospheres turn into winds when certain physical conditions are met. In GRS 1915+105, for instance, ionized absorption is sometimes evident in the Fe K band with no significant blue-shift (e.g., *Lee et al.*, 2002; *Neilsen et al.*, 2019). In other phases, a disk wind is clearly detected (e.g., *Ueda et al.*, 2009; *Neilsen and Lee*, 2009); indeed, the wind can be as fast as $v/c = 0.03$ (*Miller et al.*, 2016; *Zoghbi et al.*, 2016). It is particularly interesting to search for winds and atmosphere–wind connections in compact binaries, since even the outer disk may be too small to launch thermal disk winds.

The goals of better understanding disk atmospheres, winds, and wind driving mechanisms motivated us to observe 4U 1916−053 for an additional 250 ks in *Chandra* Cycle 19. In Section 2, we describe the observations and data reduction process. Section 3 details the analysis procedure that we employed, and the outcomes. In Section 4, we discuss our results in the context of other recent studies of disk atmospheres and winds.

3.4 Observations and Data Reduction

4U 1916−053 has been observed with the Chandra/HETG on eleven occasions: once in 2005 (ObsID 4584, 46 ks) plus ten observations in 2018 (totalling 250 ks). The source was faint enough during all observations for the exposures to be conducted in the ACIS TE (Timed Exposure) mode and FAINT data mode.

The data from all eleven observations were reduced using CIAO version 4.7 and CALDB version 4.7.6. A barycenter correction was applied to the data using the *axbary* routine. The CIAO routines *tg_findzo*, *tg_create_mask*[1], *tg_resolve_events*, *tgextract*, *mkgrmf*, and *fullgarf* were used to extract the first-order HEG and MEG spectrum, redistribution matrix, and ancillary response files for each observation. Plus and minus orders were combined using *combine_grating_spectra*. Time filtering of spectra (including the removal of dips and bursts events, as well obtaining phase-resolved spectra) was done using the *dmcopy* routine.

Lightcurves for the ten 2018 observations of 4U 1916−053 are shown Figure 3.1. Each successive observation is separated by $1-3$ days except for a ~ 45 day gap, separating the data set in two epochs. Visually, the lightcurves suggest that the two sets represent two distinct luminosity states. This is also apparent when examining the 2−9 keV continua for all observations (including the archival HETG observation, ObsID 4584): The continuum becomes harder as the luminosity increases, ranging from the least-luminous and softest Group B observations to the brightest and hardest spectrum of ObsID 4584.

[1]The width_factor_hetg parameter in this routine was set to 10 in order to reduce contamination from MEG photons onto the HEG, thereby greatly increasing the sensitivity of the HEG above the FeK band.

An examination of the extracted spectra reveals the presence of ionized, H-like absorption lines in the Fe K band and at $\sim$ 2 keV (Si XIV). The low signal-to-noise ratio in individual spectra, however, makes it impossible to extract useful information for each observation. The continuum shapes for observations within each of the two sets show only minor discrepancies, therefore we combined the spectra of each set to produce two combined spectra corresponding to each epoch. We will refer to these combined spectra as Spectrum A and Spectrum B. Although the continuum of ObsID 4584 is not too dissimilar to the continua of the observations in Spectrum A (comparable spectral shape, but the former is noticeably more luminous), the observations are separated by $\sim$14 years and therefore the absorption in the system might be different. We therefore chose to analyze this observation separately and refer to it as Spectrum Γ. The raw, low S/N spectra of individual observations were combined using the standard Gehrels errors delivered by the standard CIAO pipeline. Once combined, we replaced the errors in the average spectra with Poissonian errors in order to more accurately represent the errors once the spectra were binned.

The light curves also display both dipping and burst events. Although these contribute very little information to the integrated spectrum for each observation, these events were initially removed entirely when extracting each spectrum in an effort to remove any line absorption originating from the dips. The dips display complexity in their geometry: the shape, depth, and duration of dips changes between and within each observation, as well as the occasional appearance of secondary dips at roughly twice the orbital frequency. Any detailed analysis on the nature of the structure producing the dips is beyond the scope of this work. However, regardless of shape, all dips have clearly defined starting and ending points, and the lack of any orbital modulation other than discrete dips strongly suggests that any absorption coming from the outer disk is confined to the dipping events.

3.5 Analysis & Results

Spectral modeling was performed using SPEX version 3.05.00 (*Kaastra et al.*, 1996, 2018) and SPEXACT version 3.05.00 atomic database and associated routines. The data were binned when necessary using the "obin" command, which rebins a spectrum to the optimal bin size given the particular statistics of a given source. Continuum fits were performed in the 1.9 to 9.0 keV range. Each individual HETG spectrum was a composite of their MEG and HEG spectra, where the higher resolution HEG made up the 3.8 to 9.0 keV range, while the MEG covered the 1.9 to 3.0 keV portion due to its higher effective area at low energies. There are no lines of significance in the 3.0 to 3.8 portion of any of the 3 spectra.

The continuum for all three data sets was modeled with a blackbody (bb in SPEX) plus a disk blackbody (dbb), modified by interstellar absorption (absm). The neutral absorbing column is low and was fixed at $N_H = 4 \times 10^{21}$ cm^{-2}, broadly consistent with the aforementioned 2.3×10^{21} cm^{-2} value (*HI4PI Collaboration et al.*, 2016) after accounting for differences in abundances and models. The best-fit temperatures and normalization parameters for the blackbody and disk blackbody components are within the acceptable ranges for these parameters, suggesting a neutron star temperatures of 2.2, 1.8, and 1.7 keV, and a disk temperatures of 0.9, 0.8, and 0.9 keV for Spectrum Γ, A, and B, respectively.

The residuals of the best-fit continua reveal similar ionized absorption features among the 3 different spectra. Strong Fe XXVI and Si XIV absorption lines appear near their respective rest energies, likely originating in a disk atmosphere. The Fe XXVI line in Spectrum A, in particular, displays some complexity: a blue wing that could indicate the presence of a disk wind. The same complexity is perhaps also present in Spectrum B. In both spectra, however, this blue wing is only present in the profile of the Fe XXVI line. In addition, there is possible weak absorption feature in residuals for both Spectrum Γ and Spectrum A at ~ 6.8 and ~ 6.9 keV, respectively. Although these features are relatively weak, the lack of instrumental features at these energies and their presence in two of our spectra suggests

that these may be real absorption lines. If real, it is unlikely these are blue-shifted Fe XXV absorption lines originating in a rapidly out-flowing gas given the lack of either an Fe XXVI or, alternatively, lower ionization lines (such as Ar XVI or Ca XX) at the same blueshift. Instead, these features could be highly redshifted Fe XXVI absorption, perhaps originating in a gravitationally redshifted absorber located near the compact object ($r < 100\ GM/c^2$). In this case residuals at ~ 6.6 keV in Spectrum A could be the accompanying Fe XXV line complex.

We modeled the line absorption using PION, a photoionized absorption model within SPEX. Unlike pre-calculated grid models, for instance those from XSTAR (*Kallman and Bautista*, 2001) or CLOUDY (*Ferland et al.*, 2017), PION self-consistently calculates the ionization balance of the absorber in real time, accounting for the changing shape of the ionizing continuum during the fitting process and as it is reprocessed by successive absorbers. We note that PION models H-like lines as proper spin-orbit doublets, so any subtle shifts are not the result of unmodeled line structure.

An important consideration in this analysis was the composition of the absorber. Optical studies of 4U 1916−053 strongly indicate that the companion in the system is likely a Helium-rich white dwarf (*Joss*, 1978; *Nelemans et al.*, 2006); therefore, the disk in 4U 1916−053 is likely also Helium-rich. To first order, only the Hydrogen and Helium content is altered when a progenitor star evolves into Helium-rich white dwarf. Assuming a progenitor with standard solar abundances, the metal-to-helium ion abundances by number are $\sim 3\times$ the metal-to-Hydrogen ion solar abundances. PION assumes a Hydrogen-rich absorber. Although individual abundances can be set for every ion (up to z = 30), it is unclear how setting an arbitrarily low Hydrogen abundance relative to Helium affects the calculation of the ionization balance or the normalization of the re-emission component. Instead, we adopted a more conservative approach wherein we increased the metal abundances relative to Hydrogen by a factor of 3, therefore treating each Hydrogen ion as a proxy Helium ion. This ensures that we obtain the correct absorbing columns while ensuring that

Table 3.1: Parameters for Best-Fit Absorption Models

Individual Spectra						
Spectrum	Model	Parameter	Zone 1	Zone 2	Zone 3	χ^2/ν
Spectrum A	3 Zone	N_{He} (10^{22} cm^{-2})	$50^{\ddagger}_{-10}$	$10^{+40\ddagger}_{-9\ddagger}$	$1.3^{+15.0}_{-1.1}$	536/488 = 1.10
		log ξ	$4.45^{+0.25}_{-0.05}$	$4.80^{\ddagger}_{-1.6}$	$3.8^{1.0\ddagger}_{-1.1}$	–
		v_{abs} (km s^{-1})	230^{+500}_{-270}	$-1700^{+1700\ddagger}_{-1300}$	4200^{+2900}_{-1600}	–
		v_{turb} (km s^{-1})	$270^{+230\ddagger}_{-220\ddagger}$	$300^{\dagger}$	$1000^{\dagger}$	–
		σ_{emis} (km s^{-1})	5400^{+15000}_{-4000}	–	–	–
		L_{phot} (10^{36} erg/s)	8.2 ± 2.2	–	–	–
Spectrum B	1 Zone	N_{He} (10^{22}cm^{-2})	33^{+47}_{-4}	–	–	491/493 = 0.996
		log ξ	$4.4^{+0.4}_{-0.1}$	–	–	–
		v_{abs} (km s^{-1})	230^{+140}_{-130}	–	–	–
		v_{turb} (km s^{-1})	150^{+80}_{-50}	–	–	–
		σ_{emis} (km s^{-1})	–	–	–	–
		L_{phot} (10^{36} erg/s)	5.2 ± 1.5	–	–	–
Spectrum Γ	2 Zone	N_{He} (10^{22}cm^{-2})	34^{+25}_{-4}	–	$50^{\dagger}$	482/486 = 0.99
		log ξ	$4.25^{+0.20}_{-0.05}$	–	$5.3^{+0.7}_{-0.3}$	–
		v_{abs} (km s^{-1})	280 ± 160	–	6500^{+1300}_{-1200}	–
		v_{turb} (km s^{-1})	200^{+150}_{-70}	–	$1000^{\dagger}$	–
		σ_{emis} (km s^{-1})	9300 ± 6000	–	–	–
		L_{phot} (10^{36} erg/s)	10 ± 3	–	–	–

NOTE – Best-fit parameter values for the absorption model that best describes each spectrum, as described in the text. The parameters of absorber include the equivalent *Helium* column (N_{He}), the ionization parameter (ξ), the systematic velocity shift of the absorber (v_{abs}), the turbulent velocity of the absorber (v_{turb}), the dynamical broadening of the re-emission (σ_{emis}), and the ionizing luminosity (from 13.6 eV to 13.6 keV). Quoted errors are at the 1σ level. The absorption in all spectra are dominated by a disk atmosphere (Zone 1): a *nearly* static absorber which has fairly constant properties (N_{He}, log ξ, and v_{abs}) for all observations. Frozen parameters are marked with †. Errors that reach the fitting range for the parameter before the required change in χ^2 are marked with ‡. For Zone 2 and 3, v_{turb} was kept frozen as these components are optically thin and not sensitive to line ratios. A large v_{turb} of 1000 km s^{-1} was chosen that would approximately capture the width of the highly redshifted features (Zone 3) seen in Spectrum A and Γ. For Spectrum Γ, N_{He} was frozen at $5\times$ 10^{23} cm^{-2} (approximately the point at which a *Helium* absorber becomes Compton-thick) as an alternative to the Compton-thin Zone 3 scenario in Spectrum A.

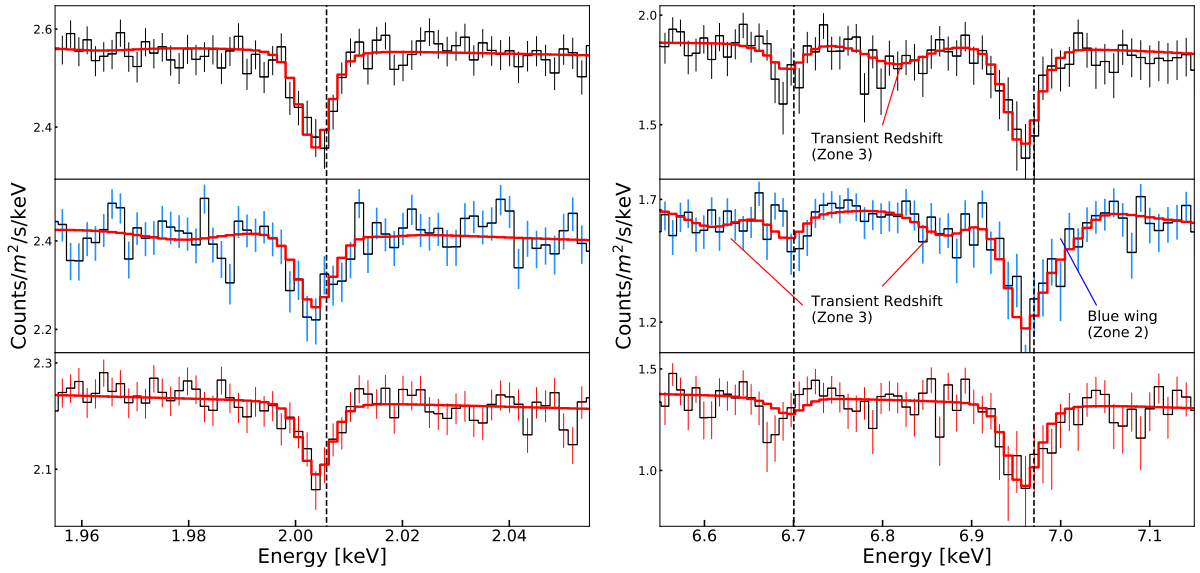

Figure 3.2: From top to bottom, the HETG spectra for Spectrum Γ, A, and B, with the Si XIV region (MEG) and Fe K band (HEG) plotted in the left and right panels, respectively. The best-fit model listed in Table 3.1 plotted in red. Black dotted vertical lines plot the rest energies for Si XIVα (2.0055 keV), Fe XXVα (6.70040 keV), and Fe XXVIα (6.96607 keV). (The weighted average of the H-like spin-orbit doublets is quoted and plotted.) The bulk of Si XIV and Fe XXVI, including line centers, display clear and consistent redshifts ranging from 230 to 290 km s^{-1}. A blue-wing can be seen in the Fe XXV and Fe XXVI lines in Spectrum A (middle-right panel).

the ionization balance calculations work as intended. Although this approximation underestimates the ion to electron ratio by a factor of two, the electron density mostly affects plasmas where collisional ionization is prominent, while it is the ion number density that sets the photoionization balance.

All spectra were initially fit with a two absorption zone model: the first (Zone 1) accounting for the bulk of the absorption from the atmosphere, plus an additional blue-shifted absorber (Zone 2) to model any residual absorption owing to a possible disk wind. Dynamically broadened re-emission was added to models when required by the data, assuming a covering factor of $\Omega/4\pi = 0.4$. This choice of covering factor is informed by the upper limit of $\Omega/4\pi \leq 0.5$ (based on a spherical shell where only half is not obscured by the accretion disk itself) and by a minimum covering factor given by the inclination of the source. As will be clear in the following section, this choice of covering was ultimately inconsequential. In addition, if a second component was found not to be statistically significant for a particular

spectrum, it was removed and the spectrum was fit again with a single absorber. In the case of Spectrum Γ and A, we included an additional PION layer (Zone 3) to test the significance of the weak features at ~ 6.8 and ~ 6.9 keV using a highly redshifted and broad absorber.

3.5.1 Fits

Parameters for the best-fit models to Spectrum A, B, and Γ are listed in Table 3.1. For simplicity, we only list the model that best describes each spectrum. In all observations, the bulk of the absorption occurs in Zone 1 in the form of a disk atmosphere: a (nearly) static absorber with consistent properties, such as high absorbing columns ($N_{He} \sim 40 \times 10^{22}$ cm^{-2}) and ionization ($\log \xi \sim 4.4$), across all observations. Absorption owing to a static disk atmosphere of this kind is not only common, but expected among near edge-on ultra-compact systems. Of the three spectra, only Spectrum A required an additional, blue-shifted absorber (Zone 2) in order to capture both the blue-wing in the Fe XXVI line profile and the shift in Si XIV simultaneously. We discuss this possible wind in section 3.5.4.2.

Strikingly, the disk atmospheres in all three spectra show a consistent and unambiguous redshift of ~ 250 km s^{-1} that is evident and statistically significant (see Section 3.5.2) in both the Fe XXVI and Si XIV lines (the two most prominent lines), and in agreement with other absorption features. The redshift is not a product of fitting a skewed line with a red wing in what otherwise would be a static absorber. As can be seen in Figure 3.2, the line centers of both Fe and Si lines are redshifted to the best-fit value and the bulk of their equivalent widths are below their rest energies (vertical dashed lines). This redshift is also present regardless of whether one or two absorbers are used to model each spectrum. We discuss the origin of the redshift in Section 3.5.2.

3.5.2 The Persistent Redshift

The detection of ionized absorption lines at or near their rest-energies in near edge-on sources is clear evidence of a static atmosphere above the disk surface, as these are nearly

ubiquitous at high-inclinations and absent at moderate to low inclination sources. As noted in Section 3.5.1, the atmospheric absorption found in all the Chandra/HETG spectra of 4U 1916−053 (which encompasses the majority of the absorption) has a consistent redshift ranging from 230 to 290 km s^{-1}. The presence of this shift is notable, as it is unusually high compared to the expected relative radial velocity (and dispersion) in the galaxy and could be evidence of a kick. If the radial velocity of system is small, however, the shift could instead originate in an inflow or a gravitationally redshifted atmosphere. In this section we analyze each of these possibilities.

First, we established the significance of the redshift by performing a simultaneous fit of the three spectra. We performed three variations of the same test, where we tracked the increase in χ^2 between the best-fit redshifted atmosphere model and the best-fit atmosphere model with velocities fixed at zero. In the first test, the absorber used to fit the three spectra shared the same column, ionization, and velocity. In the second test, only the velocity was linked between the three spectra, while all parameters were fit independently in the third test. We obtained $\Delta\chi^2$ values of 36, 37, and 38 for 3, 7, and 9 free parameters, respectively. This corresponds to a significance for the first test above 5σ and above 4σ for the second and third tests. The significance of the redshift is high despite using only one absorption zone with no re-emission to model all three spectra. Finally, we added the three spectra into a single combined A + B + Γ spectrum and fit the time-averaged absorption. We obtained an average redshift of 260^{-80}_{+80} km s^{-1} with lower limits of 150 (2σ), 120 (3σ), 90 (4σ), and 50 (5σ) km s^{-1}. These results are summarized in Table 3.2.

An overview of the *Chandra X–Ray Observatory's* performance (*Marshall et al.*, 2004) reports average systematic errors on the absolute wavelength calibration for both the MEG and HEG of less than 100 km s^{-1}. Systematic errors in the absolute wavelength calibration of the HETG arise from reconstructing the wavelength grid relative to the location zeroth order of the spectrum. This absolute wavelength calibration error, however, corresponds to the error in *individual* lines in *individual* spectra, as opposed to the exercise of determining

the shift of an absorber by fitting *multiple lines*. The aforementioned study demonstrates how the *average* error in the shift of the *emitter* is considerably lower once multiple lines are considered. Given that our 3 spectra were produced by combining 11 total observations, each with their own independent spectral extraction (and therefore independent wavelength error) yet still produce a consistent redshift suggests that systematic errors in the energy grid of the HETG are not significant. Much smaller uncertainties on velocities, such as an analysis on Capella which achieved errors at the 90% level of ~ 30 km s^{-1} (*Ishibashi et al.*, 2006), are commonly accepted.

In galactic coordinates, 4U 1916−053 is located -8.5 degrees away from the galactic plane. With distance estimates ranging from 7 to 11 kpc (*Smale et al.*, 1988; *Yoshida et al.*, 1995), it lies at ~ 1.5 kpc above the disk of the milky way, most likely making it a member of the thick disk of the Milky Way. Figure 3.3 shows the expected systematic velocity of the source for a range of distances, where we adopted a thick-disk rotational lag (relative to the thin-disk, ~ 220 km s^{-1}) of ~ 50 km s^{-1} and a thick-disk velocity dispersion of ~ 50 km s^{-1} (*Pasetto et al.*, 2012). The mean relative velocity is plotted in blue and the shaded regions represent $1\times$ and $2\times$ the local velocity dispersion. Based on the recent distance estimate of 9.0 ± 1.3 kpc (*Galloway et al.*, 2008), the expected velocity of the system is 37 ± 54 km s^{-1} with a 2σ upper limit of 142 km s^{-1}, below the 2σ lower limit on the redshift in the disk atmosphere of 150 km s^{-1}. Even without constraints on the distance, there is little to no overlap between the 2σ regions in Figure 3.3.

Although the predicted galactic motions are small, a *natal kick* may produce a radial velocity corresponding to the observed redshift. Indeed, pulsar kicks have been observed in the 100-1000 km s^{-1} range (see *Atri et al.*, 2019), making it difficult to rule-out radial motion. If the redshift is indeed the result of the radial velocity of the system, however, then all absorption features otherwise expected to be at rest velocities should display the same redshift. In 4U 1916−053 and other dippers, particularly strong absorption lines are detected during dipping events, and typically associated with the outermost edge of the

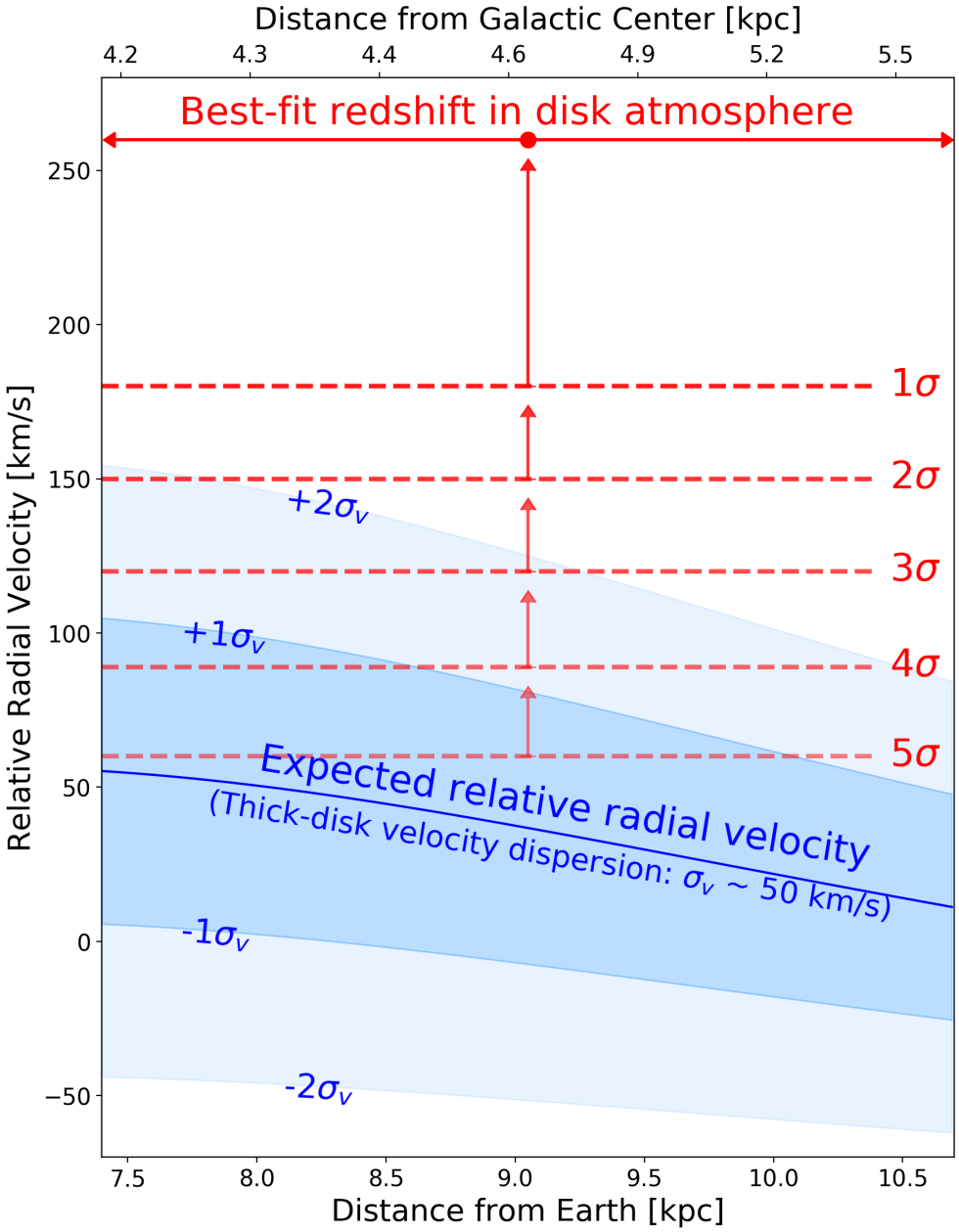

Figure 3.3: The predicted relative radial velocity of 4U 1916−053 as a function of its distance from the galactic center, based on its distance from earth (9.0 ± 1.3 kpc) and galactic coordinates. The mean velocity is plotted in blue using a thick-disk rotational lag (relative to the thin-disk) of $\sim$ 50 km s^{-1}, while the the shaded regions represent integer multiples of the thick-disk velocity dispersion ($\sim$ 50 km s^{-1}). The best-fit disk atmosphere redshift for the combined A + B + Γ spectrum is plotted in red, with the 1σ to 5σ confidence regions plotted as dashed lines. The small overlap between 2σ confidence regions below $\sim$7.7 kpc is eliminated once uncertainties in the distance are folded in. The observed redshift cannot easily be attributed to the kinematics of the thick disk.

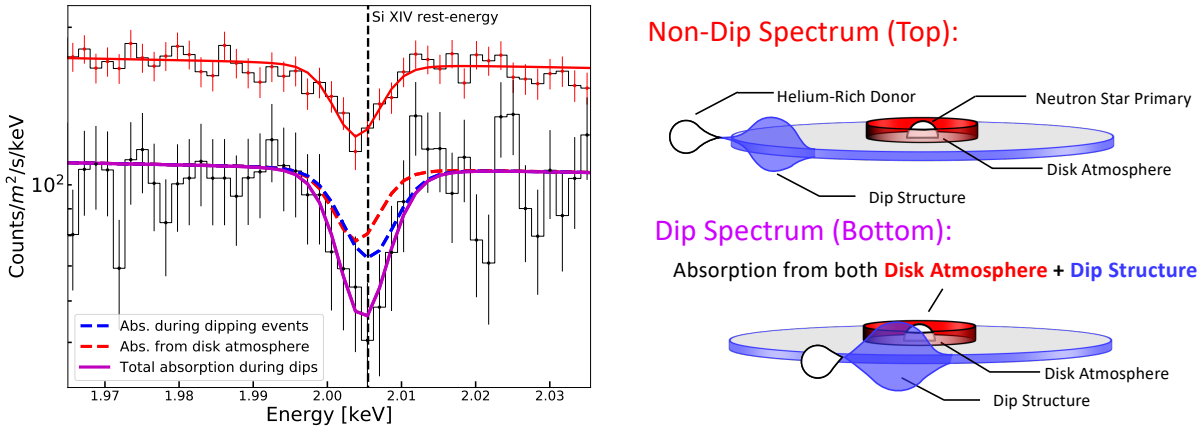

Figure 3.4: Spectrum B dip (bottom, black) and non-dip (top, red) MEG spectra in the Si XIV region. The redshifted atmospheric absorption during non-dip spectra does not capture the Si XIV line during dip events, as well as other lower-ionization lines below 2 keV. The excess absorption is best-fit with a slightly *blue-shifted* absorber ($v_{abs} = -80 \pm 110$ km s^{-1}), where the 2σ confidence regions of this velocity shift in the outer disk ($v_{dip} < 90$ km s^{-1}) and the redshift in the disk atmosphere ($v_{atm.} > 150$ km s^{-1}) do not overlap. This suggests that the systematic radial velocity of the source is small and not responsible for the persistent redshift observed in the disk atmosphere.

accretion disk (*Díaz Trigo et al.*, 2006). Based on the orbital phase and kinematics of dipping events, the velocity shift of these excess absorption lines from the outer disk should be dominated by the systematic velocity of the source. All dips were initially filtered-out from the spectra analyzed in this work. However, the 250 ks of new *Chandra* exposure makes it possible to extract sensitive spectra from the numerous dip events in Spectrum B.

If the inner disk atmosphere is truly static, and if the dips truly originate in the outermost disk, then dip spectra should contain absorption lines from the inner disk atmosphere *and* the outermost disk. We therefore modeled the dip spectrum using the same best-fit model for Spectrum B listed in Table 3.1, plus an additional absorber. Due to the modest S/N in the Fe K region of the dip spectrum, we focused only on the MEG spectrum between 1.5 and 2.5 keV. Our resulting fits suggested a relatively low ionization log $\xi \sim 2.2$, a helium column of $N_{He} \sim 10^{22}$ cm^{-2}, and a small turbulent velocity of $v_{turb} \sim 50$ km s^{-1}.

Figure 3.4 shows the Si XIV line for both dip (black) and non-dip spectra (red) with their corresponding best-fit models. The rest-energy of the Si XIV line is plotted as the vertical dashed line, and the contribution of the redshifted atmosphere is plotted in red for both spectra. It is clear that there is significant absorption in the dip spectrum that is not being

Table 3.2: Velocity Shift Comparisons

Disk Atmosphere Redshift			**Relative Radial Velocity**				
Combined A+B+Γ Spectrum (km s^{-1})					Expected Galactic Motion (km s^{-1})	Dips (km s^{-1})	Posteriors (km s^{-1})
Best-fit value		260^{+80}_{-80}	Best-fit or mean value:		40 ± 50	-80 ± 110	5 ± 42
Lower Limits:	2σ	> 150	Upper Limits:	2σ	**<140**	**<90**	85
	3σ	> 120		3σ	190	170	**<130**
	4σ	> 90		4σ	...	...	...
	5σ	> 60		5σ			

NOTE – Comparison between the redshift measured in the disk atmosphere (left) and the radial velocity of the system (right). Best-fit or mean expected values are quoted with their 1σ confidence regions. Lower limits to the redshift in the disk atmosphere and upper limits to the systematic radial velocity of the system are quoted based on their 2σ, 3σ, 4σ, and 5σ errors. Values in bold correspond to the closest integer significance at which the redshift in the disk atmosphere does not match the radial velocity. The posterior probability resulting from the thick-disk kinematics and the measured excess absorption in the outer disk yields a near 3σ difference from the shift in the disk atmosphere.

captured by the absorber used to model the atmosphere in the non-dip spectrum. Visually, the excess absorption does not share the same velocity shift as the line originating in the atmosphere (red), with most of the excess dip absorption contributing at slightly higher energies, consistent with no velocity shift. The combined line profile itself is not quite centered at the rest-energy of Si XIV. This is confirmed by spectral fitting, where the excess (plotted in blue) is best-fit with a slightly *blue-shifted* ionized absorber $v_{dip} = -80 \pm 110$ km s^{-1} (with a 2σ upper limit of 90 km s^{-1}). Despite the lower S/N of the dip spectrum, we can rule out the possibility of both the atmosphere and dips absorption sharing the same redshift at a modest confidence level of 2.5σ by fitting the strongest lines in the 1.5 to 2.5 keV range. Indeed, the posterior probability resulting from combining the thick disk kinematics (the prior) with this outer disk shift suggests a near zero velocity shift and a 3σ upper limit of ~ 130 km s^{-1}.

The lack of a *positive* velocity shift in the outer disk suggests that the systematic velocity of 4U 1916−053 (its projected kick velocity, if any) is significantly lower than the ∼260 km s^{-1} redshift observed in the atmosphere, and formally consistent with zero. This analysis strongly suggests that the persistent redshift seen in all spectra is associated with an inner disk atmosphere.

A failed wind or inflow could, in principle, be responsible for the observed redshift. The most direct evidence of such a flow would be the presence of inverse P-Cygni profiles. These are missing from our data, yet ruling out an inflow in this fashion likely requires much higher quality spectra. Still, an inflow of this sort seems unlikely. First, an inflow would require some mechanism that removes enough angular momentum from the atmosphere in a much lower density environment compared to those found in the disk. This mechanism would have to produce an inflow with a very low covering factor, as we do not observe ionized absorption lines, much less redshifted lines, in sources viewed at lower inclinations. This means the inflow, which must originate at relatively large radii, would have a small vertical extent. The presence of X-ray bursts suggest that the magnetic field of the neutron star is likely not strong enough to induce a collimated inflow.

The specific properties of the absorber also render unlikely an inflow. In the almost 300ks of new and archival Chandra/HETG exposures of 4U 1916−053, the source displays a range of spectral states over a period of ∼14 years. Despite the large temporal separation, the observed redshift appears to be constant for all observations even as source undergoes noticeable changes in accretion state. This would suggest that whatever physical mechanism was responsible for removing the angular momentum from the atmosphere would necessarily produce the same redshift despite different physical conditions within the disk.

We find that the most likely explanation for this redshift is that of a static atmosphere, located close enough to the compact object to be subject to a ∼260 km s^{-1} gravitational redshift. Unlike a putative inflow, a gravitationally redshifted disk atmosphere (or, GRDA for short) would be more consistent with the static atmospheres we expect to see in these sources and with the behavior of the absorption in this source in particular. This explanation only invokes general relativity in the weak limit, requiring the absorber to be located at around $\sim 1200\ GM/c^2$, or $\sim 1800\ (\frac{M_{NS}}{M_\odot})$ km.

Table 3.3 lists the properties of the disk atmosphere found in our spectra, using three different methods for measuring the radius from the compact object to absorber. The first

Table 3.3: Disk Atmosphere Geometry and Physical Properties

Spectrum		Radius		n_{He}	f	$z_{Grav.}$	$v_{corr.}$	$v_{corr,2M_\odot}$
		(10^8 cm)	(GM/c^2)	(10^{14} cm^{-3})		(km s^{-1})	(km s^{-1})	(km s^{-1})
A	R_{Upper}	$5.4^{+2.0}_{\ddagger}$	$3600^{+1300}_{\ddagger}$	$9.3^{\ddagger}_{-4.5}$	$1.0^{\dagger}$	$70^{\ddagger}_{-30}$	160^{+230}_{-220}	90 ± 230
	$R_{Orbital}$	$4.65^{+4.7}_{-4.1}$	3100^{+3200}_{-2800}	13^{+13}_{-10}	$0.9^{\ddagger}_{-0.8}$	100^{+90}_{-100}	120^{+500}_{-240}	–
	R_z	2.0 ± 1.7	1300 ± 1200	70^{+130}_{-50}	$0.4^{\ddagger}_{-0.4}$	$260^{\dagger}$	$0^{\dagger}$	–
B	R_{Upper}	$5.4^{+1.8}_{-4.4}$	3700^{+1200}_{-3000}	$6.0^{+5.2}_{-4.9}$	$1.0^{\dagger}$	80^{+70}_{-30}	150^{+160}_{-140}	60^{+200}_{-140}
	$R_{Orbital}$	–	–	–	–	–	–	–
	R_z	$2.0^{+1.1}_{-1.2}$	1300 ± 800	50^{+30}_{-40}	$0.36^{+0.36}_{-0.25}$	$228^{\dagger}$	$0^{\dagger}$	–
Γ	R_{Upper}	17^{+3}_{-11}	11000^{+2000}_{-7000}	$4.0^{+2.6}_{-1.9}$	$1.0^{\dagger}$	26^{+16}_{-5}	260^{+170}_{-160}	230^{+170}_{-160}
	$R_{Orbital}$	$1.5^{+0.9}_{-1.0}$	1000 ± 600	480^{+300}_{-360}	$0.09^{+0.08}_{-0.06}$	290^{+180}_{-170}	0^{+240}_{-230}	–
	R_z	1.6 ± 0.9	1100 ± 600	500 ± 300	$0.09^{+0.08}_{-0.06}$	$285^{\dagger}$	$0^{\dagger}$	–

NOTE – Physical properties of the disk atmosphere of Spectrum A, B, and Γ as a function of the upper limit of on the photoionization radius ($R_{Upper} = f \cdot L/N_{He}\xi$), the radius given by the dynamical broadening of the re-emission ($R_{Orbital}$), and the radius given by the observed redshift (R_z). A neutron star mass of $1M_\odot$ was assumed to calculate some values. When using R_{Upper}, only z_{Grav} and $v_{corr.}$ depend on mass. Values for $v_{corr.}$ assuming at $2M_\odot$ are listed in the last column. A Filling factor of unity is assumed using R_{Upper}. In the case of both $R_{Orbital}$ and R_z, only the density (n_{He}) and filling factor (f) depend on mass. For $2M_\odot$ neutron star, the density decreases by a factor of 4 and the filling factor increases by a factor of 2.

is the upper limit on the photoionization radius, $R < R_{upper} \equiv L/N_{He}\xi$, where $R = f \cdot R_{upper}$ and f is the filling factor. We assumed a filling factor of unity for simplicity. The second is the radius given by the dynamical broadening of the re-emission from the gas, $R = GM/\sigma^2_{emis}$, assuming the velocity broadening (σ^2_{emis}) probes the local Keplerian velocity. In the case of a GRDA, the measured redshift can be used in order to directly measure this radius in units of GM/c^2, assuming the redshift is entirely due to gravity. The radius, $R = R_z$, is also included in Table 3.3.

For simplicity, the gravitational redshift (z_{Grav}) and the resulting corrected velocity (v_{corr}) values at $R = R_{Upper}$ listed in Table 3.3 were calculated assuming a neutron star mass of $1M_\odot$ (values for v_{corr} for $2M_\odot$ were also included). Being an upper limit on the distance of the absorber from the central engine, R_{Upper} places a lower limit on z_{Grav} which only increases with neutron star mass. In the case of Spectrum A and B, R_{Upper} suggests that the disk atmosphere must be gravitationally redshifted by at least $\sim$70 km s^{-1}, which increases to $\sim$150 km s^{-1} for a mass of $2M_\odot$. In the case of Spectrum Γ, this lower limit

is significantly smaller. Uncertainties on the distance and SED shape make R_{Upper} an imperfect upper limit. It is notable that the radius given by the broadening of the re-emission, $R = R_{Orbital}$, is consistent with the radii determined by associating the redshift with a gravitational shift. However, this velocity broadening value is poorly constrained and assumes an semi–arbitrary choice of emission covering factor, and therefore we advise caution when interpreting this result. Ultimately, the picture of a static, photoionized disk atmosphere deep in the gravitational potential is self-consistent. Please see Table 3 for all of the relevant measurements, and velocities corrected to the assumed rest frame of the absorption.

If the observed redshift is entirely gravitational, it is possible to constrain other aspects of the disk atmosphere by insisting on the radii being equal. For instance, the filling factors, f, for Spectrum A and B range from ~ 0.3 to $\sim$0.6 for neutron star masses of 1 and 2 $M_{\odot}$, respectively. This suggests a low degree of clumping within the atmosphere; in this respect, the atmosphere may differ substantially from winds that are observed downstream in this and other sources. At 1 $M_{\odot}$, the atmosphere in Spectrum Γ would be significantly more clumpy by comparison, although this low filling factor of $f \sim 0.1$ is far from unphysical. It is also possible to derive gas densities in the atmosphere; these range from $15 < \log n_{He} < 16.7$. This range of gas densities are comparable to those inferred in studies of disk winds in accreting black holes (e.g., *Miller et al.*, 2016; *Trueba et al.*, 2019). At the higher end, these values are comparable with densities expected within the disk ($15 < \log n_e < 19$, see *García et al.*, 2016). Finally, we note that when the radial location of the absorber is known, the local Keplerian velocity is defined; then, if the turbulent broadening can be measured via fits to multiple lines, the measured width of time-averaged absorption lines gives the size of the central engine. Using these data, a value of $R \simeq 60^{+20}_{-30}\ GM/c^2$ results. However, it is likely more appropriate to treat this as an upper limit. This technique is the subject of a forthcoming paper (Trueba et al. 2020, in preparation).

A disk atmosphere located at $\sim$ 1200 GM/c^2 would likely require magnetic pressure

support in order to produce the columns we observe along our line of sight, as any plausible gas temperatures produce far less thermal energy than required. Numerical models of MRI (see *Balbus and Hawley*, 1991) disks suggest than magnetic pressure support can not only dominate the upper layers of the disk, but can also result in a more extended vertical structure (*Blaes et al.*, 2006), much like the absorbing atmosphere along our line of sight. As an order of magnitude comparison, we estimated the local magnetic field ($B \sim \sqrt{8\pi P}$) required to maintain hydrostatic equilibrium via $dP/dz \simeq sin\,\theta \cdot GM\rho/r^2$, where $sin\,\theta \simeq r/z$ and $dP/dz \sim P/z$, and therefore $P \simeq GM\rho/r \cdot z^2/r^2$. Using the largest densities in Table 3.3 and a large z/r 0.3, we get a local magnetic field of $\sim$ 2 10^5 G, which is still below the upper limit on the magnetic field given by *Shakura and Sunyaev* (1973) of $\sim$ 5 10^5 G (equation 2.19).

3.5.3 Redshifted Lines in Archival Data

A large number of neutron star X-ray binaries are currently known, so it is unlikely that a gravitationally redshifted disk atmosphere would be unique to 4U 1916−053. However, no redshifts like those now discovered in 4U 1916−053 have been reported in the literature. In longer-period systems with larger disks, a longer path length through the extended disk atmosphere may simply wash-out the signature of the inner disk atmosphere. Particularly amongst ultra-compact and short period dipping/eclipsing X-ray bursters, however, wherein the magnetic field of the neutron star is weak and the accretion disk is small, we should find evidence of redshifted atmospheres. We examined the available Chandra/HETG archival data for sources that fit these criteria. The same data reduction procedure as in section 3.4 was followed.

Of the few sources in our sample, we found very similar redshifts of $\sim$300 km s^{-1} in the spectra of both XTE J1710−281 and AX J1745.6−2901. As per the absorption seen in 4U 1916−053, it is the bulk of the line absorption that is redshifted, with multiple lines displaying the same redshift. In the only HETG spectrum of AX J1745.6−2901, the

redshift is present in both He and H-like iron absorption lines, at a significance of $\sim 2.5\sigma$. Unfortunately, the neutral ISM column is too high to confirm this redshift via Si XIV. This is not the case for the brighter of the two archival spectra of XTE J1710−281, which instead showed multiple strong redshifted absorption lines between 1.0−2.6 keV as well as Fe K. The ∼320 km s^{-1} redshift is unmistakable and significant at well over 5σ (Trueba et al. 2020 in prep).

The Chandra observation of AX J1745.6−2901 was a conducted as part of a campaign involving both XMM-Newton and NuSTAR (see *Ponti et al.*, 2018b). To date, a spectral analysis of this spectrum has not been published and no redshift has been reported. This is likely due to the relatively low S/N of the spectrum. More surprising is the case of XTE J1710−281, where the highly significant redshift has also not been reported. It is possible that carefully screening against dips and bursts, and our use of the relatively new "optimal" binning algorithm, has enabled us to extract more information from new and archival data.

We note that possible redshifts were also found in the spectra of other sources (e.g., EXO 0748−676), but these were either low S/N spectra or displayed complex absorption with multiple velocities. The remaining spectra contained either no absorption lines or, in the case of sources with longer orbital periods, lines at rest velocities. Based on the galactic coordinates of both XTE J1710−281 (356.3571 +06.9220, likely in the thick disk) and AX J1745.6−2901 (359.92030 -00.04204), a natal kick would likely be required in order to attribute the observed redshifts entirely to the relative radial velocities of either of these systems. Ultimately, robust radial velocity measurements are required in order to confirm the origin of these redshifts. However, these results are promising in that they are consistent with a physical connection between the processes that give rise to disk atmospheres with redshifted lines, be it gravitational redshift from an inner disk atmosphere or some persistent, semi–spherical inflow.

3.5.4 Transient Absorption Features

In the previous section, we mentioned evidence of transient absorption features in our spectra aside from the primary absorber, which we attribute to a redshifted inner disk atmosphere. The first is evidence of absorption between 6.8 and 6.9 keV in both Spectrum A and Γ, which we attribute to a much more highly redshifted disk atmosphere. The second is evidence of a disk wind in Spectrum A, which appears as a blue wing in the Fe XXVI absorption line at ~ 6.97 keV (as well as perhaps some complexity in the Si XIV line near ~ 2 keV). In this section, we will discuss alternative interpretations and fits to the data, their significance, and some physical implications of these results.

3.5.4.1 The Transient Redshift

The putative highly redshifted component deserves additional scrutiny and caution. It is present in two of the three spectra in question (only missing from the lowest S/N spectrum: Spectrum B), suggesting it may not simply be noise. In addition, if we divide the best-fit column density by its -1σ error (analogous to assessing the significance of a Gaussian line using its normalization and error) we can obtain a crude estimate of the significance for this component. In the case of Spectrum Γ, possible fits to this component displayed a strong degeneracy between N_{He} and $\log \xi$ for values of N_{He} above $\sim 20 \times 10^{22}$ cm^{-2}, which is why we froze this parameter in the fit reported in Table 3.1. In order to determine the significance in this spectrum, we re-fit the data by thawing the N_{He} parameter and then performing an error search with the $\log \xi$ parameter frozen at its new best-fit value. Freezing $\log \xi$ was necessary in this case: for lower N_{He} values, the fit will yield a lower ionization in order to produce a comparable line depths, making this test meaningless. We obtained a column of 34^{+4}_{-12} (10^{22} cm^{-2}), which corresponds to a significance of $\sim 3\sigma$. In addition, we performed an f-test comparing our model to a single-zone model and also obtined a significance of 3σ.

This test was not as straightforward in the case of Spectrum A. Although visually these features are similar in both spectra, the errors on the column for this component suggest

a significance of barely above 1σ. This, in part, is due to the complexity of the model for Spectrum A. As previously mentioned, an F-test suggests a 3σ improvement over the single zone model. However, given the low significance suggested by the errors on the N_{He} parameter, we advise caution when interpreting the significance of this component. Notably, we have established that the bulk of the observed absorption originates in an atmosphere that is redshifted, possibly as a result of local gravitational redshift. This component may simply be a different portion of this atmosphere arising at smaller radii.

Alternatively, these components could be evidence of a highly *blueshifted* absorber, corresponding to gas outflowing at velocities near $\sim 0.03c$. In both Spectrum Γ and Spectrum A, however, the most prominent feature motivating the analysis of this transient absorber is located near ~ 6.8 keV, which in the case of a *blueshifted abosorber* would correspond to He-like Fe XXV absorption. The location of the corresponding blueshifted Fe XXVI line shows little evidence of an absorption line, although weak Fe XXVI absorption is plausible given the quality of the data. Prominent Fe XXV lines with little Fe XXVI absorption suggest a gas of fairly low-ionization which is often accompanied by absorption from He-like and H-like Ca, Ar, Si, and S (to name a few), none of which we find at or near the blueshifts suggested by the feature at 6.8 keV, making the high-blueshift interpretation unlikely.

This was confirmed by spectral fitting, as we were completely unable to fit a blueshifted component onto the feature near ~ 6.8 keV in Spectrum A using a photoionized absorption model. In the case of Spectrum Γ, however, the significance of a highly blueshifted absorber ($\chi^2/dof = 487/485$) is comparable to that of the highly redshifted one ($\chi^2/dof = 482/486$). If the feature at ~ 6.8 keV is real in both spectra, then it seems more likely for these absorbers to originate via similar physical mechanisms. This means that it is unlikely that we are detecting a dramatically blueshifted absorber in one observation and a dramatically redshifted one in another, especially when the main feature in both is located at essentially the same energy. Our fits to Spectrum A would then suggest that this is more likely an extremely redshifted inner disk atmosphere rather than a near-UFO. Given the quality of

the data, however, the nature of this feature will remain unclear until further observation.

3.5.4.2 Evidence of a Disk Wind

Previous studies on the best Chandra/HETG LMXB wind spectra have been able to model and identify multiple velocity components of the absorbing wind complex. In cases such as 4U 1630−472 (*Miller et al.*, 2015a; *Trueba et al.*, 2019) and GRS 1915+105 (*Miller et al.*, 2016), although the individual velocity components are all blended to produce multiple skewed line profiles, the resulting line spectrum displays different velocity shifts for lines corresponding the different ionization and column densities of the separate absorbers. In these cases, models with multiple absorbers are *required* to describe the data.

The same analysis can be applied to 4U 1916−053 where, instead of a wind complex, the presence of both a static atmosphere and a weakly absorbing wind may require the use of multiple absorbers. Of the three spectra, compelling evidence for a disk wind can only be found in Spectrum A. Although the shape of the Fe XXVI line in Spectrum B is similar to that in Spectrum A, a two component model resulted in no significant improvement to the fit because of the lower S/N of the spectrum, as well as the asymmetry in the line being less pronounced.

The three component model of spectrum A (including a wind; see Table 3.1) yields a $\chi^2/dof = 536/488 = 1.10$, a modest but non-trivial improvement of $\Delta\chi^2 = 23$ over the best-fit single-component model ($\chi^2/dof = 559/495 = 1.14$). An F-test quantifies this as a 3σ improvement over the one component model. Visually, the one component model is unable to capture shifts and depths of both the Si XIV and Fe XXVI simultaneously. Since the redshift of the single absorber model is lower than that in the atmosphere plus wind model, the resulting fit underestimates the red portion of Si XIV and greatly over-estimates the absorption in the red portion of Fe XXVI. In our fitting experiments, we found that adding dynamically broadened re-emission from the same absorbing gas could help achieve better fits to both Si and Fe lines. Although this is true even in the single component model,

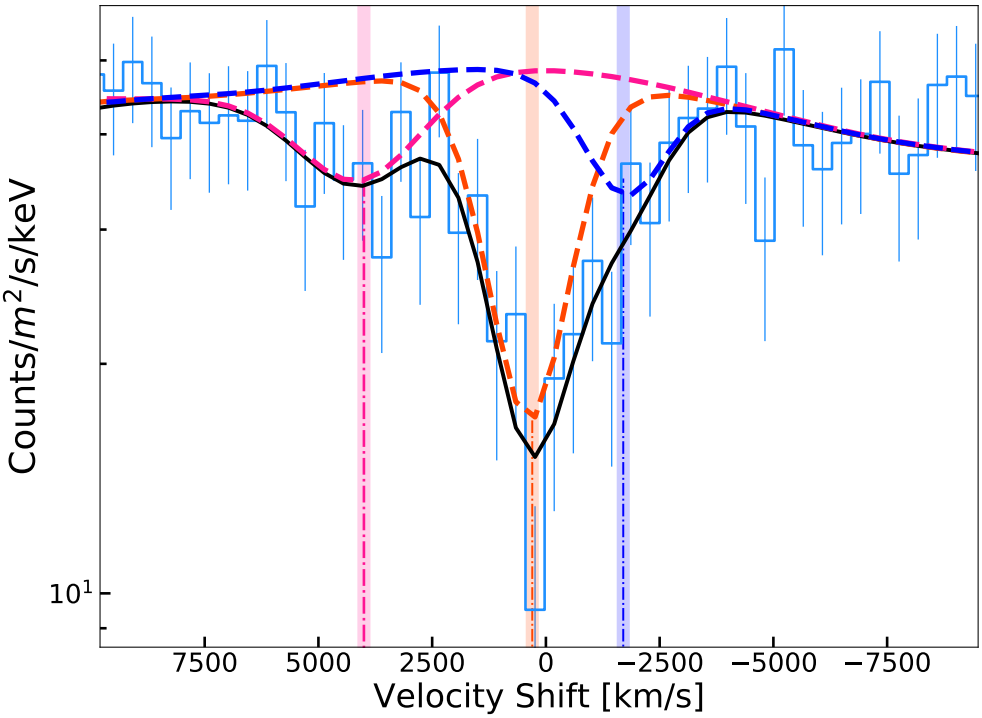

Figure 3.5: The combined first-order HEG portion of 4U 1916−053 from Spectrum A, with the best-fit 3-zone model. The combined Fe XXVI line profile is plotted in velocity space relative to the rest energy of Fe XXVI. The contribution of the putative highly redshifted absorber ($v \sim 4300$ km s^{-1}, plotted in pink) can also be seen near ~ 6.6 and ~ 6.8 keV in Figure 3.2. A blue-shifted disk wind component ($v \sim -1700$ km s^{-1}, plotted in blue) is required to fit the extended blue wing of the line. Separately, the bulk of the composite line requires modestly redshifted Si and Fe absorption (plotted in red) owing to the disk atmosphere. In this model, the Si XIV line is captured by a single absorber (Zone 1, the disk atmosphere).

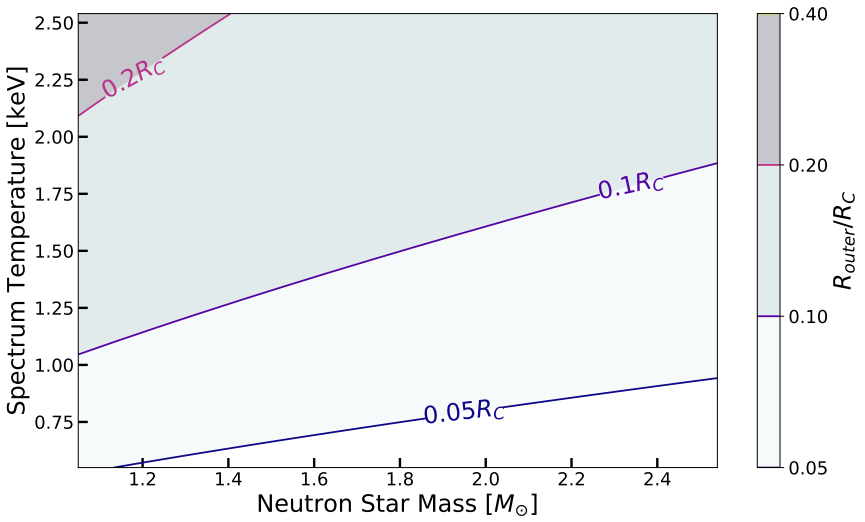

Figure 3.6: Ratio of the disk outer-radius (based on the orbit of the donor star, for an orbital period of 50 minutes) over the Compton radius, as function of neutron star mass and the temperature of the comptonizing spectrum. Within the plausible range of temperatures (based on fitting the disk and neutron star temperatures) and neutron star mass, this outer radius never exceeds 0.2× the Compton radius.

adding broad emission lines to the wind or the highly redshifted component (Zone 3) only makes these features more pronounced. Adding re-emission, therefore, did not improve the fit of the single component model. Individually, the addition of either a wind absorber (Zone 2) or the highly redshifted absorber (Zone 3) resulted in only marginal improvements to the model. Instead, the model requires re-emission and two additional absorbers in order to adequately describe the data. However, the errors reported in Table 3.1 indicate that most parameters for this absorber are poorly constrained. In particular, the negative 1σ error on the absorbing column ($N_{He} = 10^{40}_{-9} \times 10^{22}$ cm^{-2}) approaches unity with the best-fit value and would suggest that the wind is only significant to 1σ. This is in part driven by the complexity of the model that requires a larger change in χ^2. Given the tension between the significance suggested by the F-test and the error in N_{He}, we advise caution when interpreting this result.

The large uncertainty in the outflow velocity of the absorber, however, is due to a local χ^2 minimum in a different region of parameter space. The best-fit model reported in Table 3.1 fits the bulk of the absorption lines with the absorber corresponding the redshifted

disk atmosphere and the blueshifted absorber fits the blue-wing of the Fe XXVI line, only (see Figure 3.5). As can be seen in the middle panel of Figure 3.2, however, the Si XIV line profile also demonstrates some evidence of complexity in the form of a blue-wing. We performed an alternative fit to Spectrum A in order to capture the blue-wings of both Fe XXVI and Si XIV line profiles, which we report in Table 3.4. Although the parameters are quite different, statistically, the fits nearly identical. Strikingly, this new fit suggests that the redshift in the atmosphere is much stronger (~ 600 km s^{-1}), while the blueshift in the "wind" component is much lower (~ -200 km s^{-1}) and is essentially consistent with zero. A plausible interpretation is that, in this spectrum, we are probing different regions of the disk atmosphere, where the inner atmosphere is noticeably redshifted while the outer regions are only slightly redshifted. It is important to note that the redshift of the atmosphere given by the former model is consistent with the fits of Spectrum B, Spectrum Γ, and the combined A + B + Γ Spectrum, while the alternative model gives a much larger redshift (~ 600 km s^{-1}) and less self-consistency.

The possible presence of a disk wind in UCXBs such as 4U 1916−053 can provide key insights about the physical mechanisms that drive disk winds in accreting black holes and neutron stars in general. Magnetic winds in LMXBs are of particular interest as they provide an observational evidence of different magnetic processes mediating mass and angular momentum transfer within the disk. Furthermore, evidence of self-similar winds driven via MHD pressure, possibly as a result of the magnetorotational instability, has been uncovered in GRO J1655-40 (*Fukumura et al.*, 2017) and 4U 1630−472 (*Trueba et al.*, 2019) through their density and velocity structure.

Determining whether a wind is driven via magnetic processes has primarily relied on ruling out alternative driving mechanisms via estimates of their launching radii. Although radiation pressure driving (via line driving) can be ruled-out given the high degree of ionization within the gas, thermally driven winds could still arise via Compton heating of the disk surface by energetic photons from the central engine. In principle, this can only occur

Table 3.4: Alternative Fit to Spectrum A

Parameter	Zone 1	Zone 2	Zone 3
N_{He} (10^{22}cm^{-2})	$45^{+5\ddagger}_{-20}$	$20^{+30\ddagger}_{-18}$	$1.3^{+15.0}_{-1.1}$
log ξ	$4.5^{+0.3\ddagger}_{-0.1}$	$4.4^{+0.4\ddagger}_{-0.5}$	$3.7^{1.0}_{-0.9}$
v_{abs} (km s^{-1})	580^{+740}_{-550}	$-220^{+220\ddagger}_{-1800\ddagger}$	4200^{+2800}_{-2600}
v_{turb} (km s^{-1})	$70^{+430\ddagger}_{-20\ddagger}$	$300^{\dagger}$	$1000^{\dagger}$
σ_{emis} (km s^{-1})	$8000^{+12000\ddagger}_{-7000\ddagger}$	–	–
χ^2/ν			533/488 = 1.09

NOTE – Parameter values for the alternative fit to Spectrum A. Unlike the fit listed in Table 3.1, Zone 2 captures the blue-wing in both Fe XXVI *and* Si XIV lines. The fact that the data can be described by this alternative fit drives much of the degeneracy when fitting this spectrum.

at radii larger the Compton Radius (or, R_C), where the temperature of the disk surface allows a sizable portion of the gas to exceed the local escape velocity (*Begelman et al.*, 1983), although this limit may extend down to $0.1R_C$ (*Woods et al.*, 1996). In sources such as GRS 1915+105 (*Miller et al.*, 2015a, 2016), GRO J1655−40 (*Miller et al.*, 2006b, 2008, 2015a; *Neilsen and Homan*, 2012; *Kallman et al.*, 2009), and (among others) 4U 1630−472 (*Miller et al.*, 2015a; *Trueba et al.*, 2019), wind launching radii derived by modeling the photoionzed wind absorption (and, in some cases, wind re-emission) have been well below R_C, suggesting magnetic driving. In the helium rich disk of 4U 1916−053, $R_C = 2 \cdot 10^{10} \times (M_{BH}/M_{\odot})/T_{C8}$ cm, where the mean molecular weight of *fully ionized* helium gas ($\mu_{He} \sim 1.3$) makes this limit larger ($\sim 2\times$) compared to solar abundances.

There are, however, uncertainties that can significantly limit our ability to measure wind launching radii. In most cases, the lack of an independently measured gas density means that we can only place an upper limit the radius given by photoioinization parameter, $\xi = L/nr^2$. This is worsened by our imperfect understanding of the luminosity and shape of the ionizing continuum, as well as poorly constrained distances to these sources. In the case of 4U 1916−053 and UCXBs in general, the outermost radius of their small disks (truncated by the orbit of the companion) is itself a useful upper limit on the launching radius of a possible disk wind. Given the orbital period of the X-ray dips and range of possible neutron star masses, we can obtain estimates of this outermost radius through

basic Keplerian mechanics, which we can then compare to the Compton radius. Unlike the photoionization radius, this upper limit is model independent and does not depend on the distance, luminosity, or SED shape.

Figure 3.6 shows a contour plot of the ratio of outermost disk radius over R_C, as a function of neutron star mass and spectrum temperature. The outermost radius is given by $R_{outer} \sim R_{donor} \times 0.5/(1+q)^{1/3}$ (*Paczyński*, 1967), $R_{outer} \sim R_{donor} \times 0.6/(1+q)$, where R_{donor} is the orbital radius of donor star and q is the binary mass ratio (we assume q $<<$ 1 in order to establish an upper limit). Our understanding of the broadband continuum is poor within the narrow Chandra energy range, making it difficult to constrain the temperature of disk (at low energies), the temperature of the neutron star, and which of these determines the Compton temperature. Instead of a assuming a single temperature, we chose to plot this ratio for a range of possible temperatures. Our results suggest that the outermost radius of the disk is smaller than the Compton radius, with the largest ratio indicating a disk smaller than $\sim 0.2R_C$. Although $0.1R_C$ is the commonly used analytical lower limit for thermal driving, only winds launched from the outermost edge of the disk from the low-mass neutron stars and the highest Compton temperatures seem compatible with thermal driving. The strict upper limit set by the size of the accretion disk suggests that the possible disk wind found in Spectrum A of 4U 1916−053 would likely be magnetic.

3.6 Discussion and Conclusions

We have analyzed three Chandra/HETG spectra of the short-period neutron-star X-ray binary 4U 1916−053. Two of these are groups of spectra selected from 250 ks of new exposure, and the third was an old archival exposure. In each case, the bulk of the absorption observed in the steady (non-dip, non-burst) phases is redshifted ($z = 8 \times 10^{-4}$). It likely arises in an ionized, static, inner disk atmosphere ($R \simeq 1200\ GM/c^2$), where gravitational red-shifts are small but nonzero. This interpretation is fully consistent with detailed photoionization modeling including re-emission shaped by local Keplerian motion.

Two of the spectra show evidence of a more strongly red-shifted absorption component, corresponding to $z = 1.4 \times 10^{-2}$ and $R \simeq 70\ GM/c^2$. One of the spectra shows a clear extended blue wing on the H-like Fe XXVI absorption line, signaling a transient disk wind.

This disk wind, if real, likely requires some form of magnetic driving. The orbital period of the X-ray dips indicates that the disk itself is smaller than the Compton radius, suggesting that any disk wind found in this system is likely magnetic (*Woods et al.*, 1996; *Proga and Kallman*, 2002; *Proga*, 2003). Unlike the disk winds found in most neutron star and black hole systems, then, thermal driving can be ruled out without the uncertainties involved with modeling photoionized absorption. However, alternative fits suggest that the blue wings in both Fe XXVI and Si XIV could, instead, arise from outer portions of the same inner disk atmosphere. In this case the data can be fit with two absorbers, the first redshifted by ~ 600 km s^{-1} and the second compatible with no shift.

In this new Chandra/HETG dataset, a near fivefold increase in total exposure of 4U 1916−053, we have uncovered evidence of what is perhaps the largest gravitational redshift ever detected in absorption at ~ 250 km s^{-1}. By comparison, the surface redshifts detected in white dwarfs are of the order of ~ 35 km s^{-1}, with the strongest redshift at 75 km s^{-1} (*Falcon et al.*, 2010). Archival Chandra/HETG spectra of sources such as XTE J1710−281 and AX 1745.6−2901 reveal comparable redshifts (~ 300 km s^{-1}) that have not been previously reported. As with 4U 1916−053, these redshifts are significantly higher than the expected relative radial velocity within galaxy and seem to support the interpretation that these redshifts are gravitational. Comparable redshifts in the Chandra/HETG spectrum of MAXI J1305−704 suggest that gravitationally redshifted disk atmospheres may also be present in black hole systems, although *Miller et al.* (2014) make note of issues with this observation that put these results in question. Redshifted absorption features have also been claimed in the spectrum of some AGN. These features, however, are transient, detected at CCD energy resolution (and calibration), and could perhaps be attributed to noise given the quality of the data. Unlike AGN, the redshifted absorption we find in the disk atmospheres

of UCXBs is highly significant (4.5 to 5σ, depending on the test) and, except for hard states in which the gas is over-ionized, persistent.

These results suggest that UCXBs (as well as sources with slightly longer orbital periods) harbor disk atmospheres with similar properties, where the bulk of the absorption occurs at $R \simeq 1000\ GM/c^2$, resulting in a detectable gravitational redshift. If this is indeed the case, these atmospheres would form a new class of absorbers in which distance from the compact object could be directly measured with unprecedented accuracy. This also places a hard upper limit on the size of the central engine and would likely require it to be significantly smaller than the radius at which the atmospheric absorption occurs.

We advise caution when considering these results, especially given the possible alternative explanations for the observed redshifts. In this work, however, we have demonstrated the great wealth of information that has been gained from a significant increase in Chandra exposures of 4U 1916−053 and untapped value of studying these sources with Chandra/HETG. We find that additional Chandra exposures of 4U 1916−053 could increase the significance of the static lines we find the dips (See Figure 3.4) and more robustly rule-out radial velocities as the source of redshift without the need of optical or IR observations. The additional exposures could also increase the significance of a wind, if one is present. Further Chandra/HETG observations of sources such as AX 1745.6−2901 could also increase the significance of the redshift to the level that we observe in 4U 1916−053 and XTE J170−281.

In anticipation of near-future missions such as XRISM, this work further establishes ultra-compact sources such as 4U 1916−053 (as well as AX 1745.6−2901 and XTE J1710−281) as high-priority targets. The dramatic increase in both spectral resolution (near Fe K) and effective area are ideally suited to perform the analysis described in this work and provide results at a much higher significance with shorter exposures. Our results provide XRISM with clear science goals for these sources, with simple observational signatures (primarily constraining the velocity shift in the atmosphere and during dips) that maximize XRISM's capabilities. In addition, XRISM will be able to confirm whether transient features such as

the disk wind and highly redshifted absorber are real and perhaps probe the physics that underlie the disk atmosphere throughout disk.

CHAPTER IV

A Spectroscopic Angle on Central Engine Size Scales in Accreting Neutron Stars

4.1 Preface

This chapter appears in the Astrophysical Journal, Volume 925, pp 113 (Trueba et al., 2022). The paper is co-authored by Jon M. Miller, Andrew C. Fabian, Jelle Kaastra, Timothy R. Kallman, Anne Lohfink, Renee M. Ludlam, Daniel Proga, John Raymond, Christopher Reynolds, Mark Reynolds, and Abderahmen Zoghbi, and is reproduced here with minor stylistic revisions.

4.2 Abstract

Analyses of absorption from disk winds and atmospheres in accreting compact objects typically treat the central emitting regions in these systems as point sources relative to the absorber. This assumption breaks down if the absorbing gas is located within $few \times 1000 \cdot GM/c^2$, in which case a small component of the absorber's Keplerian motion contributes to the velocity-width of absorption lines. Here, we demonstrate how this velocity-broadening effect can be used to constrain the sizes of central engines in accreting compact objects via a simple geometric relationship, and develop a method for modeling this effect. We apply this method on the Chandra/HETG spectra of three ultra-compact and short period neutron

star X-ray binaries in which evidence of gravitationally redshifted absorption, owing to an inner-disk atmosphere, has recently been reported. The significance of the redshift is above 5σ for XTE J1710−281 (this work) and 4U 1916−053, and is inconsistent with various estimates of the relative radial velocity of each binary. For our most sensitive spectrum (XTE J1710−281), we obtain a 1σ upper bound of 310 km s^{-1} on the magnitude of this geometric effect and a central engine of size $R_{CE} < 60\ GM/c^2$ (or, $< 90\ GM/c^2$ at the 3σ level). These initial constraints compare favorably to those obtained via microlensing in quasars and approach the sensitivity of constraints via relativistic reflection in neutron stars. This sensitivity will increase with further exposures, as well as the launch of future microcalorimeter and grating missions.

4.3 Introduction

Robust observational constraints on the physical size of the central emitting regions of accreting compact objects remain key to much of our understanding of both the nature of the compact object itself (be it a black hole or neutron star) and the accretion process in these systems. Prior to the first detection of gravitational wave emission from a black hole merger (*Abbott et al.*, 2016), observational studies of black holes relied primarily on electromagnetic emission from gas near the event horizon and therefore studies were (and predominantly still are) limited to those actively accreting. Indeed, the compactness of the emitting regions in active galactic nuclei (or, AGN) was key in establishing that AGN emission is powered by accreting supermassive black holes (*Lynden-Bell*, 1969; *Rees*, 1984). Compactness also played a role in identifying compact object accretion as the mechanisms responsible for the emission in multiple galactic X-ray sources in early X-ray observations (*Shklovsky*, 1967).

The increased sensitivity of X-ray observatories (spectroscopy and timing alike) has led to the development of sophisticated analytical tools capable of constraining the size of these central emitting regions, hereafter referred as central engines, to scales of a few

gravitational radii (GM/c^2). Fluorescent X-ray emission lines originating from surface gas in the inner radii of the disk, for instance, are subject to Doppler shifts and boosting due to the Keplerian motion of the disk, as well as general relativistic effects that can be used to map these regions (*Fabian et al.*, 1989; *George and Fabian*, 1991). This technique has been successful in measuring the spins of several stellar mass black holes (e.g. *Brenneman and Reynolds*, 2006; *Miller and Miller*, 2015; *Draghis et al.*, 2020) by constraining the size of the innermost stable circular orbit (or, ISCO) via spectral fitting of the resulting relativistic profile of Fe fluorescent lines. These are complemented by independent constraints based on fitting the continuum with relativistic disk emission models and sophisticated radiative transfer calculations through the surface atmosphere of the disk (*McClintock et al.*, 2014; *Miller et al.*, 2009; *Reynolds*, 2021).

Despite the success of these techniques, important questions remain unanswered at the limit of our current sensitivity. Our understanding of the nature of the X-ray corona in both X-ray binary systems and AGN remains, in many respects, limited. Constraining the geometry of the corona will likely be key in determining much about its physical origin (*Merloni and Fabian*, 2001); although studies suggest the corona is compact (*Fabian et al.*, 2015, 2017), a robust scientific case still requires further constraints from a diverse sample of source types, luminosity/accretion states, and independent observational techniques.

In this work, we present a novel approach to measuring the size of central engines in accreting compact objects via absorption line widths. Especially in low mass X-ray binaries (or, LMXBs), disk winds and disk atmospheres have been observed in multiple high-inclination black hole (or, BH) and neutron star (or, NS) systems. Based on their ionization and densities, these are known to emerge from the surface of the disk and may originate as close as $few \times 1000\ GM/c^2$ from the compact object (see *Miller et al.* 2008; *Neilsen and Homan* 2012; *Miller et al.* 2015a; *Trueba et al.* 2019 for disk winds in BH LMXBs; *Trueba et al.* 2020 and *Ponti et al.* 2018b for disk atmospheres in NS ultra-compact X-ray binaries; see *Różańska et al.* 2011 for numerical models) and, by necessity, retain much of their

Keplerian motion as they intercept the observer's line-of-sight. As the separation between the absorber and central engine decreases, the orbital motion of the absorber becomes non-negligible: parts of the emitting area are absorbed by gas in which the Keplerian motion is not entirely orthogonal to the line-of-sight. As a result, parts of the emitting area are absorbed by gas that is slightly *redshifted*, while others are absorbed by slightly *blueshifted* gas.

This differential absorption effect results in a specific form of line broadening, the degree of which depends solely[1] on the orbital radius of the absorber, the local Keplerian velocity, and the size of the central engine. If constraints can be placed on the orbital quantities of the absorber (e.g. via the photoionization parameter, P-Cygni profiles, or gravitational redshift), the size of the central engine can be constrained provided the spectrum is sensitive enough to measure the degree of velocity broadening.

This technique was first mentioned in *Trueba et al.* (2020) on the NS ultra-compact X-ray binary (or, UCXB) 4U 1916−053, and was facilitated by the independent constraint on the absorbing radius via the gravitational redshift in the disk atmosphere. We note that including the effects of a finite rather than point-like source has been common in other facets of astronomy, such as studies of young stars (e.g. *Calvet et al.* 1993). Similar geometric effects on the continuum in NS binaries have also been subject to study (e.g *Różańska et al.*, 2018).

The best Chandra/HETG spectra of absorption phenomena in LMXB systems, both in terms of signal-to-noise and prominence of absorption lines, are those of disk winds in black hole LMXBs; however, these tend to display complex absorption from multiple distinct absorption zones (see *Miller et al.*, 2015a) that complicate this type of analysis. Although these sources may ultimately prove to be excellent laboratories for applying this technique in the future, the aforementioned complexities coupled with the intricacies of relying on the photoionization parameter to derive the geometry of the system mean that these are not

[1]There is also a dependence on inclination; however, this effect is minimal in high-inclination sources such as the dipping and eclipsing systems analyzed in this work.

ideal candidates for developing and initial testing of this new approach.

This work was motivated by the discovery of redshifted absorption lines in the Chandra/HETG spectrum of the neutron star UCXB 4U 1916−053 in *Trueba et al.* (2020, hereafter T20), where the bulk of the absorption was found to be redshifted. The analysis suggests that the absorption is consistent with a nominally static inner disk atmosphere and the observed redshift is argued to be gravitational in origin. Although absorption from static disk atmospheres are commonly detected in these ultra-compact and short-period sources (*Ponti et al.*, 2014, 2018b,a; *Younes et al.*, 2009; *Gavriil et al.*, 2012), these are poorly understood and subject to limited observation, especially with the Chandra/HETG. T20 also identifies archival Chandra/HETG spectra for two other short-period NS sources with prominent absorption lines redshifted by a comparable magnitude, XTE J1710−281 and AX J1745.6−2901, suggesting a physical connection.

We present results on the Chandra/HETG spectra of the three ultra-compact and short period neutron star LMXBs identified in T20 as sources harboring redshifted disk atmospheres: 4U 1916−053, XTE J1710−281, and AX J1745.6−2901. In Section 4.5 we perform spectral fits to photoionized disk atmosphere absorption in these sources and discuss the possible physical origin of the observed redshift in each. In Section 4.6 we explain in detail the mechanics of the central engine velocity-broadening effect on absorption lines and demonstrate why the specific analysis techniques we developed are required to properly model this effect. We conclude by discussing the constraints we obtain from these sources and compare the performance of this method in Section 4.7.

This new method for constraining the size scales of central engines in accreting compact objects is not limited to this specific class of objects and can be applied to a much more diverse sample (e.g. black hole LMXBs with absorbing disk winds); however, as will be discussed in Section 4.6, gravitationally redshifted absorption is particularly sensitive to these techniques due to (a) its proximity to the central engine, and (b), the significantly reduced uncertainty involved in measuring the orbital radius of the absorber compared with

Table 4.1: Sources and Observations

Obs.ID	Exp. time (ks)	Count Rate (counts s^{-1})	Date (YYYY/MM/DD
		XTE J1710−281	
12468^X	73.3	7.02	2011/07/23
12469	73.3	7.86	2011/08/07
		4U 1916−053	
4584	46.06	19.79	2004/08/07
20171	21.57	13.09	2018/06/11
21103	28.41	15.40	2018/06/12
21104^Y	22.54	16.15	2018/06/13
21105^Y	21.17	16.81	2018/06/15
20172	29.87	11.19	2018/07/31
21662	28.89	12.50	2018/08/01
21663	29.83	11.93	2018/08/02
21664	21.90	12.50	2018/08/05
21106	20.59	10.47	2018/08/06
21666	18.64	11.93	2018/08/06
		AX J1745.6−2901	
17857	117.2	8.28	2015/08/11

NOTE – Sources and Chandra/HETG observations used in this work. All observations were made using the ACIS-S timed exposure (or, TE) mode and FAINT data mode.^{X}Observation 2 of XTE J1710−281, not used in main analysis.^{Y}The two spectra of 4U 1916−053 which do not display noticeable dips in their lightcurves.

commonly used techniques.

4.4 Sources, Observations, and Data Reduction

All three sources analyzed in this work are ultra-compact or short-period neutron star low-mass X-ray binaries. These are observed at high-inclinations, where both dips and (except for 4U 1916−052) eclipses from the companion star can be found in their X-ray lightcurves. In addition, the presence of type-I X-ray bursts in all three sources typically implies a low magnetic field strength for the central neutron star (*Galloway and Keek*, 2021).

Strictly speaking, 4U 1916−053 is the only "true" ultra-compact X-ray binary in our sample ($P_{orbital} < 1$ hour) with a $\sim$ 50-minute orbital period (*Walter et al.*, 1982). It accretes persistently from a helium-rich donor: the partially degenerate core of a low-mass star, much like a white dwarf (*Heinke et al.*, 2013; *Nelemans et al.*, 2006). At the time

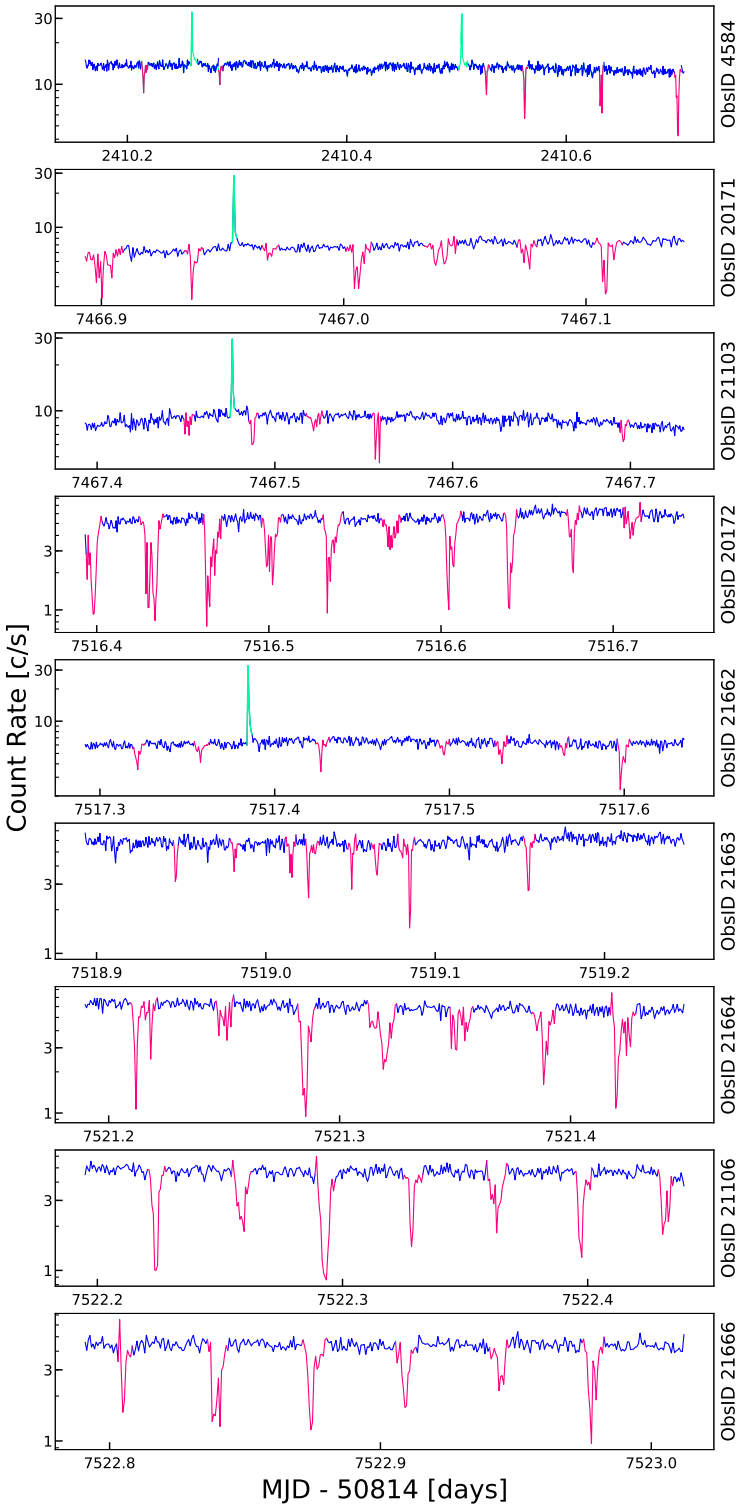

Figure 4.1: Chandra/HETG lightcurves of 4U 1916−053, observations with visible dips (ObsID 21104 and 21105 do not display noticeable dips). Time intervals corresponding to dipping periods (plotted in magenta) and X-ray bursts (green) were removed before spectral extraction. The absorption found during persistent periods is nearly constant throughout all observations (see T20). Note that the scale of the x-axes is not consistent between panels.

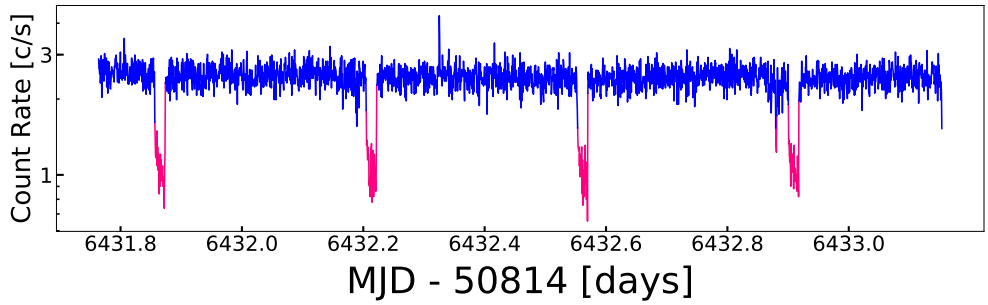

Figure 4.2: Chandra/HETG lightcurve of AX J1745.6−2901. Time intervals corresponding to dipping periods (plotted in magenta) were removed before spectral extraction.

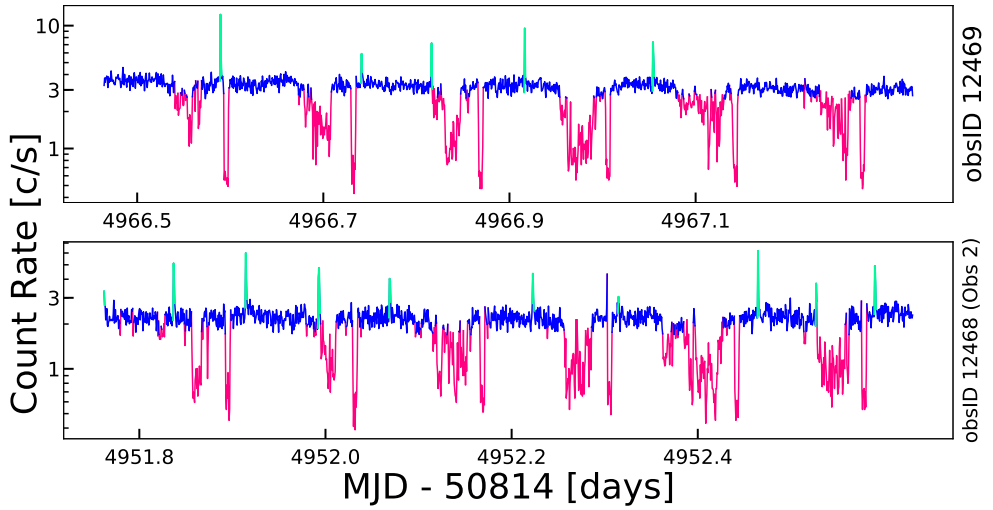

Figure 4.3: Chandra/HETG lightcurves of XTE J1710−281. Time intervals corresponding to dipping periods (plotted in magenta) and X-ray bursts (green) were removed before spectral extraction.

of writing, there are 11 Chandra/HETG observations of the system totalling $\sim$ 300 ks of combined exposure. As described in T20, the character of the absorption found in these observations during persistent periods (i.e. removing dipping and bursting events) remains nearly constant in terms of absorbing column, ionization, and velocity shift. All 11 HETG observations of this source were utilized in this work and are listed in Table 4.1.

With an orbital period of 3.28 hours (*Younes et al.*, 2009), the neutron star X-ray binary XTE J1710−053 is more accurately described as a short-period LMXB, a class that shares many characteristics with ultra-compact systems. In addition to X-ray bursts, the system displays X-ray dips as well as eclipses from its stellar companion. Though the spectral type

of the donor remains unknown (*Jain and Paul*, 2011), there is no evidence to suggest it is helium-rich. Estimates based on type-I X-ray bursts by *Jonker and Nelemans* (2004) place the system at a distance of 17.3 ± 2.5 kpc, consistent with both previous and subsequent analyses (*Markwardt et al.*, 2001; *Galloway et al.*, 2008). At this distance, its galactic coordinates (356.3571 +06.9220) suggest the system is, to first order, located about 8-9 kpc opposite the galactic center and is very likely part of the thick-disk stellar population. As a result, the *mean* expected radial velocity of the system relative to the local standard of rest is negligible and, instead, the local thick-disk velocity dispersion is a more appropriate point of comparison.

There are two $\sim$ 75 ks archival Chandra/HETG observations of XTE J1710−281, separated by $\sim$ 2 weeks (see Table 4.1). This interval roughly corresponds to half the length of the $\sim$ 30 day duty-cycle in which the source flux is observed to vary between 2 to 10 mCrab (*Markwardt et al.*, 2001; *Galloway et al.*, 2008; *Younes et al.*, 2009). Highly significant redshifted absorption lines were identified in T20 for one observation (ObsID. 12469) while in the other (ObsID. 12468) these features are significantly less prominent, seeming to correspond to different phases throughout the putative duty-cycle. Both observations are included in this work.

Finally, AX J1745.6−2901 is a neutron star LMXB with an orbital period of $\sim$ 8.35 hours (30063.74±0.14 s; *Ponti et al.* 2017), accreting from a class III giant stellar companion (*Ponti et al.*, 2018b). It is located in the galactic center region, separated from Sgr A* by 1.45 arcmin at an estimated distance of at least 8 kpc (*Ponti et al.*, 2017; *Jin et al.*, 2017), and is absorbed by a large neutral ISM column of $N_{H,ISM} \sim 30 \times 10^{22}$ cm^{-2} (*Ponti et al.*, 2018b). There is a single Chandra/HETG observation of this source (ObsID. 17857), which was triggered as part of a larger joint NuSTAR+XMM campaign (*Ponti et al.*, 2018b). The source was observed with NuSTAR concurrently to the Chandra/HETG observation; however, this simultaneous observation is not used in this work. The presence of redshifted absorption lines in this observation was noted in T20.

4.4.1 Data Reduction

The data for all Chandra/HETG observations considered in this work (11 for 4U 1916−053, 2 for XTE J1710−281, and 1 for AX J1745.6−2901) were reduced using CIAO version 4.9 and CALDB version 4.7.6. All observations were performed in the ACIS-S timed exposure (TE) mode and FAINT data mode. First-order HEG and MEG spectra for each observation, as well as their corresponding redistribution matrix and ancillary response files, were extracted using the CIAO routines *tg_findzo*, *tg_create_mask*[2], *tg_resolve_events*, *tgextract*, *mkgrmf*, and *fullgarf*.

Separate plus and minus orders were combined using *combine_grating_spectra*. The same routine was used to combine the 11 separate 4U 1916−053 observations into a single high signal-to-noise spectrum. Time filtering of spectra (including the removal of dips, eclipses, and X-ray bursts) was done using the *dmcopy* routine. For 4U 1916−053, bursts and dips were filtered using the same technique as in T20: Bursts were readily identified as large positive flux spikes with fast rises and exponential decays, dips were identified as sharp negative flux variations at intervals of 3000 seconds (the orbital period) and were removed if they departed from a running average flux by more than 20 percent. This was possible due to the well-defined nature of dipping events in the lightcurves for this source (see Figure 4.1), as was the case for the dips observed for AX J1745.6−2901 (Figure 4.2). Per Figure 4.3, a large fraction of the dips observed in the lightcurves for the pair of XTE J1710−281 observations were not as clearly defined; therefore, we generated GTIs by filtering time bins in the X-ray lightcurves for ObsID 12469 in which the count rate fell below 2.5 counts per second, where the average persistent rate was $\sim$ 4 counts per second. For ObsID 12468, these rates are 1.7 and 2.2 counts per second, respectively.

[2]The width_factor_hetg parameter in this routine was set to 10 in order to reduce contamination from MEG photons onto the HEG, thereby greatly increasing the sensitivity of the HEG in the Fe K band and above.

4.5 Baseline fits

Before implementing our central engine model (Section 4.6), it was necessary to first perform spectral fits to the photoionized absorption in our spectra *without* taking this specific line-broadening effect into account. As will be discussed in Section 4.6.1, standard analysis tools are ill-equipped to account for this effect; the model we developed required the use of multiple photoionized absorbers, and the fits obtained in this section serve as the baseline for this more complex model. In addition, the Chandra/HETG spectra of XTE J1710−281 and AX J1745.6−2901 have not been subject to detailed photoionization modeling in the literature and, with the exception of T20, there are no published constraints of the redshift in their disk atmospheres.

Spectral modeling was performed using SPEX version 3.05.00 (*Kaastra et al.*, 1996, 2018) and SPEXACT version 3.05.00 atomic database and associated routines. All data were binned using the "obin" command, which re-bins a spectrum to the optimal bin size given the particular statistics of a given source (for more detail, see *Kaastra and Bleeker* 2016). Although other binning schemes were tested in order to boost the signal-to-noise (or, S/N) ratio of some of our spectra, we ultimately decided against it as the aims of this work require the highest resolution possible. All fits and errors were obtained using χ^2 statistics.

The spectra of both XTE J1710−281 and 4U 1916−053 contain multiple absorption lines from H and He-like ions in the 1 to 2 keV energy band, as well as H and He-like Fe absorption in the Fe K band. Our initial scheme was based on utilizing the higher effective area of the MEG at lower energies (despite its lower resolution compared to the HEG) to fit 1 to 4.5 keV portion of the spectrum, while using the HEG from 4.5 to 8.5 keV where its effective area is higher. We modified this scheme by removing the 2.1 to 3 keV region of the MEG, a band that contains some lines but is significantly affected by instrumental features. AX J1745.6−2901 is much more heavily absorbed by neutral gas, meaning much of the flux in the lower energy band is lost, and there is little evidence of absorption outside of the Fe K band. We therefore fit this spectrum in the 5 to 9 keV range using only the

Table 4.2: Parameters for Best-Fit Absorption Models

Source	Spectrum	Model	Parameter	Zone 1	Zone 2	χ^2/ν
4U 1916−053	Combined	1 Zone	N_{He} (10^{22}cm^{-2})	$50^{\ddagger}_{-37}$	–	2162.7/2090 = 1.03
			log ξ	$4.5^{+0.1}_{-0.5}$	–	–
			v_z (km s^{-1})	200 ± 50	–	–
			v_{turb} (km s^{-1})	160^{+40}_{-30}	–	–
			L_{phot} (10^{36} erg/s)	9.0 ± 2.2	–	–
		2 Zone	N_{He} (10^{22} cm^{-2})	$50^{\ddagger}_{-16}$	5^{+35}_{-3}	2127.2/2087 = 1.02
			log ξ	$4.8^{\ddagger}_{-0.7}$	$3.8^{+0.7}_{-0.3}$	–
			v_z (km s^{-1})	490^{+160}_{-150}	$0^{\dagger}$	–
			v_{turb} (km s^{-1})	$100^{+130}_{-50\ddagger}$	$70^{+70}_{-20\ddagger}$	–
			L_{phot} (10^{36} erg/s)	9.3 ± 2.3	–	–
XTE J1710−281	Obs 1	1 Zone	N_H (10^{22}cm^{-2})	7^{+8}_{-3}	–	2226/1975 = 1.13
			log ξ	3.0 ± 0.1	–	–
			v_z (km s^{-1})	310 ± 50	–	–
			v_{turb} (km s^{-1})	90^{+30}_{-20}	–	–
			L_{phot} (10^{36} erg/s)	5.6 ± 1.4	–	–
		2 Zone	N_H (10^{22}cm^{-2})	$50^{+50\ddagger}_{-40}$	$0.6^{+0.4}_{-0.3}$	2158/1971 = 1.09
			log ξ	3.5 ± 0.3	$2.6^{+0.1}_{-0.2}$	–
			v_z (km s^{-1})	300 ± 100	250 ± 280	–
			v_{turb} (km s^{-1})	$50^{+40}_{\ddagger}$	$500^{\ddagger}_{-210}$	–
			L_{phot} (10^{36} erg/s)	8.0 ± 2.0	–	–
	Obs 2	1 Zone	N_H (10^{22}cm^{-2})	$100^{\ddagger}_{-87}$	–	2195.6/1946 = 1.13
			log ξ	$4.2^{+0.3}_{-0.2}$	–	–
			v_z (km s^{-1})	-20^{+120}_{-180}	–	–
			v_{turb} (km s^{-1})	$50^{+170}_{\ddagger}$	–	–
			L_{phot} (10^{36} erg/s)	5.3 ± 1.3	–	–
AX J1745.6−2901		1 Zone	N_H (10^{22}cm^{-2})	$96^{+4\ddagger}_{-56}$	–	497/432 = 1.15
			log ξ	4.0 ± 0.2	–	–
			v_z (km s^{-1})	270^{+240}_{-230}	–	–
			v_{turb} (km s^{-1})	100^{+40}_{-30}	–	–
			L_{phot} (10^{36} erg/s)	8.9 ± 2.2	–	–

NOTE – Best-fit parameter values for the absorption model that best describes each spectrum. All errors are at the 1σ level. Errors truncated by the parameter fitting range are marked with a ‡ symbol, frozen parameters are marked with a † symbol (see text for more detail).

HEG.

All spectra were fit with a simple continuum model consisting of both blackbody and disk blackbody additive components (BB and DBB in SPEX), modified by neutral ISM absorption (ABSM in SPEX). In the case of AX J1745.6−2901, the disk blackbody component was not needed. The photoionized absorption was modelled using PION, a self-consistent X-ray photoionized absorption model in SPEX (*Mehdipour et al.*, 2016; *Kaastra et al.*, 2018). PION calculates a new ionization balance with each iteration of a fit based on the changing continuum, therefore the model was constructed so that each PION component uses the naked continuum model to calculate the ionization balance *before* being absorbed by the ISM. For each PION component, we fit the equivalent hydrogen column (N_H), the photoionization parameter ($\log \xi$), the average systematic velocity of the absorber (v_z), and its turbulent velocity (v in SPEX; hereafter v_{turb}).

The best-fit models to photoionized absorption in our spectra are found in Table 4.2. Quoted errors are at the 1σ level. Although PION does produce some continuum absorption, our continuum parameters were set as free parameters in order to ensure a good continuum fit regardless of how the parameter space of the photoionized absorber is being sampled. As is often the case for sources with simple continua in the narrow Chandra band, these changes in the underlying continua have little to no effect on the quality of the fit. We therefore treated these as nuisance parameters and based our confidence regions on the number of free parameters in our absorption components. Please see Appendix B for more details.

4.5.1 4U 1916-053

A similar analysis of the photoionized absorption in the neutron star UCXB 4U 1916−053 was performed in T20, where the nearly 300 ks worth of Chandra/HETG data of the source was grouped into three separate spectra corresponding to the epoch of observation and broadly similar continuum. Fits to these spectra revealed redshifted absorption from a disk atmosphere where the absorbing column, ionization, and velocity shift were nearly constant

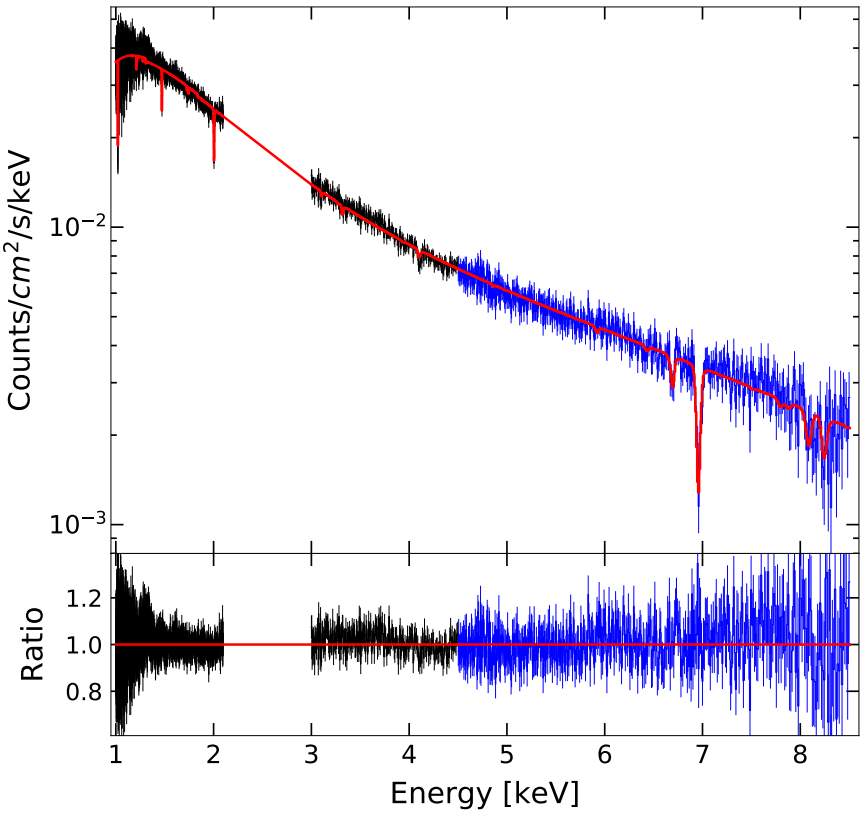

Figure 4.4: Chandra/HETG spectrum of 4U 1916−053, single-zone model. The MEG portion of the spectrum (1-4.5 keV) is plotted in black, while the HEG portion (4.5-8.5 keV) is plotted in blue here to highlight where each arm of the HETG was used to fit each band (2.1-3 keV was omitted due to instrumental features, see text).

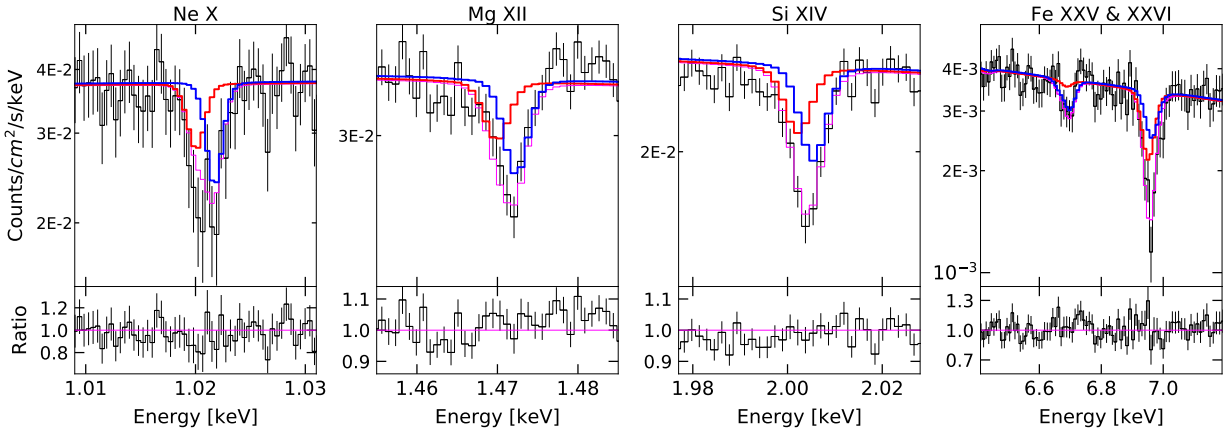

Figure 4.5: The 2-zone model for the Chandra/HETG spectrum of 4U 1916−053, focusing on four of the most prominent absorption features. The best-fit model is plotted in magenta, while the contribution from the individual absorption zones are plotted in red and blue for Zone 1 and Zone 2, respectively. Starting from the left, the first three panels plot the MEG spectrum, showing comparable contributions from Zones 1 and 2 in Ne X (1.02 keV), Mg XII (1.47 keV), and Si XIV (2.01 keV), though the lower-ionization component (Zone 2) is more prominent. The rightmost panel shows the HEG spectrum of the Fe K band. The redshifted Zone 1 makes up the majority of the Fe XXVI absorption (6.97 keV), while Fe XXV is captured almost entirely by Zone 2.

and within their 1σ confidence regions. The lower energy portions of the MEG in these three spectra, however, had modest sensitivity (which worsened with decreasing photon energy) and therefore the prior analysis did not include many bins below ~ 2 keV (the rest energy of Si XIV). In order to utilize the higher spectral resolution portions of our spectra, eventually maximizing the sensitivity of our central engine model, we decided to co-add all observations in an effort to improve the S/N of the combined spectrum.

As was the case with the three spectra in T20, the continuum of the combined spectrum can be described using both a blackbody and disk blackbody additive components. Although the best-fit continuum parameters are within a physically acceptable range ($T_{bb} = 1.8 \pm 0.1$ keV, $T_{dbb} = 0.80 \pm 0.05$ keV, and normalizations that suggest radii in the 5-10 km range), we do not claim these to be an accurate physical description of the underlying continuum. A physical treatment would explicitly include Comptonization and other processes. Rather, this continuum is reasonably simple, and flexible enough that unmodeled Comptonization or a non-thermal power-law component will simply be accounted for by, e.g., a slightly higher blackbody temperature and flux. This continuum is therefore suited to the purpose of establishing an ionization balance.

The best-fit, single absorption zone model (1-zone model) for 4U 1916−053 is shown in Figure 4.4, with best-fit parameters listed in Table 4.2. Note that the column parameter is listed as N_{He} for this source, as it is accreting from a helium-rich donor and therefore we report an equivalent helium column. As a consequence, we set the upper bound of N_{He} when fitting at the helium Compton-thick limit of 5×10^{23} cm^{-2}, which is half that of the Hydrogen limit because a Helium gas contains twice as many electrons *per ion* compared to a Hydrogen gas. See T20 for details about how abundances were modified to properly model this helium-rich absorption. We briefly note the Compton-thick limit for a hydrogen gas is quoted in the literature as either 10^{24} cm^{-2} or, more strictly, closer to $1.5 \cdot 10^{24}$ cm^{-2} ($\tau_e \sim 1$); the more conservative limit we adopted should be considered a soft-limit. Indeed, the best-fit model prefers a column of $5.0^{\ddagger}_{-3.7} \times 10^{23}$ cm^{-2}, though the large minus error-bar

suggests the spectrum may still be consistent with absorption below the Compton-thick regime. The best-fit values for N_{He}, log ξ, and v_{turb} are consistent to those obtained by fitting each spectrum separately in T20.

Despite its limited statistical significance, we briefly highlight a shift in v_z from 260 ± 80 km s^{-1} (T20) to 200 ± 50 km s^{-1} (this work) as it coincides specifically with the inclusion of MEG bins which contain absorption lines that typically correspond to ions with a lower degree of ionization. Per the definition of the ionization parameter, $\xi = \frac{L}{n \cdot r^2}$, and the approximation for gravitational redshift at large radii, $z_{grav} = (r/\frac{GM}{c^2})^{-1}$ (or, $c \cdot (r/r_g)^{-1}$ in velocity space), this shift may simply represent an additional absorber located at larger radii, where both the ionization and redshift are lower. For example, this absorber could represent the outermost portion of the redshifted inner disk atmosphere, where we could reasonably expect changes in ξ to be mostly sensitive to the distance r from the photoionizing source, barring a dramatically steep density gradient. Alternatively, absorption arising in the outer disk could also produce low-ionization absorption with no noticeable velocity shift even with a significantly lower density.

In order to test these alternatives, we performed a two absorption zone (2-zone) fit where two PION components were used to model the inner and outer absorbers. The best-fit 2-zone model can be found in Figure 4.5, where the contribution of each absorption zone is plotted in red and blue, respectively. The fits and errors were obtained using the same methodology as the 1-zone fits, with the exception of how v_z was treated for the outer zone. Although our fits were performed treating N_{He}, log ξ, v_z, and v_{turb} for both zones as free parameters, performing error searches required v_z to be frozen at its best-fit value of zero for the outer zone. This merely serves to prevent Zone 1 and Zone 2 from switching their proximity to the central engine within the error scans, which is extremely inefficient. The zones represent two distinct regions of parameter space and, as shown in T20, absorption in the outer disk is consistent with zero shift.

The best-fit 2-zone model yields $\chi^2/\nu = 2127.2/2087 = 1.02$; via an F-test, this rep-

resents a 5σ improvement (although the models are not nested). Zone 1 (the redshifted atmosphere) prefers the maximum value of N_{He} and log ξ, the former corresponding to the Compton-thick soft limit, while the latter is typically the limit at which log ξ becomes degenerate with N_{He}. In addition, the best-fit value of $v_z = 490^{+160}_{-150}$ km s^{-1} is now significantly larger and statistically distinct at the 1σ level from the results of the single-zone fit. Originally, we hypothesized a scenario in which the dominant absorption originated in the redshifted atmosphere and where the influence of an additional static absorber was limited. The 2-zone fit would suggest a significant contribution from this outer component in most lines (see Figure 4.5). Again, the 1-zone fit still prefers a redshifted absorber at the 5σ level.

Using the best-fit parameters from Table 4.2, we can derive some basic physical properties of the disk atmosphere: If the density of the absorbing gas can be measured independently, the orbital radius of the disk atmosphere can be obtained using the definition of the photoionization parameter, $r = \sqrt{L/n\xi}$. As is often the case, we do not have independent constraints on the gas density of the disk atmosphere. However, we can relate the density (n) to the observed column density (N_H) via $N_H = \Delta r \cdot n$, where Δr is the thickness of the absorber along the line-of-sight. Combing this with the ionization parameter, we obtain the expression

$$\xi = \frac{L}{N_H r^2 \frac{1}{\Delta r}}, \tag{4.1}$$

which can be can be re-arranged into

$$r = \frac{L}{N_H \xi} \cdot \frac{\Delta r}{r}, \tag{4.2}$$

and finally

$$r = \frac{L}{N_H \xi} \cdot f. \tag{4.3}$$

Here, we obtain an expression for the distance between the absorber and photoionizing source scaled by the filling factor (f), a scaling parameter which corresponds to the degree of clumping in a gas and where $0 < f \leq 1.0$. The quantity $r = \frac{L}{N_H \xi}$ uses the maximal filling

factor value of 1 and is, therefore, an upper-limit on the orbital radius of an absorber. In this short discussion, we assume a neutron star mass of $1.4M_{\odot}$ when converting distances to units of gravitational radii (GM/c^2), as well as assume an arbitrary error on the photoionizing luminosity of 25% (comparable to the error in various distance estimates) of the best-fit value (as reported in Table 4.2) and therefore we advise caution when interpreting these estimates.

We also note that there is evidence of some correlation between N_H and ξ in some of our fits (see Appendix B), associated with large ξ values and poorly constrained N_H errors. In these specific cases, we explicitly report errors R_{atm} assuming *perfect* correlation between N_H and ξ, along with their uncorrelated errors. Note that the difference in errors does not exceed 40%.

For the 1-zone fit, we get a disk atmosphere orbital radius of $R_{atm} = f \cdot 2800^{+5300}_{-1000\ddagger}$ ($^{+4000}_{-1000\ddagger}$ if uncorrelated) GM/c^2, where the ‡ sign indicates that an error was calculated by propagating a parameter error which was truncated by its allowed fitting range. In this case the upper error on N_{He} was truncated by the Compton-thick soft limit of 5×10^{23} cm^{-2}, which corresponds to the lower error when used to calculate the radius. Using the maximum filling factor value of unity ($f = 1$), which assumes an absorber that is both perfectly homogeneous (i.e. no clumps) and where its width (ΔR) is comparable to its distance to the photoionizing source, we obtain a minimum gravitational redshift of $z_{grav} \cdot c > 110^{+50\ddagger}_{-70}$ km s^{-1}. At this limit, the 1σ errors overlap with those obtained from the measured redshift in the atmosphere of $v_z = 200 \pm 50$ km s^{-1}.

We also note that, in addition to the gravitational redshift, $z_{grav} = (r/\frac{GM}{c^2})^{-1}$, there is an additional term corresponding to the transverse Doppler effect that arises due to the orbital motion of the gas. This effect produces an additional redshift of magnitude $z_{TDE} = 0.5 \cdot v_{\perp}^2/c^2 = 0.5 \cdot z_{grav}$, and therefore the total redshift at radius r becomes $z_{total} = 1.5 \cdot (r/\frac{GM}{c^2})^{-1}$, where $v_{\perp}^2$ is the Keplerian velocity of the absorbing gas, orthogonal to the line-of-sight. The aforementioned minimum redshift, therefore, becomes $z_{total} \cdot c > 170^{+70\ddagger}_{-110}$

km s^{-1}, placing the measured and radius-derived redshifts in better agreement.

In the case of our 2-zone fit, we obtain a value of $R_{atm} = f \cdot 1400^{+2700}_{-350‡}$ ($^{+2400}_{-350‡}$ if uncorrelated) GM/c^2, and corresponding $z_{grav} \cdot c > 210^{+90‡}_{-140}$ km s^{-1} and $z_{total} \cdot c > 320^{+130‡}_{-210}$ km s^{-1}. Though the upper error for z_{grav} is truncated by the fitting range for ξ and N_{He}, the 1σ confidence regions of redshift implied by the photoionization radius suggests a minimum redshift on the order of what was found in T20, while z_{total} is in 1σ agreement with the best-fit value of $v_z = 490^{+160}_{-150}$ km s^{-1} even when assuming a filling factor of unity. In the case of the outer absorption zone (Zone 2), we obtain a radius of $R_{outer} \approx f \cdot (1.4^{+1.4}_{-1}) \times 10^5$ GM/c^2. Adopting a maximal filling factor of unity, these values seem more consistent with absorption from the outer disk; however, we cannot rule out smaller filling factors and therefore absorption in the inner few $\times 1000$ GM/c^2. Using the orbital period of dips in the outer disk and (again) assuming a neutron star mass of $1.4M_\odot$, we obtain an outermost disk radius of 1.7×10^5 GM/c^2. This value is within the poorly constrained 1σ errors of R_{outer}.

4.5.2 XTE J1710-281

The two Chandra/HETG spectra of XTE J1710−281 have been the subject of spectral analysis only once in *Raman et al.* (2018), an analysis that focuses mostly on the nature of the absorption during dipping periods. Although a photoionization analysis was performed using the XSPEC model zxipcf[3] (an XSTAR-based partial covering pre-calculated absorption model), the work makes no mention of the highly significant redshift in prominent lines below 3 keV that we found in both our own reduction of the data (as will be discussed in this section) and via TGCat, and instead focused on the discovery of ionized Fe absorption. In this work we focus primarily on the observation with most prominent absorption, which we refer to as Obs 1 (ObsID 12469). We also present our analysis of the more tenuous absorption in Obs 2 (ObsID 12468) in order track changes in the absorbing disk atmosphere.

[3]This model used the XSTAR grid model used in *Reeves et al.* (2008), assuming a simple powerlaw continuum with $\Gamma = 2$. A major drawback is that this grid utilizes only 12 points to sample the ionization parameter over 9 orders of magnitude, and therefore it likely does not capture the full information in a rich, high resolution absorption spectrum (*Reynolds et al.*, 2012).

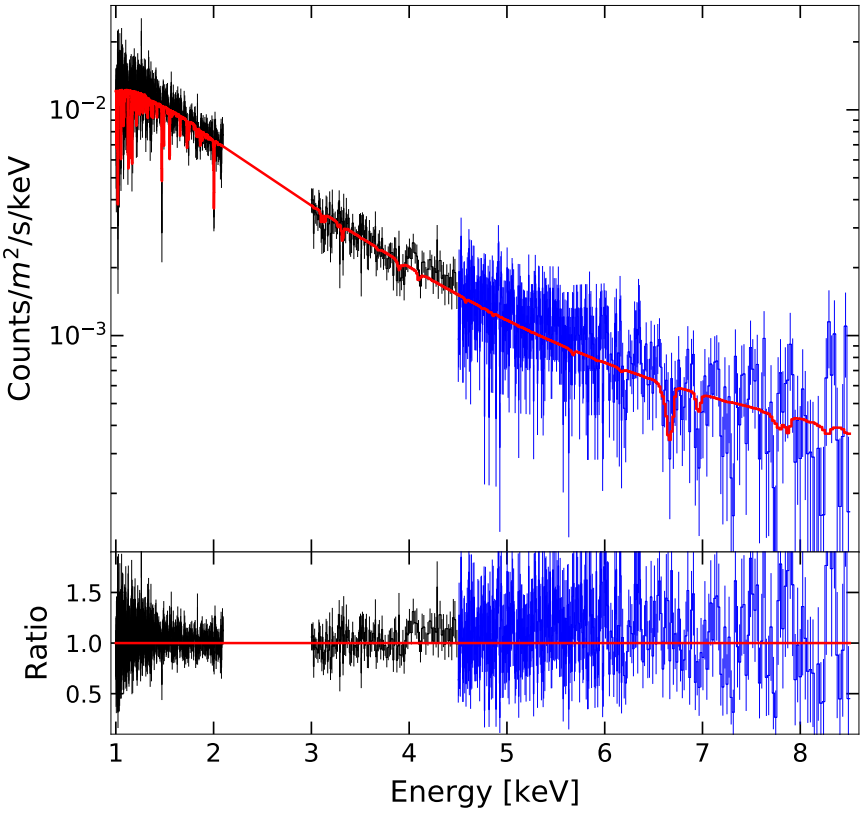

Figure 4.6: Chandra/HETG spectrum of XTE J1710−281, single-zone model. The MEG portion of the spectrum (1-4.5 keV) is plotted in black, while the HEG portion (4.5-8.5 keV) is plotted in blue here to highlight where each arm of the HETG was used to fit each band (2.1-3 keV was omitted due to instrumental features, see text).

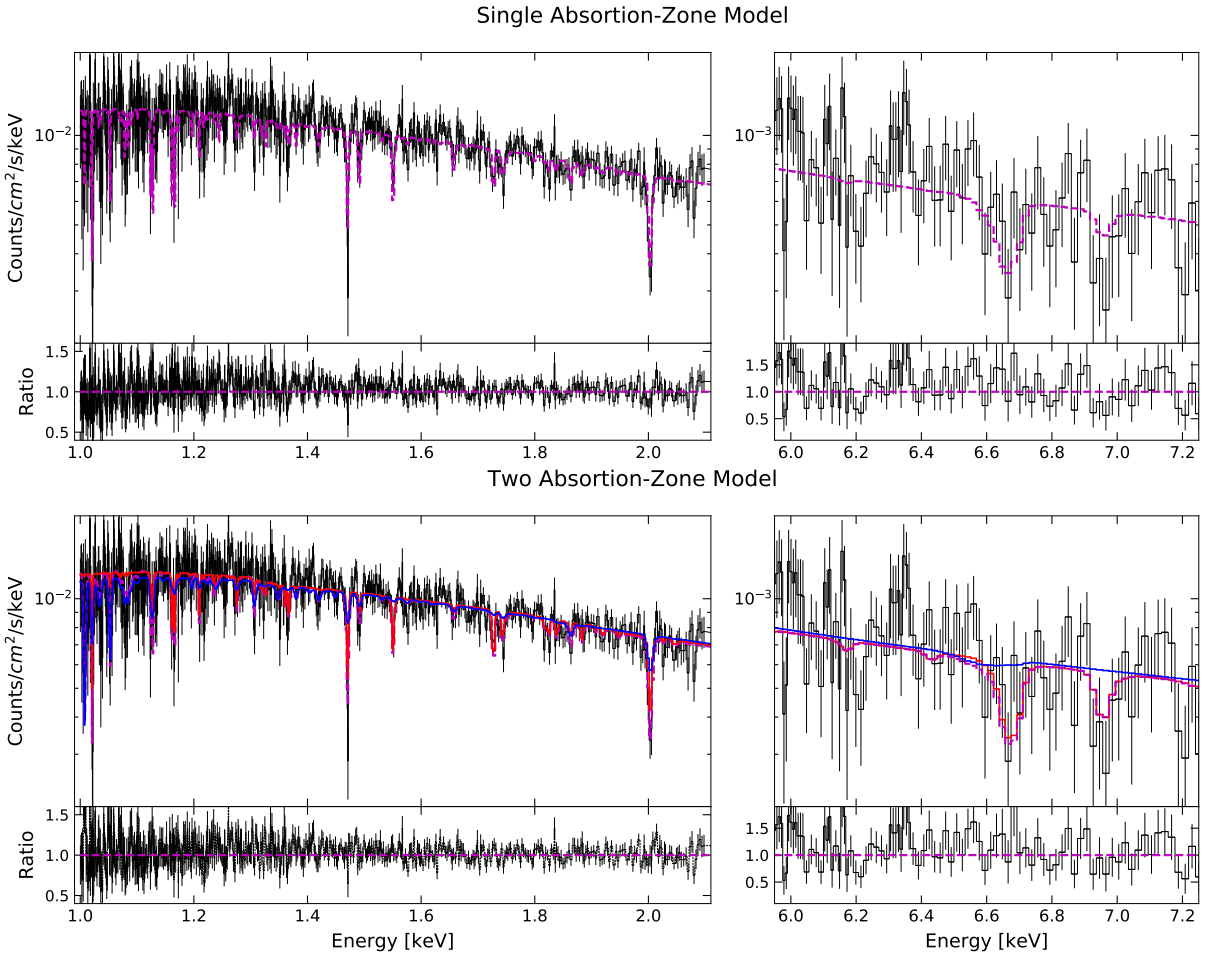

Figure 4.7: The 1-zone (top) and 2-zone (bottom) models for the Chandra/HETG spectrum of XTE J1710−281 (observation 1). The MEG portion is plotted from 1 to 2.1 keV in the left panels, while the Fe K region of the HEG spectrum is plotted in the right panels. The best-fit model is plotted with a dashed magenta line, while the separate Zone 1 and 2 components (of the 2-zone model) are plotted in red and blue, respectively. Here, the data is binned to a minimum S/N of 1 (using the "vbin" command in SPEX) for plotting purposes only - fitting was done at a lower level of binning (via the "obin" command, see text).

As with our fits to 4U 1916−053, the continuum for both Chandra/HETG observations of XTE J1710−281 were fit using a combination of disk blackbody and blackbody additive components, modified by interstellar absorption. We again obtained best-fit continuum parameters that are within a physically acceptable range: for Obs 1 we obtain a blackbody and disk blackbody temperatures of $kT_{bb} = 3.0^{\ddagger}_{-1.1}$ keV and $kT_{dbb} = 1.05 \pm 0.05$ keV, respectively, and normalizations that suggest emitting areas with radii in the 2-5 km range. The continuum in Obs 2, however, requires drastically lower blackbody and disk blackbody temperatures of $1.7^{+0.5}_{-0.2}$ keV and $0.8^{+0.2}_{-0.2}$ keV, and for the blackbody radius to be 5 times larger than in Obs 1.

The best-fit single absorption zone model parameters for Obs 1 of XTE J1710−281 (see Figure 4.6 and 4.7) listed in Table 4.2 are well-constrained. In particular, we observe a redshift in the disk atmosphere of $v_z = 310 \pm 50$ km s^{-1}, with 3σ and 5σ lower bounds of $v_z > 220$ and > 180 km s^{-1}, respectively. Due to its location and distance in the thick-disk of the Milky Way (see Section 4.4), we expect a near zero *mean* relative radial velocity in this region and therefore make direct comparisons to the local velocity dispersion, instead. Given a thick-disk velocity dispersion of 50 km s^{-1} (*Pasetto et al.*, 2012), this roughly corresponds to a 3σ difference between the measured redshift and the expected kinematics of the galaxy.

The high significance of the redshift compared to its expected relative radial velocity suggests that the redshift is perhaps not linked to the motion of the system along the line-of-sight; rather it is potentially due gravitational redshift or inflowing gas instead. Unfortunately, we were unable to model the excess absorption during dipping events in order to obtain a direct radial velocity measurement, as was done with 4U 1916−053 in T20; time-resolved spectra of the few short dips available in the available XTE J1710−281 data were too poor in quality for lines to be identified. However, we were able to make direct comparisons to the starkly different absorption found in Obs 2 (Figure 4.8). Although parameters such as N_H are very poorly constrained, we do obtain a velocity shift for the

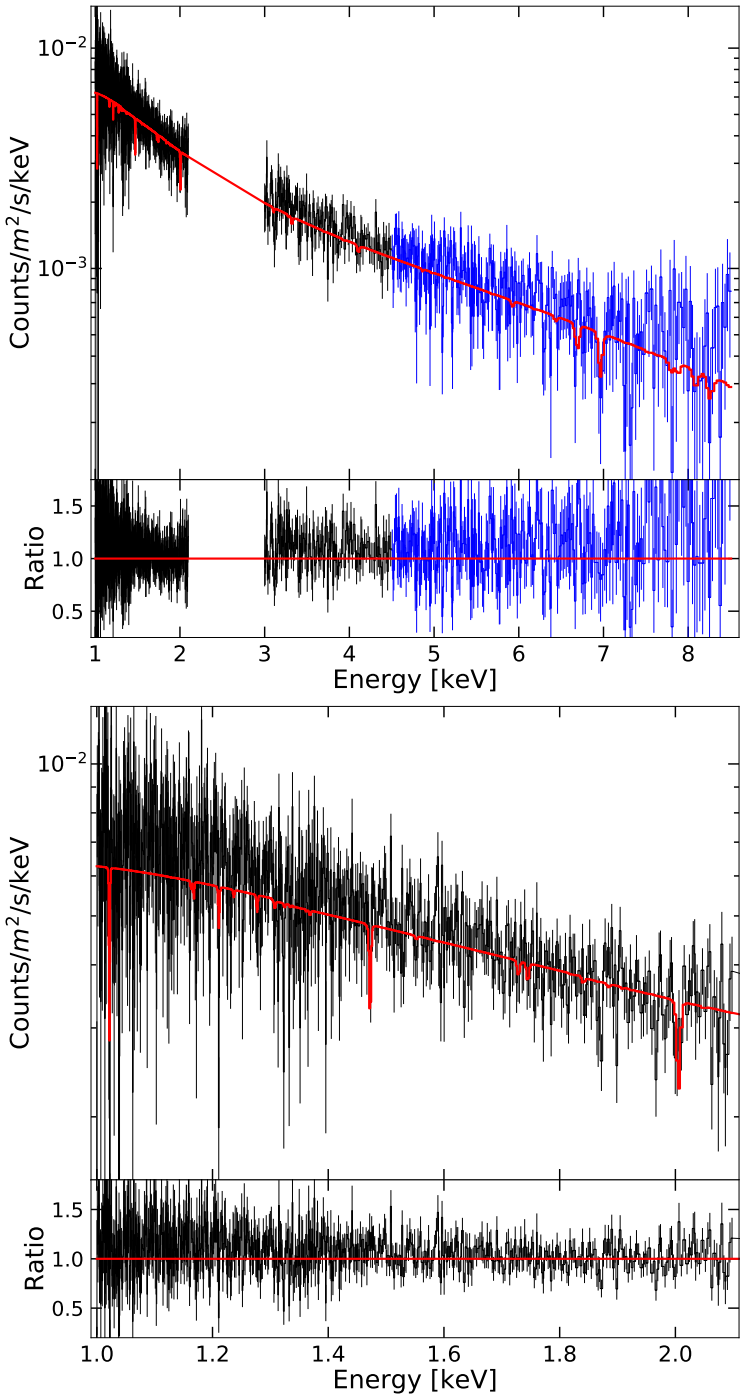

Figure 4.8: *Top:* Chandra/HETG spectrum of the alternate observation of XTE J1710−281 (observation 2). The MEG portion of the spectrum (1-4.5 keV) is plotted in black, while the HEG portion (4.5-8.5 keV) is plotted in blue. Best-fit model is plotted in red. Fe XXV and XXIV absorption, though tenuous, is more apparent in this observation, however. *Bottom*: The lower energy band of the MEG spectrum. Though the spectrum contains few prominent absorption lines, these were sufficient to constrain the shift for the observed absorption of $v_z = -20^{+120}_{-180}$, distinct from the redshift from observation 1 at the 2σ level. The discrepancy suggests that the redshift measured in observation 1 is not due to the radial velocity of the system, consistent with its expected velocity given its location in the galaxy. See text for more detail.

absorbing gas of $v_z = -20^{+120}_{-180}$ km s^{-1}. We find that this velocity shift is distinct to the redshift measured in Obs 1 at the 2σ level.

We cannot rule out the possibility that the absorption in Obs 2 could, in principle, be produced by a disk wind with an outflow velocity of ~ 300 km s^{-1} that is coincidentally cancelled out by the radial velocity of the system - a velocity we found to be in excess of the local mean by a factor of at least 4 times the local velocity dispersion. We argue it is far likelier that this absorption is due to (radially) static gas located at large orbital radii where any gravitational redshift is negligible. The near-zero velocity-shift we measured for Obs 2 therefore reflects the small radial velocity of the system we expect in comparison to the large and well-constrained redshift found in Obs 1, which we argue is likely either gravitational or due to the inflow of gas, though the lack of inverse P-Cygni profiles makes the latter scenario less compelling.

A gravitational redshift of 310 ± 50 km s^{-1} corresponds to a distance from the central neutron star of $R_z = 970 \pm 160\ GM/c^2$ (or, $1600^{+400}_{-200}\ GM/c^2$ once corrected for the transverse Doppler effect). Using Equation 4.3 and assuming a neutron star mass of $1.4 M_\odot$, we derive a radius based on the photoionization using the best-fit parameters in Table 4.2 of $R_{atm} = f \cdot 4.0^{+7.0}_{-3.0} \times 10^5\ GM/c^2$. Assuming the maximal value of $f = 1$ we obtain a radius at which the gravitational redshift is negligible and therefore this quantity has little use as an upper limit, as it does not restrict the location of the absorber to the inner disk. In fact, a filling factor of ($f = 0.01$) is required for these radii to agree at the 1σ level while preferring a much lower value of $f = 0.002$. Incidentally, the column and ionization values for Obs 2 imply a much smaller upper limit on the radius by comparison, though these are so poorly constrained that they are consistent with radii in the 10^4 to $10^5\ GM/c^2$ range.

The small filling factor values, and corresponding high-degrees of clumpiness, derived from our single zone model of Obs 1, are by no means unphysical and have been reproduced in simulations of AGN outflows (see *Mościbrodzka and Proga*, 2013; *Dannen et al.*, 2020), as well as observed in some LMXB disk winds (*Miller et al.*, 2015a; *Trueba et al.*, 2019). How-

ever, if the observed redshifted absorption in both 4U 1916−053 and XTE J1710−281 are instances of the same physical phenomenon and are produced by the same physical mechanisms, the apparent large discrepancy in their filling factors requires further examination. Of note, the spectrum in Obs 1 contains many lines in the 1 to 3 keV region that correspond to both low and high ionization absorption, as well as H and He-like Fe absorption in the Fe K band that correspond to high ionization absorption. It is possible that this spectrum contains both high and low ionization absorption, in which case the parameters used to derive the radii and filling factors for Obs 1 may be an average of these absorbers. As with 4U 1916−053, we performed a two absorption-zone (2-zone) fit to test this hypothesis.

The best-fit 2-zone model shown in Figure 4.7 and listed in Table 4.2 results in two *distinct* absorption zones and an f-test derived statistical improvement over the single-zone model above the 5σ level. The bulk of the absorption is dominated by Zone 1, an apparent disk atmosphere redshifted by 300 ± 100 km s^{-1} and with the expected higher ionization and absorbing column of an inner-disk atmosphere, though the latter is poorly constrained. These parameters suggest a radius of $R_{atm} = f \cdot 2.5^{+4.0}_{-2.5\ddagger}$ ($2.5^{+3.0}_{-2.5\ddagger}$ if uncorrelated) $\times 10^4$ GM/c^2. In this case, the lower bound obtained via standard error propagation is largely uninformative, especially given that the upper error on N_H is truncated by the fitting range and is of the order of the best-fit value. As a crude estimate of this lower-bound, we calculated R_{atm} fixing N_H at its upper 1σ value and propagating other errors (L_{phot} and ξ). We find a lower bound of $R_{atm} = 1.3 \pm 0.9 \times 10^4$ GM/c^2 where a filling factor of $f \sim 0.5$ results in a radius at which the total (gravitational plus transverse) redshift agrees with the observed shift at the 1σ level, and in much better agreement with our results from 4U 1916−053.

The low ionization and absorbing column for Zone 2, in contrast, suggest absorption at much larger radii. However, this absorption zone appears to be redshifted as well and by a similar amount to Zone 1. The redshift is poorly constrained and significant only slightly above the 1σ level, suggesting that Zone 2 could still be consistent with absorption

in the outer disk. Alternatively, this absorption could represent higher density clumps that are co-spatial with the main absorption from Zone 1, resulting in a two-phase inner disk atmosphere. These clumps could even represent a higher-denser component at lower scale-heights of the disk atmosphere which only narrowly intercepts our line-of-sight, resulting in very low absorbing columns. The latter two scenarios require filling factors ranging from 10^{-3} down to 10^{-4} in order to match the observed redshift.

4.5.3 AX J1745.6-2901

The single Chandra/HETG spectrum of AX J1745.6−2901 was observed as a part of a large joint monitoring campaign with XMM-Newton and NuSTAR (*Ponti et al.*, 2018b). Although the Chandra spectrum is omitted, the analysis by *Ponti et al.* (2018b) clearly established the presence of absorption lines in the Fe K band of the XMM-Newton spectra owing to a recurring, transient, photoionized disk atmosphere which can be observed when the source is a soft state and displays near-constant ionization and absorbing column values. This photoionized absorption disappears during hard spectral states, possibly as a result of (a) over-ionization from hard X-rays, (b) a lower absorbing column correlated to a drop in mass accretion rate during low-luminosity states, or perhaps more likely (c) a combination of both. This is a clear indication that the absorption is local to the system and does not originate in the ISM. Curiously, this state dependence mirrors the well-documented anti-correlation between disk winds and the presence of a jet during hard states (*Miller et al.*, 2006b, 2008; *Neilsen and Lee*, 2009; *King et al.*, 2012; *Miller et al.*, 2012; *Ponti et al.*, 2012). This specific Chandra observation has been used in previous analyses (e.g. *Mossoux and Grosso*, 2017; *Jin et al.*, 2018; *Wang et al.*, 2020; *Subroweit et al.*, 2020) which focus on the dust-scattering halo around the source, the environment in the galactic center, and/or Sag A* itself, making this the first analysis of the HETG spectrum of AX J1745.6−2901.

AX J1745.6-2901 is located near the galactic center and, unlike 4U 1916−053 and XTE J1710−281, it is absorbed by a large neutral ISM column ($N_{H,ISM} \sim 32\times\ 10^{22}$ cm^{-2}; *Ponti*

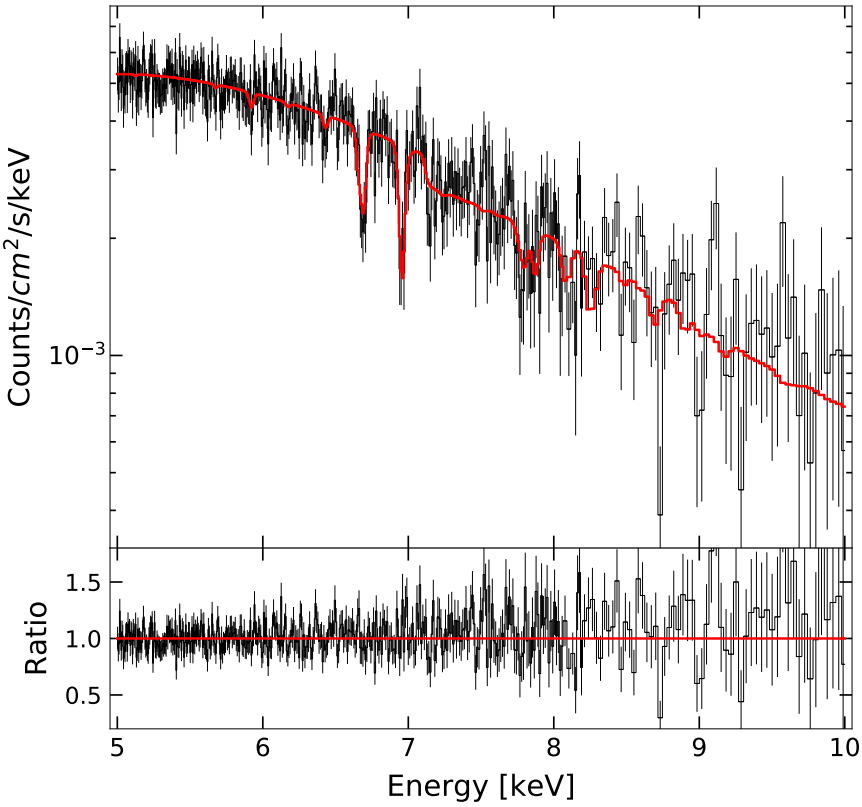

Figure 4.9: Chandra/HETG spectrum of AX J1745.6−2901, best-fit model plotted in red.

et al. 2018b) and therefore a significant amount of the spectrum below 4 keV is lost. We were unable to find statistically significant absorption lines in these regions, although this could be attributed to the low S/N in these portions of the spectra. The spectrum features strong Fe XXV and Fe XXVI absorption lines at ~ 6.7 and ~ 6.97 keV, respectively, as well as their corresponding β transitions, along with Ni absorption, above 7.5 keV (see Figure 4.9).

In view of the high column density and its effect on the low-energy portion of the spectrum, we restricted our analysis to the 5-10 keV portion of the HEG spectrum. In this range, we are able to describe the continuum using only a blackbody component ($kT_{bb} = 1.4 \pm 0.1$ and normalization of $K_{bb} = 2.5^{+0.9}_{-0.1} \times 10^{12}$ cm^2), modified by a neutral absorber.

Our best-fit model shown in Figure 4.9 listed in Table 4.2 largely agree with results from *Ponti et al.* (2018b) on the XMM-Newton spectrum of AX J1745.6−2901 during soft states. The best-fit N_H value of $96^{+4\dagger}_{-56} \times 10^{22}$cm^{-2} is poorly constrained and is truncated

by the upper limit on its fitting range (Compton-thick regime), yet it is well within 1σ of those found in the XMM-Newton CCD spectrum ($\sim 40 \pm 30\times\ 10^{22}\mathrm{cm}^{-2}$), as is the case with our well-constrained log ξ values compared to most fits reported in *Ponti et al.* (2018b). These ionizations and columns suggest a filling factor scaled radius (assuming an NS mass of $1.4M_{\odot}$) of $R_{atm} = f \cdot 4500^{+4800}_{-2500\ddagger}$ ($^{+3500}_{-2500\ddagger}$ if uncorrelated) GM/c^2 (this work) and $R_{atm} = f \cdot 1.1 \pm 1.0 \times 10^4\ GM/c^2$ (*Ponti et al.* 2018b values), though the latter assumes the same photoionizing luminosity as the Chandra observation and were included simply for comparison. These upper limits place the disk atmosphere within the innermost $\sim 10^4\ GM/c^2$ of the disk, consistent with a possible gravitational redshift. The previously mentioned limitations involving this spectrum result in comparatively poor velocity shift constraints. As reported in Table 4.2, our best-fit velocity shift of $v_z = 270 \pm 240$ is significant only slightly above the 1σ level. In addition, dispersed photons from an extended dust-scattering halo (*Jin et al.*, 2018) could also be responsible for the lack of sensitivity and loss of spectral resolution in this spectrum.

We briefly note that we tested an alternative continuum model using a thermal comptonization model (COMT in SPEX) with a plasma temperature fixed above 50 keV in order to determine whether our choice of continuum had an effect on the ionization. This resulted in a worse statistical fit ($\chi^2/\nu = 502/431$), though the best-fit ionization ($\log \xi \sim 3.84$) is within errors of the model listed in Table 4.2.

4.5.4 Physical Implications

It is notable that, at the time of writing, these redshifted atmospheres are found exclusively in short period systems. Although redshifted absorption has been reported in the Chandra/HETG spectra of some BH LMXBs such as GRS 1915+105 (*Miller et al.*, 2020) and MAXI J1305−704 (*Miller et al.*, 2014), the former likely represents a "failed wind" while the latter suffers from instrumental issues (though we note that MAXI J1305−704 has a relatively short orbital period of ~ 9.36 hours, *Mata Sánchez et al.* 2021).

A possible explanation likely involves a selection effect with the geometry of these systems: though some numerical models predict observable ionized Fe absorption from disk atmospheres originating much closer to the compact object than 1000 GM/c^2 (see *Różańska et al.* 2011), nominally hydrostatic atmospheres may have intrinsically smaller scale-heights (e.g. *Różańska et al.*, 2015, in AGN) compared to the outflowing disk winds observed in other NS and BH LMXBs and, therefore, may require higher viewing angles in order to intercept the observer's line-of-sight. A near edge-on viewing angle may be relatively unobstructed in short-period systems, while absorption in the outer radii of sources with much larger disks (or the disk itself) may obstruct the line-of-sight (see *Jimenez-Garate et al.*, 2002). The disk atmospheres in these lower luminosity ($L < 10^{37}$ erg s^{-1}) short-period sources share a similar state dependence to disk winds in more luminous BH LMXBs ($L \sim 10^{38-39}$ erg s^{-1}; see *Ponti et al.* 2014; *Miller et al.* 2015a; *Bianchi et al.* 2017), suggesting perhaps a similar physical origin that is sensitive to the mass accretion rate.

4.6 The Central Engine Model

Studies of absorption phenomena, especially in accreting compact objects, typically treat the central emitting region as a point source. The underlying assumption is that that the entire "face" of the emitting area is absorbed by gas with near constant properties in the plane orthogonal to the line-of-sight, though still allowing variation along the line-of-sight. Partial covering absorbers in AGN (e.g. *Reeves et al.*, 2009; *Gallo et al.*, 2015) are a notable exception in which only fraction of the total emitting area is absorbed while rest of the emission passes unabsorbed, though for the most part this effect is noticeable only as it pertains to the shape of the continuum.

The methods and results from *Calvet et al.* (1993) on the absorption from outflows in FU Ori are particularly relevant to this work: they developed physically and geometrically motivated wind models which accounted for the different velocity components of the absorbing gas along the line-of-sight to different portions of the emitting area (consisting of the

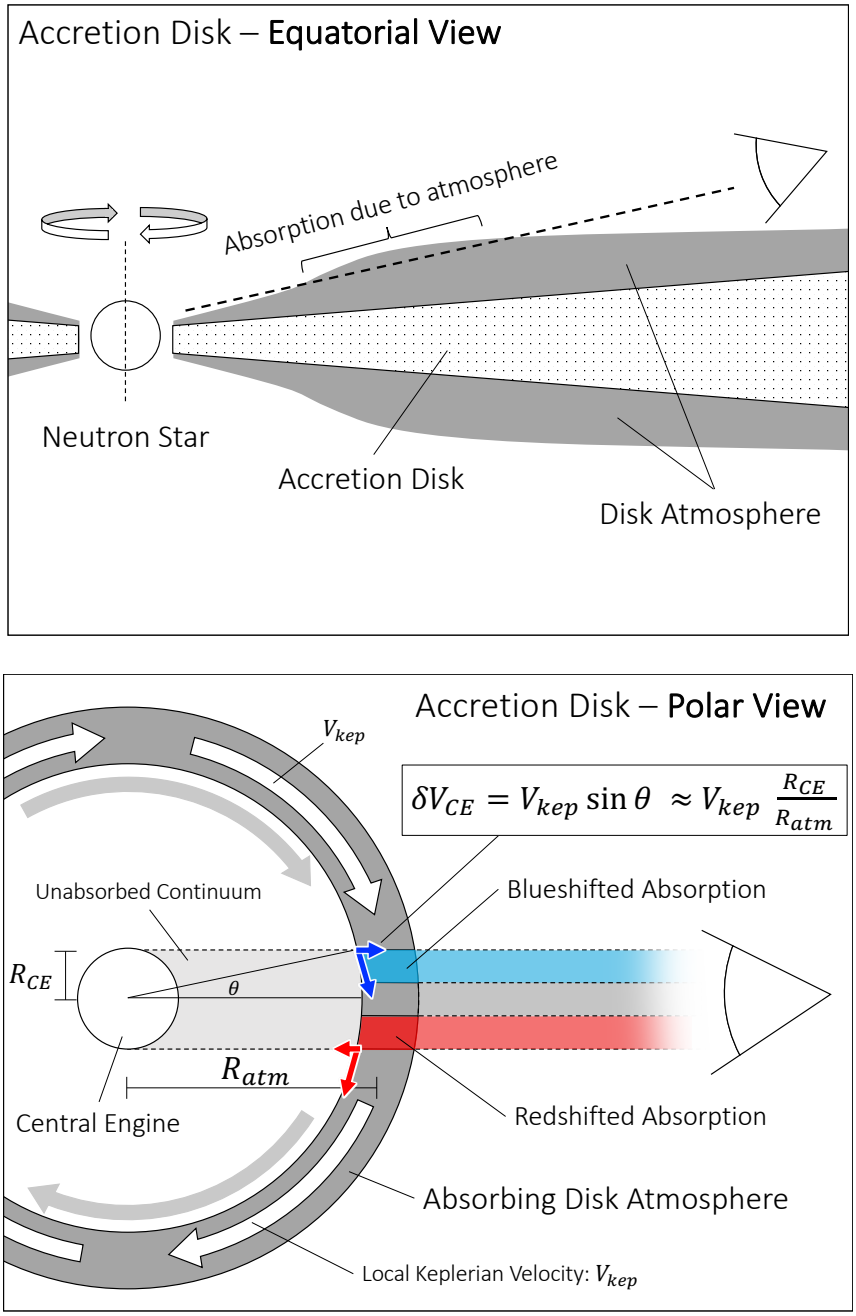

Figure 4.10: Schematic of the line broadening effects caused by the size of the central engine. The top panel shows a cross−section of a plausible, albeit exaggerated geometry for the absorbing disk atmosphere. The bottom panel shows a polar view of the same disk geometry. The gray ring represents the absorbing portion of the disk atmosphere that is along the line of sight (as seen in the left panel). The circular region labelled as the central engine in right panel encompasses all of the central X-ray emitting components of the system, including the emitting surface of the neutron star, the inner radii of the disk, and/or any corona that may be present and, therefore, R_{CE} represents a weighted average (see Section 4.7 for more detail).

extended inner regions of the disk; many stellar radii in size). They found that disk wind and stellar wind models produced noticeably different absorption line profiles as a product of these geometric effects, and that the disk wind was a better description of the observed line profiles.

As in FU Ori systems, certain absorption phenomena in X-ray binaries (disk winds and atmospheres, in particular) can produce similar, albeit subtle observational effects due to their geometry. These absorbers originate from the surface of the disk and therefore retain most, if not all, of their Keplerian motion. Naturally, in cases in which the absorber is located at large orbital radii (such as absorption from the outer disk; e.g. X-ray dips) the central engine can be treated as a point source - the Keplerian motion of the absorber is entirely orthogonal to the line-of-sight and therefore produces no observational signature. If this separation between the absorber and central engine is significantly smaller, however, portions of the absorbing gas will have some small component of their Keplerian motion passed along line-of-sight, resulting in some fraction of the emitting area being absorbed by blueshifted gas, while another (equal) fraction by redshifted gas. This effect is illustrated in the schematic shown in Figure 4.10. The figure shows a disk geometry as seen from above, where the axis of rotation is pointing towards the page. As the separation between the central engine and the rotating absorber decreases, opposite portions of the emitting area will be absorbed by gas rotating towards (blueshifted) and away from the observer (redshifted).

Ultimately, this effect manifests itself as a form velocity broadening on *absorption* lines. Crucially, the degree of this *geometric* line-broadening effect (δV_{CE}) depends only on the orbital radius of the absorbing disk-atmosphere (R_{abs}, or R_{atm} in the specific case of a disk atmosphere), its Keplerian velocity (V_{kep}), and the size of the central engine (R_{CE}), based on a simple geometric relationship

$$\delta V_{CE} = V_{kep}\ sin\theta. \tag{4.4}$$

The inclination of the source was omitted from this expression as all our sources are observed nearly edge-on, as evidenced by the presence of X-ray dips and eclipses (Figures 4.1-4.3). A factor of $sin\ i$ should be included for lower inclination sources.

Assuming small angles, $sin\ \theta$ becomes R_{CE}/R_{atm}. Re-arranging terms allows us to define the size of the central engine size as

$$R_{CE} = R_{atm}\frac{\delta V_{CE}}{V_{kep}}. \tag{4.5}$$

This simple expression is the central motivation for this work: if an absorber is located at an orbital distance at which this effect is non-negligible, then the size of the central engine can be constrained simply by measuring the degree of line broadening and constraining the orbital radius and velocity of the absorber. In this case, the central engine may be composed of the emitting regions of the NS, the inner radii of the disk, and/or a corona; R_{CE}, therefore represents a weighted average (see Section 4.7 for more detail).

An obvious limitation on the sensitivity of this method is the fact that there are likely multiple sources of line-broadening acting simultaneously on the spectrum, the most important of which is turbulent motion in the absorbing gas, itself. Moreover, the possible presence of additional absorbers with different mean line-of-sight velocities or perhaps even a modest velocity gradient within a "single" absorber could affect the sensitivity of this method. As we discuss in Section 4.6.1, 4.7, and Appendix C, this specific type of geometric line-broadening (δV_{CE}) displays very different behavior as compared to turbulent broadening, especially in regards to how it affects line ratios. Although we argue in the following sections that these forms of line broadening have little effect on our sensitivity, we still report our results strictly as upper limits.

Extraneous sources of line broadening aside, the sensitivity of this method is limited primarily by our ability to constrain (a) the distance and Keplerian velocity of the absorber, and (b) the degree of line-broadening due to this geometric effect. The photoionization parameter formalism can be used to estimate this distance (as discussed in Section 4.5);

however, this typically requires an independent constraint on the gas density of the absorber ($r = \sqrt{L/n\xi}$). Deriving a Keplerian velocity from this radius estimate would only compound this source of uncertainty when using equation 4.5, and requires a measurement of the mass of the compact object.

Gravitationally redshifted inner-disk atmospheres in ultra-compact and short-period X-ray binaries are ideal laboratories in which to apply this method. First, the location of the absorption is determined *solely* by the magnitude of the measured redshift. At radii larger than $few \times 10\ GM/c^2$, the gravitational redshift is well described by the approximation $z \simeq 1/R$, where R is given in units of GM/c^2. Having measured a gravitational redshift, the orbital distance of the disk atmosphere is given in units of GM/c^2 by

$$R_{atm} = \frac{c}{v_z}, \tag{4.6}$$

where the uncertainty in this quantity depends only on the uncertainty of the measured redshift. This expression, however, neglects an additional redshift term corresponding to the transverse Doppler effect (or, TDE) that arises from the orbital motion of the gas, $z_{TDE} = 0.5 \cdot v_{\perp}^2/c^2 = 0.5 \cdot z_{grav}$. Corrected for this effect, expression 4.6 becomes

$$R_{atm} = 1.5\frac{c}{v_z}. \tag{4.7}$$

It is important to note that this expression is only valid in the limit that the redshift, z, is small; however, this approximation only begins to break down when the absorber is located at $\sim 10\ GM/c^2$ (where the deviation is at $\sim 3\%$).

In addition, the corresponding Keplerian velocity can be derived directly from the orbital radius, provided it is given in gravitational units; the Keplerian velocity of an absorbing disk atmosphere can therefore be described *solely* in terms of the measured redshift as

$$V_{Kep} = \frac{c}{\sqrt{R_{atm}}} = \sqrt{c \cdot v_z/1.5}, \tag{4.8}$$

and therefore the uncertainty in this velocity depends only on the uncertainty of the measured redshift. Equation 4.5 can be re-written in terms of the measured redshift and geometric velocity-broadening, δV_{CE}, as

$$R_{CE} = \delta V_{CE} \cdot \frac{R_{atm}^{3/2}}{c} = \delta V_{CE} \cdot \frac{1.5^{3/2} \cdot c^{1/2}}{v_z^{3/2}}, \tag{4.9}$$

where $1.5^{3/2} \simeq 1.84$.

This expression is powerful in that it reduces our sources of uncertainty to only two parameters that are directly measurable in our spectra, allowing us to constrain the size of the central engine (in units of GM/c^2) without significant model dependencies and uncertainties regarding the mass and luminosity of the source. Re-arranging this expression to

$$\delta V_{CE} = R_{CE} \cdot \frac{c}{R_{atm}^{3/2}} \tag{4.10}$$

highlights the fact that, for a constant R_{CE}, the magnitude of this effect decreases dramatically with larger values of R_{atm}. The redshifts measured in our sources suggest orbital radii of the order of 1000 GM/c^2; despite their lower quality, spectra of gravitationally redshifted disk atmosphere absorption are likely much more sensitive to this effect. This direct dependence on R_{atm} does require for this distance to be fairly constant throughout any exposures being added to produce a spectrum. This is not likely to be problematic in short observations displaying little variation in persistent flux (i.e. excluding dips and bursts), though we advise caution when adding multiple exposures across different epochs. In the case of 4U 1916−053, the constancy in N_{He}, log ξ, and (most importantly) v_z throughout three epochs strongly suggests a narrow range in R_{atm} (see T20).

4.6.1 Model construction

Although δV_{CE} arises from a simple geometric relationship (see Figure 10), extracting this quantity from the data requires a procedure that can account for other sources of line

broadening likely present in the data. The most important of these is turbulent broadening, a mechanism that can noticeably affect the equivalent widths (or, EWs) of strong absorption lines with saturated cores. These two forms of velocity broadening are not equivalent and cannot be used interchangeably in any model: Turbulent broadening is accrued by integrating multiple velocity components radially along the line of sight, whereas geometric broadening - δV_{CE} - arises from multiple velocity components absorbing separate parts of the emitter.

A complete discussion on the differences between these two forms of line broadening and their effects on EWs can be found in Appendix C. In short, any absorption lines (including saturated lines) that are primarily shaped by geometric broadening retain a relatively constant EW as geometric effects become more important, whereas the EW of saturated lines primarily shaped by turbulent broadening increases (often significantly) as turbulence increases. The v_{turb} parameter in PION (or any absorption model) can therefore be extremely sensitive to line ratios between weak and strong (saturated) absorption lines, as the EW of weak lines does not increase with v_{turb}. For spectra containing both weak and strong absorption lines (as is the case in all of our spectra), any linewidth constraints using this parameter as a proxy for δV_{CE} will mostly reflect the model's ability to achieve the observed line ratios and will significantly underpredict the errors for δV_{CE} (confirmed via fitting tests in Section 4.6.2), leading to falsely tight constraints on R_{CE}. A preferable approach would be one that allowed both forms of line-broadening to be fit simultaneously using two independent parameters, where the errors on δV_{CE} were decoupled from EWs or line ratios and determined solely by its effect on the shape of the line.

In this work, we adopted a semi-literal approach to modeling this scenario: We utilized multiple absorption components, with each component absorbing its corresponding portion of the emitting area. All components shared identical gas properties (N_H, log ξ, v_{turb}, and v_z), with the exception of an *additional* velocity shift corresponding to this geometric effect (as in Figure 4.10), unique to each component. This approach allowed us to fit the degree

of geometric broadening directly via the δV parameter while still allowing v_{turb} (as well as N_H, $\log \xi$, and the mean redshift in the atmosphere) to vary freely.

In the simple case of an absorbed emitter *not* subject to these geometric effects, the velocity-dependent flux, $F(V)$, is given by

$$F(V) = F_0 e^{-\tau(V)}, \tag{4.11}$$

where, for simplicity, F_0 represents a flat continuum. The $\tau(V)$ function is a convenient short-hand for $\tau(V) = N \cdot \sigma(V)$, where $\sigma(V)$ is the frequency-dependent (transformed to velocity space) opacity from an arbitrary absorption line, though $\sigma(V)$ can also be used to represent an *entire set* of absorption lines originating from the same absorber. Note that in the following discussion, the same treatment applies regardless of which choice of line-profile (e.g. Lorenz, Gaussian, or Voigt) or absorption model (with multiple lines) is most appropriate for a given scenario; any thermal, turbulent, or natural broadening is accounted for within the $\sigma(V)$ function.

Including geometric effects in this scenario requires separating the emitter into multiple flux components, $dF_i(V)$; individual components can be described using Equation 4.11 with the distinction that each component is subject to an additional velocity shift specific to its location, $dF_i(V) \sim dF_0 e^{-\tau(V+\Delta V_i)}$ (see Appendix C for a more detailed review).

In an idealized description of this scenario, assuming a circular emitting area, the total absorbed flux, $F(V)$, can be described by

$$F(V) = \frac{2}{\pi} \int_{-1}^{1} F_0 e^{-\tau(V,x)} \sqrt{1 - x^2}\, dx, \tag{4.12}$$

where

$$\tau(V, x) = \tau(V + x \cdot \delta V_{CE}). \tag{4.13}$$

The dimensionless parameter, x, normalizes the contribution for each absorption compo-

nent: x ranges from -1 to 1, therefore the velocity divergence for each component appropriately goes from $-\delta V_{CE}$ to $+\delta V_{CE}$ (see Figure 4.10), and components which diverge the most in terms of velocity contribute the least in terms of area absorbed. Alternatively, a hypothetical rectangular-shaped central engine would result in a larger contribution from components where the velocity divergence is largest, meaning that that for a fixed velocity width constraint, assuming a rectangular central engine would translate to a tighter constraint on R_{CE} compared to a circular geometry. While a rectangular geometry might in some instances be a better physical description of the system (e.g. equatorial bands in the NS surface, or thin concentric emitting rings in a disk), we adopted a circular geometry as it provides more conservative (larger) upper-bounds on R_{CE}. See Appendix D for a more complete discussion of different central engine geometries.

A good approximation for integral in Equation 4.12 involves the use of multiple absorbers with different velocity components. Unfortunately, photoionized absorption models such as PION require significant computational power; the benefit of adding more absorbers is quickly outweighed by the computational cost. Based on the plausible values of $-\delta V_{CE}$ compared to typical line-widths, the resolution of the HETG, as well as fitting experiments, we found that we could adequately describe this effect using only three absorbers (hereafter constituent absorbers): a central absorber with no *additional* velocity shift, and two absorbers each corresponding to the redshifted and blueshifted (relative to the mean redshift) edges of the Keplerian absorber (in essence what is shown in Figure 4.10). Expression 4.12 then becomes

$$F(V) = F_0/3(e^{-\tau(V-\delta V)} + e^{-\tau(V)} + e^{-\tau(V+\delta V)}). \tag{4.14}$$

This approach utilizes equal emitting areas for each absorption velocity component - in this case, dividing a circular area into three equal fractions, as described in Appendix D. The fitting parameter δV can be directly related to the quantity we are interested in, δV_{CE},

via a simple weighted integral which results in

$$\delta V \simeq 0.6 \cdot \delta V_{CE}. \tag{4.15}$$

Notably, assuming a rectangular-shaped central engine would shift this ratio to $0.7 \cdot \delta V_{CE}$, resulting in R_{CE} constraints that would be $\sim 15\%$ tighter compared to those reported in Section 4.6.2.

The model was built in SPEX by adapting our single-zone baseline models from Section 4.5. In XSPEC parlance (for simplicity), a hypothetical baseline model can be written as

$$\text{powerlaw}(N, \Gamma) \times PION(N_H, \xi, v_{turb}, v_z).$$

We modified this baseline model by splitting the emitting area of each continuum component into three equal components with linked parameters, where the total continuum emission remained unchanged. We then replaced the single PION absorption component with three identical PION components (corresponding to each constituent absorber), with the exception of an additional fitting parameter, δV. The resulting model can now be written as

$$\begin{aligned} &\text{powerlaw}(N/3, \Gamma) \times PION(..., v_z + \delta V) + \\ &\text{powerlaw}(N/3, \Gamma) \times PION(..., v_z) + \\ &\text{powerlaw}(N/3, \Gamma) \times PION(..., v_z - \delta V). \end{aligned}$$

Due to the manner in which model components and parameters are defined in SPEX, the actual construction of the model differed slightly from the description above. In this work, the velocity parameter (v_z) was linked between two of the PION components by a factor of -1, while the velocity for the remaining PION component was frozen at zero. All of the absorbers were then modified using a redshift model (REDS in SPEX) to account for the

Table 4.3: Constraints on the Size of the Central Engine from R_{CE}-model Fits

Source name	Model	Redshift-related quantities				R_{CE} constraints		
		$c \cdot z_{atm}$	R_{atm}	V_{kep}	δV_{CE}	R_{CE}	Upper limits	
		(km s^{-1})	(GM/c^2)	(km s^{-1})	(km s^{-1})	(GM/c^2)	(3σ)	(5σ)
XTE J1710−281	1-zone	290 ± 40	1500^{+300}_{-150}	7700^{+500}_{-600}	$180^{+130}_{-130\ddagger}$	$40^{+20}_{\ddagger}$	< 90	< 130
	2-zone	280 ± 50	1600^{+400}_{-200}	7500^{+600}_{-700}	$50^{+230}_{\ddagger}$	< 60	< 90	< 140
4U 1916−053	1-zone	210 ± 60	2100^{+900}_{-400}	6500^{+900}_{-1000}	340^{+150}_{-290}	110^{+90}_{-90}	< 370	< 900
	2-zone	490^{+200}_{-170}	900^{+600}_{-200}	9900^{+1800}_{-1900}	$50^{+420}_{\ddagger}$	< 60	< 150	< 520

NOTE – Central engine radius constraints (R_{CE}) obtained from our best-fit R_{CE}-models; R_{CE} was calculated using the best-fit redshift, $c \cdot z_{atm} (= v_z)$, and geometric linewidth, δV_{CE} (for a full list of model parameters, see Table 4.4), per Equation 4.9 (corrected for the transverse Doppler effect). Confidence regions for R_{CE} were obtained from $\Delta\chi^2$-grids in z_{atm} vs. δV_{CE} space by calculating R_{CE} values along contour line corresponding to each confidence level (see Figures 4.11 and 4.13). We also included values for the orbital radius of the disk atmosphere (R_{atm}) and Keplerian velocity (V_{kep}) based on the best-fit redshift, per Equations 4.7 and 4.8.

mean redshift obtained in Section 4.5. The resulting shifts are, in this velocity shift regime, identical to the XSPEC model description above. Again, the same absorption parameters from the baseline models (N_H, log ξ, v_{turb}, and the mean redshift in the atmosphere) where linked between the three constituent absorbers and were allowed to vary as free parameters in the central engine model.

4.6.2 Results from the Central Engine Model

Parameters for the best-fit central engine models (for simplicity, R_{CE}-model) for XTE J1710−281 and 4U 1916−053 are listed in Tables 4.3 (those relevant to R_{CE}) and 4.4 (full parameter list). We included two versions of the central engine model for each source based on their 1 and 2 absorption zone baseline models from Section 4.5. Compared to their baseline counterparts, we found slight shifts in both continuum and absorption parameters in the R_{CE}-models (Table 4.4) that are within the 1σ errors listed Table 4.2, and therefore not significant. The additional degree of freedom, however, did result in larger errors in the mean redshift. The redshifts (and uncertainties) used to calculate the central engine radius (or, R_{CE}) and reported in Table 4.3 were obtained with the R_{CE}-model. The R_{CE}-model

results for AX J1745.6−2901 were not included in these tables due to their low significance. We briefly comment on the source at the end of this section.

In complex models, error estimates based on single-parameter scans or based on propagating errors from connected quantities can under-estimate the true errors. Our solution was simply to compute χ^2 grids in z_{atm} vs δV_{CE} parameter space (the two parameters required to compute R_{CE}), and then extracting contour lines at each value of $\Delta\chi^2$ corresponding to the desired significance level. The largest and smallest values of R_{CE} along each contour therefore represent the bounds of our confidence regions, a much better representation of the uncertainty in this constraint. We set a lower limit of 50 km s^{-1} on the fitting range of the δV_{CE} parameter for all fits. This δV_{CE} value corresponds to an emitter with a radius of 10 R_{CE} absorbed by a disk atmosphere redshifted located at 1500 GM/c^2 (or, redshifted by $\sim$ 300 km s^{-1}), per Equations 4.7-4.10. This limit is large compared to most plausible values of neutron star radii though it is appropriate given the sensitivity of the data: the threshold at which the model becomes insensitive to small values of δV_{CE} is well above the 50 km s^{-1} limit and, therefore, the smallest possible χ^2 value should be contained within our χ^2 grids. Crucially, this means that the positive errors on R_{CE} (calculated via $\Delta\chi^2$) are unaffected by this limit.

We note that all constraints on δV_{CE} and R_{CE} should likely be treated as upper-limits: The R_{CE} -model treats both δV_{CE} and v_{turb} as free parameters and, though we do not expect much degeneracy between these two forms of velocity broadening (see Appendix C), the errors on δV_{CE} may attribute some fraction of the turbulent velocity broadening to the central engine. The positive errors on δV_{CE} provide a robust upper-limit, as they allow δV_{CE} to encompass as much of the velocity broadening as is statistically acceptable, including those not accounted for in the model. Conversely, negative error bars on δV_{CE} may be underestimated if this parameter is responsible for other unmodeled sources of velocity broadening. Although none of our spectra display a preference for larger δV_{CE} values (above the 1σ level), we advise caution when interpreting lower bounds on any constraint on R_{CE} .

Table 4.4: Absorption Parameters for Best-Fit R_{CE}-models

Parameter	Zone 1	Zone 2
	4U 1916−053	
N_{He} (10^{22}cm^{-2})	$50^{\dagger}_{-36}$	–
log ξ	$4.4^{+0.1}_{-0.5}$	–
v_z (km s^{-1})	210 ± 60	–
v_{turb} (km s^{-1})	150^{+40}_{-30}	–
δV_{CE} (km s^{-1})	$340^{+150}_{-290\ddagger}$	–
χ^2/ν		2153.8/2089 = 1.03
	(2-zone model)	
N_{He} (10^{22} cm^{-2})	$50^{\ddagger}_{-20}$	$5^{+45\ddagger}_{-3}$
log ξ	$4.8^{+\ddagger}_{-0.4}$	$3.8^{+1.0\ddagger}_{-0.3}$
v_z (km s^{-1})	490^{+200}_{-170}	$0^{\dagger}$
v_{turb} (km s^{-1})	$100^{+120}_{-50\ddagger}$	$60^{+80}_{-10\ddagger}$
δV_{CE} (km s^{-1})	$50^{+420}_{\ddagger}$	
χ^2/ν		2127.2/2087 = 1.02
	XTE J1710−281	
N_H (10^{22}cm^{-2})	8^{+8}_{-4}	–
log ξ	3.1 ± 0.1	–
v_z (km s^{-1})	290 ± 40	–
v_{turb} (km s^{-1})	100^{+30}_{-30}	–
δV_{CE} (km s^{-1})	$180^{+130}_{-130\ddagger}$	–
χ^2/ν		2460/2182 = 1.13
	(2-zone model)	
N_H (10^{22}cm^{-2})	$40^{+60\dagger}_{-30}$	$0.5^{+0.4}_{-0.3}$
log ξ	$3.4^{+0.3}_{-0.2}$	$2.6^{+0.2}_{-0.2}$
v_z (km s^{-1})	280 ± 50	= Zone 1
v_{turb} (km s^{-1})	$50^{+40}_{\ddagger}$	$500^{\ddagger}_{-190}$
δV_{CE} (km s^{-1})	$50^{+230}_{\ddagger}$	= Zone 1
χ^2/ν		2397/2179 = 1.1

NOTE – Best-fit parameter values for the R_{CE}-model that best describes each spectrum. The R_{CE}-model was applied only on observation 1 of XTE J1710−281. All errors are at the 1σ level. Errors truncated by the parameter fitting range are marked with a ‡ symbol, frozen parameters with a † symbol. Parameter values are within errors of the best-fit baseline parameters from Table 4.2, with the exception of the additional geometric velocity broadening parameter, δV_{CE}.

Table 4.5: R_{CE}-model results for XTE J1710−281

Range	$c \cdot z_{atm}$ (km s^{-1})	δV_{CE} (km s^{-1})	R_{CE} (GM/c^2)	Upper limits (3σ)	(5σ)
A	300^{+60}_{-50}	$250^{+160}_{-200\ddagger}$	$50^{+40}_{\ddagger}$	< 150	< 260
B	290 ± 40	$180^{+130}_{-130\ddagger}$	$40^{+20}_{\ddagger}$	< 90	< 130
C	290 ± 40	$230^{+100}_{-120\ddagger}$	$50^{+20}_{-30\ddagger}$	< 90	< 120

NOTE – Constraints from the R_{CE}-model of XTE J1710−281, using three different fitting ranges of the HETG spectrum and binning schemes. Range A is the baseline fitting range, using the MEG from 1.0-2.1 and 3.0-4.5 keV, and the HEG from 4.5-8.5 keV, both optimally binned. Range B is the same as A, except a few HEG bins around the strongest lines in the low energy band were included (also optimally binned). Range C included the entire HEG from 1.0 to 2.1 keV, more coarsely binned to a minimum S/N of 1.

The best-fit single absorption zone R_{CE}-model for XTE J1710−281 reported in Table 4.3 was obtained by using the same Chandra/HETG fitting range used in Section 4.5 with exception that, instead of entirely omitting the HEG below 4.5 keV, a *few* HEG spectral bins at locations where strong lines known to be present in the MEG spectrum: these are 1.01 to 1.03 keV (Ne X), 1.45 to 1.5 keV (Mg XII) and from 1.98 to 2.02 keV (Si XIV). The entire HEG was *not* included in this lower energy band due to the continuum being relatively noisy in a region that contains multiple weak lines, while binning the data more heavily (compared to optimal binning) partially defeated the purpose of including portions of the higher-resolution HEG arm. However, we did find that the strong Ne X, Mg XII, and Si XIV lines identified in the MEG spectrum to be highly significant in the HEG spectrum, as well.

Constraints on R_{CE} for XTE J1710−281 using different fitting ranges are listed in Table 4.5. For comparison, we also included a range C fit, using the entire HEG from 1.0-2.1 keV. Here, the HEG is more heavily binned (minimum S/N of 1 using the "vbin" command in SPEX) in the lower energy band.

Compared to R_{CE}-model fits that adhere strictly to the baseline fitting range (range A), we obtained noticeably tighter redshift, δV_{CE}, and, therefore, R_{CE} constraints by adding these few HEG bins around strong lines (range B). Again, values of N_H, ξ, v_{turb}, and z_{atm} (v_z) are well within 1σ errors of, *and virtually identical* to, those in the baseline model (see

Table 4.4). Including additional (albeit more heavily binned) HEG spectral bins in range C resulted in a slight loss of sensitivity to δV_{CE}, while ultimately having little effect on the final R_{CE} constraints. This constancy between B and C however, is also reflected in the parameters which are *not* listed in Table 4.5, where we again find that values and errors of N_H, ξ, and v_{turb} using range C are *virtually identical* to those obtained using both range A and B.

These results are reassuring: all three fits effectively represent the same minimum in parameter space - the improvement between A and B is therefore most likely the result of increasing the sensitivity of our combined data set by including high resolution HEG bins. In the interest of not including a large number of coarsely binned spectral bins, we adopted range B when reporting our results.

The constraints on the central engine for Chandra/HETG spectrum of XTE J1710−281 suggest upper bounds on the radius of 60 GM/c^2 and 90 GM/c^2 at the 1 and 3σ levels, respectively. These correspond to 1 and 3σ limits of 120 and 190 km for a 1.4$M_\odot$ central neutron star. Although we report these values as upper limits due to the possibility of extraneous sources of line broadening that may affect our results, the best-fit R_{CE} value itself suggests a point-like central engine. Given the sensitivity of the spectrum, the fit is unable to differentiate between R_{CE} values below 40 GM/c^2.

The model's preference for a small central engine ($< 40GM/c^2$, or $<$ 80 km for a 1.4$M_\odot$ NS) is unsurprising considering the size scales we are probing, such as a neutron star and/or the inner radii of an accretion disk (especially in weakly magnetized neutron stars that display X-ray bursts). However, it is important to consider whether these results represent meaningful constraints on the size of the central engine, albeit limited by the sensitivity of the data, or whether we are simply probing the underlying uncertainty of other forms of velocity broadening, such as microturbulence.

As a simple test, we used our baseline fits to obtain the uncertainty on the v_{turb} parameter to the same 1 to 5σ significance levels probed for the R_{CE}-model, essentially treating the

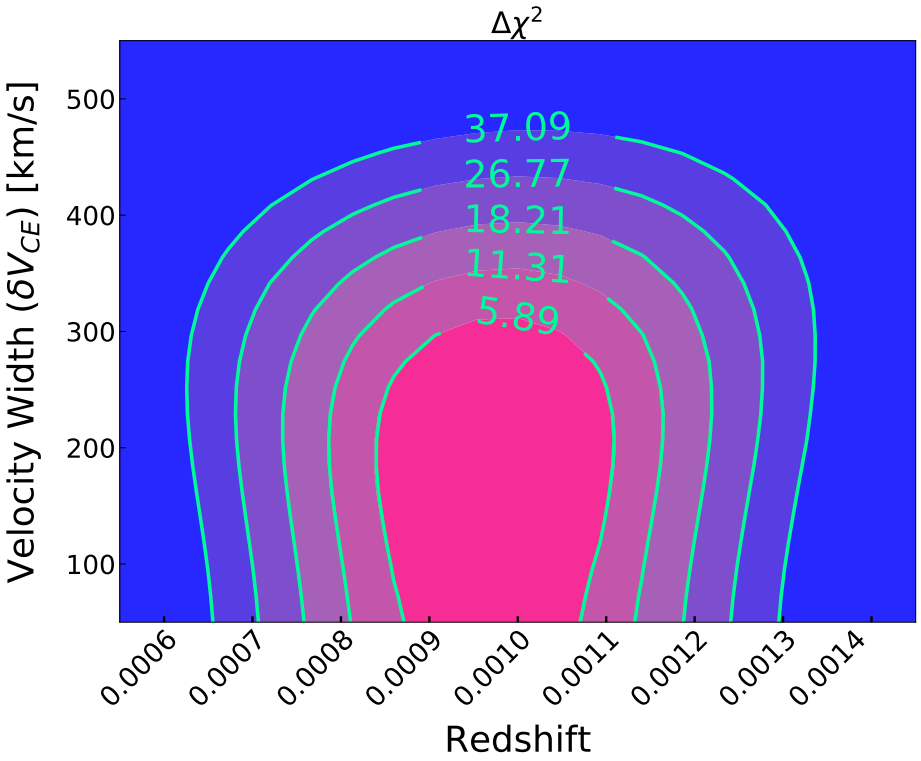

Figure 4.11: Contour plot of $\Delta\chi^2$ grid for the R_{CE}-model of XTE J1710−281 (single-zone), in redshift vs δV_{CE} space. Labelled contours indicate the $\Delta\chi^2$ level corresponding to 1-5σ confidence regions. The values and errors for δV_{CE} and z_{atm} listed in Table 4.3 were obtained from this grid. Errors on R_{CE} were obtained by calculating R_{CE} values along each contour line and extracting the largest and smallest values for each confidence level.

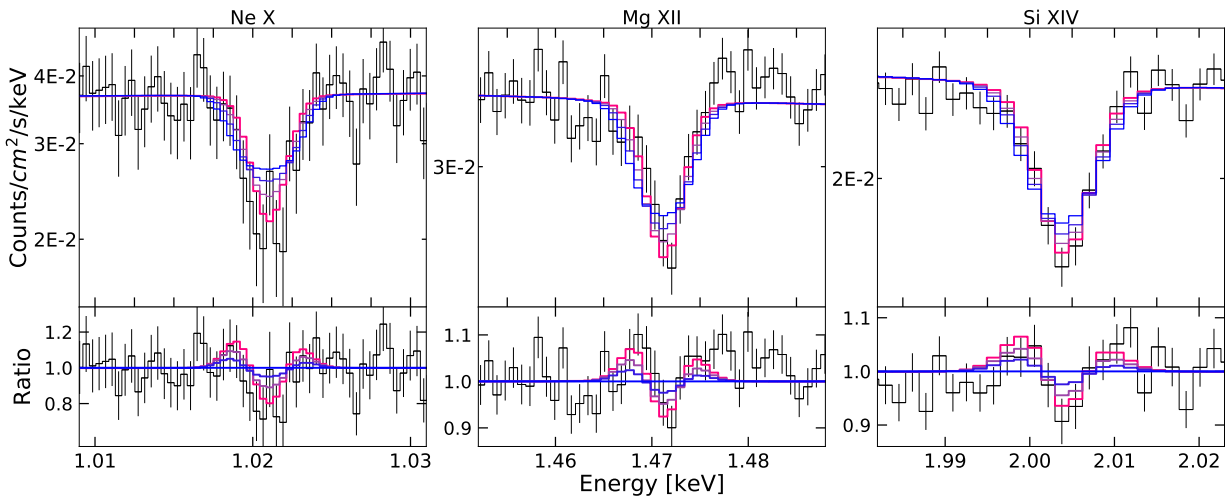

Figure 4.12: R_{CE} model for 4U 1916−053 for select lines. Best-fit model is plotted in fuchsia, while the positive 5σ error on δV_{CE} plotted is in blue. 1 and 3σ errors on δV_{CE} were plotted in magenta to show intermediate levels of confidence between the best-fit model and those at 5σ. Bottom panels show residuals to model at the $+5\sigma$ error of δV_{CE} to illustrate the improvement to the fit as δV_{CE} approaches its best-fit value.

v_{turb} parameter as a proxy for the geometric half-width parameter δV_{CE}. We obtain upper bounds on v_{turb} of 120, 170, and 260 km s^{-1} for 1, 3, and 5σ sigma errors, respectively. By comparison, the R_{CE}-model using the same fitting range (Range A, see Table 4.5) suggests upper bounds of 410, 520, and 630 km s^{-1} on the velocity half-width. Note that the 5σ bounds on v_{turb} still fall short of the 1σ bounds on δV_{CE} - this cannot be attributed to increased complexity of the model as only one free parameter was added. It is clear that v_{turb} significantly under-predicts the degree of geometric broadening allowed by the spectrum and, as expected, appears to be more sensitive to line-ratios (see Section 4.6.1 and Appendix C). Note that even if adding geometric broadening does not result in a statistically improvement in the fit that would suggest a large central engine that is apparent in the data (as appears to be the case in our spectra), these upper-limits are still robust in that they rule out R_{CE} values that would *necessarily* produce a statistically observable effect on the spectrum.

Also included in Table 4.3 is the R_{CE}-model based on the two absorption zone baseline fit of XTE J1710−281, as a point of comparison. This model was constructed by assuming both absorption zones are approximately co-spatial and, therefore, each was split into three constituent absorbers (6 in total) in order to model the effect of the central engine for both

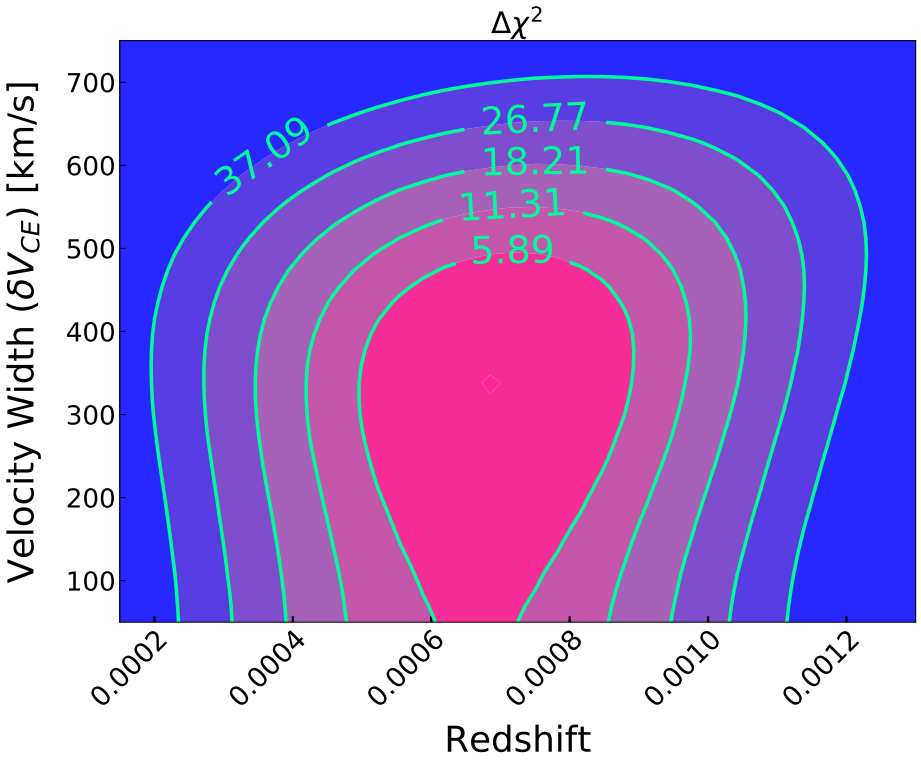

Figure 4.13: Contour plot of $\Delta\chi^2$ grid for the R_{CE} model of 4U 1916−053 (single-zone), in redshift vs δV_{CE} space. Labelled contours indicate the $\Delta\chi^2$ level corresponding to 1-5σ confidence regions. The values and errors for δV_{CE} and z_{atm} listed in Table 4.3 were obtained from this grid. Errors on R_{CE} were obtained by calculating R_{CE} values along each contour line and extracting the largest and smallest values for each confidence level.

absorption zones. The mean redshift and velocity width were coupled to the same value for both zones. Naturally, this 2-zone model introduces more model dependencies; given the quality of the spectrum, we advise caution when interpreting these specific results. It is worth noting, however, that the constraints on the central engine are virtually identical between the 1 and 2-zone models.

The single zone R_{CE}-model for 4U 1916−053, by comparison, yields noticeably worse constraints on R_{CE}, suggesting upper bounds of 200 GM/c^2 and 370 GM/c^2 for 1 and 3 σ errors, respectively. The lower sensitivity of these constraints is primarily driven two factors: First, the lower magnitude of the observed redshift significantly reduces the sensitivity of the method, as given by equations 4.9 and 4.10. Second, the lower quality and fewer absorption lines in this spectrum further reduce our ability to constrain the velocity broadening, resulting in large upper bounds on the δV_{CE} parameter. Figure 4.12 still shows the model's preference for smaller degrees of geometric velocity broadening.

As with XTE J1710−281, we tested the effect of adding portions of the HEG in the 1 to 3 keV region at energies where we identify the strongest lines in the MEG spectrum. We found that, due to the low S/N of the HEG spectrum at these energies, there was little improvement to our constraints by adding these bins. We therefore omit all HEG bins for this source below 6 keV; the fits reported in Table 4.3 for 4U 1916−053 were performed using the same baseline fitting range from Section 4.5.

By comparison, we obtained significantly tighter constraints from the two absorption zone R_{CE}-model for 4U 1916−053. Unlike XTE J1710−281, this 2-zone fit was performed assuming the outer absorption zone (Zone 2 in Table 4.2) originates in the outer disk and has a fixed velocity shift of 0 (see Section 4.5.1 for details). Velocity widths in this absorber should not be affected by the size of the central engine and, therefore, only the redshifted absorption zone (Zone 1) was split into three constituent absorber. Again, especially in light of the significant improvement in our constraints, we advise caution interpreting this particular result due to the increased model dependency of the 2-zone fit. Moreover, the

improvement in our constraints is not the result of improved velocity width constraints: if the large velocity widths observed in our 1-zone fit are indeed the result of some velocity structure, the addition of a second absorption component should afford the model enough flexibility to account for this velocity width. Instead, we see our velocity width constraints *worsen* with the addition of the absorber, due in part to the added degrees of freedom. The improved constraints on R_{CE} are the product of the much larger magnitude of the mean redshift of the atmosphere, which increases the sensitivity of the method as described by equation 4.10.

As discussed in Section 4.5.1, the larger redshift measured for Zone 1 in the 2-zone fit of 4U 1916−053 could indeed be real, in which case the improved constraints on R_{CE} would be perfectly valid. However, further Chandra/HETG observations of this source are required to make a more compelling case for this scenario due to the complexity of the model. In this work, we report the results of our 1-zone fit as our primary results for this source.

Finally, we applied the R_{CE}-model to the low S/N HEG spectrum of AX J1745.6−2901. We found that, due to the additional degree of freedom (δV_{CE}) of the more complex R_{CE}-model, the mean redshift in the disk atmosphere (significant to less than 2σ in the baseline fits) yielded a significance below 1σ when using χ^2-statistics. This made it impossible to place constraints on R_{CE} at the 1σ level, as R_{atm} is unconstrained. Using Cash statistics (*Cash*, 1979), and the ΔC-statistic as a proxy for $\Delta\chi^2$, we obtained an upper limit of $R_{CE} < 1300\ GM/c^2$ at the 1σ level. This large upper bound approaches the scale of R_{atm} (the distance between the central engine and the disk atmosphere), which is, naturally, the hard upper limit on R_{CE}. Despite these poor results, we briefly highlight this source as the sensitivity and spectral resolution in the Fe K band afforded by near-future missions such as XRISM (*Tashiro et al.*, 2018) will likely greatly improve constraints on AX J1745.6−2901, in particular.

4.7 Discussion

We have shown that, at small orbital radii, absorbers originating from the surface of the disk (such as disk atmospheres) are affected by an additional form of line broadening: a geometric effect between the orbital motion of the absorbing gas and the physical size of the central emitting region of the system. We developed a spectral model capable of constraining the magnitude of this velocity broadening effect, taking into account stark differences in behavior compared to most other forms of line broadening (namely turbulent broadening). Applying this model to the Chandra/HETG spectrum of two UCXB NS sources with disk atmosphere absorption, we were able to set upper limits on the size of their central engines.

An important limitation of this method is the contribution of different emission components of the central engine and their interaction with the Keplerian absorber. Currently, our method outputs a weighted average of the central engine size, where we treat the total emission from different continuum components as a single entity that can be described by a single characteristic radius, R_{CE}. If, for example, the continuum is composed primarily of a neutron star and the inner radii of the accretion disk, the approximation holds as we expect similar size scales and flux contributions to the continuum from both components.

This approximation may become problematic if there is a large discrepancy in both the size of the components and the energy bands at which they contribute. For instance, if the continuum flux in the Fe K band is dominated by emission from a compact neutron star while a larger, radially-extended corona dominates below 3 keV, then the linewidths in these energy bands would be affected differently: the compact neutron star would have little effect on linewidths and would contribute relatively narrow absorption lines across the entire Chandra band; however, in the combined spectrum, its contribution would only be significant in the Fe K band. Conversely, the much larger corona would display much broader absorption lines, but mostly contribute only in the low energy band.

The magnitude of this effect is somewhat overstated in this hypothetical example. In

the case of XTE J1710−281, any discrepancy is likely negligible given that our fits were mostly based on absorption lines located within a narrow band between 1 to 3 keV where dramatic changes in the contribution from different components seem largely implausible. This is likely true even in our fits to 4U 1916−053, which were dependent on absorption spanning almost the entire Chandra band: we found that Fe XXV and XXVI absorption lines were largely insensitive to the δV_{CE} parameter due to the lower resolution of the Chandra/HETG at these energies. Moreover, for these sources in particular, their soft spectra displaying prominent absorption are typically associated with states in which the continuum is dominated by a combination of neutron star and disk blackbody emission.

These results are the first attempt at constraining the size scales of central engines in both accreting neutron stars and compact objects, in general, using this method. It is therefore important to contextualize these constraints, the scope of the method, and its pitfalls, with those from other established techniques.

To first order, constraints via relativistic reflection lines probe exclusively the size of the ISCO. Although this quantity is particularly useful when constraining BH spin, it can be used in neutron star systems to constrain the innermost radius of the disk (likely larger than the ISCO in NS sources) and therefore set an upper limit on the radius of the neutron star itself. Constraints based on NuSTAR data of three neutron star sources by *Ludlam et al.* (2019) place upper bounds of 12.0 (GX 3+1), 18.6 (4U 1702−429), and 40.2 (4U 0614+091) GM/c^2 on the inner radius of the disk at a significance of 90% (assuming near-zero spin). Similar analyses report constraints of 24 GM/c^2 and 15 GM/c^2 for 4U 1636−536 (*Mondal et al.*, 2021) and Serpens X-1 (*Mondal et al.*, 2020), respectively. Though reflection modeling may allow constraints down to ~ 10 GM/c^2 for the most sensitive spectra, our constraints for XTE J1710−281, in particular, via linewidths are promising compared to a representative set of results from a well-established method. At the 2σ level (95%), we set an upper-bound of 80 GM/c^2 on the radius of central emitting area of this source. This result does not compare unfavorably considering the limited Chandra/HETG exposures on

this class of objects and the comparatively low effective area of CXO, in general; future high-resolution X-ray spectroscopy missions will greatly improve on the sensitivity of this method. Crucially, the ISCO is likely not the benchmark with which to compare R_{CE} results, as the peak luminosity contribution of the disk occurs at radii 2-3 times larger (*Zhu et al.*, 2012; *McClintock et al.*, 2014). If R_{CE} is more representative of the half-light radius (see Appendix D), then this benchmark should be closer to $20 - 25\ GM/c^2$ for sources with zero spin.

Though these initial results are larger compared to *the most* sensitive constraints via modeling the reflection spectrum in neutron stars systems, it is important to note that our constraints comprise a weighted average of the entire central engine, including any X-ray corona that may be present, and not just the scale of the ISCO. Relativistic reflection can, to some extent, probe the geometry of the corona: these models are sensitive to the height of the corona along the rotation axis of a black hole (or, neutron star), while the emissivity slope and cut-off energy of the reflected spectrum often imply compact coronae (*Wilkins and Fabian*, 2012; *Miller et al.*, 2015b). Combined with timing measurements, these techniques can be powerful tools for probing the geometry of the corona (*Fabian et al.*, 2015, 2017). Conversely, relativistic reflection models have also shown some degeneracy with (and even preference for) radially extended coronae (*Wilkins and Fabian*, 2011; *Wilkins and Gallo*, 2015). While it is difficult to quantify the robustness of constraining the geometry of the corona via the relativistic reflection method alone, these constraints are certainly not as robust as those for the ISCO. By comparison, our linewidth method allows us to probe any component of the central engine indiscriminately, whether the dominant emission is due to the disk, a neutron star, or a corona.

Compared specifically to measurements of black hole spin obtained using either the continuum fitting method or relativistic reflection, our constraints are categorically worse: both methods have been able to constrain the size of the ISCO down to scales smaller than 10 GM/c^2, compared to our best constraints for XTE J1710−281 of $R_{CE} < 60GM/c^2$. An im-

portant limitation is that both continuum fitting and relativistic reflection methods depend on careful modelling of the source continuum. In the case of relativistic reflection, difficulty with modelling the hard X-ray tail due to degeneracies with other continuum components can significantly affect the spin constraint. For continuum fitting, some model dependencies exist in terms of the radiative transfer through the disk surface atmosphere (among others), though these have shown to have little effect on spin measurements (*Reynolds*, 2014, 2019). Degeneracies with other continuum components is typically a non-issue with continuum fitting in the context of spin measurements, as these are limited to soft, geometrically thin-disk states where the inner radius disk extends down to the ISCO and where other continuum components (such as a power-law) make up less that 25% of the observed luminosity (*Steiner et al.*, 2009; *Gou et al.*, 2014), though this method is limited to BH systems. More importantly, continuum fitting requires independent constraints on the distance and inclination of the system, as well as a measurement of the mass of the black hole, limiting the continuum fitting method to only a handful of BH LMXBs (*Reynolds*, 2019, 2021). Linewidths may eventually contribute meaningful constraints on black hole spin as more sensitive spectra from both current and future high-resolution spectroscopy missions become available, finding a niche in select sources and/or spectral states in which the sensitivity of other methods may be reduced. The method, however, probes the entire central engine and not just the scale of the ISCO, a feature that might instead significantly limit its applicability in this context.

Both reverberation mapping and microlensing in quasars provide direct measurements of the geometry of the X-ray corona, although these methods can only be applied in AGN. Among the more notable results of quasar microlensing, an analysis of the lensed quasar PG 1115+080* by *Morgan et al.* (2008) derived a half-light radius for the X-ray emitting region of $\log(R/\mathrm{cm}) = 15.6^{+0.6}_{-0.9}$. In gravitational radii (adopting the same mass estimate of $1.2\times10^9 M_\odot$) this translates to a 1σ upper-bound of $\sim 80\, GM/c^2$. These are larger compared to our R_{CE} constraints on XTE J1710−281, and are more comparable in their sensitivity

to our results for 4U 1916−053, which set the scale of the central engine at $R_{CE} = 110 \pm 90$ GM/c^2.

Naturally, our constraints using linewidths will improve with further Chandra/HETG exposures of these sources, as well as exposure from future microcalorimeter missions such as XRISM (*Tashiro et al.*, 2018) and ATHENA (*Barcons et al.*, 2017). Both 4U 1916−053 and especially AX J1745.6−2901 will benefit from the higher effective area and spectral resolution in the Fe K band from these missions. At lower energies, both ATHENA and future grating spectrometer mission ARCUS (*Smith et al.*, 2016) will provide 2-3 times the resolving power with a significant increase in effective area, allowing for better constraints on sources such as XTE J1710−281.

4.8 Conclusions

We have presented a new method for determining the size of the central emitting regions in accreting neutron stars via measurements of widths of absorption lines. We applied this method on three ultra-compact and/or short period LMXBs in which we identified redshifted absorption lines originating in an inner disk atmosphere; both in this work and in T20 we present evidence that these are gravitational redshifts from atmospheres originating in the inner disk. The main results of this work are as follows:

1. Spectral fits to the ionized disk atmosphere absorption show highly significant redshifts (above 5σ) in two of three sources: XTE J1710−281 (310 ± 50 km s^{-1}) and 4U 1916−053 (200 ± 50 km s^{-1}). The shifts are largely inconsistent with various estimates of the relative radial velocity of these systems, while the ionization and absorbing columns of the atmosphere suggest the absorption originates in the inner disk, consistent with a gravitational redshift. The redshifts suggest the absorption originates at 1500^{+200}_{-200} R_g (XTE J1710−281), 2200^{+600}_{-300} R_g (4U 1916−053), and 1700^{+9500}_{-800} R_g (AX J1745.6−2901), once corrected for the transverse Doppler effect.

2. By using the gravitational redshift in the disk atmospheres to infer a radius, our constraints for the size of the central emitting regions in these systems were obtained independent of mass and distance to the source. However, the robustness of the methods developed and presented in this work is independent of the validity of the gravitational redshift result.

3. We developed a method that correctly accounts for the effect the size of the central engine has on linewidths, allowing for constraints on R_{CE}.

4. We found that the large number of absorption lines in our spectra allowed for better constraints on the magnitude of the observed redshift, as well as allowed us to constrain the degree of velocity broadening due to microturbulence. In turn, the degeneracy between turbulent velocities and the line-widths produced by the size of the central engine was greatly reduced. In contrast, the line-poor spectrum of AX J1745.6−2901 resulted in poor constraints on R_{CE}.

5. We are able to constrain the (weighted averaged) radius of the central engine of XTE J1710−281 down to $< 60\ R_g$ (at the 1σ-level). This initial effort approaches the sensitivity of constraints on the size of the innermost radius of many accreting neutron stars via modeling of relativistic reflection, though our constraints are not limited to setting the scale of the inner radius of the disk and encompass the entire central emitting area. These constraints also compare favorably to constraints via microlensing on black hole systems. In the case of the NS UCXB 4U 1916−053, we are able to constrain the central engine down to $< 200\ R_g$.

The scientific results reported in this work are based on observations made by the Chandra X-ray Observatory and data obtained from the Chandra Data Archive. N. T. acknowledges helpful discussions with Kevin Whitley and Nuria Calvet. R.M.L. acknowledges the support of NASA through Hubble Fellowship Program grant HST-HF2-51440.001. We thank the anonymous referee for comments and suggestions that improved this work. N.T.

acknowledges the support of the Horace H. Rackham School of Graduate Studies through the Rackham Predoctoral Fellowship.

CHAPTER V

Concluding Remarks

This dissertation presents three main contributions to our understanding of absorption phenomena in X-ray binaries and highlights the importance of high-resolution spectroscopic studies of these absorbers in furthering our understanding of the accretion process. These studies offer some new insights to important science in the diverse sample of objects considered in this work, spanning a large range of luminosities, including BH and NS sources, as well as both Hydrogen *and* Helium-rich accretion disks. Moreover, the results presented in this work strengthen possible connections between seemingly unrelated phenomena, such as disk winds and redshifted disk atmospheres both originating as close as 1000 GM/c^2. Finally, this dissertation highlights important lessons and recommendations regarding spectral modeling techniques of Chandra/HETG data. New spectral modeling techniques I developed in this work, such as phase resolved spectroscopy of dip absorption (Chapter III) or the use of linewidths to set the scale of the central engine (Chapter IV), offer new angles to science central to next chapter of the Chandra/HETG and the first chapters of XRISM (*Tashiro et al.*, 2018), ATHENA (*Barcons et al.*, 2017), and ARCUS (*Smith et al.*, 2016) observations.

5.1 Main Science Results

The works presented in this dissertation attempt to add clarity to our understanding of the physical nature of X-ray absorbers and their interplay with underlying disk physics. The results from Chapter II build on the case for magnetically driven winds in BH LMXBs, while highlighting important considerations in analysis techniques that may prove key before the launch of missions like XRISM. In Chapters III and IV, we present the discovery of gravitationally redshifted absorption in short-period NS XRBs owing to an inner disk atmosphere. This discovery raises questions about the physics of these absorbers and their relation to disk winds, and highlight the importance of further observations of these poorly understood class of XRBs. Finally, Chapter IV presents a new technique constraining the size of the central engine by measuring the velocity widths of absorption lines.

5.1.1 Magnetic Winds

In Chapter II, we used sophisticated and physically self-consistent photoionization models to describe the absorbing disk wind in all available Chandra/HETG archival data of the black hole candidate 4U 1630−472. This work implemented lessons learned from over a decade of disk wind studies in order to produce the most complete physical description of the observed wind complex allowed by the data, including components such as dynamically-broadened wind re-emission. The depth of observations allowed us to track changes in the wind as a function of spectral state and, perhaps most importantly, helped us identify wind features that are broadly consistent between similar observations.

Our results provide further evidence that winds in BH LMXBs are, at least in part, likely driven via magnetic processes. Four observations that were triggered within a short time period captured the source in a disk-dominated spectral state: The structure of the wind complex was found to remain broadly constant during this period, simultaneously requiring both a high velocity and ionization absorber and a lower velocity and ionization absorber to describe each of the four spectra. We find that launching radii (based on two

density-independent estimates) for the faster, more ionized wind absorption components are too small for thermal driving to effectively drive an outflow. Moreover, the observed outflow velocities and estimated densities for these components are inconsistent with models of thermally driven outflows. This is not the case for the slower, less ionized outer wind component: Launching radii and other criteria do not rule-out thermal driving, meaning this outer component may be driven by either thermal or magnetic processes.

A quantitative description of the wind structure is not possible for individual observations, as each consists of only two absorption components. Our spectral models reveal that wind parameters remain broadly constant in the set of 4 mutually contemporaneous observations, allowing us to constrain the *average* wind structure by combining results from individual spectral fits and treating them as representative of a single characteristic outflow. We found that both the radial density and velocity structure of the wind complex is quantitatively consistent with theoretical models of self-similar winds driven via MHD pressure. Although the nature of the outer wind component is still not clear, these results favor magnetic driving. This approach may prove useful in determining wind driving mechanisms in cases where launching radii and velocities cannot rule-out a thermal wind. Moreover, this approach allows for a quantitative comparisons to models of MHD winds despite individual observations consisting of only 2 absorbers.

5.1.2 Redshifted Inner Disk Atmospheres

The study presented in Chapter III analyzes data from a 2018 proprietary Chandra/HETG campaign (250ks) on the ultra-compact X-ray binary 4U 1916−053. The accretion disk in this class of objects is known to be small from the short orbital period (in this case ~ 50 minutes) of the donor, corresponding to a small orbital separation. Any absorption (such as wind) originating from the surface of these small disks would likely probe the similar regimes as the innermost wind components in BH LMXBs.

We discovered redshifted absorption lines originating in a inner disk atmosphere located

at $\sim 1200\ GM/c^2$ from the central NS, the first strong evidence of gravitationally redshifted absorption in accreting compact objects and likely the largest ever measured in absorption. In order to test alternative hypotheses for the origin of the redshift, we modelled the *excess* absorption in phase-resolved spectra of X-ray dipping events. This analysis was only possible owing to the large number of X-ray dips in our sample. We found a near-zero velocity shift in the *outer-disk* that is inconsistent with the redshift in the disk atmosphere, suggesting that the relative radial velocity of the system is likely small and, therefore, not responsible for the observed redshift.

In addition, we found redshifts of similar magnitude and significance in archival data of other short-period NS systems with absorbing disk atmospheres that are *not* reported in the literature - XTE J1710−281 and AX J1745.6−2901 - suggesting that these inner disk atmospheres may form part of a newly discovered class of absorbers with a shared physical origin. A complete photoionization treatment for these two sources is presented in Chapter IV. The simple relationship between gravitational redshift and orbital radius ($z \simeq 1/r$ for $r > 10\ GM/c^2$) means that the location of these atmospheres within the disk can be mapped (in units of GM/c^2) with unprecedented accuracy, independent of mass and luminosity. Like magnetic winds in black hole X-ray binaries, the extreme nature of these atmospheres may be indicative of magnetic processes within the disk.

5.1.3 Central Engines

Typically, central engines in accreting neutron stars and black holes are treated as point sources when modeling disk wind and atmosphere absorption: The Keplerian motion of the intervening gas is small and orthogonal to the line-of-sight. This treatment breaks down if the distance between the absorber and central engine is small ($few \times 1000\ GM/c^2$): Portions of the emitting area are absorbed by gas in which the orbital motion is not *entirely* orthogonal to the line-of-sight, and therefore a component of the absorber's Keplerian velocity is passed to the observer. As a result, opposite portions of the emitter are absorbed

by increasingly *redshifted* and *blueshifted* gas.

In Chapter IV we developed the basic methodology *required* to model this effect, as the geometric line width *cannot* be modeled using built-in broadening parameters (such as the turbulent velocity) in existing models: turbulent broadening is known to affect equivalent-widths (EWs) of saturated lines and, therefore, is sensitive to ratios of strong to weak lines, whereas EWs remain *exactly* constant regardless of the *geometric* line width.This analysis technique allowed us to constrain the size of the central engine in a sample of NS UCXBs down to 60 GM/c^2 , aided by the simplicity of estimating the orbital distance and velocity of the absorber solely by measuring the gravitational redshift in the atmosphere.

This novel spectroscopic technique provides new angles to central engines in accreting compact objects, allowing for constraints in regimes and spectral states where other methods may underperform. Unlike relativistic reflection (*Fabian et al.*, 1989) and continuum fitting (*McClintock et al.*, 2014) methods that are limited to setting the scale of the innermost stable circular orbit (ISCO), the geometric width is sensitive to all components of the central engine such as the poorly understood X-ray corona.

5.2 Future Directions

Near-future X-ray microcalorimeter mission XRISM will deliver significantly higher spectral resolution in the Fe K band and a larger effective area compared to the Chandra/HETG (though HEG/MEG resolution will still outperform XRISM at $\sim$ 2 keV and lower energies). Eventually, the ATHENA X-IFU will match the HETG resolution at 2 keV, surpass the XRISM resolution at 7 keV, and greatly surpass both missions in terms of effective area. These giant leaps in terms of spectral sensitivity will help answer many questions raised by the results in this dissertation - results that push the capabilities of the Chandra/HETG to its limits. The increased sensitivity of these future X-ray facilities will likely require increasingly complex and sophisticated models in order to describe the collected data, amplifying some of the issues raised in this dissertation about current analysis techniques.

5.2.1 Disk Winds in the XRISM and ATHENA Era

The imminent increase in spectral resolution and effective area from X-ray microcalorimeter missions will reveal both absorption and emission features of disk winds in unprecedented detail. The increased complexity and sensitivity of the spectra will, in turn, require more complex models to describe the data. Performing the kind of analyses presented in this dissertation on higher resolution data with more model components will inevitably strain computational resources and exacerbate difficulties in the fitting process.

As highlighted in Chapters II through IV, difficulties in navigating the complex parameter space during spectral fitting and error searches is already a challenge when fitting 2 or more absorbers. Bright XRISM spectra will inevitably require more absorbers to achieve a statistically acceptable fit, exponentially increasing the complexity of parameter space. A plausible solution would be to assume the absorption complex has some radial structure in terms of column, ionization, and velocity than can be described via some power law. Though this would not reduce computation times given the same number of absorbers, it would significantly reduce the complexity of the parameter space. This is not a new approach: *Fukumura et al.* (2017) strictly adhere to this methodology in order to test models of MHD driven wind. Though this approach is not intended to achieve the best statistical fit to the data, the resulting fits would likely be a good starting point for before decoupling absorption components and fitting each component separately.

The approach presented in Chapter II combines wind properties derived from separate, albeit similar, observations in order to characterize the *average* structure of the wind complex in 4U 1630−472. This approach may prove useful in the XRISM and ATHENA era, whereby fitting comparatively simple models to a series of short observations may reveal as much as a complex model describing a single deep exposure. Tracking the structure and evolution of disk winds will likely be key in understanding the origin the outflow.

Finally, the increased effective area of both XRISM (in Fe K) and ATHENA will be critical for detecting extremely broad wind re-emission features we expect from innermost

wind components. Given the lack of independent wind density constraints in most cases, spectra with high quality wind re-emission/P-Cygni profiles will be a key improvement in constraining wind launching radii.

5.2.2 Follow-up on Gravitational Redshift Results

Our results from Chapters III and IV have shown that low-luminosity ultra-compact/short-period X-ray binaries are some of the most interesting yet under-studied and under-observed compact accretors, and should be high-priority targets for both current and future high-resolution X-ray spectroscopy missions. In addition to any new science yet to be revealed in these systems, emphasis should be placed on the nature of the redshift discussed in Chapters III and IV. These efforts should include both observational and theoretical efforts to rule-out relative radial velocities and inflows as culprits for the observed redshifts.

The additional 250 ks of Chandra/HETG exposures of 4U 1916−053, still ongoing at the time of writing, will likely increase the significance of the results from Chapters III and IV provided the absorption in these observations is similar to what was found the 2018 dataset. Additional high-quality exposures of X-ray dips with strong absorption lines, in particular, could rule-out redshifts due to the relative radial velocity of the system if the spectra are consistent with the results reported in Chapter III. Alternatively, the character of the absorption in these new data may be markedly different, in which case tracking changes in the redshift as a function of source luminosity and other properties of the absorber may reveal the nature of the redshift. The portion of the disk atmosphere that intersects the line-of-sight may, for instance, shift its location towards larger orbital radii; as this radius increases, the observed redshift should approach the radial velocity of the system asymptotically.

Although the Chandra/HETG spectrum of 4U 1916−053 is most sensitive to lines in the 1 to 3 keV band, such as Si XIV, strong Fe XXV and XXVI absorption make this an excellent target for XRISM. The higher spectral resolution and effective area in the Fe K band may

reveal broad re-emission from the disk atmosphere consistent with the gravitational redshift interpretation. Conversely, XRISM may reveal inverse P-Cygni if, instead, the absorber is some form of quasi-spherical inflow. ATHENA will improve on both observatories without sacrificing spectral resolution at lower energies.

Evidence of Fe XXV and XXVI absorption can be found in the noisy Fe K band spectrum of XTE J1710−281; XRISM may reveal interesting absorption in the Fe K band where Chandra/HETG is limited in terms of effective area and, to a lesser extent, resolution. However, the richest absorption features are overwhelmingly found in the 1 to 3 keV band where the Chandra/HETG will, in most ways, outperform XRISM. With ATHENA being over a decade away, further exposures of XTE J1710−281 should be a high-priority for Chandra/HETG. Clear challenges exist in observing this source: its poorly understood 30-day duty cycle means it is unclear what features will be revealed. This variability, however, may be key for tracking changes in the disk atmosphere, as discussed in Chapter IV.

AX J1745.6−2901 should be a high-priority transient source. Fe XXV and XXVI are the only prominent absorption features found in the spectrum, and the significance of our redshift constraints are limited by the large ISM column, possibly obscuring absorption lines at lower energy bands, as well as the lower Fe K band resolution of the HEG. Further Chandra/HETG exposures would help increase the significance of the observed redshift, however, the capabilities of XRISM make it an ideal facility for studying this source. The well-established behavior of absorption lines in this system as a function of spectral state (*Ponti et al.*, 2017) means monitoring missions can aid in triggering XRISM observations when absorption is likely to be present. Moreover, this behavior closely follows the state dependence of disk winds in BH LMXBs, making AX J1745.6−2901 ideal for studying the connection between disk winds and inner disk atmospheres.

5.2.3 Central Engines: Theoretical Background and Models

Two major pitfalls with the approach presented in Chapter IV to model and constrain the geometric line width necessitate the development of proper spectral models designed specifically to account for the geometric width, as well as a more robust theoretical treatment to account for different central engine geometries. First, our implementation of the R_{CE}-model is both computationally expensive and impractical for the user, as it requires the use of multiple absorbers in order to describe a "single" absorption layer. Setting up this model in SPEX is complex and, most importantly, means that the same ionization balance is calculated multiple times. This problem will worsen at higher spectral resolutions, as the finer energy grid further increases computation time and will likely require more than the three-absorber approximation presented in Chapter IV. While Chapter IV provides a blueprint on how to properly model the geometric line width, the lack of an accessible implementation of this spectroscopic technique will significantly limit its adoption in the field, and delay the publication of important scientific results for both current (Chandra/HETG) and future (XRISM, ATHENA, and ARCUS) high-resolution X-ray spectroscopy missions.

Furthermore, the theoretical treatment presented in Chapter IV and Appendix C is based on an oversimplified toy model geometry of the central engine, where we relate the value of the δV_{CE} parameter to a physical size scale via a scaling factor that accounts for different geometries. This approximation will likely be inadequate at higher spectral-resolution and sensitivity, as it does not strictly account for the relative flux contribution of different velocity components. Emission from equatorial bands in the surface of a neutron star (the boundary layer), for instance, will result in relatively uniform flux contribution, while a circular emitter will produce a velocity profile that is peaked near lower-velocity components. Moreover, our model assumes the emitter is isothermal and does not account for the flux in different bands arising in regions of different size. The geometric line width of Fe XXVI ($\sim$7 keV) could differ drastically from Si XIV ($\sim$2 keV) depending on the temperature profile of the disk.

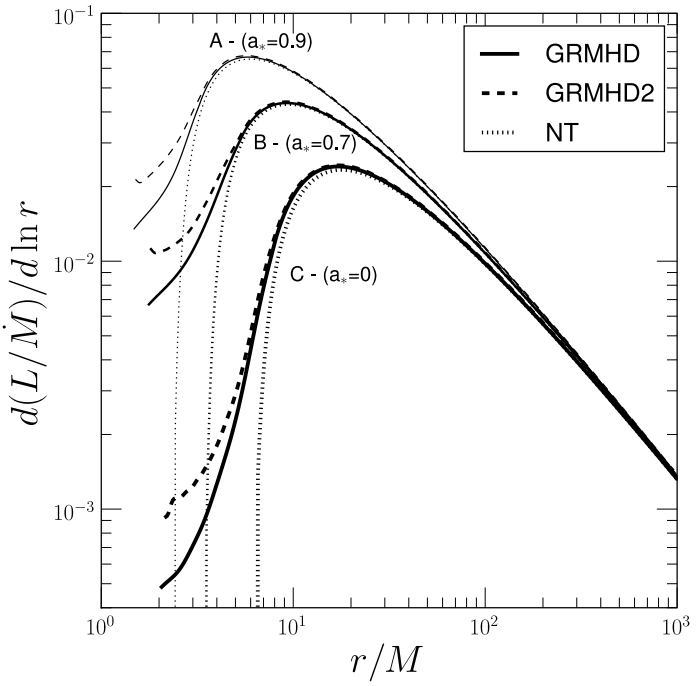

Figure 5.1: *Zhu et al.* (2012) models of disk emission as a function of black hole spin, showing the relative luminosity contribution (normalized for mass accretion rate, $\dot{M}$) at different radii, r (normalized by the mass of the black hole, M). Though emission extends down to radii smaller than r_{ISCO}, the relative luminosity contribution ($d(L/\dot{M})/d\ln r$) peaks at larger radii.

Developing a more complete and robust theoretical background is also critical in order to interpret results from the model. In disk-dominated states, for example, the geometric line width will more strongly reflect the half-light radius, several times larger than the innermost stable circular orbit (ISCO, see Figure 5.1; *McClintock et al.*, 2014; *Zhu et al.*, 2012), a departure from discussions of the reflection spectrum (*Fabian et al.*, 1989) or continuum fitting (*McClintock et al.*, 2014) methods. In more complex geometries, such as optically-thin/thick X-ray coronae, the half-light radius is strongly dependent on unknowns such as its density structure and shape (Chapter IV). This diverse set of complex emission phenomena in these systems require a comprehensive theoretical treatment.

APPENDICES

APPENDIX A

Markov chain Monte Carlo

MCMC analysis was implemented via `emcee` (*Foreman-Mackey et al.*, 2013), using the standard Metropolis-Hastings sampling algorithm. At each step of a chain, SPEX is fed a set of parameter values: N_H, $\log \xi$, $v_{\rm abs}$, and $\sigma_{\rm emis}$ for each wind zone. SPEX then performs a fit of the disk normalization, the only free parameter, using the continuum fitting range described in Section 2.5.1. The more sophisticated atomic physics in SPEX, including wind re-emission, only affect the shape and depth of the absorption lines and are therefore turned off during this fit. This process is substantially faster than including the normalization, which is degenerate with column density, as a degree of freedom in the MCMC analysis. Once the continuum is fit, both re-emission and the full atomic physics in SPEX are turned back on, and a new χ^2 is obtained using the line-focused fitting range (Section 2.5.1).

In addition to the parameter boundaries listed in Section 2.5.2, we also set dynamic boundaries based on the geometry of the system. An upper limit on the photoionization radius, $R_{phot} = \sqrt{L/n_H\xi}$, can be set using $N = n\Delta r$. By setting $f = \Delta r/r \leq 1$, the upper limit becomes $R_{phot} \leq L/N_H\xi$, where f is the filling factor and Δr is the thickness of the wind. However, we relaxed this constraint to $f \sim \Delta r/r \leq 1.2$, in order to account for uncertainties in the distance and mass of the black hole. We use this inequality as a prior to constrain our fitting parameters: The orbital radii implied by velocity broadening must be

below the limit set by the wind's plasma properties, $R_{\rm orbital} = GM/\sigma^2_{\rm emis} \leq L/\xi N_H$, where $GM/c^2 = r_g$. Although luminosity and r_g depend on assumed values of either distance or black hole mass, the accepted ranges for these values suggest that this uncertainty should have minimal impact on our results.

We ran our chains with sixteen walkers for 4000 steps each. Several MCMC experiments were conducted in the process of finding a minimum for each, therefore the 64000 steps presented in this work only represent the final run in a series of experiments. We checked for convergence using the Gelman-Rubin fitting statistic, where we only considered a parameter converged when this value reached below 1.2 while ensuring the variance on the posterior distribution was not a product of how walkers where initialized. Parameter errors were determined using the highest posterior density (or, HPD) interval method, in which the shortest interval that contains, for example, 68% of the posterior distribution corresponds to the 1σ error interval.

APPENDIX B

Treatment of Continuum Parameters

In Section 4.5 we discussed how continuum parameters (such as the temperatures and normalizations of the DBB and BB additive models) must be set as free parameters when fitting the photoionized absorption in order to account for some continuum absorption in the PION model. These continuum parameters, however, were treated as nuisance parameters when calculating confidence regions for the photoionized absorption model parameters: the $\Delta\chi^2$ value corresponding to a particular significance level (say, 1σ) was based on the number of free PION parameters (N_H, $\log \xi$, v_z, and v_{turb}; therefore $\Delta\chi^2 = 4.72$) and did not include the number free continuum parameters.

The justification for this based on three points: 1) Our continuum model is flexible enough to adapt and compensate for any amount of continuum absorption from the photoionized absorber and produce an equally good continuum fit throughout the parameter space explored in our fits. The change in χ^2 we observe is, therefore, determined solely by the absorption model's ability to fit spectral bins which contain absorption lines. 2) The continuum absorption is dominated by electron scattering and is mostly gray. Although the shape of the continuum might shift slightly to compensate for some energy-dependent absorption due to ions that have not been completely stripped of electrons, this change is not significant enough to affect the ionization parameter. 3) The change in the underly-

ing continuum is "physically uninteresting" and it is not in conflict with any independent constraints of the continuum parameters.

A quantitative test for point 1) is not straightforward: Though SPEX does not offer the option directly to treat the continuum and line absorption components of absorbers separately, it is possible to effectively remove the absorption line component of the absorber by setting the velocity broadening parameter, v_{turb} (v in SPEX), to an arbitrarily large number. We found that for a lower ionization ($\log \xi = 2.8$) line-rich absorber with a large column ($N_H = 10^{24}$ cm^{-2}), an unphysically large velocity broadening of $v = 10^7$ km s^{-1} ($\sim 30 \cdot c$) produces an absorber with *precisely* the same degree of continuum absorption without any absorption lines; this includes the larger amount of energy-dependent absorption at these low ionizations. Alternatively, using a value of $v < c$ resulted in some degree of absorption from ultra-broad lines contributing to the apparent continuum absorption. Given that the continuum absorption is entirely unaffected by the degree of velocity broadening, we adopted $v = 10^7$ km s^{-1} when testing for continuum effects.

Our test model consisted of taking the best-fit 1-zone model of 4U 1916−053 (a model that has both a large column and a large uncertainty in the ionization) and freezing the PION parameters to their best-fit values. The resulting spectrum was then absorbed by an *additional* PION layer with the same best-fit N_{He} and $\log \xi$ values, except the velocity broadening parameter was set to $v = 10^7$ km s^{-1} in order to convert this layer exclusively into a continuum absorber. Finally, the continuum was fit again to account for the additional continuum absorption. The resulting model should be nearly identical to the best-fit model listed in Table 4.2, with the exact same degree of *line* absorption, with the exception that the continuum optical depth is doubled and, therefore, the underlying continuum is brighter to compensate. Indeed, despite this significant increase in continuum absorption, we observed a minimal $\Delta\chi^2 < 0.2$ compared to the baseline model.

This model allowed us vary the degree continuum absorption independently without affecting the original PION layer which produces the absorption lines. By maintaining the

line-producing layer frozen at best-fit parameters, our test model was nominally able to track the quality of the continuum fit while keeping the absorption lines constant: if the continuum model is truly flexible enough to account for any degree of continuum absorption, then the change in χ^2 should be negligible regardless of choice of N_{He} and log ξ in the additional continuum absorption layer. Crucially, however, if the shape of the underlying continuum were to change enough to affect the ionization parameter, this should also present itself as a change in χ^2 in the test model: the PION layer frozen at the best-fit log ξ value would no longer produce the same absorption line spectrum as in the baseline model. As a result, our test model is able to quantitatively test both points 1) and 2).

The blue contour maps (with white contour labels) in Figure B.1 plot the $\Delta\chi^2$ grid for the 1-zone baseline model of 4U 1916−053 in N_{He} vs log ξ space. In the top panel, the red contours show the $\Delta\chi^2$ grid of the test model over the same parameter space, while in the middle panel we plot the $\Delta\chi^2$ grid of the test model as a percentage of the $\Delta\chi^2$ of the baseline model in yellow contours.

Although the $\Delta\chi^2$ grid for the test model is evidently not perfectly flat, the change is negligible relative to the baseline model: we only see a change in χ^2 larger than 1.0 well outside the 8σ confidence region of the baseline model, while the $\sim 1-2\sigma$ innermost contours appear to be affected by less than $\Delta\chi^2 < 0.2$. As a percentage, $\Delta\chi^2$ from the test model is only as large as 4% in a small region and never exceeds 7%, hovering at 1% or lower. Even a 4% change appears to have a little to no effect on the location of contours once we subtract the test model $\Delta\chi^2$ grid from the baseline grid, as can be seen in the bottom panel of Figure B.1 (yellow contours).

It is clear from this test that, although the underlying continuum may change to account for different degrees of continuum absorption, this 1) has a negligible effect on the quality of the continuum fit and 2) has little effect on the continuum shape and therefore does not affect the ionization parameter. This, however, does not necessarily mean changes in the underlying continuum can be entirely disregarded. Scanning for errors in the absorbing column

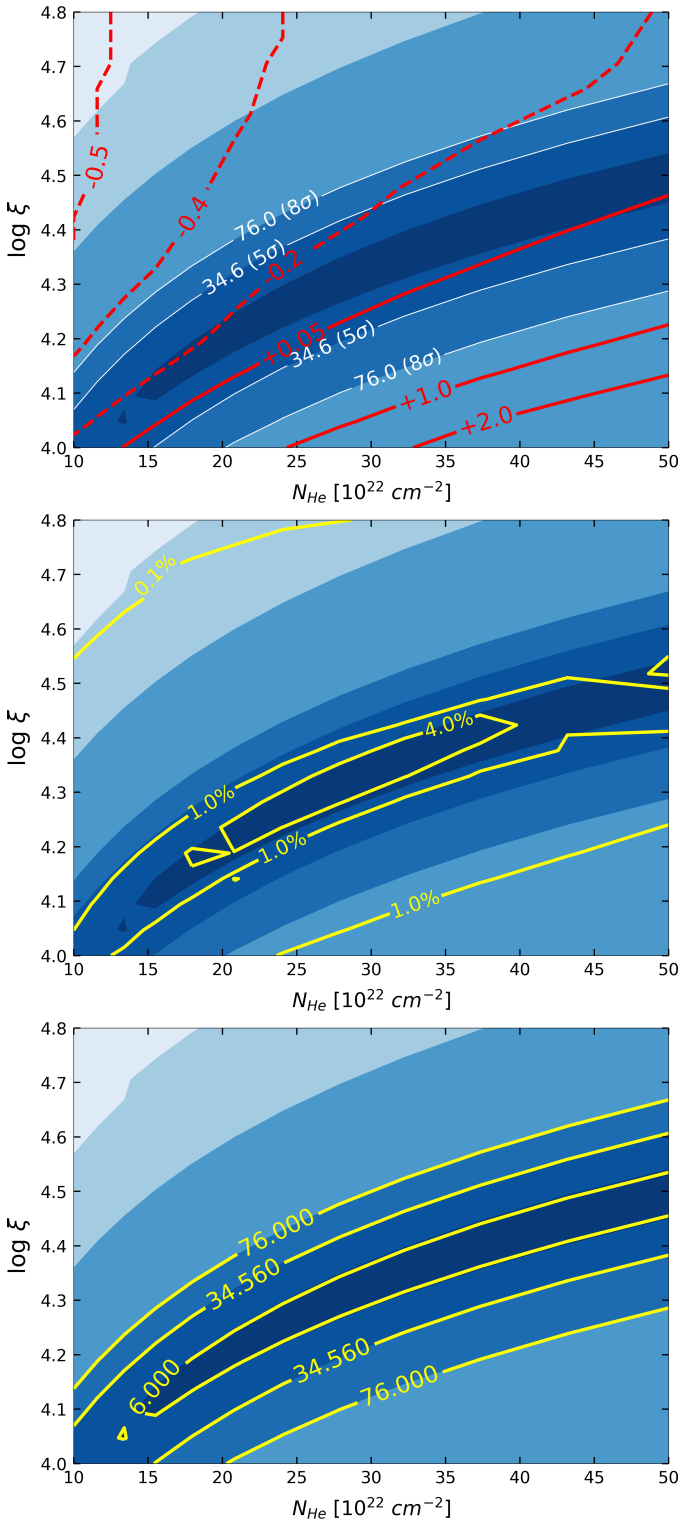

Figure B.1: The N_{He} vs log ξ $\Delta\chi^2$ surface for the 1-zone baseline fit for 4U 1916−053, plotted in blue with white contour lines. *Top:* Red contours plot the $\Delta\chi^2$ of the test model in response to the changing underlying continuum. *Middle:* Same as top panel, plotted as a percentage of the blue contours. *Bottom:* $\Delta\chi^2$ contours for baseline fit after subtracting the $\Delta\chi^2$ due to the changing continuum.

of some hypothetical absorber could, for instance, shift the the source luminosity from being well-below Eddington to super-Eddington, shift the NS temperature to unrealistic values, or require a significantly different neutral ISM column compared to the literature. None of these are the case for our three low-luminosity sources: we only see slight modest changes to the continuum parameters (e.g. changes in DBB and BB temperatures under 1%) other than normalizations for additive components, and at most a $\sim 25\%$ shift in luminosity.

Notably, while this shift in the underling luminosity should increase the uncertainty in the L_{phot} values reported in Table 4.2 for our most heavily absorbed sources (namely, 4U 1916−053 and AX J1745.6−2901), the quoted errors for quantities such as $r = \frac{L}{N_H \xi}$ should remain unaffected: The underlying source luminosity can be written in terms of L_0, the luminosity assuming no continuum absorption, as

$$L_u = L_0 e^{\sigma N_H}. \tag{B.1}$$

For simplicity, we assume gray opacity due only to electron scattering, and therefore $\sigma \sim 6.6 \cdot 10^{-25}$ cm^2. The upper limit on the photoionization radius then becomes $r = \frac{L_0 e^{\sigma N_H}}{N_H \xi}$, which we can then differentiate in terms of N_H as

$$\frac{dr}{dN_H} = \frac{L_0 e^{\sigma N_H}}{N_H \xi}(\sigma - \frac{1}{N_H}), \tag{B.2}$$

simplified as

$$\frac{dr}{dN_H} = r(\sigma - \frac{1}{N_H}). \tag{B.3}$$

For the purpose of this discussion, we ignore linear terms corresponding to the other parameters (namely log ξ). The uncertainty on r due solely to N_H then becomes

$$\delta_r = \pm |r(\sigma - \frac{1}{N_H}) \cdot \delta_{N_H}|. \tag{B.4}$$

Rewriting δ_{N_H} as some fraction of N_H, we get

$$\delta_r = \pm|r(\sigma N_H - 1) \cdot \delta_x|. \tag{B.5}$$

where $\delta_x = \delta_{N_H}/N_H$.

For small values of N_H ($\sim 17{\cdot}10^{22}$ cm^{-2} or smaller) we find that Equation B.5 approaches $\delta_r \sim \pm|r\delta_x|$, the error on r if we disregard any changes in the underlying continuum ($<$ 10% discrepancy). As expected, changes in the underlying luminosity of sources absorbed by small columns, such as XTE J1710−281, are negligible. On the other hand, as N_H approaches $\sim 150 \cdot 10^{22}$ cm^{-2}, then δ_r approaches zero. This makes sense: increasing (or decreasing) the value of N_H in the denominator of $r = \frac{L}{N_H \xi}$ is counteracted by increasing (or decreasing) the value of L, resulting in a constant r in this regime.

Our fits avoid this regime by limiting N_H to $< 100 \cdot 10^{22}$ (or $N_H < 50 \cdot 10^{22}$, for He) cm^{-2}. At this limit, $\delta_r \sim \pm|r \cdot 0.4\delta_x|$, meaning that the quoted errors in Section 4.5 are actually *overestimated* by not correcting for this change in continuum. However, standard error propagation assumes relatively small Gaussian errors - fits with large N_H values are accompanied by large minus errors on N_H, meaning that plus errors on r are in the regime where $\delta_r \sim \pm|r\delta_x|$.

B.1 Marginalization

For clarity, what follows is a formal description of how the fitting and error searching procedure in SPEX effectively results in the marginalization of these nuisance continuum parameters.

A simplified description of any of our spectral models can be written as

$$F_\nu = C_\nu \cdot e^{-\tau_\nu}, \tag{B.6}$$

where F_ν is the frequency dependent model flux, C_ν is the "naked" source continuum, and τ_ν is the frequency dependent optical depth of the photoionized absorber (including both line and continuum absorption). We can separate τ_ν into its absorption line ($\tau_{\nu,L}$) and continuum ($\tau_{\nu,C}$) components, and therefore Equation B.6 becomes

$$F_\nu = C_\nu \cdot e^{-\tau_{\nu,L}} \cdot e^{-\tau_{\nu,C}}. \tag{B.7}$$

The value of both $\tau_{\nu,L}$ and $\tau_{\nu,C}$ are directly proportional to N_H, while their behavior with respect to frequency depends on the value of $\log \xi$ (v_z and v_{turb} have a negligible effect on $\tau_{\nu,C}$, so we exclude them from this discussion). Equation B.7 can be further simplified by combining the underlying continuum with the continuum absorption into

$$F_\nu = \eta_\nu \cdot e^{-\tau_{\nu,L}}, \tag{B.8}$$

where $\eta_\nu = C_\nu \cdot e^{-\tau_{\nu,C}}$. This expression is useful as it describes the model flux in terms of the observed continuum, η_ν, and line absorption, $e^{-\tau_{\nu,L}}$.

After spectral fitting, the best-fit spectral model, F^*_ν, can be written as

$$F^*_\nu = C^*_\nu \cdot e^{-\tau^*_{\nu,L}} \cdot e^{-\tau^*_{\nu,C}}, \tag{B.9}$$

where $\tau^*_{\nu,L}$ and $\tau^*_{\nu,C}$ are the optical depths of the absorber at the best-fit N_H and $\log \xi$, and where C^*_ν is the underlying continuum given the resulting value of $\tau^*_{\nu,C}$. Simplified, this becomes

$$F^*_\nu = \eta^*_\nu \cdot e^{-\tau^*_{\nu,L}}, \tag{B.10}$$

where η^*_ν describes the total *observed* continuum (including continuum absorption) for the best-fit model.

Using Equations B.8 and B.10 we can describe what happens during a grid search in N_H vs $\log \xi$ space. A set of $N_{H,i}$ and $\log \xi_j$ test values are selected and a new continuum

absorption, $e^{-\tau_{\nu,C,i,j}}$, is computed. SPEX then performs a spectral fit of the continuum parameters to produce the new model spectrum

$$F_{\nu,i,j} = \eta_{\nu,i,j} \cdot e^{-\tau_{\nu,L,i,j}} \tag{B.11}$$

based on the new continuum absorption. As shown in our test model, this new observed continuum, $\eta_{\nu,i,j}$, is nearly identical to the observed continuum in the best-fit model,

$$\eta_{\nu,i,j} \simeq \eta^*_\nu. \tag{B.12}$$

Generalizing with Equation B.8, we can say

$$F_{\nu,i,j} = \eta^*_\nu \cdot e^{-\tau_{\nu,L,i,j}}. \tag{B.13}$$

The key point here is that, since the continuum fit does not change, the η^*_ν quantity is a constant, and therefore the quality of our fit depends solely on the absorption lines produced by the absorber, $e^{-\tau_{\nu,L,i,j}}$. During the grid search, the SPEX fitting routines effectively marginalize over these continuum parameters and, therefore, the fit statistic is only tracking changes in the model's ability to describe spectral bins containing absorption lines.

Crucially, we only use the example of a grid search in this discussion as it is a clear and convenient way to demonstrate how the continuum is effectively marginalized in our fits. Statistically, the same principles apply when SPEX is running standard fitting routines and especially error search algorithms.

APPENDIX C

The Effects of Velocity Broadening on Equivalent Widths

In this section, we describe in detail the differences between the two forms of velocity broadening discussed in this work and their effects on equivalent widths. The purpose of this section is both to clarify why the R_{CE}-model is designed as described in Section 4.6.1, as well as justify how these two forms of velocity broadening can be decoupled.

The geometric velocity broadening effect described in Section 4.6 arises from the fact that different parts of an emitting area are absorbed by gas with different line-of-sight velocities. This is subtly different to most commonly observed forms of velocity broadening in absorption, such as turbulent broadening, in which different velocity components are located along the line-of-sight yet absorb the entire emitting area equally. To illustrate this, we construct a simple toy model consisting of a uniform emitting area and two absorption scenarios involving an absorber with an arbitrary column N. In both scenarios, the properties of the emitting area and absorber are identical with the exception of how the absorber is divided into two velocity components.

In the first scenario, the absorber is divided equally into two velocity components along

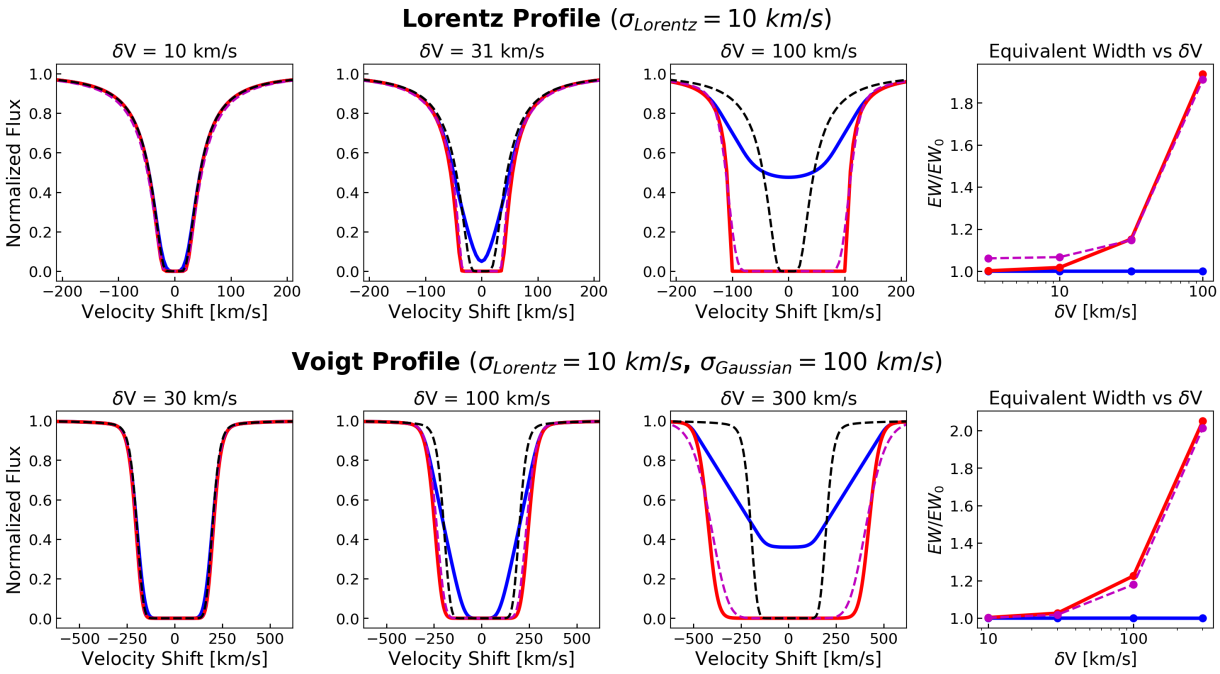

Figure C.1: Line profiles produced by applying additional velocity broadening. The base line-profiles (black dashed lines) are subject to both forms of velocity broadening described in the text: multiple velocity components in series (Equation C.2, akin to turbulent broadening; solid red lines), as well as in parallel (Equation C.4; solid blue line). In both scenarios, the same uniform velocity distribution was used (see text). Panels on the right show the equivalent widths at each velocity broadening value, normalized by the equivalent width of the base profile.

the line-of-sight. Based on Equation 4.11, the resulting spectrum can be described as

$$F(\nu) = F_0 \times e^{-\tau(\nu)/2} \times e^{-\tau(\nu+\Delta\nu)/2}, \tag{C.1}$$

which can be simplified as

$$F(\nu) = F_0 e^{-\tau(\nu)/2-\tau(\nu+\Delta\nu)/2}. \tag{C.2}$$

Here, the frequency dependent optical depth (say, for a line) requires dividing by a factor of 2, since $\tau = N \cdot \sigma(\nu)$ and total column N is divided equally between the two halves of the absorber.

In the second scenario, the absorber is again divided into two velocity components but now each velocity component only absorbs its corresponding half of the emitting area. Since the absorber is no longer divided along the line-of-sight, however, each half is absorbed by the entire column N. The resulting spectrum can be described using

$$F(\nu) = \frac{1}{2}F_0 e^{-\tau(\nu)} + \frac{1}{2}F_0 e^{-\tau(\nu+\Delta\nu)}, \tag{C.3}$$

simplified as

$$F(\nu) = \frac{F_0}{2}(e^{-\tau(\nu)} + e^{-\tau(\nu+\Delta\nu)}). \tag{C.4}$$

It is clear from Equations C.2 and C.4 that these two scenarios are not equivalent - the most pronounced observable difference is in the behavior of equivalent widths of strong lines with saturated cores.

The effects of line-of-sight (e.g. turbulent, thermal) velocity broadening on the equivalent widths of strong lines are well-known and are central to discussions on the curve of growth. Using our toy model for a qualitative comparison: if at line center $\tau(\nu)$ is very large and the line core becomes saturated, the entire continuum at ν would be almost entirely absorbed (Equation C.2). This is the case even when the column is divided by a factor of two. As a result, the EW of lines with saturated cores increases as the degree of velocity broadening

increases. Conversely, Equation C.4 shows how, even if the value of $\tau(\nu)$ approaches infinity, this component will *at most* completely absorb up to half of the continuum. The degree to which the other half of the continuum is absorbed depends solely on the value of $\tau(\nu + \Delta\nu)$.

Using Equation C.4 it is straightforward to show how, instead of increasing, the EW of an absorption line remains *exactly* constant regardless of the degree of geometric velocity broadening. Per the definition of the equivalent width, the total flux removed by an absorption lines is equal to the quantity

$$F_0 \cdot \mathrm{EW} = F_0 \int d\nu - \int F_\nu \, d\nu. \tag{C.5}$$

In the case of an absorption lines NOT subject to geometric broadening, $F(\nu) = F_0 e^{-\tau(\nu)}$, and therefore the equivalent width is given by

$$\mathrm{EW} = \int 1 - e^{-\tau(\nu)} \, d\nu. \tag{C.6}$$

Adding geometric broadening to this scenario, $F(\nu) = \frac{F_0}{2}(e^{-\tau(\nu)} + e^{-\tau(\nu+\Delta\nu)})$, and therefore Equation C.5 becomes

$$F_0 \cdot \mathrm{EW} = F_0 \int d\nu - \frac{F_0}{2} \int (e^{-\tau(\nu)} + e^{-\tau(\nu+\Delta\nu)}) \, d\nu \tag{C.7}$$

Simplifying this expression, we obtain

$$\mathrm{EW} = \frac{1}{2} \int 1 - e^{-\tau(\nu)} \, d\nu + \frac{1}{2} \int 1 - e^{-\tau(\nu+\Delta\nu)} \, d\nu. \tag{C.8}$$

Comparing Equations C.6 and C.8 it is clear that, unless the value of $\int 1 - e^{-\tau(\nu+\Delta\nu)} \, d\nu$ is noticeably different to $\int 1 - e^{-\tau(\nu)} \, d\nu$, then equivalent width of the line remains. This makes sense: by adding geometric broadening, we split the emitting area in two halves and simply added a velocity shift to one of them. Since we do not expect the equivalent width

of a line to change by simply adding a velocity shift, each half still contributes half of the total equivalent width.

For confirmation, we calculated several line profiles with different degrees of geometric velocity broadening, plotted in Figure C.1. Unlike our simple 2 component examples, these profiles were calculated using as many as 1000 velocity components, assuming a rectangular velocity profile where δV_i spans linearly from $-\delta V$ to $+\delta V$ and each velocity component contributes equally. The base profile (black dashed line) remains constant, while the profile subject to geometric broadening is plotted in blue. The same rectangular velocity profile was also applied to the absorber along the line-of-sight (as in Equation C.2, solid red line). This profile is analogous to turbulent broadening, though in the case of turbulent broadening we expect a Gaussian velocity distribution. As a simple point of comparison, we used an ad-hoc scaling actor to convert δV into a Gaussian velocity width ($\sigma_{\delta V}$) and therefore compute comparable Voigt profiles (dashed magenta line).

The computed equivalent width for each profile is plotted in the rightmost panels of Figure C.1, normalized by the equivalent width of the base profile. As expected, the equivalent width remains constant in the case of geometric broadening, while it increases when the absorber is slit along the line-of-sight (note that the total column N remains constant for all profiles).

APPENDIX D

Different Central Engine Geometries

As introduced in Section 4.6.1, the assumed "shape" of the central engine can affect the interpretation of any R_{CE} constraint using the method described in this work. At higher spectral resolutions, different geometries may ultimately affect the shape of the observed line profile; given the sensitivity of our data and how the R_{CE}-model is designed in this work, this discussion mostly focused on how the fit parameter, δV, can be related to δV_{CE} quantity (see Figure 4.10, Section 4.6).

The model as described in Section 4.6.1 splits the total emitting area into 3 components of equal area: a central region absorbed by gas with no additional velocity shift, and two exterior regions absorbed by gas subject to an additional blueshift ($-\delta V$) or redshift ($+\delta V$). Figure D.1 shows an equatorial view of two toy model geometries: a circular and rectangular emitting region relative to the axis of rotation. In the case of the rectangular emitter, the relationship between the mean velocity shift for each component is trivial (see Figure D.1) given that δV changes linearly along this narrow projection of the orbital velocity (hereafter, the x-axis). Conversely, splitting the circular emitting region equally along the x-axis results in a slender central region that extends to a small fraction of the δV_{CE} value compared to the exterior regions. Crucially, the mean velocity shift for the exterior regions is calculated via a weighted average, as the portions of the emitter that are subject to the largest velocity

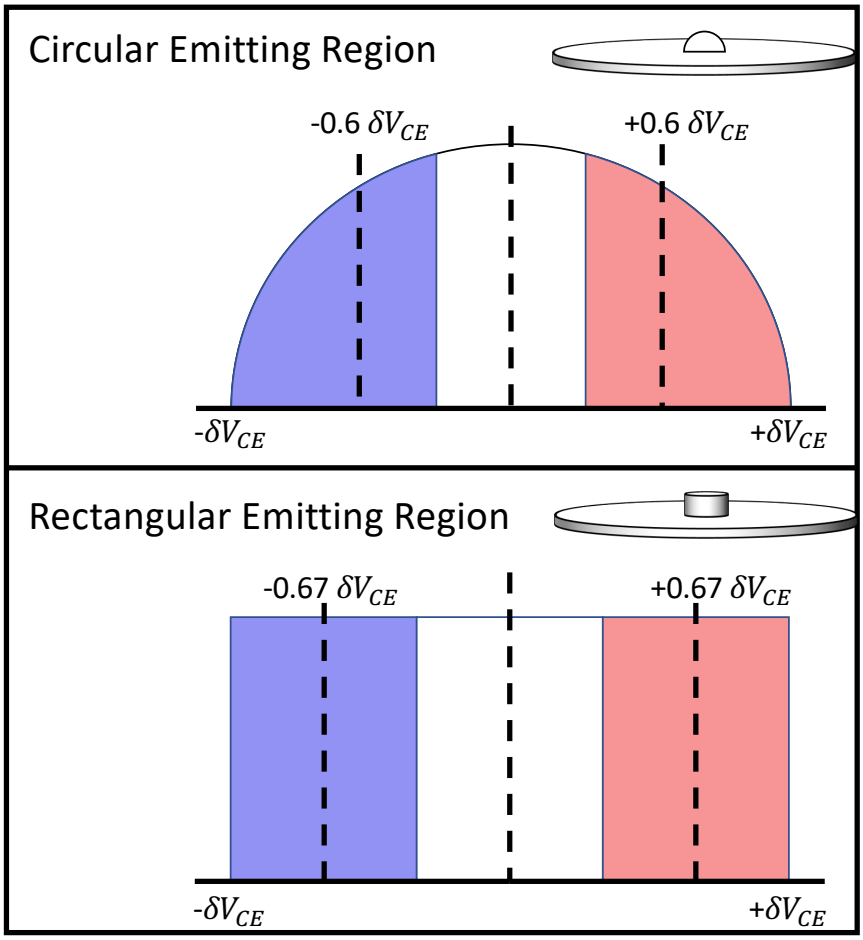

Figure D.1: Equatorial view of circular (top) and rectangular (bottom) central engine geometries. The horizontal x-axis corresponds to the projection (along the line-of-sight) of the Keplerian motion of the absorbing gas (see Figure 4.10). By definition, the extent of each area along the x-axis spans from $-\delta V_{CE}$ to $+\delta V_{CE}$, and vertical dashed lines plot the location of the (weighted) mean δV for each area component.

shift contribute the least in terms of of emitting area. This can be seen in Figure D.1, where the mean δV value (vertical dashed lines) of the exterior regions are smaller compared to those in the rectangular region.

Using equal-area components in our R_{CE}-model allows us to account for many central engine geometries in ways that alternative approaches do not. For instance, a best-fit δV value for a given spectrum could be interpreted as meaning $\delta V_{CE} = 1.5\delta V$ when assuming a broadly rectangular central engine geometry, or $\delta V_{CE} = 1.7\delta V$ when assuming a circular emitting region. Alternatively, changing the relative contribution of each emitting area would require multiple fits to account for each geometry.

D.1 An Optically-Thin Corona

Thus far this discussion has focused on different central engine geometries for emitting regions that can be treated as "solid" surfaces: regions, such as the surface of a neutron star, in which the relative flux contribution of a certain portion of the emitter depends solely on its surface area. If, instead, the central engine in question was composed of optically-thin emitting gas, then the relative flux contribution of different spatial components (in this case, along the x-axis) depends both on the apparent area and the amount of material along the line-of-sight. The purpose of the following discussion is to provide a crude quantitative comparison between an R_{CE} value derived from our model and a characteristic size-scale (e.g. the half-light radius) in the case of a simple toy model optically-thin corona.

Our toy model corona consists of a truncated sphere of gas in which the flux contribution from each area element (dA) is proportional only to the total amount of material along the line-of-sight ($dF(x, y) \propto \tau(x, y)$, where the y-axis is the vertical axis in Figures D.1 and D.2). This quantity is strongly dependent on the density structure of the sphere; however, the absolute value of the gas density is unimportant as we only care about relative flux contribution. This simple toy model also assumes a uniform continuum spectral energy distribution throughout the sphere. It is important to point out that any realistic model

of a central corona may diverge significantly from any of these assumptions. The core of the corona, for instance, may be sufficiently dense to become optically-thick. In this case, an analysis of the relative flux contribution of different area elements will most likely yield results that lie somewhere in between the "solid" emitting surface and the optically-thin scenarios. Given the scope of this work, we limit this discussion by only exploring these two extreme scenarios.

We tested two different density profiles for our toy model corona: a constant density sphere and an inverse square profile ($n(r) \propto r^{-2}$; often referred to as a singular isothermal sphere profile in hydrostatic systems). In order to avoid the problematic singularity in the latter, we included a softening term to the profile ($n(r) \propto \frac{1}{c+r^2}$) and tested different degrees of softening relative to the truncation radius imposed by our toy model. Figure D.2 shows the relative flux contribution along the x-axis. Although we are no longer dealing solely with area elements, this analysis allows us to treat the relative flux contribution in an analogous manner to that of the solid emitting surfaces (Figure D.1). As with the rest of this analysis, we divide the emitter into 3 components of equal flux contribution (or, equal normalization during spectral modeling). Instead of the δV_{CE} parameter, defined as the velocity shift at the edge of the of a well-defined emitting region in Section 4.6 (see Figure 4.10), we define an analogous quantity for this optically-thin scenario: δV_h, or the velocity shift at the half-light radius (or, R_h). Values along the x-axis, as well as the weighted average velocity shift for each component (the fitting parameter δV), are normalized by the magnitude of R_h and δV_h, respectively, calculated in each scenario. Note that, unlike the rest of this analysis, R_h is calculated by integrating the flux contribution *radially* (on the image plane), as opposed to along the x-axis.

The top three panels of Figure D.2 show the relative flux contribution in the case of an inverse square density profile, each with a different degree of softening (spanning three orders of magnitude). The inclusion of the softening factor means this toy model is no longer self-similar relative to the truncation radius. However, the magnitude of the δV

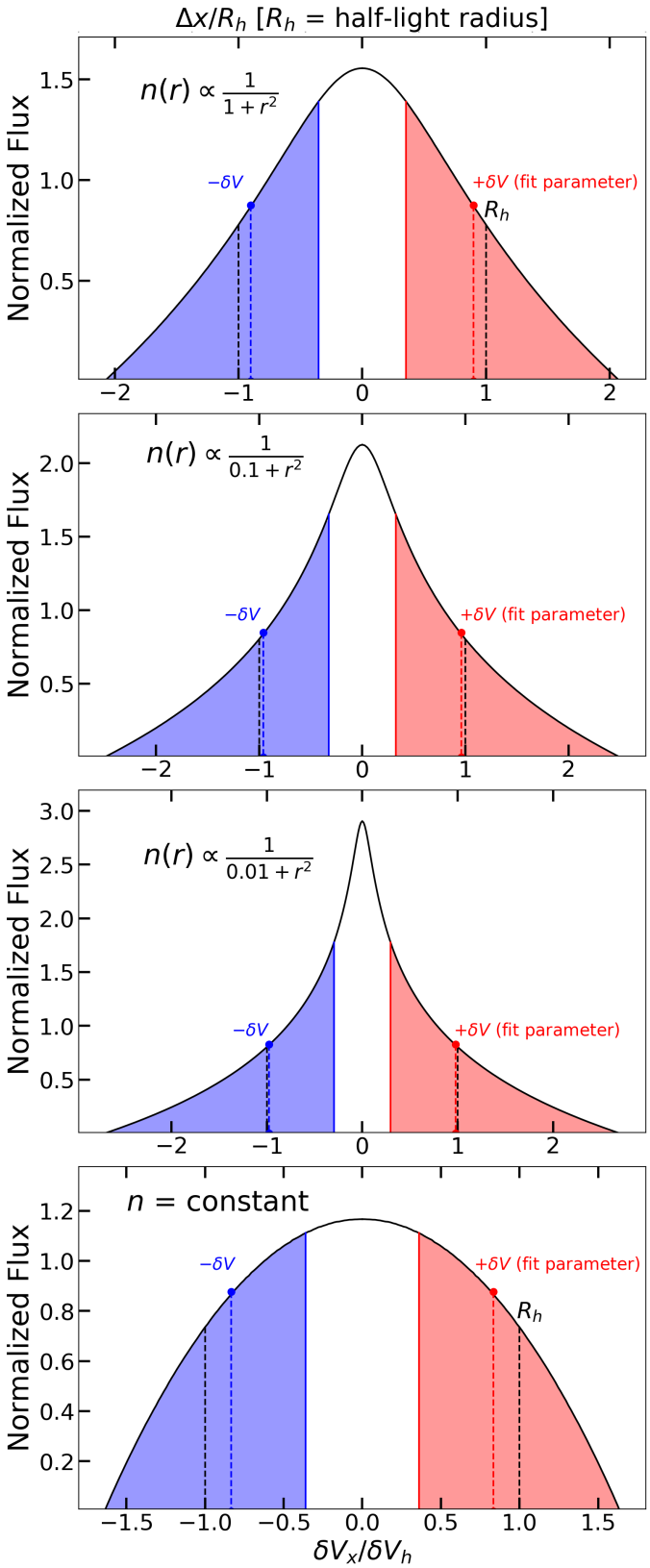

Figure D.2: The relative luminosity contribution along the x-axis for a toy model optically-thin corona.

fitting parameter approaches the velocity shift at the half-light radius, R_h, asymptotically. Even in the case of strong softening (the top panel), δV differs from this value by less than 10%. Alternatively, the constant density scenario (bottom panel) is completely self-similar. In this case, we find the magnitude of the δV parameter is $0.83 \cdot \delta V_h$.

Taken literally, the results from our various toy models could be used to interpret fits obtained with the R_{CE}-model. For instance, a best-fit δV value of 100 km s^{-1} could be interpreted as a δV_{CE} of either 150 (rectangular) or 170 (circular) km s^{-1} for a "solid" (optically-thick) emitter, or as a δV_h ranging from 100 (inverse-square density profile) to 120 (constant density) km s^{-1} for an optically-thin spherical emitter. It is clear, however, that most of these differences are too subtle relative to the sensitivity of our data and the simplicity of the model. The key takeaway from this discussion is that the δV fit-parameter in the R_{CE}-model (as constructed in Section 4.6.1) under-estimates the δV_{CE} physical quantity by $\sim 50 - 70\%$ in the case of solid emitters, while it is representative of the half-light radius in optically-thin emitters.

BIBLIOGRAPHY

BIBLIOGRAPHY

Abbott, B. P., et al. (2016), Observation of Gravitational Waves from a Binary Black Hole Merger, *Phys. Rev. Lett.*, *116*(6), 061102, doi:10.1103/PhysRevLett.116.061102.

Abe, Y., Y. Fukazawa, A. Kubota, D. Kasama, and K. Makishima (2005), Three Spectral States of the Disk X-Ray Emission of the Black-Hole Candidate 4U 1630- 47, *PASJ*, *57*, 629–641, doi:10.1093/pasj/57.4.629.

Armas Padilla, M., Y. Ueda, T. Hori, M. Shidatsu, and T. Muñoz-Darias (2017), Suzaku spectroscopy of the neutron star transient 4U 1608-52 during its outburst decay., *MNRAS*, *467*(1), 290–297, doi:10.1093/mnras/stx020.

Armitage, P. J. (2011), Dynamics of Protoplanetary Disks, *ARA&A*, *49*(1), 195–236, doi:10.1146/annurev-astro-081710-102521.

Atri, P., et al. (2019), Potential kick velocity distribution of black hole X-ray binaries and implications for natal kicks, *MNRAS*, *489*(3), 3116–3134, doi:10.1093/mnras/stz2335.

Augusteijn, T., E. Kuulkers, and M. H. van Kerkwijk (2001), The IR counterpart of the black-hole candidate 4U 1630-47, *A&A*, *375*, 447–454, doi:10.1051/0004-6361:20010855.

Bai, X.-N., J. Ye, J. Goodman, and F. Yuan (2016), Magneto-thermal Disk Winds from Protoplanetary Disks, *ApJ*, *818*(2), 152, doi:10.3847/0004-637X/818/2/152.

Balbus, S. A., and J. F. Hawley (1991), A Powerful Local Shear Instability in Weakly Magnetized Disks. I. Linear Analysis, *ApJ*, *376*, 214, doi:10.1086/170270.

Barcons, X., et al. (2017), Athena: ESA's X-ray observatory for the late 2020s, *Astronomische Nachrichten*, *338*(153), 153–158, doi:10.1002/asna.201713323.

Begelman, M. C., C. F. McKee, and G. A. Shields (1983), Compton heated winds and coronae above accretion disks. I. Dynamics., *ApJ*, *271*, 70–88, doi:10.1086/161178.

Bianchi, S., G. Ponti, T. Muñoz-Darias, and P.-O. Petrucci (2017), Photoionization instability of the Fe K absorbing plasma in the neutron star transient AX J1745.6-2901, *MNRAS*, *472*(2), 2454–2461, doi:10.1093/mnras/stx2173.

Blaes, O. M., S. W. Davis, S. Hirose, J. H. Krolik, and J. M. Stone (2006), Magnetic Pressure Support and Accretion Disk Spectra, *ApJ*, *645*(2), 1402–1407, doi:10.1086/503741.

Blandford, R. D., and D. G. Payne (1982), Hydromagnetic flows from accretion disks and the production of radio jets., *MNRAS*, *199*, 883–903, doi:10.1093/mnras/199.4.883.

Boirin, L., A. N. Parmar, D. Barret, S. Paltani, and J. E. Grindlay (2004), Discovery of X-ray absorption features from the dipping low-mass X-ray binary XB 1916-053 with XMM-Newton, *A&A*, *418*, 1061–1072, doi:10.1051/0004-6361:20034550.

Brenneman, L. W., and C. S. Reynolds (2006), Constraining Black Hole Spin via X-Ray Spectroscopy, *ApJ*, *652*(2), 1028–1043, doi:10.1086/508146.

Calvet, N., L. Hartmann, and S. J. Kenyon (1993), Mass Loss from Pre–Main-Sequence Accretion Disks. I. The Accelerating Wind of FU Orionis, *ApJ*, *402*, 623, doi:10.1086/172164.

Capitanio, F., R. Campana, G. De Cesare, and C. Ferrigno (2015), Missing hard states and regular outbursts: the puzzling case of the black hole candidate 4U 1630-472, *MNRAS*, *450*(4), 3840–3854, doi:10.1093/mnras/stv687.

Cash, W. (1979), Parameter estimation in astronomy through application of the likelihood ratio., *ApJ*, *228*, 939–947, doi:10.1086/156922.

Chakravorty, S., J. C. Lee, and J. Neilsen (2013), The effects of thermodynamic stability on wind properties in different low-mass black hole binary states, *MNRAS*, *436*(1), 560–569, doi:10.1093/mnras/stt1593.

Chakravorty, S., et al. (2016), Absorption lines from magnetically driven winds in X-ray binaries, *A&A*, *589*, A119, doi:10.1051/0004-6361/201527163.

Dannen, R. C., D. Proga, T. Waters, and S. Dyda (2020), Clumpy AGN Outflows due to Thermal Instability, *ApJ*, *893*(2), L34, doi:10.3847/2041-8213/ab87a5.

Dauser, T., J. Garcia, J. Wilms, M. Böck, L. W. Brenneman, M. Falanga, K. Fukumura, and C. S. Reynolds (2013), Irradiation of an accretion disc by a jet: general properties and implications for spin measurements of black holes, *MNRAS*, *430*(3), 1694–1708, doi:10.1093/mnras/sts710.

Davis, S. W., C. Done, and O. M. Blaes (2006), Testing Accretion Disk Theory in Black Hole X-Ray Binaries, *ApJ*, *647*(1), 525–538, doi:10.1086/505386.

Díaz Trigo, M., A. N. Parmar, L. Boirin, M. Méndez, and J. S. Kaastra (2006), Spectral changes during dipping in low-mass X-ray binaries due to highly-ionized absorbers, *A&A*, *445*(1), 179–195, doi:10.1051/0004-6361:20053586.

Díaz Trigo, M., S. Migliari, J. C. A. Miller-Jones, and M. Guainazzi (2014), XMM-Newton observations reveal the disappearance of the wind in 4U 1630-47, *A&A*, *571*, A76, doi:10.1051/0004-6361/201424554.

Done, C., M. Gierliński, and A. Kubota (2007), Modelling the behaviour of accretion flows in X-ray binaries. Everything you always wanted to know about accretion but were afraid to ask, *A&A Rev.*, *15*(1), 1–66, doi:10.1007/s00159-007-0006-1.

Done, C., R. Tomaru, and T. Takahashi (2018), Thermal winds in stellar mass black hole and neutron star binary systems, *MNRAS*, *473*(1), 838–848, doi:10.1093/mnras/stx2400.

Draghis, P. A., J. M. Miller, E. M. Cackett, E. S. Kammoun, M. T. Reynolds, J. A. Tomsick, and A. Zoghbi (2020), A New Spin on an Old Black Hole: NuSTAR Spectroscopy of EXO 1846-031, *ApJ*, *900*(1), 78, doi:10.3847/1538-4357/aba2ec.

Drew, J. E., and D. Proga (2000), Radiation-driven accretion disk winds, *NEwA Rev*, *44*(1-2), 21–26, doi:10.1016/S1387-6473(00)00007-5.

Fabian, A. C. (2012), Observational Evidence of Active Galactic Nuclei Feedback, *ARA&A*, *50*, 455–489, doi:10.1146/annurev-astro-081811-125521.

Fabian, A. C., M. J. Rees, L. Stella, and N. E. White (1989), X-ray fluorescence from the inner disc in Cygnus X-1., *MNRAS*, *238*, 729–736, doi:10.1093/mnras/238.3.729.

Fabian, A. C., A. Lohfink, E. Kara, M. L. Parker, R. Vasudevan, and C. S. Reynolds (2015), Properties of AGN coronae in the NuSTAR era, *MNRAS*, *451*(4), 4375–4383, doi:10.1093/mnras/stv1218.

Fabian, A. C., A. Lohfink, R. Belmont, J. Malzac, and P. Coppi (2017), Properties of AGN coronae in the NuSTAR era - II. Hybrid plasma, *MNRAS*, *467*(3), 2566–2570, doi:10.1093/mnras/stx221.

Falcke, H., E. Körding, and S. Markoff (2004), A scheme to unify low-power accreting black holes. Jet-dominated accretion flows and the radio/X-ray correlation, *A&A*, *414*, 895–903, doi:10.1051/0004-6361:20031683.

Falcon, R. E., D. E. Winget, M. H. Montgomery, and K. A. Williams (2010), A Gravitational Redshift Determination of the Mean Mass of White Dwarfs. DA Stars, *ApJ*, *712*(1), 585–595, doi:10.1088/0004-637X/712/1/585.

Fender, R. P., T. M. Belloni, and E. Gallo (2004), Towards a unified model for black hole X-ray binary jets, *MNRAS*, *355*(4), 1105–1118, doi:10.1111/j.1365-2966.2004.08384.x.

Ferland, G. J., et al. (2017), The 2017 Release Cloudy, *RMxAA*, *53*, 385–438.

Foreman-Mackey, D., D. W. Hogg, D. Lang, and J. Goodman (2013), emcee: The MCMC Hammer, *PASP*, *125*(925), 306, doi:10.1086/670067.

Fukumura, K., D. Kazanas, I. Contopoulos, and E. Behar (2010), Magnetohydrodynamic Accretion Disk Winds as X-ray Absorbers in Active Galactic Nuclei, *ApJ*, *715*(1), 636–650, doi:10.1088/0004-637X/715/1/636.

Fukumura, K., F. Tombesi, D. Kazanas, C. Shrader, E. Behar, and I. Contopoulos (2015), Magnetically Driven Accretion Disk Winds and Ultra-fast Outflows in PG 1211+143, *ApJ*, *805*(1), 17, doi:10.1088/0004-637X/805/1/17.

Fukumura, K., D. Kazanas, C. Shrader, E. Behar, F. Tombesi, and I. Contopoulos (2017), Magnetic origin of black hole winds across the mass scale, *Nature Astronomy*, *1*, 0062, doi:10.1038/s41550-017-0062.

Gallo, E., R. P. Fender, and G. G. Pooley (2003), A universal radio-X-ray correlation in low/hard state black hole binaries, *MNRAS*, *344*(1), 60–72, doi:10.1046/j.1365-8711.2003.06791.x.

Gallo, L. C., et al. (2015), Suzaku observations of Mrk 335: confronting partial covering and relativistic reflection, *MNRAS*, *446*(1), 633–650, doi:10.1093/mnras/stu2108.

Galloway, D. K., and L. Keek (2021), Thermonuclear X-ray Bursts, in *Astrophysics and Space Science Library*, *Astrophysics and Space Science Library*, vol. 461, edited by T. M. Belloni, M. Méndez, and C. Zhang, pp. 209–262, doi:10.1007/978-3-662-62110-3_5.

Galloway, D. K., D. Chakrabarty, M. P. Muno, and P. Savov (2001), Discovery of a 270 Hertz X-Ray Burst Oscillation in the X-Ray Dipper 4U 1916-053, *ApJ*, *549*(1), L85–L88, doi:10.1086/319134.

Galloway, D. K., M. P. Muno, J. M. Hartman, D. Psaltis, and D. Chakrabarty (2008), Thermonuclear (Type I) X-Ray Bursts Observed by the Rossi X-Ray Timing Explorer, *ApJS*, *179*(2), 360–422, doi:10.1086/592044.

Gambino, A. F., R. Iaria, T. Di Salvo, S. M. Mazzola, A. Marino, L. Burderi, A. Riggio, A. Sanna, and N. D'Amico (2019), Spectral analysis of the dipping LMXB system XB 1916-053, *A&A*, *625*, A92, doi:10.1051/0004-6361/201832984.

Gammie, C. F. (1996), Layered Accretion in T Tauri Disks, *ApJ*, *457*, 355, doi:10.1086/176735.

García, J. A., A. C. Fabian, T. R. Kallman, T. Dauser, M. L. Parker, J. E. McClintock, J. F. Steiner, and J. Wilms (2016), The effects of high density on the X-ray spectrum reflected from accretion discs around black holes, *MNRAS*, *462*(1), 751–760, doi:10.1093/mnras/stw1696.

Gatuzz, E., M. Díaz Trigo, J. C. A. Miller-Jones, and S. Migliari (2019), Chandra high-resolution spectra of 4U 1630-47: the disappearance of the wind, *MNRAS*, *482*(2), 2597–2611, doi:10.1093/mnras/sty2850.

Gavriil, F. P., T. E. Strohmayer, and S. Bhattacharyya (2012), An Fe XXIV Absorption Line in the Persistent Spectrum of the Dipping Low-mass X-Ray Binary 1A 1744-361, *ApJ*, *753*(1), 2, doi:10.1088/0004-637X/753/1/2.

George, I. M., and A. C. Fabian (1991), X-ray reflection from cold matter in Active Galactic Nuclei and X-ray binaries., *MNRAS*, *249*, 352, doi:10.1093/mnras/249.2.352.

Gierliński, M., and C. Done (2004), Black hole accretion discs: reality confronts theory, *MNRAS*, *347*(3), 885–894, doi:10.1111/j.1365-2966.2004.07266.x.

Gonzalez, A. G., D. R. Wilkins, and L. C. Gallo (2017), Probing the geometry and motion of AGN coronae through accretion disc emissivity profiles, *MNRAS*, *472*(2), 1932–1945, doi:10.1093/mnras/stx2080.

Gou, L., J. E. McClintock, R. A. Remillard, J. F. Steiner, M. J. Reid, J. A. Orosz, R. Narayan, M. Hanke, and J. García (2014), Confirmation via the Continuum-fitting Method that the Spin of the Black Hole in Cygnus X-1 Is Extreme, *ApJ*, *790*(1), 29, doi:10.1088/0004-637X/790/1/29.

Grinberg, V., et al. (2015), Long term variability of Cygnus X-1. VII. Orbital variability of the focussed wind in Cyg X-1/HDE 226868 system, *A&A*, *576*, A117, doi:10.1051/0004-6361/201425418.

Grinberg, V., et al. (2017), The clumpy absorber in the high-mass X-ray binary Vela X-1, *A&A*, *608*, A143, doi:10.1051/0004-6361/201731843.

Hanke, M., J. Wilms, M. A. Nowak, K. Pottschmidt, N. S. Schulz, and J. C. Lee (2009), Chandra X-Ray Spectroscopy of the Focused Wind in the Cygnus X-1 System. I. The Nondip Spectrum in the Low/Hard State, *ApJ*, *690*(1), 330–346, doi:10.1088/0004-637X/690/1/330.

Harrison, R. E., et al. (2021), ALMA CN Zeeman Observations of AS 209: Limits on Magnetic Field Strength and Magnetically Driven Accretion Rate, *ApJ*, *908*(2), 141, doi:10.3847/1538-4357/abd94e.

Hartmann, L., and S. J. Kenyon (1996), The FU Orionis Phenomenon, *ARA&A*, *34*, 207–240, doi:10.1146/annurev.astro.34.1.207.

Hartmann, L., N. Calvet, E. Gullbring, and P. D'Alessio (1998), Accretion and the Evolution of T Tauri Disks, *ApJ*, *495*(1), 385–400, doi:10.1086/305277.

Hasinger, G., and M. van der Klis (1989), Two patterns of correlated X-ray timing and spectral behaviour in low-mass X-ray binaries., *A&A*, *225*, 79–96.

Hawley, J. F., C. F. Gammie, and S. A. Balbus (1995), Local Three-dimensional Magneto-hydrodynamic Simulations of Accretion Disks, *ApJ*, *440*, 742, doi:10.1086/175311.

Hawley, J. F., C. F. Gammie, and S. A. Balbus (1996), Local Three-dimensional Simulations of an Accretion Disk Hydromagnetic Dynamo, *ApJ*, *464*, 690, doi:10.1086/177356.

Heinke, C. O., N. Ivanova, M. C. Engel, K. Pavlovskii, G. R. Sivakoff, T. F. Cartwright, and J. C. Gladstone (2013), Galactic Ultracompact X-Ray Binaries: Disk Stability and Evolution, *ApJ*, *768*(2), 184, doi:10.1088/0004-637X/768/2/184.

HI4PI Collaboration, et al. (2016), HI4PI: A full-sky H I survey based on EBHIS and GASS, *A&A*, *594*, A116, doi:10.1051/0004-6361/201629178.

Higginbottom, N., and D. Proga (2015), Coronae and Winds from Irradiated Disks in X-Ray Binaries, *ApJ*, *807*(1), 107, doi:10.1088/0004-637X/807/1/107.

Higginbottom, N., D. Proga, C. Knigge, and K. S. Long (2017), Thermal Disk Winds in X-Ray Binaries: Realistic Heating and Cooling Rates Give Rise to Slow, but Massive, Outflows, *ApJ*, *836*(1), 42, doi:10.3847/1538-4357/836/1/42.

Hueso, R., and T. Guillot (2005), Evolution of protoplanetary disks: constraints from DM Tauri and GM Aurigae, *A&A*, *442*(2), 703–725, doi:10.1051/0004-6361:20041905.

Hung, D. M. H., E. G. Blackman, K. J. Caspary, E. P. Gilson, and H. Ji (2019), Experimental confirmation of the standard magnetorotational instability mechanism with a spring-mass analogue, *Communications Physics*, *2*(1), 7, doi:10.1038/s42005-018-0103-7.

Iaria, R., et al. (2015), Signature of the presence of a third body orbiting around XB 1916-053, *A&A*, *582*, A32, doi:10.1051/0004-6361/201526500.

Ishibashi, K., D. Dewey, D. P. Huenemoerder, and P. Testa (2006), Chandra/HETGS Observations of the Capella System: The Primary as a Dominating X-Ray Source, *ApJ*, *644*(2), L117–L120, doi:10.1086/505702.

Jain, C., and B. Paul (2011), Eclipse timings of the LMXB XTE J1710-281: orbital period glitches, *MNRAS*, *413*(1), 2–6, doi:10.1111/j.1365-2966.2010.18110.x.

Jimenez-Garate, M. A., J. C. Raymond, and D. A. Liedahl (2002), The Structure and X-Ray Recombination Emission of a Centrally Illuminated Accretion Disk Atmosphere and Corona, *ApJ*, *581*(2), 1297–1327, doi:10.1086/344364.

Jin, C., G. Ponti, F. Haberl, and R. Smith (2017), Probing the interstellar dust towards the Galactic Centre: dust-scattering halo around AX J1745.6-2901, *MNRAS*, *468*(3), 2532–2551, doi:10.1093/mnras/stx653.

Jin, C., G. Ponti, F. Haberl, R. Smith, and L. Valencic (2018), Effects of interstellar dust scattering on the X-ray eclipses of the LMXB AX J1745.6-2901 in the Galactic Centre, *MNRAS*, *477*(3), 3480–3506, doi:10.1093/mnras/sty869.

Jonker, P. G., and G. Nelemans (2004), The distances to Galactic low-mass X-ray binaries: consequences for black hole luminosities and kicks, *MNRAS*, *354*(2), 355–366, doi:10.1111/j.1365-2966.2004.08193.x.

Joss, P. C. (1978), Helium-burning flashes on an accreting neutron star: a model for X-ray burst sources., *ApJ*, *225*, L123–L127, doi:10.1086/182808.

Juett, A. M., and D. Chakrabarty (2006), Detection of Highly Ionized Metal Absorption Lines in the Ultracompact X-Ray Dipper 4U 1916-05, *ApJ*, *646*(1), 493–498, doi:10.1086/504863.

Kaastra, J. S., and J. A. M. Bleeker (2016), Optimal binning of X-ray spectra and response matrix design, *A&A*, *587*, A151, doi:10.1051/0004-6361/201527395.

Kaastra, J. S., R. Mewe, and H. Nieuwenhuijzen (1996), SPEX: a new code for spectral analysis of X & UV spectra., in *UV and X-ray Spectroscopy of Astrophysical and Laboratory Plasmas*, pp. 411–414.

Kaastra, J. S., A. J. J. Raassen, J. de Plaa, and L. Gu (2018), SPEX X-ray spectral fitting package, Zenodo, doi:10.5281/zenodo.2419563.

Kallman, T., and M. Bautista (2001), Photoionization and High-Density Gas, *ApJS*, *133*(1), 221–253, doi:10.1086/319184.

Kallman, T., and A. Dorodnitsyn (2019), Warm Absorber Diagnostics of AGN Dynamics, *ApJ*, *884*(2), 111, doi:10.3847/1538-4357/ab40aa.

Kallman, T. R., M. A. Bautista, S. Goriely, C. Mendoza, J. M. Miller, P. Palmeri, P. Quinet, and J. Raymond (2009), Spectrum Synthesis Modeling of the X-Ray Spectrum of GRO J1655-40 Taken During the 2005 Outburst, *ApJ*, *701*(2), 865–884, doi:10.1088/0004-637X/701/2/865.

King, A. L., J. M. Miller, J. Raymond, A. C. Fabian, C. S. Reynolds, T. R. Kallman, D. Maitra, E. M. Cackett, and M. P. Rupen (2012), An Extreme X-Ray Disk Wind in the Black Hole Candidate IGR J17091-3624, *ApJ*, *746*(2), L20, doi:10.1088/2041-8205/746/2/L20.

King, A. L., J. M. Miller, J. Raymond, M. T. Reynolds, and W. Morningstar (2015), High-resolution Chandra HETG Spectroscopy of V404 Cygni in Outburst, *ApJ*, *813*(2), L37, doi:10.1088/2041-8205/813/2/L37.

King, A. L., A. Lohfink, and E. Kara (2017), AGN Coronae through a Jet Perspective, *ApJ*, *835*(2), 226, doi:10.3847/1538-4357/835/2/226.

King, A. L., et al. (2013), Regulation of Black Hole Winds and Jets across the Mass Scale, *ApJ*, *762*(2), 103, doi:10.1088/0004-637X/762/2/103.

King, A. L., et al. (2014), The Disk Wind in the Rapidly Spinning Stellar-mass Black Hole 4U 1630-472 Observed with NuSTAR, *ApJ*, *784*(1), L2, doi:10.1088/2041-8205/784/1/L2.

King, A. R., J. E. Pringle, and M. Livio (2007), Accretion disc viscosity: how big is alpha?, *MNRAS*, *376*(4), 1740–1746, doi:10.1111/j.1365-2966.2007.11556.x.

Kubota, A., and K. Makishima (2004), The Three Spectral Regimes Found in the Stellar Black Hole XTE J1550-564 in Its High/Soft State, *ApJ*, *601*(1), 428–438, doi:10.1086/380433.

Kubota, A., K. Makishima, and K. Ebisawa (2001), Observational Evidence for Strong Disk Comptonization in GRO J1655-40, *ApJ*, *560*(2), L147–L150, doi:10.1086/324377.

Lee, J. C., C. S. Reynolds, R. Remillard, N. S. Schulz, E. G. Blackman, and A. C. Fabian (2002), High-Resolution Chandra HETGS and Rossi X-Ray Timing Explorer Observations of GRS 1915+105: A Hot Disk Atmosphere and Cold Gas Enriched in Iron and Silicon, *ApJ*, *567*(2), 1102–1111, doi:10.1086/338588.

Li, L.-X., E. R. Zimmerman, R. Narayan, and J. E. McClintock (2005), Multitemperature Blackbody Spectrum of a Thin Accretion Disk around a Kerr Black Hole: Model Computations and Comparison with Observations, *ApJS*, *157*(2), 335–370, doi:10.1086/428089.

Ludlam, R. M., et al. (2019), NuSTAR Observations of the Accreting Atolls GX 3+1, 4U 1702-429, 4U 0614+091, and 4U 1746-371, *ApJ*, *873*(1), 99, doi:10.3847/1538-4357/ab0414.

Luketic, S., D. Proga, T. R. Kallman, J. C. Raymond, and J. M. Miller (2010), On the Properties of Thermal Disk Winds in X-ray Transient Sources: A Case Study of GRO J1655-40, *ApJ*, *719*(1), 515–522, doi:10.1088/0004-637X/719/1/515.

Lynden-Bell, D. (1969), Galactic Nuclei as Collapsed Old Quasars, *Nature*, *223*(5207), 690–694, doi:10.1038/223690a0.

Maeda, Y., K. Koyama, M. Sakano, T. Takeshima, and S. Yamauchi (1996), A New Eclipsing X-Ray Burster near the Galactic Center: A Quiescent State of the Old Transient A1742-289, *PASJ*, *48*, 417–423, doi:10.1093/pasj/48.3.417.

Markwardt, C. B., J. H. Swank, and T. E. Strohmayer (2001), Discovery of the Orbital Period of the Bursting and Dipping Source XTE J1710-281, in *American Astronomical Society Meeting Abstracts*, *American Astronomical Society Meeting Abstracts*, vol. 199, p. 27.04.

Marshall, H. L., D. Dewey, and K. Ishibashi (2004), In-flight calibration of the Chandra high-energy transmission grating spectrometer, in *X-Ray and Gamma-Ray Instrumentation for Astronomy XIII*, *Society of Photo-Optical Instrumentation Engineers (SPIE) Conference Series*, vol. 5165, edited by K. A. Flanagan and O. H. W. Siegmund, pp. 457–468, doi:10.1117/12.508320.

Mata Sánchez, D., A. Rau, A. Álvarez Hernández, T. F. J. van Grunsven, M. A. P. Torres, and P. G. Jonker (2021), Dynamical confirmation of a stellar mass black hole in the transient X-ray dipping binary MAXI J1305-704, *MNRAS*, *506*(1), 581–594, doi:10.1093/mnras/stab1714.

McClintock, J. E., R. A. Remillard, M. P. Rupen, M. A. P. Torres, D. Steeghs, A. M. Levine, and J. A. Orosz (2009), The 2003 Outburst of the X-Ray Transient H1743-322: Comparisons with the Black Hole Microquasar XTE J1550-564, *ApJ*, *698*(2), 1398–1421, doi:10.1088/0004-637X/698/2/1398.

McClintock, J. E., R. Narayan, and J. F. Steiner (2014), Black Hole Spin via Continuum Fitting and the Role of Spin in Powering Transient Jets, *Space Sci. Rev.*, *183*(1-4), 295–322, doi:10.1007/s11214-013-0003-9.

Mehdipour, M., J. S. Kaastra, and T. Kallman (2016), Systematic comparison of photoionised plasma codes with application to spectroscopic studies of AGN in X-rays, *A&A*, *596*, A65, doi:10.1051/0004-6361/201628721.

Mehdipour, M., et al. (2018), Multi-wavelength campaign on NGC 7469. III. Spectral energy distribution and the AGN wind photoionisation modelling, plus detection of diffuse X-rays from the starburst with Chandra HETGS, *A&A*, *615*, A72, doi:10.1051/0004-6361/201832604.

Merloni, A., and A. C. Fabian (2001), Accretion disc coronae as magnetic reservoirs, *MNRAS*, *321*(3), 549–552, doi:10.1046/j.1365-8711.2001.04060.x.

Miller, J. (2017), Accretion physics: It's not U, it's B, *Nature Astronomy*, *1*, 0070, doi:10.1038/s41550-017-0070.

Miller, J., R. Wijnands, P. Wojdowski, P. Groot, A. Fabian, M. van der Klis, and W. Lewin (2002), X-ray Absorption Lines in the Galactic Black Hole Candidate XTE J1650-500, *The Astronomer's Telegram*, *81*, 1.

Miller, J. M., J. Raymond, A. C. Fabian, R. Wijnands, M. van der Klis, and W. H. G. Lewin (2004a), Variability in the X-ray Warm Absorber in GX 339-4, *The Astronomer's Telegram*, *221*, 1.

Miller, J. M., J. Raymond, A. Fabian, D. Steeghs, J. Homan, C. Reynolds, M. van der Klis, and R. Wijnands (2006a), The magnetic nature of disk accretion onto black holes, *Nature*, *441*(7096), 953–955, doi:10.1038/nature04912.

Miller, J. M., J. Raymond, C. S. Reynolds, A. C. Fabian, T. R. Kallman, and J. Homan (2008), The Accretion Disk Wind in the Black Hole GRO J1655-40, *ApJ*, *680*(2), 1359–1377, doi:10.1086/588521.

Miller, J. M., C. S. Reynolds, A. C. Fabian, G. Miniutti, and L. C. Gallo (2009), Stellar-Mass Black Hole Spin Constraints from Disk Reflection and Continuum Modeling, *ApJ*, *697*(1), 900–912, doi:10.1088/0004-637X/697/1/900.

Miller, J. M., J. Raymond, A. C. Fabian, C. S. Reynolds, A. L. King, T. R. Kallman, E. M. Cackett, M. van der Klis, and D. T. H. Steeghs (2012), The Disk-wind-Jet Connection in the Black Hole H 1743-322, *ApJ*, *759*(1), L6, doi:10.1088/2041-8205/759/1/L6.

Miller, J. M., A. C. Fabian, J. Kaastra, T. Kallman, A. L. King, D. Proga, J. Raymond, and C. S. Reynolds (2015a), Powerful, Rotating Disk Winds from Stellar-mass Black Holes, *ApJ*, *814*(2), 87, doi:10.1088/0004-637X/814/2/87.

Miller, J. M., et al. (2004b), Chandra/High Energy Transmission Grating Spectrometer Spectroscopy of the Galactic Black Hole GX 339-4: A Relativistic Iron Emission Line and Evidence for a Seyfert-like Warm Absorber, *ApJ*, *601*(1), 450–465, doi:10.1086/380196.

Miller, J. M., et al. (2006b), Simultaneous Chandra and RXTE Spectroscopy of the Microquasar H1743-322: Clues to Disk Wind and Jet Formation from a Variable Ionized Outflow, *ApJ*, *646*(1), 394–406, doi:10.1086/504673.

Miller, J. M., et al. (2014), Chandra Spectroscopy of MAXI J1305-704: Detection of an Infalling Black Hole Disk Wind?, *ApJ*, *788*(1), 53, doi:10.1088/0004-637X/788/1/53.

Miller, J. M., et al. (2015b), New Constraints on the Black Hole Low/Hard State Inner Accretion Flow with NuSTAR, *ApJ*, *799*(1), L6, doi:10.1088/2041-8205/799/1/L6.

Miller, J. M., et al. (2016), The Accretion Disk Wind in the Black Hole GRS 1915+105, *ApJ*, *821*(1), L9, doi:10.3847/2041-8205/821/1/L9.

Miller, J. M., et al. (2020), An Obscured, Seyfert 2-like State of the Stellar-mass Black Hole GRS 1915+105 Caused by Failed Disk Winds, *ApJ*, *904*(1), 30, doi:10.3847/1538-4357/abbb31.

Miller, M. C., and J. M. Miller (2015), The masses and spins of neutron stars and stellar-mass black holes, *Phys. Rep.*, *548*, 1–34, doi:10.1016/j.physrep.2014.09.003.

Mitsuda, K., et al. (1984), Energy spectra of low-mass binary X-ray sources observed from Tenma., *PASJ*, *36*, 741–759.

Miškovičová, I., et al. (2016), Chandra X-ray spectroscopy of focused wind in the Cygnus X-1 system. II. The non-dip spectrum in the low/hard state - modulations with orbital phase, *A&A*, *590*, A114, doi:10.1051/0004-6361/201322490.

Mondal, A. S., G. C. Dewangan, and B. Raychaudhuri (2020), On the disc reflection spectroscopy of NS LMXB Serpens X-1: analysis of a recent NuSTAR observation, *MNRAS*, *494*(3), 3177–3185, doi:10.1093/mnras/staa1001.

Mondal, A. S., B. Raychaudhuri, and G. C. Dewangan (2021), Evidence of disc reflection in the X-ray spectrum of the neutron star low-mass X-ray binary 4U 1636-536, *MNRAS*, *504*(1), 1331–1339, doi:10.1093/mnras/stab921.

Morgan, C. W., C. S. Kochanek, X. Dai, N. D. Morgan, and E. E. Falco (2008), X-Ray and Optical Microlensing in the Lensed Quasar PG 1115+080, *ApJ*, *689*(2), 755–761, doi:10.1086/592767.

Morrison, R., and D. McCammon (1983), Interstellar photoelectric absorption cross sections, 0.03-10 keV., *ApJ*, *270*, 119–122, doi:10.1086/161102.

Mościbrodzka, M., and D. Proga (2013), Thermal and Dynamical Properties of Gas Accreting onto a Supermassive Black Hole in an Active Galactic Nucleus, *ApJ*, *767*(2), 156, doi:10.1088/0004-637X/767/2/156.

Mossoux, E., and N. Grosso (2017), Sixteen years of X-ray monitoring of Sagittarius A*: Evidence for a decay of the faint flaring rate from 2013 August, 13 months before a rise in the bright flaring rate, *A&A*, *604*, A85, doi:10.1051/0004-6361/201629778.

Muñoz-Darias, T., R. P. Fender, S. E. Motta, and T. M. Belloni (2014), Black hole-like hysteresis and accretion states in neutron star low-mass X-ray binaries, *MNRAS*, *443*(4), 3270–3283, doi:10.1093/mnras/stu1334.

Neilsen, J., and J. Homan (2012), A Hybrid Magnetically/Thermally Driven Wind in the Black Hole GRO J1655-40?, *ApJ*, *750*(1), 27, doi:10.1088/0004-637X/750/1/27.

Neilsen, J., and J. C. Lee (2009), Accretion disk winds as the jet suppression mechanism in the microquasar GRS 1915+105, *Nature*, *458*(7237), 481–484, doi:10.1038/nature07680.

Neilsen, J., M. Coriat, R. Fender, J. C. Lee, G. Ponti, A. K. Tzioumis, P. G. Edwards, and J. W. Broderick (2014), A Link between X-Ray Emission Lines and Radio Jets in 4U 1630-47?, *ApJ*, *784*(1), L5, doi:10.1088/2041-8205/784/1/L5.

Neilsen, J., et al. (2019), A Bright Flare from GRS 1915+105 with NICER, *The Astronomer's Telegram*, *12793*, 1.

Nelemans, G., P. G. Jonker, and D. Steeghs (2006), Optical spectroscopy of (candidate) ultracompact X-ray binaries: constraints on the composition of the donor stars, *MNRAS*, *370*(1), 255–262, doi:10.1111/j.1365-2966.2006.10496.x.

Novikov, I. D., and K. S. Thorne (1973), Astrophysics of black holes., in *Black Holes (Les Astres Occlus)*, pp. 343–450.

Paczyński, B. (1967), Gravitational Waves and the Evolution of Close Binaries, *AcA*, *17*, 287.

Pasetto, S., et al. (2012), Thick disk kinematics from RAVE and the solar motion, *A&A*, *547*, A70, doi:10.1051/0004-6361/201219464.

Ponti, G., R. P. Fender, M. C. Begelman, R. J. H. Dunn, J. Neilsen, and M. Coriat (2012), Ubiquitous equatorial accretion disc winds in black hole soft states, *MNRAS*, *422*(1), L11–L15, doi:10.1111/j.1745-3933.2012.01224.x.

Ponti, G., T. Muñoz-Darias, and R. P. Fender (2014), A connection between accretion state and Fe K absorption in an accreting neutron star: black hole-like soft-state winds?, *MNRAS*, *444*(2), 1829–1834, doi:10.1093/mnras/stu1742.

Ponti, G., K. De, T. Muñoz-Darias, L. Stella, and K. Nandra (2017), The puzzling orbital period evolution of the LMXB AX J1745.6-2901, *MNRAS*, *464*(1), 840–849, doi:10.1093/mnras/stw2317.

Ponti, G., S. Bianchi, T. Muñoz-Darias, and K. Nandra (2018a), Measuring masses in low mass X-ray binaries via X-ray spectroscopy: the case of MXB 1659-298, *MNRAS*, *481*(1), L94–L99, doi:10.1093/mnrasl/sly120.

Ponti, G., et al. (2018b), NuSTAR + XMM-Newton monitoring of the neutron star transient AX J1745.6-2901, *MNRAS*, *473*(2), 2304–2323, doi:10.1093/mnras/stx2425.

Pounds, K. A., and J. N. Reeves (2009), Quantifying the fast outflow in the luminous Seyfert galaxy PG1211+143, *MNRAS*, *397*(1), 249–257, doi:10.1111/j.1365-2966.2009.14971.x.

Proga, D. (2000), Winds from Accretion Disks Driven by Radiation and Magnetocentrifugal Force, *ApJ*, *538*(2), 684–690, doi:10.1086/309154.

Proga, D. (2003), Numerical Simulations of Mass Outflows Driven from Accretion Disks by Radiation and Magnetic Forces, *ApJ*, *585*(1), 406–417, doi:10.1086/345897.

Proga, D., and T. R. Kallman (2002), On the Role of the Ultraviolet and X-Ray Radiation in Driving a Disk Wind in X-Ray Binaries, *ApJ*, *565*(1), 455–470, doi:10.1086/324534.

Proga, D., J. M. Stone, and T. R. Kallman (2000), Dynamics of Line-driven Disk Winds in Active Galactic Nuclei, *ApJ*, *543*(2), 686–696, doi:10.1086/317154.

Raman, G., C. Maitra, and B. Paul (2018), Observation of variable pre-eclipse dips and disc windsin the eclipsing LMXB XTE J1710-281, *MNRAS*, *477*(4), 5358–5366, doi:10.1093/mnras/sty918.

Rees, M. J. (1984), Black Hole Models for Active Galactic Nuclei, *ARA&A*, *22*, 471–506, doi:10.1146/annurev.aa.22.090184.002351.

Reeves, J., C. Done, K. Pounds, Y. Terashima, K. Hayashida, N. Anabuki, M. Uchino, and M. Turner (2008), On why the iron K-shell absorption in AGN is not a signature of the local warm/hot intergalactic medium, *MNRAS*, *385*(1), L108–L112, doi:10.1111/j.1745-3933.2008.00443.x.

Reeves, J. N., V. Braito, E. Nardini, F. Hamann, G. Chartas, A. P. Lobban, P. T. O'Brien, and T. J. Turner (2018), Resolving the X-Ray Obscuration in a Low-flux Observation of the Quasar PDS 456, *ApJ*, *867*(1), 38, doi:10.3847/1538-4357/aae30c.

Reeves, J. N., et al. (2009), A Compton-thick Wind in the High-luminosity Quasar, PDS 456, *ApJ*, *701*(1), 493–507, doi:10.1088/0004-637X/701/1/493.

Reis, R. C., and J. M. Miller (2013), On the Size and Location of the X-Ray Emitting Coronae around Black Holes, *ApJ*, *769*(1), L7, doi:10.1088/2041-8205/769/1/L7.

Remillard, R. A., and J. E. McClintock (2006), X-Ray Properties of Black-Hole Binaries, *ARA&A*, *44*(1), 49–92, doi:10.1146/annurev.astro.44.051905.092532.

Reynolds, C. S. (2014), Measuring Black Hole Spin Using X-Ray Reflection Spectroscopy, *Space Sci. Rev.*, *183*(1-4), 277–294, doi:10.1007/s11214-013-0006-6.

Reynolds, C. S. (2019), Observing black holes spin, *Nature Astronomy*, *3*, 41–47, doi:10.1038/s41550-018-0665-z.

Reynolds, C. S. (2021), Observational Constraints on Black Hole Spin, *ARA&A*, *59*, doi:10.1146/annurev-astro-112420-035022.

Reynolds, C. S., L. W. Brenneman, A. M. Lohfink, M. L. Trippe, J. M. Miller, A. C. Fabian, and M. A. Nowak (2012), A Monte Carlo Markov Chain Based Investigation of Black Hole Spin in the Active Galaxy NGC 3783, *ApJ*, *755*(2), 88, doi:10.1088/0004-637X/755/2/88.

Reynolds, C. S., et al. (2015), NuSTAR Observations of the Powerful Radio Galaxy Cygnus A, *ApJ*, *808*(2), 154, doi:10.1088/0004-637X/808/2/154.

Różańska, A., J. Madej, P. Konorski, and A. SaĻowski (2011), Iron lines in model disk spectra of Galactic black hole binaries, *A&A*, *527*, A47, doi:10.1051/0004-6361/201015626.

Różańska, A., J. Malzac, R. Belmont, B. Czerny, and P. O. Petrucci (2015), Warm and optically thick dissipative coronae above accretion disks, *A&A*, *580*, A77, doi:10.1051/0004-6361/201526288.

Różańska, A., B. Bełdycki, J. Madej, and T. P. Adhikari (2018), Effect of the neutron star size on the total spectrum from LMXB, in *XXXVIII Polish Astronomical Society Meeting*, vol. 7, edited by A. Ró&żańska, pp. 285–290.

Seifina, E., L. Titarchuk, and N. Shaposhnikov (2014), Black Hole Mass Determination in the X-Ray Binary 4U 1630-47: Scaling of Spectral and Variability Characteristics, *ApJ*, *789*(1), 57, doi:10.1088/0004-637X/789/1/57.

Shakura, N. I., and R. A. Sunyaev (1973), Black holes in binary systems. Observational appearance., *A&A*, *24*, 337–355.

Shapiro, S. L., A. P. Lightman, and D. M. Eardley (1976), A two-temperature accretion disk model for Cygnus X-1: structure and spectrum., *ApJ*, *204*, 187–199, doi:10.1086/154162.

Shklovsky, I. S. (1967), On the Nature of the Source of X-Ray Emission of Sco XR-1., *ApJ*, *148*, L1, doi:10.1086/180001.

Smale, A. P., K. O. Mason, N. E. White, and M. Gottwald (1988), X-ray observations of the 50-min dipping source XB 1916-053., *MNRAS*, *232*, 647–660, doi:10.1093/mnras/232.3.647.

Smith, R. K., et al. (2016), Arcus: the x-ray grating spectrometer explorer, in *Space Telescopes and Instrumentation 2016: Ultraviolet to Gamma Ray*, *Society of Photo-Optical Instrumentation Engineers (SPIE) Conference Series*, vol. 9905, edited by J.-W. A. den Herder, T. Takahashi, and M. Bautz, p. 99054M, doi:10.1117/12.2231778.

Steiner, J. F., J. E. McClintock, R. A. Remillard, R. Narayan, and L. Gou (2009), Measuring Black Hole Spin Via the X-Ray Continuum-Fitting Method: Beyond the Thermal Dominant State, *ApJ*, *701*(2), L83–L86, doi:10.1088/0004-637X/701/2/L83.

Subroweit, M., E. Mossoux, and A. Eckart (2020), Synchrotron Self-Compton Scattering in Sgr A* Derived from NIR and X-Ray Flare Statistics, *ApJ*, *898*(2), 138, doi:10.3847/1538-4357/ab9947.

Sunyaev, R. A., and L. G. Titarchuk (1980), Comptonization of X-Rays in Plasma Clouds - Typical Radiation Spectra, *A&A*, *86*, 121.

Tashiro, M., et al. (2018), Concept of the X-ray Astronomy Recovery Mission, in *Space Telescopes and Instrumentation 2018: Ultraviolet to Gamma Ray*, *Society of Photo-Optical Instrumentation Engineers (SPIE) Conference Series*, vol. 10699, edited by J.-W. A. den Herder, S. Nikzad, and K. Nakazawa, p. 1069922, doi:10.1117/12.2309455.

Tetarenko, B. E., J. P. Lasota, C. O. Heinke, G. Dubus, and G. R. Sivakoff (2018), Strong disk winds traced throughout outbursts in black-hole X-ray binaries, *Nature*, *554*(7690), 69–72, doi:10.1038/nature25159.

Titarchuk, L. (1994), Generalized Comptonization Models and Application to the Recent High-Energy Observations, *ApJ*, *434*, 570, doi:10.1086/174760.

Tombesi, F., F. Tazaki, R. F. Mushotzky, Y. Ueda, M. Cappi, J. Gofford, J. N. Reeves, and M. Guainazzi (2014), Ultrafast outflows in radio-loud active galactic nuclei, *MNRAS*, *443*(3), 2154–2182, doi:10.1093/mnras/stu1297.

Tomsick, J. A., I. Lapshov, and P. Kaaret (1998), An X-Ray Dip in the X-Ray Transient 4U 1630-47, *ApJ*, *494*(2), 747–752, doi:10.1086/305240.

Tomsick, J. A., S. Corbel, A. Goldwurm, and P. Kaaret (2005), X-Ray Observations of the Black Hole Transient 4U 1630-47 during 2 Years of X-Ray Activity, *ApJ*, *630*(1), 413–429, doi:10.1086/431896.

Trueba, N., J. M. Miller, J. Kaastra, A. Zoghbi, A. C. Fabian, T. Kallman, D. Proga, and J. Raymond (2019), A Comprehensive Chandra Study of the Disk Wind in the Black Hole Candidate 4U 1630-472, *ApJ*, *886*(2), 104, doi:10.3847/1538-4357/ab4f70.

Trueba, N., et al. (2020), A Redshifted Inner Disk Atmosphere and Transient Absorbers in the Ultracompact Neutron Star X-Ray Binary 4U 1916-053, *ApJ*, *899*(1), L16, doi:10.3847/2041-8213/aba9de.

Ueda, Y., K. Yamaoka, and R. Remillard (2009), GRS 1915+105 in "Soft State": Nature of Accretion Disk Wind and Origin of X-ray Emission, *ApJ*, *695*(2), 888–899, doi:10.1088/0004-637X/695/2/888.

Ueda, Y., et al. (2010), Suzaku Observation of GRS 1915+105: Evolution of Accretion Disk Structure during Limit-cycle Oscillation, *ApJ*, *713*(1), 257–268, doi:10.1088/0004-637X/713/1/257.

Vlemmings, W. H. T., et al. (2019), Stringent limits on the magnetic field strength in the disc of TW Hya. ALMA observations of CN polarisation, *A&A*, *624*, L7, doi:10.1051/0004-6361/201935459.

Walter, F. M., K. O. Mason, J. T. Clarke, J. Halpern, J. E. Grindlay, S. Bowyer, and J. P. Henry (1982), Discovery of a 50 MN binary period and a likely 22 magnitude optical counterpart for the X-ray burster 4U 1915-05., *ApJ*, *253*, L67–L71, doi:10.1086/183738.

Wang, Q. D., J. Li, C. M. P. Russell, and J. Cuadra (2020), Colliding winds in and around the stellar group IRS 13E at the galactic centre, *MNRAS*, *492*(2), 2481–2496, doi:10.1093/mnras/stz3624.

Wang, Y., and M. Méndez (2016), The XMM-Newton spectra of the 2012 outburst of the black hole candidate 4U 1630-47 revisited, *MNRAS*, *456*(2), 1579–1586, doi:10.1093/mnras/stv2814.

Waters, T., and D. Proga (2018), Magnetothermal disc winds in X-ray binaries: poloidal magnetic fields suppress thermal winds, *MNRAS*, *481*(2), 2628–2645, doi:10.1093/mnras/sty2398.

White, N. E., and J. H. Swank (1982), The periodic absorption events from 4U 1915-05., *ApJ*, *253*, L61–L66, doi:10.1086/183737.

Wilkins, D. R., and A. C. Fabian (2011), Determination of the X-ray reflection emissivity profile of 1H 0707-495, *MNRAS*, *414*(2), 1269–1277, doi:10.1111/j.1365-2966.2011.18458.x.

Wilkins, D. R., and A. C. Fabian (2012), Understanding X-ray reflection emissivity profiles in AGN: locating the X-ray source, *MNRAS*, *424*(2), 1284–1296, doi:10.1111/j.1365-2966.2012.21308.x.

Wilkins, D. R., and L. C. Gallo (2015), Driving extreme variability: the evolving corona and evidence for jet launching in Markarian 335, *MNRAS*, *449*(1), 129–146, doi:10.1093/mnras/stv162.

Woods, D. T., R. I. Klein, J. I. Castor, C. F. McKee, and J. B. Bell (1996), X-Ray–heated Coronae and Winds from Accretion Disks: Time-dependent Two-dimensional Hydrodynamics with Adaptive Mesh Refinement, *ApJ*, *461*, 767, doi:10.1086/177101.

Yoshida, K., H. Inoue, K. Mitsuda, T. Dotani, and F. Makino (1995), The Dipping Low-Mass X-Ray Binary X1916-05 Observed with GINGA, *PASJ*, *47*, 141–152.

Younes, G., L. Boirin, and B. Sabra (2009), An XMM-Newton view of the dipping low-mass X-ray binary XTE J1710-281, *A&A*, *502*(3), 905–912, doi:10.1051/0004-6361/200811314.

Young, A. J., J. C. Lee, A. C. Fabian, C. S. Reynolds, R. R. Gibson, and C. R. Canizares (2005), A Chandra HETGS Spectral Study of the Iron K Bandpass in MCG -6-30-15: A Narrow View of the Broad Iron Line, *ApJ*, *631*(2), 733–740, doi:10.1086/432607.

Zanni, C., A. Ferrari, R. Rosner, G. Bodo, and S. Massaglia (2007), MHD simulations of jet acceleration from Keplerian accretion disks. The effects of disk resistivity, *A&A*, *469*(3), 811–828, doi:10.1051/0004-6361:20066400.

Zdziarski, A. A., J. Poutanen, J. Mikolajewska, M. Gierlinski, K. Ebisawa, and W. N. Johnson (1998), Broad-band X-ray/gamma-ray spectra and binary parameters of GX 339-4 and their astrophysical implications, *MNRAS*, *301*(2), 435–450, doi:10.1046/j.1365-8711.1998.02021.x.

Zhu, Y., S. W. Davis, R. Narayan, A. K. Kulkarni, R. F. Penna, and J. E. McClintock (2012), The eye of the storm: light from the inner plunging region of black hole accretion discs, *MNRAS*, *424*(4), 2504–2521, doi:10.1111/j.1365-2966.2012.21181.x.

Zoghbi, A., et al. (2016), Disk-Wind Connection during the Heartbeats of GRS 1915+105, *ApJ*, *833*(2), 165, doi:10.3847/1538-4357/833/2/165.